QUASIELASTIC (e,e$'$p) REACTIONS AND PROTON PROPAGATION THROUGH NUCLEI

by

DEREK VAN WESTRUM

B. S., University of Colorado, 1992

A thesis submitted to the

Faculty of the Graduate School of the

University of Colorado in partial fulfillment

of the requirements for the degree of

Doctor of Philosophy

Department of Physics

1998

This thesis for the Doctor of Philosophy degree by

Derek van Westrum

has been approved for the

Department of

Physics

by

____

Edward R. Kinney

____

Donald F. Geesaman

Date ______________________

The final copy of this thesis has been examined by the signators, and we find that both the content and the form meet acceptable presentation standards of scholarly work in the above mentioned discipline.

van Westrum, Derek (Ph. D., Physics)

QUASIELASTIC (e,e′p) REACTIONS AND PROTON PROPAGATION THROUGH NUCLEI

Thesis directed by Associate Professor Edward R. Kinney

Coincidence (e,e′p) cross sections for the quasielastic scattering of electrons from hydrogen, carbon, iron, and gold nuclei were measured at squared four-momentum transfers of 0.64, 1.28, 1.79, and 3.25 $(\mathrm{GeV/c})^2$. By dividing the experimental cross section for a given momentrum transfer and target by the cross section calculated in the Plane Wave Impulse Approximation, the transparency of the nuclear medium to the recoiling proton can be defined. This transparency is studied as a function of momentum transfer and nuclear size.

The goal of the experiment is to study both the quasielastic scattering reaction mechanism and the propagation of protons through atomic nuclei. Where they overlap, the results agree with those measured in previous experiments. The results are used to identify important aspects of the final state interactions between the recoiling proton and residual nucleus, to verify the single-nucleon knockout picture of the reaction, and to provide a baseline for future experiments at higher momentum transfers.

DEDICATION

For Julie. 8.

ACKNOWLEDGMENTS

It is an awesome task to set down on paper a list of all the people who are in some part responsible for where I am today. The categories range from help in solving some problem directly related to my dissertation, to shaping the fundamental ways in which I work and think. Below is my attempt to create such a list.

First and foremost, I would never have made it without the love, affection, and inspiration I get from my wife, Julie. Knowing that she was behind me in whatever I chose to do made some really tough decisions that much easier. The fact that she moved to Virginia with me "for a few months" ha! means I am indebted to her for as long as she will keep me around. Her pep talks, patience, and insistence that I stay artistic in the midst of all this logic and analysis, provided me with a balance for which I will be eternally grateful.

Next, my family. How does one thank their family? I learned at an early age that not every family sits around the table debating religion, science, life, and meaning. Not every father sits his son down to teach him about relativity, imaginary numbers, and unit analysis (especially not lawyer fathers!). Not every family provides the absolute best they can for their son in terms of education, opportunity, and moral support. I cannot even begin to express how thankful I am for what they have done for me.

Outside of my family, I was lucky too. I often wonder what would have happened to me if I had not grown up with Robert "Roudy" Hildreth. I did not realize it at the time, of course, but our friendly scholastic competition from elementary through high school was invaluable. For me, it was Roudy who made it "cool" to do well in school, and that was absurdly important in some of those formative years. I

shudder to think at who I would be now without having known him. It is at least safe to say that without him, there would have been no "Smedley's Van"—arguably the greatest band on earth.

I suppose providence's back up plan for me, had Roudy not been around, is Ken Knowles. Keeping my mind (relatively!) sharp with questions and debates, and keeping my body in shape via mountain bike rides and ski trips, Ken always seems to be up for whatever I feel I need to do to strike a balance in my life. Every graduate student, holed-up in their ivory tower, needs a friend like Ken to "bust them out" every now and then.

Every undergraduate should also be lucky enough to come across a professor like Rod Smythe. If he had not picked me out of his off-semester EM class to work as an undergraduate research assistant in the Nuclear Physics Lab, I never would have even contemplated graduate school. He got me excited about physics by *doing* it as opposed to just reading about it. Second only to my father, Rod was instrumental in teaching me that there is *always* a right way to do something—planning and foresight are values I will always associate with him.

Though Rod Smythe got me into graduate school, it was Eric Belz who kept me there. During the dark ages, when I felt like I knew nothing and was completely overwhelmed, it was Eric who calmed me down, showed me the ropes, and pointed me to what was important. And he was the only person I ever saw ride the whole "monkey skull" stretch above the mine in Left Hand Canyon. Most impressive.

My time at CEBAF (Jeffy Lab!) will always be remembered as being spent with smart, professional, fun people: from the Bobos—Paul Hood, Steve Knight, and Mark Hoegerl—who showed me how hard it is possible to work when the job needs to get done, to the Hall C staffers—Rolf Ent, Joe Mitchell, Steve Wood, Dave Mack, and Bill Vulcan—who tirelessly took deep breaths and pointed this newbie in the right direction. In addition, the graduate students, postdocs, and faculty from

institutions all over the world made my job at CEBAF and my stay in Virginia not only tolerable, but often downright enjoyable. For example, Thia Keppel is simply the coolest: not only for her great parties and her willingness to car-sit, but it was she who suggested living in Ghent—quite possibly the best advice I ever got! Steve Wood introduced me to Linux, which in a very real sense made this thesis possible. And finally, rest assured that Dave Potterveld's willingness and enthusiasm to get my Argonne computer problems solved is not a universal trait. He always helped, no questions asked, and more than once bailed me out.

Bart Terburg deserves special mention as it was he who showed me that the Tidewater area can actually be fun. I will never forget our "Hampton Roads Appreciation Days" or our many forays to Nick's "Fabulous" Sea Food Pavilion. I am grateful that Bart's uncanny knack for being able to have fun anywhere, anytime, turned out to be infectious.

My "big brother" at CEBAF was John Arrington. His long, *in-depth* answers to questions both dumb and deep were always correct and always included some piece of insight that had escaped me. Every time, I got the sense that my question was now his question, and that he wanted to know the answer as badly (if not more so!) than I did. It is actually true that every time the Green Bay Packers play, a little part of me is secretly rooting for them.

The analysis of a nuclear physics experiment is often divided between a few graduate students, and I can safely say that no student has ever been as lucky as me to have a partner like Dipangkar Dutta. Everything about Dipangkar can be summarized in one word: Enthusiasm. No matter how arduous or tedious the task at hand, he would dive right in, working non-stop until it was completed, loving every minute of it. In fact, the uglier the job, the better—he was so excited that we finally got to have our own "Hell Week" in preparation for the PANIC conference. I thought he was sick, of course.

My colleagues back at the University of Colorado were no less instrumental in seeing me through the final stages of my dissertation. The stimulating conversations around the lunch table with Jeff Brack, Jeff Patterson, Gertjan Hofman, Steve Pollock, Greg Rakness, Marc Welliver, Mike "Killer" Keilman, and Andy Saunders were often exactly what I needed to remind me why I was doing all this: to figure out how a little part of the world works. In addition, the kinematics code provided by Jeff Patterson and the LaTeX help that was instantly available from Andy Saunders, are just two examples of the kind of comradery and cooperation among the graduate students that made working at the NPL great. Not to mention Don Edmonds, Dale Prull, and Susan Spika who were always willing to go out of their way to help me however they could.

Then there are the big three: Rolf Ent, Don Geesaman, and Ed Kinney. I hope that I again have the opportunity to work side by side with such greats in a field. Rolf Ent's love of the work is a wonderful inspiration. He has the knowledge and drive to do it all: from complex spectrometer optics problems to slinging lead bags, Rolf was willing to take the weight of the world on his shoulders and get the job done.

The incredible string of good luck I have had throughout my career continued unabated as I somehow managed to be one two graduate students on a Don Geesaman experiment. The freedom he allowed us in exploring whatever aspects of the data we found interesting was amazing, and the trust he placed in our ability to get things done correctly was a most valuable confidence booster. I could not have found a better guide to take me from square one (literally the building of the experimental end station!) to a finished dissertation.

Finally, my thesis advisor, mentor, and good friend, Ed Kinney. "Thanking" him just does not seem adequate. I know for a fact, from the stories of other students about their advisors, that there is no one comparable to Ed. The welfare

and progress of his students is his number one priority, and while examples are too numerous to list in their entirety, here are a few: personally flying out with me to introduce me to CEBAF, getting me to Germany to work on the HERMES experiment for a few weeks (a wonderful opportunity that I am truly thankful for, and one that is woefully absent in the careers of most graduate students), and flying me home from a lonely stay in Virginia to be with my family for the holidays. In addition, Ed trusted me to know what was necessary to get tasks done. Indeed he shipped a computer out to me in Virginia so I could install a new "experimental" Unix system on it. I thought it was the way to go, and he believed me. All of these gestures were taken as signs that Ed thought I was important and what I was doing was important—not many advisors go this far, and I am truly grateful.

CONTENTS

APPENDIX

FIGURES

FIGURE

TABLES

TABLE

CHAPTER 1

INTRODUCTION

1.1 Overview

This work presents the proton propagation results of Experiment E91-013. This section is intended to provide a brief overview of the method and motivation of the experiment. The chapter then continues with a more detailed introduction to electron scattering in general, the plane wave impulse approximation, various theoretical predictions, previous data, and finally a more detailed description of the actual experiment.

The experiment was performed at the Continuous Electron Beam Accelerator Facility (CEBAF, now known as Jefferson Lab) in December, 1995 and May, 1996. The purpose of the experiment is twofold: to study, in detail, the scattering of electrons from bound nucleons, and to study the propagation of nucleons through nuclear matter. This work is focused primarily on the second topic, but during the course of this chapter it will become apparent that, due to the nature of the experimental method used in E91-013, the two aspects are inherently related.

In the simplest model, the propagation of protons through the nucleus can be described by a mean free path, λ. This is the average distance a proton will travel without suffering an interaction with another particle. The mean free path can be written classically as

$$\lambda = \frac{1}{\rho \sigma_{pN}}, \tag{1.1}$$

where ρ is the nucleon density, and σ_{pN} is the proton-nucleon cross section. Given that both the density of nuclear matter and the free proton-nucleon cross sections are well known, it came as a surprise when this estimate of the mean free path, ~ 2 fm, drastically underestimated the experimentally measured value of ~ 6 fm (measured using A(e,e′) and A(p,p), and A(p,2p) reactions). It was found that the large value of λ could only be explained by including a number of nuclear effects; the three most prominent being Pauli blocking of the nucleons that proton scatters from, correlations between the proton and other nucleons, and the non-locality of the nuclear potential. The first effect is simply that nucleons struck by the proton cannot scatter into states that are already occupied, and the second is that short-range correlations between the proton and other nucleons tend to reduce the density near the struck proton. Finally, the non-locality, or energy dependence of the nuclear potential (which is often treated by giving the bound nucleons an effective mass $M^* < M$), reduces the effective cross section for proton-nucleon scattering in the nuclear medium.

In order to study these and other nuclear effects, more recent measurements of proton propagation have studied the A(e,e′p) reaction at relatively high proton kinetic energies (~ 1 GeV) and over a large range of nuclear target sizes. Instead of using the mean free path, which is density dependent, the propagation is now usually quantified via the nuclear transparency, T, defined as the fraction of scattered protons that escape from the nucleus without interaction. T is measured by dividing the number of scattered protons observed experimentally by the number expected assuming that each proton suffers no interaction on its way out of the nucleus.

The reaction, A(e,e′p), takes place as follows: An electron of known energy scatters through an angle θ_e, emitting a virtual photon. The photon imparts its energy and momentum to a bound proton. This proton may or may not undergo further interaction with the residual nucleus. If it does not, it is detected along with the scattered electron. This process can be viewed as using the electron beam to create photons of known energy and momentum (given the electron kinematics) to knock protons out of the nucleus.

The present experiment is the latest in this series of proton propagation studies. Nuclear transparency has been measured on a wide range of target sizes—carbon, iron, and gold—and over a proton kinetic energy range of 300 to 1800 MeV. These energies span the region where the proton-nucleon cross section changes rapidly. Furthermore, this energy range covers the overlap between two regions that have traditionally been described by quite different theoretical methods. The unprecedented precision of these results also allow for the study of other aspects of proton propagation, including off-shell nucleon behavior and the transparency for protons emerging from particular nuclear shells.

The remainder of this chapter discusses electron scattering in general, the A(e,e$'$p) reaction under various approximations and the interactions between the recoiling proton and the residual nucleus. The models used to describe the reaction and a detailed discussion of the cross section for scattering from a bound proton are presented. Next, the results of previous A(e,e$'$p) experiments are presented, followed by an introduction to experiment E91-013. Chapter 2 then discusses the experimental apparatus and calibrations. The extraction of the experimental data and a description of the PWIA calculation of the yields is presented in Chapter 3. Chapter 4 presents the experimental results and uncertainties, followed by a discussion of theoretical calculations and interpretations of various aspects of the experiment.

1.2 Electron Scattering and The A(e,e$'$p) Reaction

The scattering of high energy electrons from nuclei is an excellent way to extract information on both nuclear structure and the properties of bound nucleons. The advantages of using electrons as nuclear probes stem from the weakness of the electromagnetic interaction. First, an electron is able to sample nucleons from anywhere within the nuclear volume. This is to be contrasted with hadronic probes which, due to the strong interaction, are more likely to react with surface nucleons. Second, electrons are able to penetrate the interior of the nucleus without suffering sizeable distortions which is crucial in knowing, for example, the energy of the electron at the reaction vertex. Third, the electron-photon coupling can be calculated to high precision via quantum electrodynamics (QED). Finally, because the photon emitted by the electron is virtual, both the momentum transfer, $\vec{q}$, and the energy transfer, ω, can be varied independently; a real photon must obey the relation $\omega^2 - \vec{q}^{\,2} = 0$. This allows the energy transfer to be adjusted while keeping the momentum large enough such that the photon can resolve individual nucleons. (The four-momentum transfer is written as $q = (\omega, \vec{q})$, and one also defines $Q^2 \equiv -q^2 = \vec{q}^{\,2} - \omega^2$.)

Electron scattering does, however, have its disadvantages as well. Its weak interaction also means very small cross sections, and until recent advances in electron accelerator facilities, this usually resulted in statistically limited data. Also, the tiny mass of the electron means it is susceptible to sizeable energy losses by the bremsstrahlung radiation of photons. These are however, just higher order corrections to the vertex in QED and can be treated theoretically.

A typical measured inclusive electron scattering cross section is shown in Fig. 1.1 as a function of ω. [1] The lowest energy-loss peak, at $\omega \approx 4$ MeV, is due to elastic scattering, in which the nucleus remains in its ground state. Then, as ω increases, the electron starts to excite a series of nuclear states. Finally, at approximately 40 MeV, the electron scatters incoherently from individual nucleons within the nucleus. This is referred to as "quasielastic" scattering, and indeed, at this energy loss $\omega = Q^2/2M$, consistent with electron scattering from a free nucleon of mass M. The quasielastic peak is very wide ($\sim$40 MeV) due to the Fermi motion of the bound nucleons.

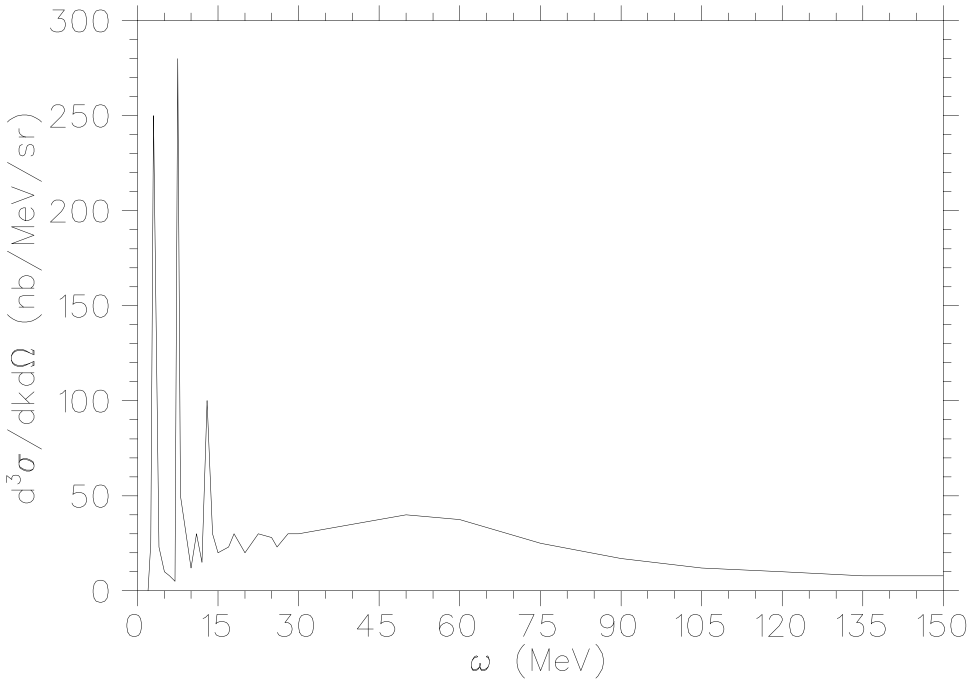

Figure 1.1. Inclusive (e,e′) Cross Section as a Function of Energy Loss, ω. The data are from Saclay. 280 MeV electrons are scattered through 60° on a ^{12}C target ($Q^2 = 0.07$ (GeV/c)^2).

Inclusive quasielastic scattering results have been used to test, and essentially confirm, the single-nucleon knockout picture of the reaction. However, especially at high energy transfers, effects like the excitation of individual nucleons and the emission of pions and multiple nucleons become possible, complicating the picture.

If the recoiling nucleon is detected in coincidence with the scattered electron, additional information on nuclear structure and the properties of bound nucleons can also be obtained. With a few assumptions (all of which are expected to improve at high energies; see the next section), one is able to reconstruct the initial energy and momentum of the detected nucleon. As a simple model of a proton in a nucleus, consider a particle bound in a square-well potential of radius a and depth

V_0:

$$V(r) = \begin{cases} -V_0 & r < a \\ 0 & r > a \end{cases} . \tag{1.2}$$

The solutions of the radial Schrödinger equation,

$$\frac{d^2 R_{nl}}{dr^2} + \frac{2}{r}\frac{dR_{nl}}{dr} - \frac{l(l+1)}{r^2} R_{nl} + \frac{2\mu}{\hbar^2}(V(r) + E_{nl})R_{nl} = 0, \tag{1.3}$$

are spherical Bessel functions,

$$R_{nl}(r) = \begin{cases} Aj_l(k_{nl}r) & r < a \\ Bh_l(i\alpha_{nl}r) & r > a \end{cases} . \tag{1.4}$$

where A and B are constants, μ is the reduced mass of the bound particle, and $k_{nl}^2 = \frac{2\mu}{\hbar^2}(E_{nl} + V_0)$. The eigenenergy of the state labeled by (nl) is E_{nl} and is determined by matching the two solutions and their derivatives at $r = a$. The energy E_{nl} is the energy necessary to remove a particle from the state (nl), and as such, it is often referred to as the "separation energy" for that state. Each state can be occupied by up to $2(2l + 1)$ protons, where the overall factor of 2 comes from the fact that protons are fermions. Starting with the most deeply bound state, a series of shells, each with energy E_{nl}, is formed as protons are added: two protons in the $1s$ state ($l = 0$), six in the $1p$ state ($l = 1$), etc. Although this model is clearly naive, a shell structure is actually observed in nuclei. The ordering of the states is altered, however, due to the shape of the actual potential (not a spherical box) and spin interactions between the nucleons (neglected here).

Figure 1.2 displays the separation energy spectrum measured at Saclay for scattering from ^{12}C. [2] One can clearly distinguish the knockout of protons from two different states: a tall, narrow peak at approximately 16 MeV and a much broader peak centered at approximately 38 MeV. The shell model predicts that the most deeply bound state is the $1s$, followed by the $1p$. Figure 1.3 shows the two momentum distributions obtained by integrating over the two peaks in Fig. 1.2. As

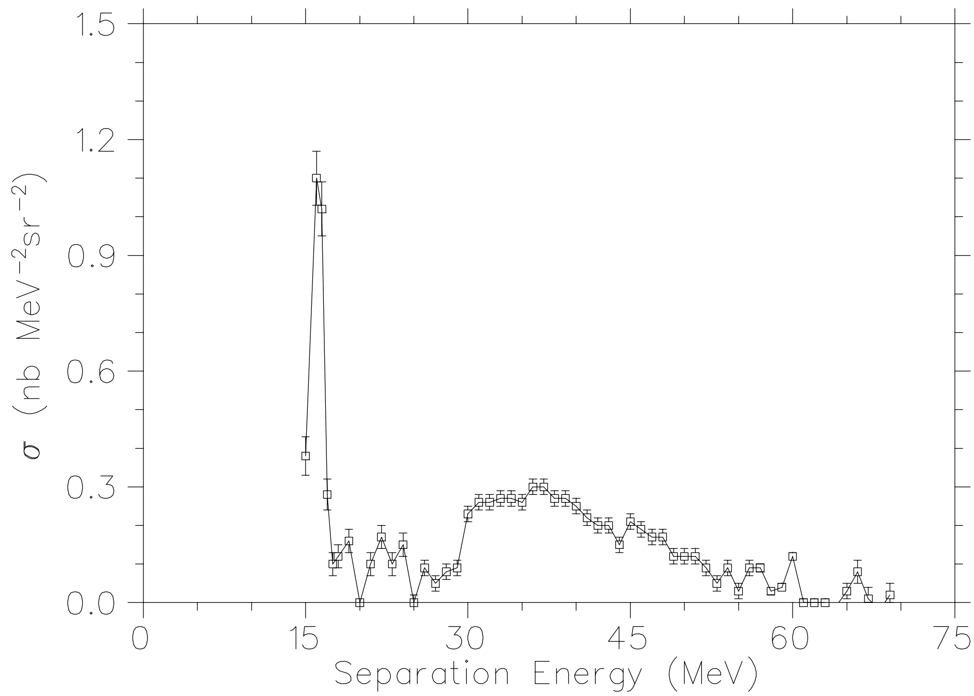

Figure 1.2. Carbon Separation Energy Spectrum. The data are from Ref 2; 497 MeV electron beam scattered from a ^{12}C target through 52.9°. The line is meant only to guide the eye.

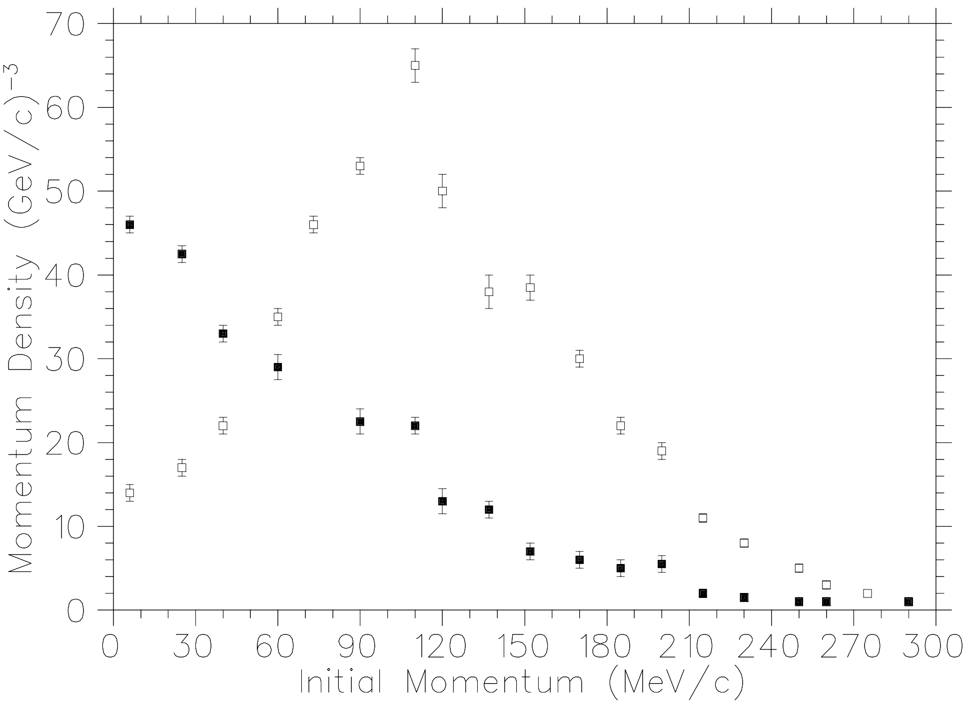

Figure 1.3. Carbon Initial Momentum Spectra from Ref. 2. The $1p$ state (separation energy 15–21.5 MeV) is shown in open squares, and the $1s$ state (separation energy 30–50 MeV) is shown in filled squares.

expected, the more deeply bound state has strength at zero momentum, consistent with $l = 0$, while the other state reaches a maximum at higher momentum ($l = 1$). The $1s$ hole state in the residual ^{11}B nucleus has a wider distribution in separation energy than the $1p$. This is due to the fact that the $1s$ state is embedded in a high density of more complicated states and thus, with the increased mixing, has a shorter lifetime. It was A(e,e′p) results like these that were said to "prove the literal truth of the shell model". [3]

1.3 The A(e,e′p) Reaction in the Plane Wave Impulse Approximation

In the so-called Plane Wave Impulse Approximation (PWIA), the A(e,e′p) reaction takes place as follows: [1, 4] In the reference frame of the laboratory, an electron with four-momentum $k = (\varepsilon, \vec{k})$ scatters through an angle θ_e to a momentum $k' = (\varepsilon', \vec{k'})$, emitting a single virtual photon with a four-momentum $q = (\omega, \vec{q}) = k - k'$. Here, neglecting the mass of the electron, the invariant momentum transfer squared, Q^2, can be written as

$$Q^2 = 4\varepsilon\varepsilon' \sin^2 \frac{\theta_e}{2}. \tag{1.5}$$

The photon interacts with a bound proton of momentum $p = (E, \vec{p}\,')$ which exits the nucleus without further interaction with final momentum $p' = (E', \vec{p}\,')$. The remaining $A - 1$ nucleus, possibly in an excited state and recoiling with momentum p_r, is undetected. The reaction is shown schematically in Figure 1.4. The PWIA is comprised of the following approximations and assumptions: only one photon is exchanged (the Born approximation), the reaction occurs quickly enough such that the dynamics of the residual nucleons can be neglected (Impulse Approximation), both the electron and proton can be described by plane-waves (Plane Wave Approximation), and that the proton undergoes no final state interactions (FSI) as it traverses the nuclear medium.

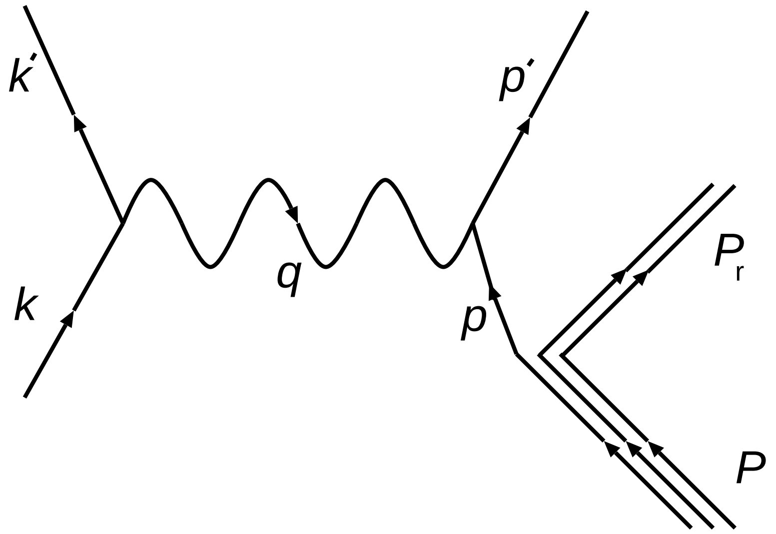

Figure 1.4. Plane Wave Impulse Approximation. The initial (final) electron momentum is denoted by k (k'), and the initial (final) proton momentum is denoted by p (p'). The momentum transfer is $q = k - k' = (\omega, \vec{q})$.

One can define the "missing" momentum as

$$\vec{p}_m \equiv \vec{p}\,' - \vec{q}, \tag{1.6}$$

which, under the PWIA (neglecting FSI) is equal to the initial momentum of the bound proton, $\vec{p}$ (and opposite to the momentum of the residual nucleus). The missing energy, defined as

$$E_m \equiv \omega - T' - T_r, \tag{1.7}$$

is the energy required to remove the proton from the nucleus (the separation energy). Here $\omega = \epsilon - \epsilon'$ and T' is the kinetic energy of the struck proton.

Because of the inherent quantum-mechanical motion of the initial protons, the final state protons are emitted over a wide range of angles and momenta. One can detect the entire initial-momentum distribution by either keeping the electron kinematics fixed, and detecting the protons over a range of angles, or by adjusting the electron kinematics such that only fixed final proton momenta (parallel to the virtual photon direction) are selected. The two methods are known as "perpendicular"

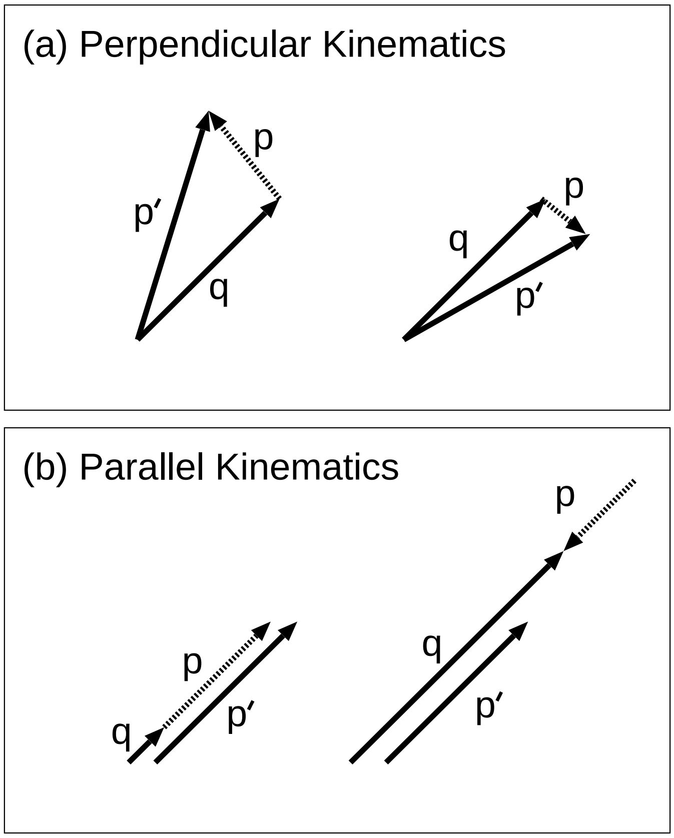

Figure 1.5. Perpendicular and Parallel Kinematics. The momentum transfer, $\vec{q}$, and the final proton momentum, $\vec{p}\,'$, are the two measured quantities (solid). They are used to infer the initial proton momentum, $\vec{p}$ (dashed). Part (a) shows two examples of perpendicular kinematics with the same $\vec{q}$. Here $\vec{p}$ is roughly perpendicular to $\vec{q}$, which is held fixed, and the proton detector is moved in angle to detect the final (and given $\vec{q}$, the initial) proton momentum distribution. Part (b) shows two examples of parallel kinematics with the same $\vec{p}\,'$. In this case, the initial proton momentum is parallel (or antiparallel) to $\vec{q}$, and the proton distribution is mapped by adjusting the electron kinematics so as to keep the proton detector fixed.

and "parallel" kinematics, respectively, in reference to the angle between the initial proton's momentum and the momentum transfer (Figure 1.5).

The combined probability of finding a bound proton with momentum $\vec{p}_m$ and separation energy, E_m, is referred to as the spectral function, $S(\vec{p}_m, E_m)$. In the Independent Particle Shell Model (IPSM), in which the bound nucleons are assumed to be non-interacting and fill distinct orbitals (with quantum numbers labeled by α), the spectral function appears as

$$S(\vec{p}_m, E_m) = \sum_{\alpha} N_\alpha |\phi_\alpha(\vec{p}_m)|^2 \mathcal{L}_\alpha(E_m), \tag{1.8}$$

where N_α is the orbital occupation number, $\phi_\alpha(\vec{p}_m)$ is the momentum-space wave function, and $\mathcal{L}_\alpha(E_m)$ is the separation energy distribution of the state α.

In the PWIA, the cross section for A(e,e′p) scattering can simply be written as the product of $S(\vec{p}_m, E_m)$, the probability of finding a bound proton with energy and momentum E_m and $\vec{p}_m$, times σ_{ep}, the cross section for electron scattering from such a proton: [1]

$$\frac{d^6\sigma}{dE' d\Omega_e dE_{p'} d\Omega_{p'}} = E' p' \sigma_{ep}(\vec{p}_m, E_m) S(\vec{p}_m, E_m). \tag{1.9}$$

1.3.1 Off-Shell Cross Section As was mentioned, in the IPSM the nucleons are considered free particles. However, this neglects the fact that they are bound and hence off-shell, meaning that in general, $E^2 \neq \vec{p}^{\,2} + M^2$ (Note that the initial proton momentum, $\vec{p}$ and the missing momentum, $\vec{p}_m$ are taken to be equivalent). The cross section for electron scattering from a bound proton necessarily depends on the proton's initial energy, and one is left with the choice of using either $E = M - E_s$ (where E_s is the separation energy, and the kinetic energy of the recoiling nucleus is neglected), or assuming $E^2 = \vec{p}^{\,2} + M^2$; the two are not equal in general. Another complication arises in the calculation of the photon-proton vertex in the (e,e′p) reaction. The assumption is usually made that the electromagnetic nuclear current, $J = (\rho, \vec{J})$, can be described by the sum of the individual, non-interacting, nucleon currents. Conservation of the nuclear current, however, implies the existence of both exchange currents between the nucleons and correlated nucleon momenta; both of which are ignored by construction in the IPSM. These ambiguities cannot be resolved without a complete, field-theoretic description of the nuclear current, which depends on the dynamic interactions of all the nucleons. Because this is an extremely difficult task, various sets of approximations and assumptions have to be employed, resulting in several off-shell cross section prescriptions.

The most often used off-shell prescription is "σ_{cc1}" of de Forest. [6] The "cc" refers to the fact that current conservation, $\vec{q} \cdot \vec{J} = \omega\rho$, is maintained, albeit in an *ad hoc* manner, by using it to eliminate the explicit dependence on the longitudinal component of the current. Here $\vec{J}$ is the nuclear current and ρ is the nuclear charge density. On-shell, relativistic Dirac spinors are employed, and the kinematics are adjusted by

$$\begin{aligned} \bar{\omega} &\equiv E' - \bar{E} \\ \bar{q} &\equiv (\bar{\omega}, \vec{q}) \\ \bar{Q}^2 &\equiv -\bar{q}^2 = \vec{q}^{\,2} - \bar{\omega}^2, \end{aligned} \tag{1.10}$$

where $\bar{E} \equiv \sqrt{\vec{p}^{\,2} + M^2}$. The cross section appears as

$$\begin{aligned} \sigma_{ep} &= \sigma_{\mathrm{Mott}} \left[\lambda^2 W_C + \left(\frac{\lambda}{2} + \tan^2 \frac{\theta}{2} \right) W_T + \lambda \left(\lambda + \tan^2 \frac{\theta}{2} \right)^{1/2} W_I \cos\phi \right. \\ &\quad \left. + \left(\lambda \cos^2\phi + \tan^2 \frac{\theta}{2} \right) W_S \right], \end{aligned} \tag{1.11}$$

where $\lambda = \frac{Q^2}{|\vec{q}|^2}$, $\theta = \cos^{-1}(\hat{k} \cdot \hat{k}')$, and $\phi = \cos^{-1}[(\hat{q} \times \hat{k}) \cdot (\hat{q} \times \hat{p}')]$. The cross section for the Coulomb scattering of electrons from a point-like, spin 1/2, infinitely massive object of charge e, is given by the Mott cross section,

$$\sigma_{\mathrm{Mott}} = \frac{4\alpha^2}{Q^2} (\varepsilon')^2 \cos^2 \frac{\theta}{2} = \frac{\alpha^2 \cos^2 \frac{\theta}{2}}{4\varepsilon^2 \sin^4 \frac{\theta}{2}}. \tag{1.12}$$

The W_X's in Eqn. 1.11 contain the nucleon structure information. In σ_{cc1} they appear as

$$
\begin{aligned}
W_C &= \frac{1}{4\bar{E}E'}\left[(\bar{E}+E')^2\left(F_1^2+\frac{\bar{q}^2}{4M^2}\kappa^2F_2^2\right)-\bar{q}^2(F_1+\kappa F_2)^2\right], \qquad (1.13)\\
W_T &= \frac{\bar{q}^2}{2\bar{E}E'}(F_1+\kappa F_2)^2,\\
W_S &= \frac{p'^2\sin^2\gamma}{\bar{E}E'}\left(F_1^2+\frac{\bar{q}^2}{4M^2}\kappa^2F_2^2\right),\\
W_I &= -\frac{p'\sin\gamma}{\bar{E}E'}(\bar{E}+E')\left(F_1^2+\frac{\bar{q}^2}{4M^2}\kappa^2F_2^2\right).
\end{aligned}
$$

Here κ is the anomalous magnetic moment of the proton, γ is the angle between $\vec{p}\,'$ and $\vec{q}$, and $F_1(\bar{Q}^2)$ and $F_2(\bar{Q}^2)$ are the usual, on-shell Dirac and Pauli nucleon form factors, respectively. The structure functions W_C, W_T, W_S, and W_I, arise from the various interactions of the electron current with the nucleon current: the longitudinal Coulomb interaction, the transverse magnetic interaction, the longitudinal-transverse interference, and the transverse-transverse interference, respectively. Finally, note that the explicit dependence of the cross section on E_m and $\vec{p}_m$ has been replaced by the equivalent dependence on q, $\vec{p}\,'$ and ω (Eqns. 1.6 and 1.7).

Although the σ_{cc1} prescription of de Forest is the most popular off-shell cross section, it is one of many, each of which handles the nuclear wave functions, off-shell kinematics, and current conservation in different ways. As discussed by Pollock *et al.*, for example, the apparent agreement between two different prescriptions cannot be taken as a sign that the models are accurate. [7] A complete discussion of the ambiguities inherent in off-shell cross section calculations is provided by Naus in Ref. 8.

1.4 Final State Interactions

Although the PWIA successfully describes the gross features of the A(e,e′p) reaction, it has its limitations. The most important effect neglected in the PWIA is the interaction of the struck proton with the residual nucleus. Large angle proton-nucleon scatterings or inelastic pion production, for example, cause a loss of this proton flux. By removing protons from the quasielastic channel, these final state interactions cause the experimental A(e,e′p) yield to be smaller than the PWIA prediction. Nuclear transparency, defined to quantify this reduction, is described below, followed by an introduction to the Distorted Wave Impulse (DWIA) and Glauber approximations—two common ways to treat FSI theoretically.

1.4.1 Nuclear Transparency A simple way to quantify the reduced experimental yield relative to the PWIA prediction is via the nuclear transparency, T, defined as

$$T \equiv \frac{\int_V d\vec{p}_m dE_m N^{exp}(E_m, \vec{p}_m)}{\int_V d\vec{p}_m dE_m N^{PWIA}(E_m, \vec{p}_m)}. \tag{1.14}$$

The experimental and PWIA-calculation yields are given by N^{exp} and N^{PWIA}, respectively, and V is the experimental acceptance. The transparency is interpreted as the probability that a proton will emerge from the nucleus without suffering a collision.

One expects the transparency to decrease as the the size of the nucleus increases, as the longer (on average) exit path provides more scattering chances. As a function of proton momentum, the transparency can be expected to mirror, approximately, the momentum dependence of the proton-nucleon cross sections, shown in Fig. 1.6. [9] For example, where the cross sections reach their maximum, the transparency can be expected to be small due to the increased reaction probability.

1.4.2 Nuclear Effects Although nuclear transparency is conceptually simple, theoretical calculations require the inclusion of various nuclear effects to obtain agreement with experimental nuclear transparency data. These effects can include Pauli blocking, nucleon-nucleon correlations, and spin-orbit interactions. [15] Coulomb distortion of the electron wave functions also becomes important for large Z nuclei. Note that some of these are effectively included in the DWIA [16]. Although a brief description is provided here, a full discussion of these effects is given in Section 4.4 in the description of the various nuclear transparency calculations.

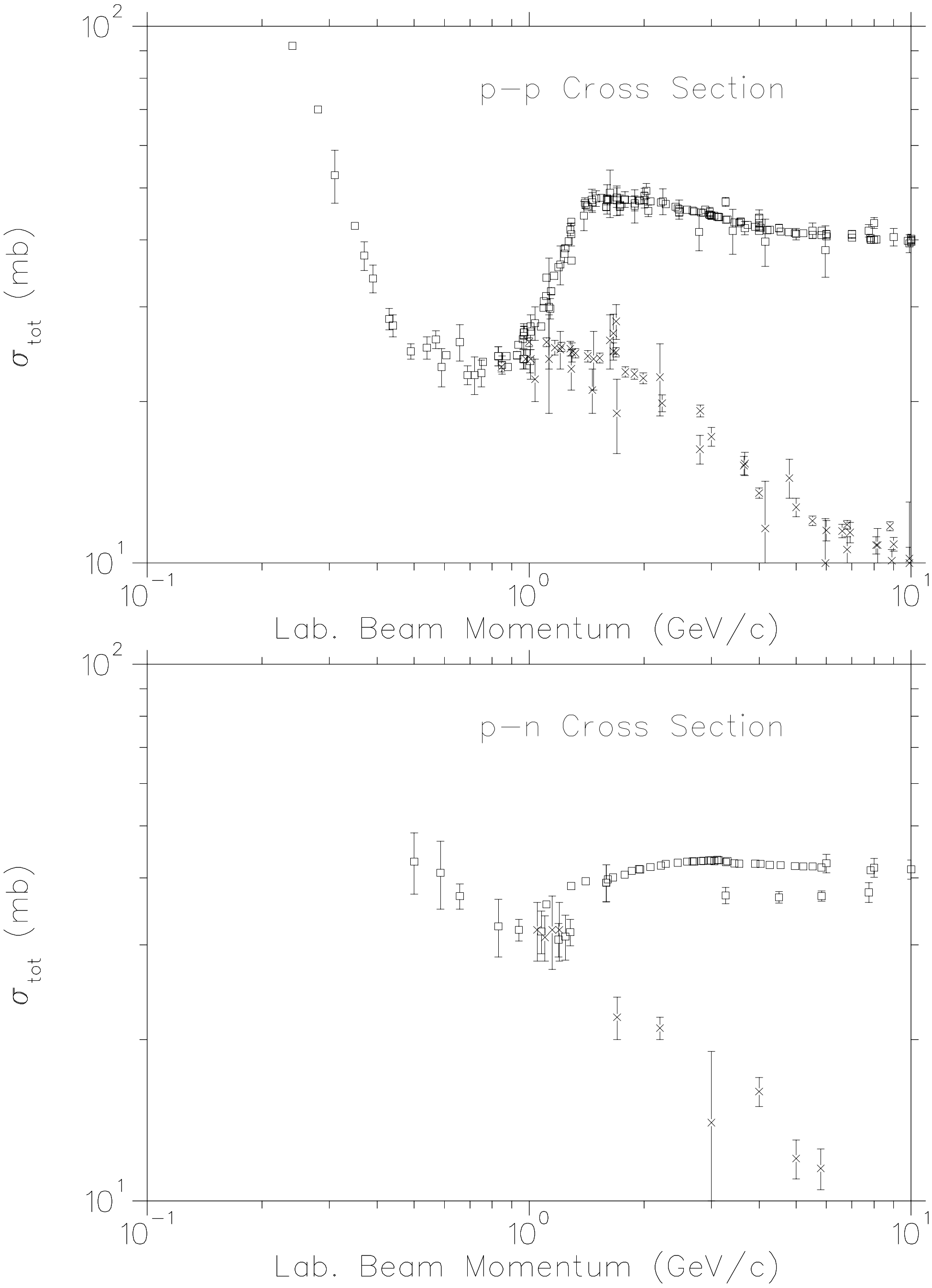

Figure 1.6. Proton–Nucleon Cross Section as a Function of Laboratory Momentum. The upper (lower) panel displays the total proton–proton(neutron) cross section. The squares (Xs) are the total (elastic) cross sections. The data are from Ref. 9

Pauli blocking refers to the fact that a small angle rescattering of the proton will only transfer a small momentum to a bound nucleon. This is not possible if the "would-be" final state of the nucleon is already occupied. The net result is that small angle rescatterings of the proton are suppressed, and the proton thus travels farther than would otherwise be expected, thereby increasing the transparency of the nucleus. (Note that large angle scatterings, which can conceivably scatter nucleons into unoccupied states, result in protons outside of the experimental acceptance.) Because of the highly repulsive nature of the nucleon-nucleon interaction at small distances, it is possible for two initial-state nucleons to scatter from each other (and are thus "correlated") with extremely large momenta. This causes a net decrease in the spectral function below the Fermi momentum, decreasing the interaction probability, and again, increasing the transparency. As was mentioned previously, a detailed calculation must take the spin-orbit interaction between the recoiling proton and residual nucleus into account, as it causes an asymmetry in the momentum distributions around $\vec{q}$. Finally, the non-locality, or equivalently, the momentum-dependence, of the nuclear potential must also be treated.

The final nuclear effect discussed here is the concept of "color transparency" (CT). Perturbative QCD calculations of hadron propagation through nuclear matter predict that, at high energies, the color forces responsible for the FSI between the nucleon and the residual nucleus become negligible. [17] The argument is based on three assumptions: [18] One, at the time of interaction, the nucleon must have fluctuated to a small size. This is due to the fact that the quark that absorbs the photon must be within a distance $1/Q$ from the other two quarks in the nucleon to be able to "communicate" the momentum transfer. Otherwise, this quark will most likely be stripped from the proton causing the formation of hadronic jets. The second assumption is that, because the nucleon is small, it undergoes a weakened interaction with the nucleus. Finally, it is assumed that due to its large kinetic energy after the

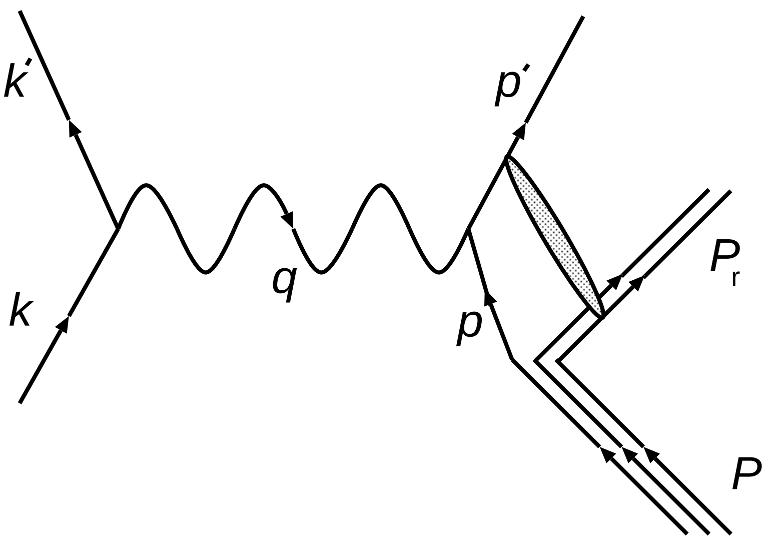

Figure 1.7: Distorted Wave Impulse Approximation.

reaction, the nucleon does not have time to fluctuate back to "normal" size until after it has left the nucleus. That is, time dilation implies that in the rest frame of the residual nucleus, the nucleon stays in its reduced-size state for a longer time.

1.4.3 Distorted Wave Impulse Approximation The most common way to treat FSI effects theoretically and still use the formalism of the PWIA, is to modify the wave function of the struck proton via an interaction with a complex, optical model potential. This constitutes the Distorted Wave Impulse Approximation, or DWIA, shown schematically in Fig. 1.7. If one neglects the spin-orbit interaction between the proton and the residual nucleus, one still has the simple cross section form of Eqn. 1.9, but $S(\vec{p}_m, E_m)$ is replaced by a distorted spectral function, $S^D(\vec{p}_m, E_m, \vec{p}\,')$ that depends explicitly on the scattered proton's momentum, p': [2]

$$S^D(\vec{p}_m, E_m, \vec{p}\,') = \sum_\alpha N_\alpha \mathcal{L}_\alpha(E_m - E_\alpha) \left| \phi^D_\alpha(\vec{p}_m, \vec{p}\,') \right|^2 . \qquad (1.15)$$

Here, N_α and E_α are the orbital occupancy and separation energy for the state $\alpha = (n, l, j)$, respectively. The distorted momentum amplitude, $\phi^D_\alpha(\vec{p}_m, \vec{p}\,')$, is given by

$$\phi_\alpha^D(\vec{p}_m,\vec{p}\,') = \frac{1}{(2\pi)^{3/2}} \int d^3r \chi_k^{-*}(\vec{r}) \exp\left(i\vec{q}\cdot\frac{A-1}{A}\vec{r}\right)\phi_\alpha(\vec{r}), \tag{1.16}$$

for a spin 0 nucleus. Here $\phi_\alpha(\vec{r})$ describes the initial bound state of the nuclear mean field and satisfies,

$$\left[-\frac{\hbar^2}{2m}\nabla^2 + V(r)\right]\phi_\alpha(\vec{r}) = E_\alpha\phi_\alpha(\vec{r}). \tag{1.17}$$

The single particle potential, $V(r)$, is usually taken to be a Woods-Saxon shape (consisting of a volume term, a Coulomb term, and a spin-orbit term).

In Eqn. 1.16, $\chi_k^{-*}(\vec{r})$ is the distorted wavefunction for the emission of a proton with final momentum $\vec{p}\,'$ from position $\vec{r}$. Note that the momentum of the proton relative to the nucleus is given by

$$\vec{k} = \frac{1}{A}[(A-1)\vec{p}\,' - \vec{p}_m], \tag{1.18}$$

and should not be confused with the electron momentum. The scattered proton wave, $\chi_k^{-*}(\vec{r})$, is also assumed to satisfy a Schrödinger equation with a complex optical potential given by

$$U_{\text{opt}} = V\left[1+\exp\left(\frac{r-R}{a}\right)\right]^{-1} + iW\left[1+\exp\left(\frac{r-R'}{a'}\right)\right]^{-1} + V_C. \tag{1.19}$$

The optical potential, $U_{opt}(r)$, contains both real and imaginary central terms and a real Coulomb potential. The parameters for the various terms in $U_{opt}(r)$ are derived from both proton-nucleus total and elastic cross section data. The main effect of the real part of the optical model potential is a distortion of the proton's kinematic variables which results in a net shift in the PWIA momentum distribution to smaller momentum. The imaginary part results in a reduction of the cross section by 30–50%. [4]

As was mentioned, the simple, factorized form of Eqn. 1.8 is possible only if both the spin-orbit interaction of the proton with the residual nucleus and the $\vec{p}$-dependence of the nuclear current are neglected. Boffi *et al.* discuss these effects and find that, in the case of the ^{12}C $1p$ shell, the factorization approximations cause an increase in the asymmetry of the missing momentum distributions about $\vec{p}_m = 0$. [11, 12] The cross section at negative (positive) missing momentum is decreased (increased) by 5–10%, although the magnitude depends on the details of the optical model and on the kinematics ("negative" missing momentum in this case refers to protons detected between $\vec{q}$ and the direction of the beam, while "positive" refers to protons detected at angles larger then $\vec{q}$—See Section 2.1). Boffi *et al.* conclude that the factorized form is a "reasonable first order approximation," but the spin-orbit interaction and $\vec{p}$-dependence of the nuclear current often need to be explicitly included to obtain agreement with experimental cross sections. Note, however, that when integrating over the entire missing momentum distribution, the effect of the increased asymmetry is reduced, and the change in the total cross section is expected to be a few percent at most.

The theoretical calculation of T in the DWIA is similar in form to that of the experimental definition, Eqn. 1.14. The transparency is taken to be the ratio of the DWIA and PWIA cross sections, integrated over missing energy and momentum:

$$T_w = \frac{\int dE_m \int d\vec{p}_m \sigma_{ep}(E_m, \vec{p}_m) S^D(E_m, \vec{p}_m, \vec{p}\,')}{\int dE_m \int d\vec{p}_m \sigma_{ep}(E_m, \vec{p}_m) S(E_m, \vec{p}_m)}. \tag{1.20}$$

1.4.4 The Glauber Approximation The transparency can also be calculated in the Glauber, or high-energy, approximation [13]. When the momentum of the struck proton is much larger than that of the nucleons in the residual nucleus ("spectator" nucleons), the change in the proton's momentum due to coherent rescattering is small. Thus the proton undergoes a negligible deflection, and its trajectory can be approximated by a straight line (the so-called eikonal approximation). In addition, because the time it takes the proton to traverse the nucleus is so small, the spectator nucleons can be approximated by fixed scattering centers. Under these approximations, the classical transparency of the nucleus is given by the probability that the path of the proton out of the nucleus contains no nucleons.

This path can be thought of as a "tube" with cross sectional area σ, given by

$$\sigma = \frac{1}{A}(Z\sigma_{pp} + N\sigma_{pn}), \tag{1.21}$$

where σ_{pp} and σ_{pn} are the proton-proton and proton-neutron cross sections, respectively (Note that depending on the specific calculation, either the total or reaction cross sections are used. See Section 4.4). If the proton is emitted at position $\vec{r}$ with momentum $\vec{p}\,'$, the Glauber transparency is given by: [14]

$$T = \frac{1}{Z}\int d^3r\rho_p(\vec{r})P(\vec{r}), \tag{1.22}$$

where $\rho_p(\vec{r})$ is the proton density at position $\vec{r}$, and P, generally a function of $\vec{r}$ and $\hat{p}'$, is the probability that no nucleons are on the proton's path:

$$P(\vec{r},\hat{p}') = \exp\left[-\int_0^\infty ds\rho(\vec{r}+\hat{p}'s)\sigma\right]. \tag{1.23}$$

Here s is the distance along the exit path of the proton (moving in the direction $\hat{p}'$), and $\rho(\vec{r}+\hat{p}'s)$, is the density of the (uncorrelated) nucleons in the residual nucleus at position $\vec{r}+\hat{p}'s$ along the exit path. The dependence of P on $\hat{p}'$ is usually neglected however, because at large momentum-transfer $\hat{p}'$ is approximately parallel to $\hat{q}$ (and the dependence of T on $\vec{q}$ is left implicit). The interpretation is that the transparency is the probability of no nucleons being on the proton's exit path integrated over all paths (weighted by the nucleon density).

Refinements to this simple picture include the effects of both the nucleon-nucleon correlations and Pauli blocking. The details of specific Glauber approximation calculations can be found in Section 4.4.

1.5 Previous Data

The first A(e,e′p) experiments were performed at Frascati in 1964 to study the validity of the shell model. Since then, such experiments have been performed at Saclay, NIKHEF, SLAC, MIT-Bates, Mainz, and more recently, CEBAF. Recent reviews of theoretical calculations and experimental results of the A(e,e$'$N) reaction are provided in Refs. 4 and 5. In addition, there exists the comprehensive review of Frullani and Mougey in Ref. 1.

The first A(e,e$'$p) experiment to study a relatively large region of missing energy for a variety of targets was performed by Mougey *et al.* at Saclay in 1975 [2]. Electrons with an incident energy of 497 MeV were scattered from ^{12}C, ^{28}Si, ^{40}Ca, and ^{56}Ni. The experiment was able to cleanly separate the $1p$ and $1s$ shells in ^{12}C(Fig. 1.2) where, as discussed earlier, their identities were confirmed through a momentum distribution analysis. The experimental resolution of 1.2 MeV in the ^{12}C missing energy spectrum also enabled the separation of the first two excited states in ^{11}B (Fig. 1.2). Using the shell model to predict normally occupied states, missing energy distributions were fit to each shell in each target. The striking result was the size of the widths of the deeply bound shells, some of which approached $\sim$40 MeV. The analysis of the data performed by Mougey *et al.* pioneered the DWIA description of the A(e,e$'$p) reaction.

The 1980s saw much study of the ^{12}C(e,e$'$p) reaction, with experiments performed at NIKHEF, and MIT-Bates. The experiments can be roughly divided into two classes. The first set consisted of high resolution experiments [19–22] performed at NIKHEF to study the knockout of protons from nuclear shells near the Fermi surface. Figure 1.8 shows the excitation energy (E_x) spectrum of the residual ^{11}B nucleus. Knockout from the $1p$ shell gives rise to three states at $E_x = 0$, 2.125, and 5.020 MeV ($\frac{3}{2}^-$ ground state, $\frac{1}{2}^-$, and $\frac{3}{2}^-$, respectively). Between 6 and 12 MeV there also exist a series of states corresponding to knockout from normally unoccupied 1d, 2s, and 1f shells. The role of two-step processes (proton knockout, followed by inelastic excitation of the ^{11}B nucleus) was determined to be a small effect [20], so the population of these normally unoccupied states was used to measure the role of nucleon-nucleon correlations in the ^{12}C nucleus. The conclusion that "long-range"

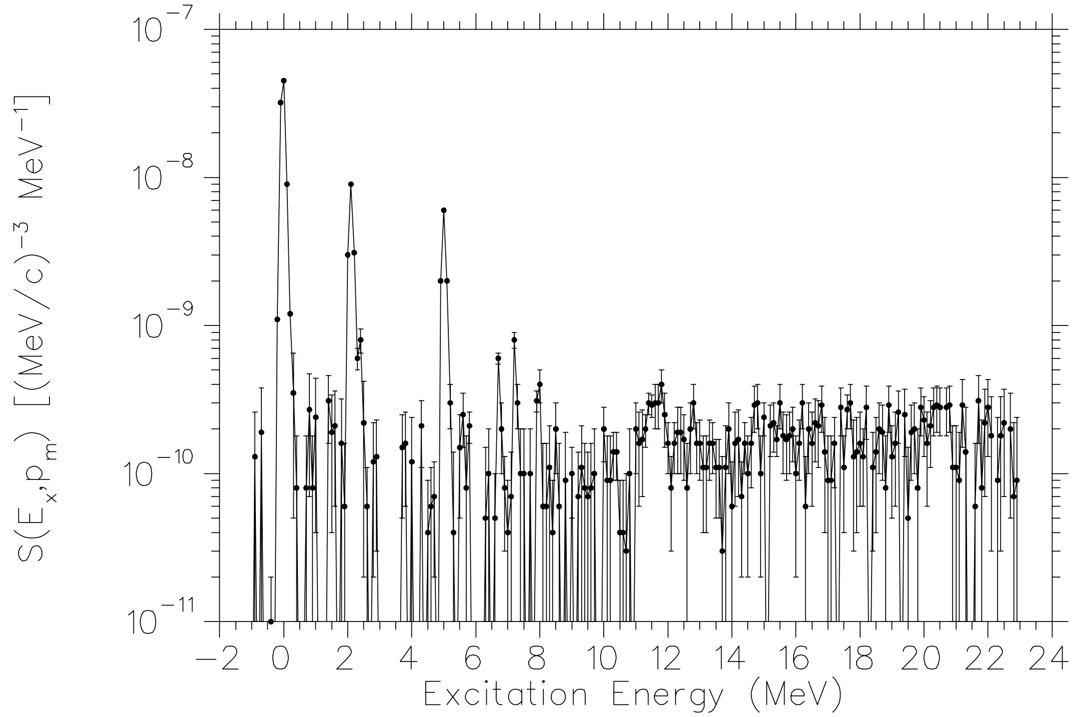

Figure 1.8. Previous Data: Proton Knockout from the ^{12}C 1p Shell. Shown is the excitation energy spectrum of the reaction ^{12}C(e,e′p)^{11}B at a central missing momentum of 172 MeV/c. The bin width is 100 keV. The data are from NIKHEF [22].

correlations populate the states above the Fermi level at the expense of the valence states below the Fermi level was subsequently verified on a wide range of targets. Here, "long-range" refers to a distance of a few fermis where, when compared with the strongly repulsive core at small distances, the nucleon-nucleon interaction is relatively weak. It is the repulsive core that gives rise to the "short-range" correlations (and high momenta) discussed in earlier in Section 1.4.2. Figure 1.9 shows the ratio of observed occupancy of the valence orbitals to the shell model prediction as a function of target mass. [24] In addition to the long-range correlations, knockout data from both the $1p$ and $1s$ shells of carbon were used to support the idea that the short-range correlations cause a uniform depletion of all shells, as strength is moved to higher missing energies and momenta. Again, this is has been verified on a wide range of targets, and is known as the violation of the "spectroscopic sum rule," in reference to the lack of observed strength relative to that expected in the shell model. As is seen in Fig. 1.9, the combination of the both the long and short-range correlations is approximately 35%, independent of target size. Comparing the spectroscopic factors of both the valence and more deeply bound states, it has been concluded that roughly 10% of the depletion is due to the long-range correlations, and the other 25% is due to the short-range correlations. [23] Further discussion of the correlation effect its various theoretical predictions will appear in Section 4.3.3.

The second set of ^{12}C(e,e$'$p) experiments focused on the separation of the longitudinal and transverse structure functions in order to study the quasifree reaction mechanism. The inclusive ^{12}C(e,e$'$) data of Barreau *et al.* showed a ratio of transverse to longitudinal strength 60% in excess of that expected in the impulse approximation (and assuming that the nuclear medium does not affect the structure of the nucleon). [25] Calculations that included effects such as correlations, final state interactions, and the possible modification of off-shell nucleon form factors could not describe the data, and therefore, coincidence (e,e$'$p) experiments were employed to

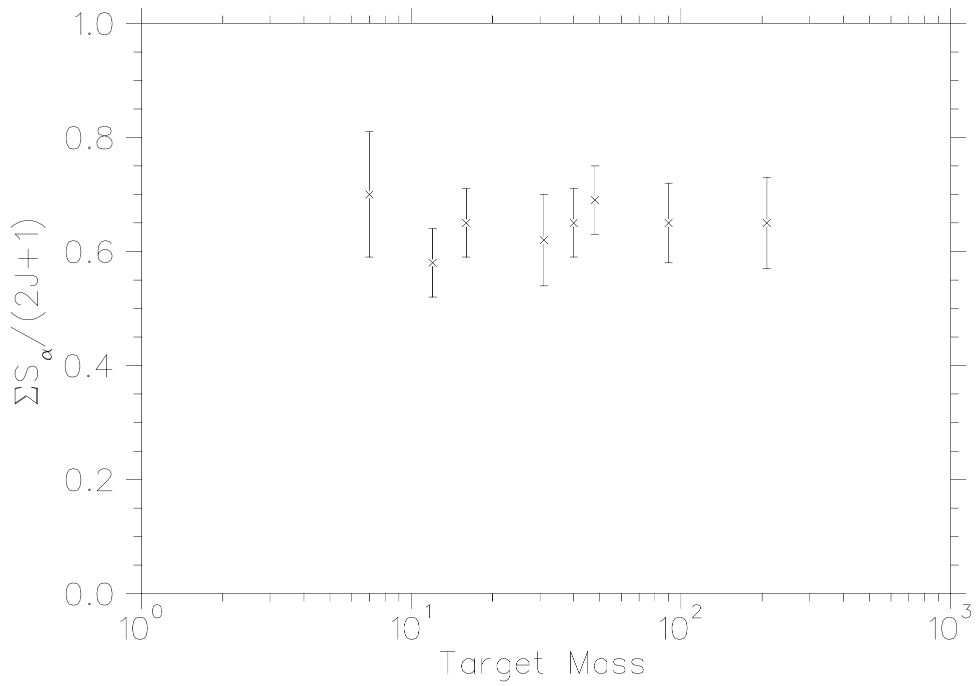

Figure 1.9. Spectroscopic Factors as a Function of A. Plotted is the ratio of the observed occupancy of valence states to that expected in the shell model, as a function of target mass. The data are from Ref. 24.

study the reaction mechanism. These experiments were performed at both MIT-Bates and NIKHEF in various kinematical regimes. An L-T separation analysis performed by van der Steenhoven *et al.* at NIKHEF was used to conclude that the ratio of the magnetic and electric form factors,

$$R_G = [(4M^2/Q^2)W_T/W_L]^{1/2} \propto G_M/G_E,$$

for a bound proton is approximately 20% greater than that of a free proton. [26] However, it was discovered that these results were based on a poor approximation, and it was later concluded that there is at most a 10% enhancement in the ratio of G_M/G_E. [23]

At missing energies above $E_{m,\mathrm{th}}$, it is possible to remove two nucleons from the nucleus. This process is expected to be mainly transverse in character, as it most likely entails scattering from the meson exchange currents (MECs) between the two (correlated) nucleons. The first experiment to find evidence of such processes was performed by Ulmer *et al.* at MIT-Bates. [27] As shown in Fig. 1.10, above $E_{m,\mathrm{th}}$ the transverse response, R_T, has a small peak presumably due to scattering from the $1s$ state, followed by uniform strength up to the highest missing energies detected. That the strength near $E_m \sim 40$ MeV is due to the scattering from 1s protons is confirmed by an identical peak in the longitudinal response, R_L, which is expected to be dominated by single particle knockout. The excess strength confirmed an earlier MIT-Bates experiment that measured scattering in the dip region above the quasielastic peak [28], and in turn, was confirmed by a later experiment at NIKHEF [29].

These early results, typified by the ^{12}C(e,e$'$p) reaction, identified and examined two related aspects of the quasielastic scattering mechanism: the observation of reduced (relative to the shell model) spectroscopic factors and the possibility of scattering from meson exchange currents. Both of these effects actually stem, in part, from correlations between nucleons. The other major aspect that needs to be

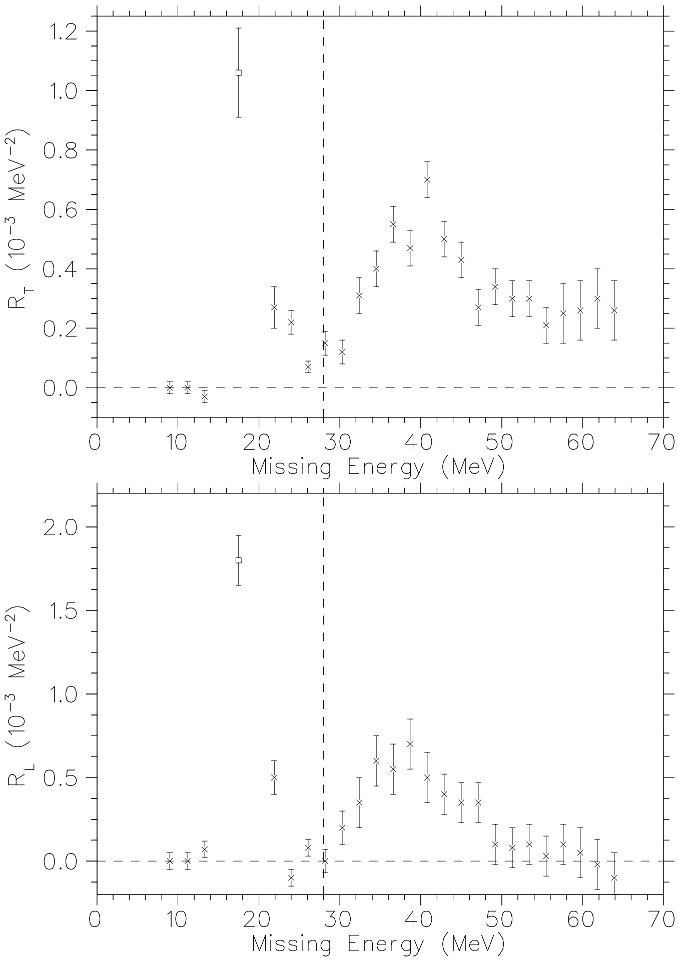

Figure 1.10. Separated Response Functions from ^{12}C. The upper (lower) panel shows the transverse (longitudinal) response function as a function of missing energy. The square points at $E_m = 17.5$ MeV have been scaled by 1/3 for plotting purposes. Both the zero axis and the two-particle emission threshold are indicated by horizontal and vertical dashed lines, repsectively.

examined in detail is the interaction of the proton with the residual nucleus. Once the nucleon correlations and FSI are understood, one can then examine more exotic effects such as possible changes in the properties of bound nucleons (and thus, in the off-shell p–N cross section).

The first experiment designed explicitly to use the A(e,e$'$p) reaction to study proton propagation through nuclei was performed in 1987 at MIT-Bates. [30, 31] Electrons at 779.5 MeV were scattered through 50.4° off ^{12}C, ^{27}Al, ^{58}Ni, and ^{181}Ta targets. The ratio of the experimental (e,e$'$p) and (e,e$'$) yields, was divided by the same ratio calculated in the PWIA to define the nuclear transparency. Figure 1.11 shows the nuclear transparency as a function of nucleon number, A, and the results of a Glauber calculation by Pandharipande and Pieper. [15] As expected, the transparency does decrease with increasing target size. The explicit inclusion of Pauli blocking, non-locality, and correlation effects was necessary to achieve agreement with the experimentally measured transparency.

Nuclear transparency experiments, especially the A(e,e$'$p) reaction, are also seen as a clean way to search for the onset of color transparency: as Q^2 increases to the point where the three assumptions that comprise the CT theory become valid, the reduced FSI should appear as an increase in the transparency of the nucleus. Experiment NE-18 at SLAC was designed to look for CT at squared momentum transfers up to 7 (GeV/c)^2. [32, 33] Figure 1.12 shows the nuclear transparency results as a function of proton momentum (including the data from MIT-Bates). Although one may be tempted to imagine a slight rise in the transparency at high proton momentum (indicating the onset of CT), it is not significant given the NE-18 error bars. As yet, no lower bound for the applicability of the CT prediction has been determined, although it is generally expected at $Q^2 \leq 10$ (GeV/c)^2.

Color transparency issues aside, the NE-18 transparency data, as a function of proton momentum, do seem to roughly mirror the p-N cross section (Fig. 1.6).

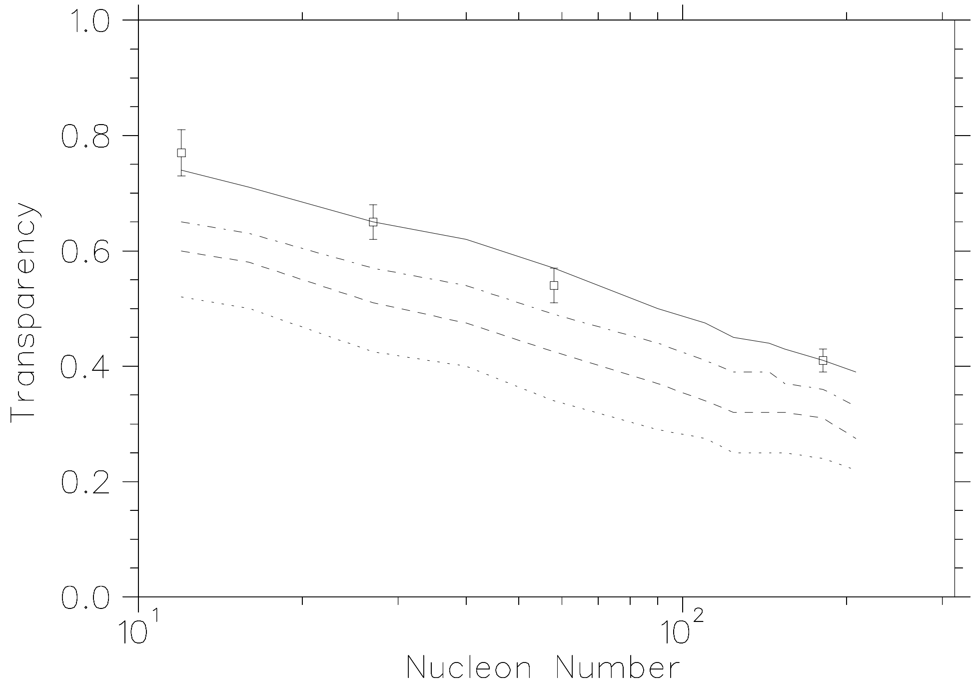

Figure 1.11. T vs. A at Q^2=0.34 (GeV/c^2). The dotted line is based on the free p-N cross section, the dashed line includes Pauli blocking, the dot-dashed line then includes non-locality effects, and the full calculation then includes correlation effects (solid). The data are from MIT-Bates. [30, 31] (Horizontal log scale.)

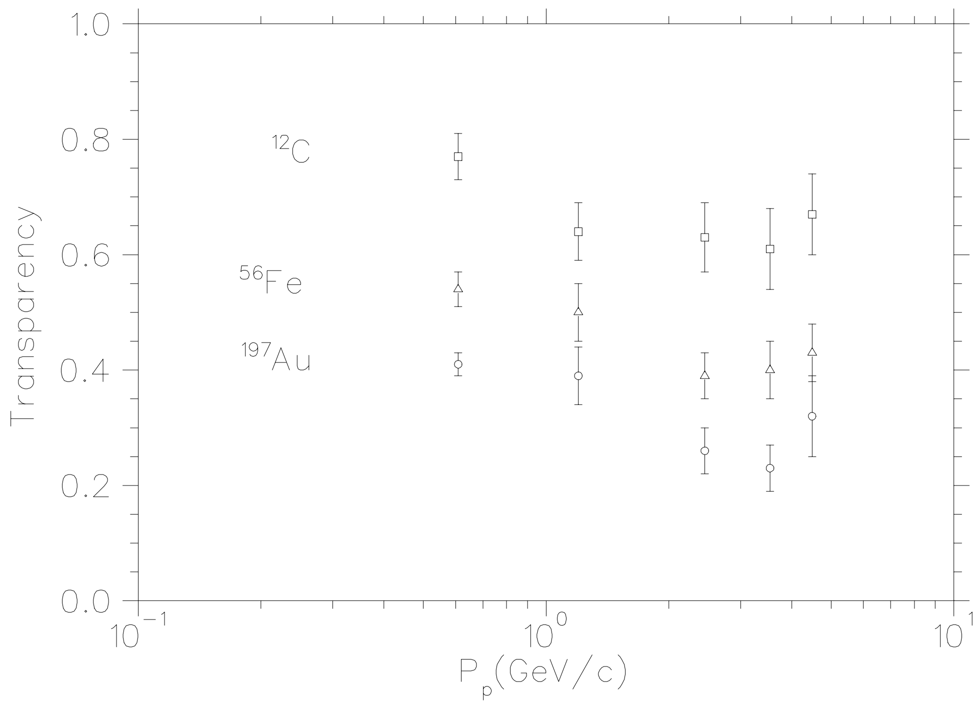

Figure 1.12. Previous Transparency vs. Proton Momentum. The squares are ^{12}C, the triangles are ^{56}Fe, and the circles are ^{197}Au. The data are from Makins *et al.* (with the exception of the MIT-Bates data for ^{12}C(squares), ^{58}Ni (triangles), and ^{181}Ta (circles) at P_p=0.6 (GeV/c)). (Horizontal log scale.)

Where the cross section rises from approximately 0.6–1 $(\mathrm{GeV/c})^2$ and then levels off, the transparency falls and levels off. There is, however, a lack of experimental data around 1 $(\mathrm{GeV/c})^2$, where the cross section changes most rapidly.

1.6 Experiment E91-013

Experiment E91-013 was performed to study several aspects of the A(e,e$'$p) reaction. Cross sections were measured on a varitey of (natural) targets (^{1}H, ^{12}C, ^{56}Fe, and ^{197}Au) and over a wide range of momentum transfers: $Q^2 = 0.64$–3.25 $(\mathrm{GeV/c})^2$. As discussed in the next chapter, the experimental apparatus allowed for much higher data rates—and therefore correspondingly more precise cross section measurements—than was possible in previous experiments.

The range of measured, final state, proton momenta (840–2550 MeV/c) covers the minimum of the p-N cross section (Fig. 1.6), the rise above pion-production threshold, and finally, the plateau above approximately 1100 MeV/c. As was mentioned, one might expect this behavior to manifest itself in the energy dependence of proton attenuation. An important question though, is to what extent is this single-nucleon knockout picture modified by multi-body effects like Pauli blocking, nucleon-nucleon correlations, and non-locality? In addition, the momentum-transfer range covered in E91-013 overlaps both the low Q^2 region, traditionally described by DWIA calculations, and the higher Q^2 region, usually described by high-energy Glauber approximation calculations. Can one model describe the complete energy dependence of the data? Finally, by taking data on a wide range of target sizes, one can determine whether or not the cross sections scale with A, as expected in the single-nucleon knockout picture.

The maximum momentum transfer of 3.25 $(\mathrm{GeV/c})^2$ is lower than the generally accepted onset of color transparency, and hence no such signal is expected. However, E91-013 data are expected to be useful not only in verifying the results of NE-18, but also in establishing a baseline from which to compare other data at higher Q^2.

Finally, it is worth noting that experiment E91-013 was also designed to separate the longitudinal and transverse response functions. The details of this aspect of the experiment are the subject of Reference 34 and outside the scope of this work. Briefly however, such a "Rosenbluth" separation is performed as follows: First, note that the cross section for scattering of an electron from a free proton can be written as

$$\left.\frac{d\sigma}{d\Omega}\right|_{\text{lab}} = \sigma_{\text{Mott}} \frac{E'}{E} \frac{1}{1+\tau} \left[G_E^2(Q^2) + \tau \left(1 + 2(1+\tau)\tan^2\frac{\theta_e}{2}\right) G_M^2(Q^2) \right], \tag{1.24}$$

where $\tau = Q^2/4M^2$. The electric and magnetic form factors, G_E and G_M, can be related to the W_C (the Coulomb, or "longitudinal" response) and W_T (the "transverse" response) structure functions already introduced (Eqn. 1.11):

$$\begin{aligned} W_C &= (1+\tau)G_E, \\ W_T &= 2\tau G_M. \end{aligned} \tag{1.25}$$

So, by measuring cross sections at kinematics with the same Q^2, but different scattering angles, one can essentially isolate the W_L and W_T terms. This allows one to test the quasielastic scattering mechanism by separating the longitudinal response, which is expected to be dominated by the single-particle knockout, from the transverse response, which is expected to be dominated by two-body (meson exchange) currents.

Finally, by measuring the asymmetry in cross sections left and right of $\vec{q}$, one can isolate the W_{LT} structure function in Eqn. 1.11. There is evidence that this term is highly sensitive to relativistic effects in the nucleus. [35, 36]

CHAPTER 2

EXPERIMENTAL METHOD/APPARATUS

2.1 Experimental Overview

Experiment E91-013 studied the (e,e$'$p) reaction on hydrogen, carbon, iron, and gold targets at momentum transfers of Q^2 =0.6, 1.3, 1.8, and 3.3 (GeV/c)^2. It was performed in the Hall C end station at the Continuous Electron Beam Accelerator Facility (CEBAF) in Newport News, Virginia. Figure 2.1 shows a plan view of the end station. After being accelerated to the desired energy, the electron beam was delivered to the hall where it impinged on the target. For $Q^2 < 3$ (GeV/c)^2, the scattered electrons were then detected in the High Momentum Spectrometer (HMS) and the recoiling proton in the Short Orbit Spectrometer (SOS). The roles of the spectrometers were reversed at the highest momentum transfer.

Table 2.1 lists the kinematic settings used in E91-013. Note that the angle at which a proton with zero initial momentum is detected—the proton kinematics being restricted by the electron kinematics—is referred to as the "conjugate" angle. The two pairs of kinematic settings, (A,D) and (C,E), are used to perform the Rosenbluth separations discussed in Section 1.6. Kinematics D and E are referred to as the "backwards" kinematics in reference to the larger electron scattering angle (relative to A and C).

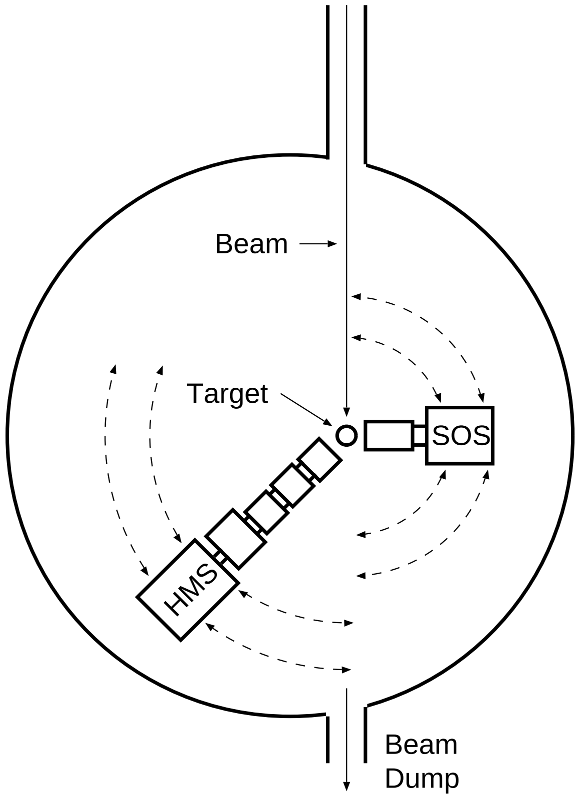

Figure 2.1: Hall C plan view.

Table 2.1: E91-013 Kinematics. The conjugate proton angles are indicated in bold face.

Label	Beam Energy (GeV)	Central Electron Angle (degrees)	Central Electron Momentum (GeV/c)	Central Proton Angle (degrees)	Central Proton Momentum (GeV/c)	Approximate Proton Kinetic Energy (MeV)	Q^2 $(\mathrm{GeV/c})^2$
A	2.445	20.5	2.075	35.4, 39.4, 43.4, 47.4, 51.4 **55.4**, 59.4, 63.4, 67.4, 71.4, 75.4	0.840	350	0.64
B	2.445	32.0	1.725	31.0, 35.0, 39.0, **43.0**, 47.0, 51.0, 55.0	1.275	700	1.28
C	3.245	28.6	2.255	32.5, 36.5, **40.5**, 44.5, 48.5, 52.5	1.550	970	1.79
D	0.845	78.5	0.475	27.8, **31.8**, 35.8, 39.8, 43.8, 47.8	0.840	350	0.64
E	1.645	80.0	0.675	**22.8**, 26.8, 30.8, 34.8	1.550	970	1.84
F	3.245	50.0	1.400	**25.1**, 27.6 30.1	2.550	1800	3.25

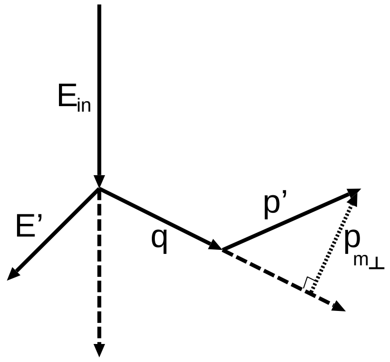

Figure 2.2. Missing Momentum Sign Convention. Shown here is the case of "positive" (by convention) missing momentum: the proton is detected on the upstream side of $\vec{q}$. "Negative" is the case with $\vec{p}'$ between $\vec{q}$ and the outgoing electron beam.

Experiment E91-013 took data in so-called perpendicular kinematics (Section 1.3). In E91-013, an arbitrary sign is applied to the magnitude of the missing momentum: positive for protons detected on the larger scattering angle side of $\vec{q}$, and negative for protons detected on the smaller angle side. Figure 2.2 summarizes the conventions.

2.2 Beam Line

The CEBAF electron beam is accelerated in stages before it reaches the end stations. The electrons are produced at the injector by thermionic emission and are initially accelerated to 45 MeV. The beam then enters the main part of the accelerator which consists of two linear accelerators connected by two semicircular arcs. Figure 2.3 shows a schematic of the accelerator layout. The electrons gain 400 MeV per linac and can be recirculated up to five times. This results in nominal beam energies of 845, 1645, 2445, 3245, or 4045 MeV. At the end of the south linac the electrons enter the Beam Switch Yard (BSY) where they are sent to one of the three end stations. For E91-013, the beam then travels through the Hall C arc, and enters the experimental end station.

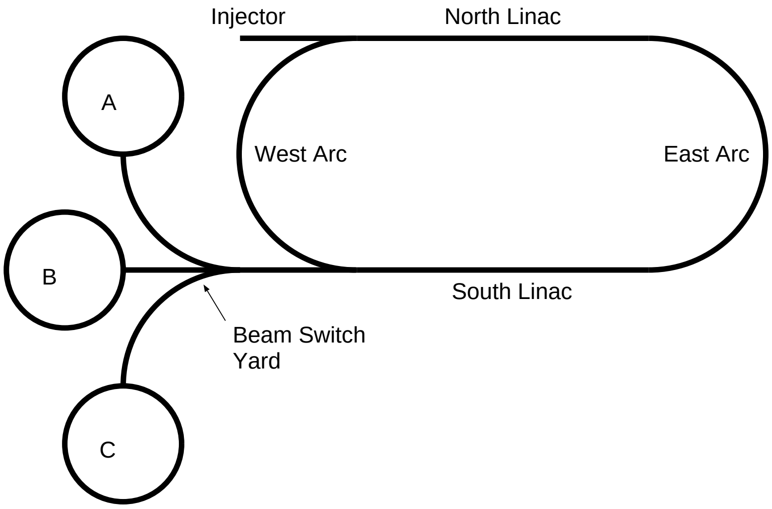

Figure 2.3: Plan view of the CEBAF Accelerator.

A schematic of one of the resonant cavities that make up the linear accelerators is shown in Fig. 2.4. The cavities are driven at 1.497 GHz (in the radio-frequency, or RF, range) such that they continuously produce accelerating fields that are synchronized with the electrons. To eliminate power loss in the cavities due to I^2R heating, they are immersed in 2 K helium so as to make them superconducting. The accelerator can have a duty cycle of 100% meaning that every RF cycle can contain an electron bunch. After being accelerated, a separator is used to send every third beam bunch to each of the three end stations meaning experiments in Hall C see pulsed beam at 499 MHz, or every 2 ns.

The position of the beam is monitored at various locations throughout the Hall C arc including approximately 1 m upstream of the target chamber entrance window. The beam position monitors (BPMs) are cavities with two pairs of antennae each (one measuring vertically, the other horizontally) that pick up the 499 MHz structure of the beam in the Hall C arc. The signals are proportional to the distance from the beam. The difference over the sum of the paired signals is converted into a position so as to be independent of current. The BPMs are read out every two

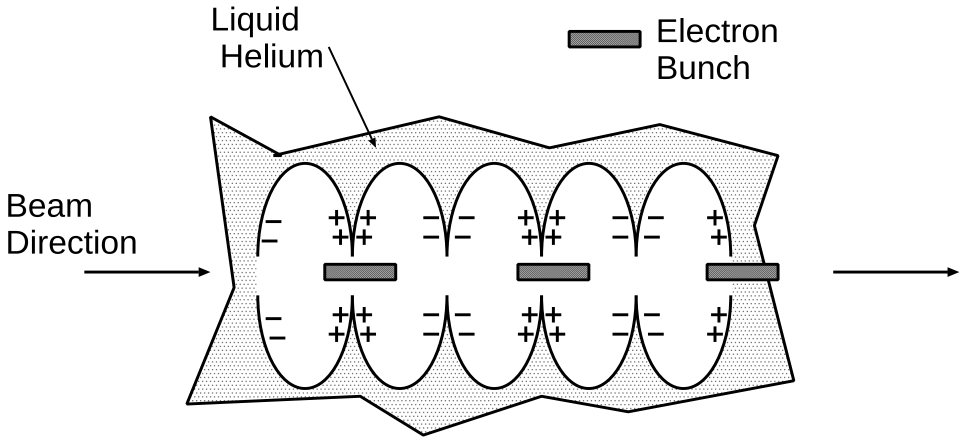

Figure 2.4. A CEBAF Accelerator Cavity. The charge, "+" and "-," resonates at a frequency such that the electron bunches (shaded regions) are continuously attracted to the next node.

seconds and have an absolute uncertainty of 1 mm and a relative error of ∼0.1 mm.

In addition to the BPMs, so called "superharps" can be used to tell not only the position of the beam, but to measure its profile as well [37]. A superharp consists of three wires on an actuated arm that can be moved through the beam (Fig. 2.5). As the wires sweep through the beam, a vertical-horizontal-vertical sequence of position/profile measurements is performed. Although the absolute error on the beam position using the superharps is smaller than that of the BPMs, superharp scans cannot be performed while data are being taken. This is because the scattering from the tungsten wires is unacceptable. Thus the BPMs were used to read out the position continuously and a superharp scan was only performed every few hours as a check/calibration. The combination of both position monitors allowed for ± 1 mm absolute uncertainty on the beam position at the target, with a relative uncertainty of ~ 0.15 mm.

Because of the small spot size of the beam, a large amount of energy can be deposited in a small volume in the target. To avoid target damage, or local boiling in the case of liquid targets, it is sometimes necessary to sweep the beam over a

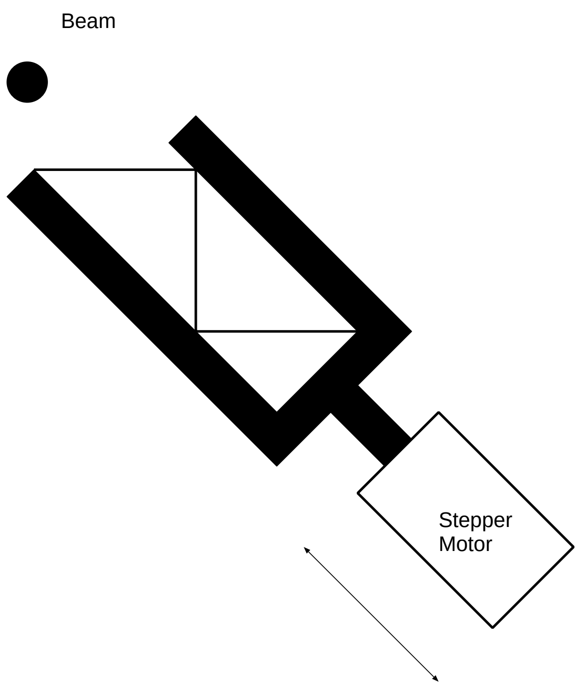

Figure 2.5. A superharp is used to measure the beam position and profile. A motor drives the harp through the beam, and an encoder records its position. As the wires pass through the beam they measure horizontal, vertical, and horizontal profiles.

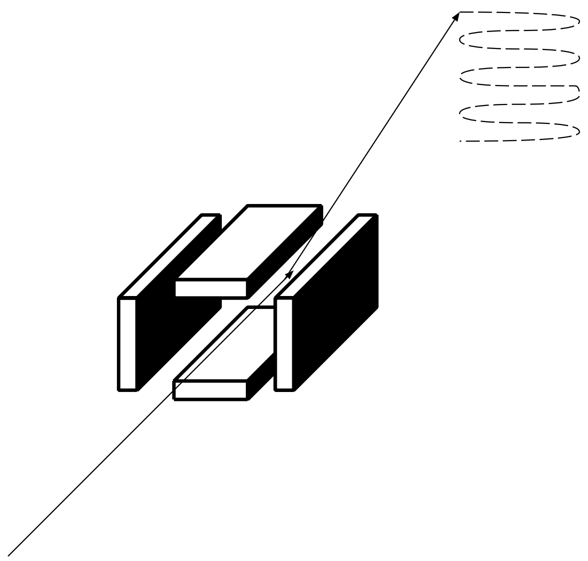

Figure 2.6. Two sets of dipole magnets are driven with a periodic current so as to form a raster pattern on the target.

larger area on the target forming a raster pattern [38]. During E91-013, this was accomplished using a sinusoidal waveform with a frequency of approximately 25 kHz to drive two sets of dipole magnets (Fig. 2.6). Depending on the beam energy, the magnets, located 21 m upstream of the target, can sweep the beam up to ± 5 mm in both the horizontal and vertical directions. Typically, a raster size of ± 0.5 mm (in both directions) was used for both the solid and cryogenic targets.

The beam energy is usually determined by measuring the electron's trajectory through the Hall C arc along with the current in the dipole magnets. During such an energy measurement, superharps are used to measure the position of the beam at the beginning, center, and end of the arc. The trajectory, combined with field map data (to convert the magnet currents into magnetic field values), allows the determination of the beam energy. The uncertainty, $\delta E/E$, of the beam energy measured with this method is approximately 2×10^{-4}. This is dominated by the uncertainty in the integrated field, $\int \vec{B} \cdot \vec{dl}$. Reference 39 discusses this beam energy measurement in detail.

As a check on this "arc measurement" method, three additional measurements, each independent of the arc dipole settings, were employed. In the first, elastic electron scattering from a composite target is measured. The difference in recoil energies, ΔE_{rec}, is used to extract the beam energy. [34] The recoil energy is given by,

$$E_{rec} = \frac{Q^2}{2M} \approx \frac{2EE'}{M} \sin^2 \frac{\theta}{2}, \tag{2.1}$$

(where the electron mass has been neglected in the second relation). The difference in recoil energies for a composite target with nuclei masses of M_1 and M_2 is then

$$\Delta E_{rec} \approx \frac{2}{E} E' \sin^2 \frac{\theta}{2} \left(\frac{1}{M_1} - \frac{1}{M_2} \right). \tag{2.2}$$

Measurement of ΔE_{rec}, E', and the electron scattering angle allows extraction of the beam energy. Using a BeO target, this method was employed at a beam energy of 845 MeV, resulting in an absolute uncertainty of approximately 2×10^{-3}. The differential recoil method becomes unfeasible at higher energies as the elastic cross sections are so small.

The beam energy can also be measured by comparing the cross sections of electron scattering from the ground state and first excited state of ^{12}C. At $Q^2 = 0.129$ (GeV/c)^2, the ratio of these cross sections has a minimum. [40] Measuring the angle of the scattered electron and using the observed minimum in the above ratio to determine Q^2, one can extract the beam energy via,

$$Q^2 = 4EE' \sin^2 \frac{\theta}{2}, \tag{2.3}$$

where

$$E' = \frac{E}{1 + \frac{2E \sin^2 \theta}{M}}. \tag{2.4}$$

Precise determination of the minimum—possible only for the 845 MeV beam energy—dominates the uncertainty: $\approx 1 \times 10^{-3}$.

The final "kinematic" method used to determine the beam energy consists of measuring the H(e,e$'$p) reaction. Given the angles and momenta of the scattered

Table 2.2: Beam Energy Measurements.

Nominal Value	Method	E_{Beam} (MeV)
845	Arc	844.56±0.19
845	Differential Recoil	844.7±1.5
845	Diffractive Minimum	844.7±0.9
1645	Arc	1648.5±0.5
2445	Arc	2449.9±0.6
2445	Elastic H(e,e′p)	2444.9±5.0

electron and proton, one can determine the beam energy. Although this method can be used at all beam energies, it is the least sensitive, as it relies on the resolution of both spectrometers.

The results of the beam energy measurements are summarized in Table 2.2. In the analysis of E91-013, the small differences between the measured and nominal values are neglected.

2.3 Charge Measurement

Because of the DC-like nature of the CEBAF beam, traditional methods of charge measurement—measuring an induced current in a pickup coil as the beam pulses pass by—become infeasible. Hall C has three Beam Current Monitors (BCMs) that measure the instantaneous beam current [49]. The first is an Unser monitor, and a simplified schematic is shown in Fig. 2.7. The first toroid measures any AC fluctuations in the beam, while the second toroid (in reality there are several) is used to measure the DC component. An AC modulator at approximately 4 kHz is used to drive the toroid through its hysteresis curve which, in the absence of beam, is symmetric. However, in the presence of a DC beam with current i, the hysteresis curve will be biased in one direction. A feedback loop is set up such that the opposite

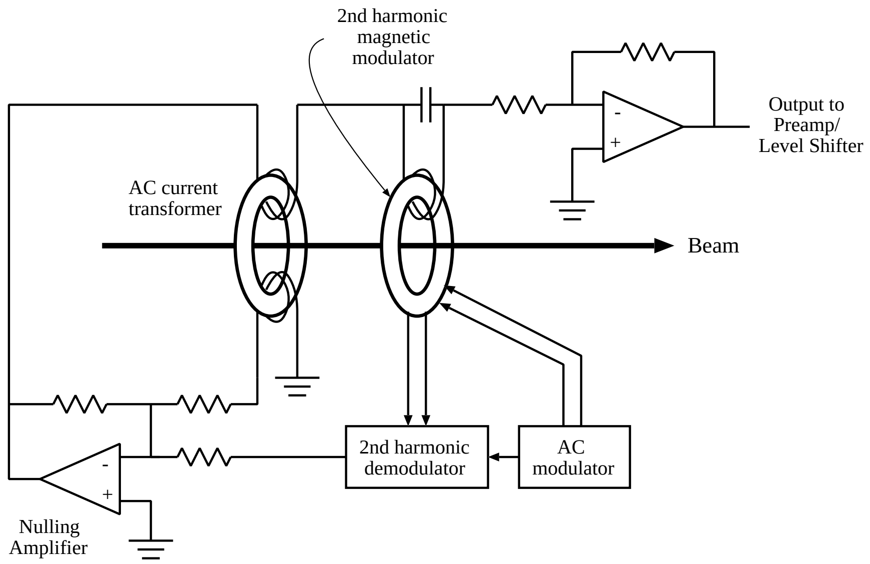

Figure 2.7: Schematic of Unser monitor

current, $-i$, is forced through another winding around the toroid so as to keep the hysteresis curve symmetric. This current, $-i$, is converted to a voltage, sent to a voltage-to-frequency (V-F) converter whose output is then sent to a scaler read by the data acquisition.

Although the Unser monitor is sensitive to thermal fluctuations (its zero offset can shift 1 μA on the order of a day), it does have the advantage of excellent linearity over a wide range of currents and a well known gain (about 4 mV/μA for the Unser and about 4000 Hz/μA for the entire system). Furthermore, it was the only current monitor that could be calibrated absolutely, and so the other monitors were adjusted to match the Unser. A precision voltage source and resistors were used to simulate a DC beam of known current in the Unser, and this was used to determine the Unser's gain to 2 parts in 10^4. The noise level in the Unser is approximately 0.2 μA.

Hall C also contains two cavity beam current monitors. The 499 MHz structure of the beam excites a 1497 MHz TM_{010} mode in resonant cavities that are placed coaxially around the beam. The electric field for this mode is radially symmetric meaning that the current measurements are somewhat insensitive to the beam position. The AC signal from a pickup antenna is amplified, sent through an RMS-to-DC converter (Analog Devices AD367), and then, as in the case of the Unser monitor, is sent through a V-F converter to a scaler.

Unlike the Unser, the cavity monitors have a good signal to noise ratio and reasonable gain stability (over the course of a few days), but cannot measure current absolutely. This is because calculation of the power output as a function of beam current is sensitive to details such as the surface finish of the cavities. Therefore a current monitor calibration algorithm was devised in which beam was sent to the hall in a series of increasing then decreasing current steps alternated with periods of no beam. The beam-off periods were used to determine the zero offset of the Unser, and the gains of the BCMs were determined by comparison with the well known gain of the Unser.

During the two run periods, E91-013 ran at currents ranging from 10-50 μA. In this current region, and with the temperature drifts, a random error of 1% is assigned to the current measurements. This is also consistent with the variation in the output of the three monitors.

2.4 Targets

Experiment E91-013 required both solid targets—carbon, iron, gold, and polyethylene (CH_2)—and a cryogenic hydrogen target. During the first run period (December 1995) only the solid targets were available; the new scattering chamber, including a cryogenic target, was added in February 1996. Figure 2.8 shows a schematic of the target scattering chamber. Either the solid target ladder or the cryo-stack can be rotated into the beam.

The solid targets are thin foils, nominally 0.75 inches tall by 1.5 inches wide.

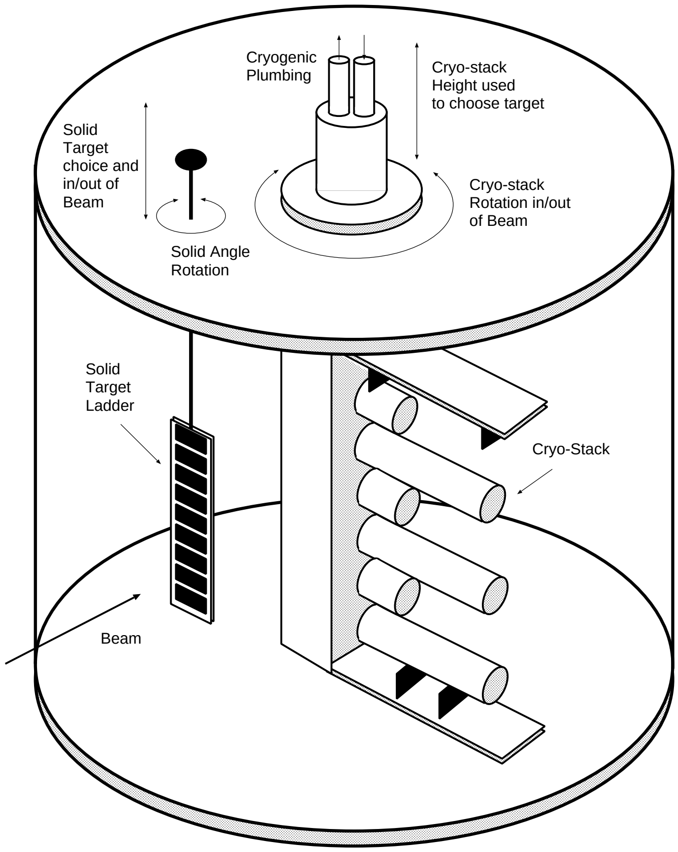

Figure 2.8. A cut-away view of the Hall C scattering chamber. The angle which the solid targets intersect the beam can be adjusted. The solid targets can be lifted out vertically to allow the cryo-stack to be rotated into the beam. The height of both the solid target ladder and cryo-stack is used to choose between the various solid or cryo- targets.

Table 2.3: Solid Target Parameters.

Target	Radiator (%)	Areal Density (g/cm^2)	Areal Density Error (%)	Dec. 1995	May 1996	Comments
C	0.5	0.230	0.2	×	×	
C	0.1	0.060	0.1	×		
C	6.0	2.561	0.05		×	
Fe	2.2	0.309	0.1	×	×	0.005" & 0.010" foils
Fe	5.4	0.748	0.05		×	0.020" & 0.020" foils
Au	3.1	0.196	0.10	×	×	0.002" & 0.002" foils
Au	6.0	0.375	0.05		×	
CH_2	0.2	0.089	0.2	×		
CH_2	0.2	0.093	0.2		×	
CH_2	1.6	0.700	0.1		×	8 foils

Table 2.3 lists the solid target dimensions. Note that in the case of the iron targets and one of the gold targets, two foils were used to achieve the desired target thickness. The solid targets are located in a vertical ladder that is controlled remotely from the counting house. The ladder is moved vertically so as to change which target is at beam height. The ladder can also be rotated around its vertical axis so as to change the angle of the target plane relative to the beam. This is done to reduce the amount of target material that particles have to traverse in order to reach the spectrometer (Fig. 2.9). The error on the target angle is approximately two degrees. The target angles used for the various kinematics are listed in Table 2.4.

The target thicknesses were measured as follows. The mass was measured using a balance with a 1.0 mg precision. A microscope with a digitized slide table was used to determine the location of each vertex to 8 μm, and the area was then calculated assuming straight edges between the vertices. The areal density is then defined as the mass/area. Note that the targets are assumed to have uniform thickness and mass density.

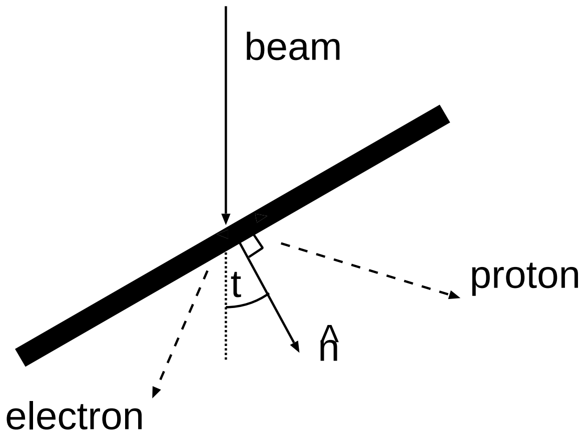

Figure 2.9. The angle of the solid target with respect to beam is altered so as to minimize the material that a scattered particles must traverse. The target angle, t, is defined to be positive when the normal to the target, $\hat{n}$ is directed towards the SOS.

Table 2.4. Target angles for each kinematic setting. The target angle is defined as the angle between the beam and the normal to the target pointing downstream. Positive target angles are towards the SOS. See Fig. 2.9. The error on the target angle is approximately 2 degrees.

Label	Electron Spectrometer Angle (degrees)	Proton Spectrometer Angle (degrees)	Target Angle (degrees)
A	20.5	55.4	20
B	32.0	43.0	10
C	28.6	40.5	10
D	78.5	31.8	-20
E	80.0	22.8	-20
F	50.0	25.1	10

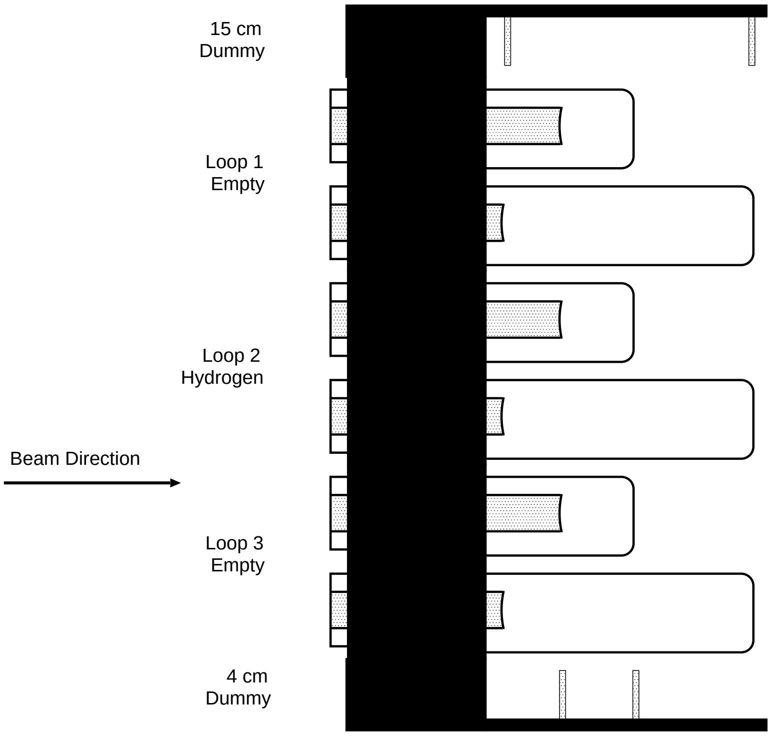

Figure 2.10: Cryogenic stack.

The carbon targets are in the form of pyrolytic graphite and have the natural isotopic abundance: 98.9% ^{12}C with a 1.1% ^{13}C contamination. The iron and gold targets also have natural abundances: 91.76% ^{56}Fe with a 5.9% ^{54}Fe and 2.1% ^{57}Fe contamination, and 100% ^{197}Au. The largest contaminant, ^{54}Fe, has only a 0.3% effect on the target thickness, and thus the target impurities are neglected in the analysis.

For calibration purposes, a liquid hydrogen target was also used during the May 1996 running. The Hall C cryogenic stack—an array of three sets of target cells—can be rotated into the beam via remote control. Each set, or "loop," has both a 15.5 cm and 4.2 cm cell. Figure 2.10 shows a detail of the cryogenic stack. Only the short cell of loop 2 was used in E91-013. The cells are thin aluminum cylinders constructed from beer can stock, 6.35 cm in diameter. The can bottom

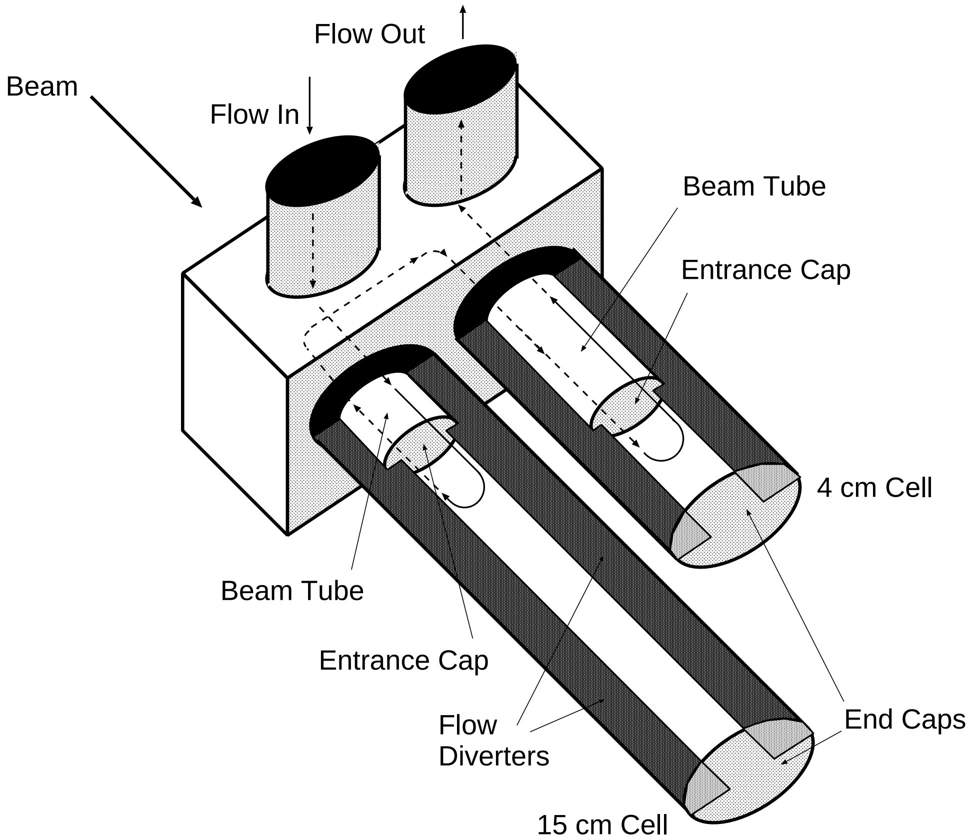

Figure 2.11. Cryogenic target loop. The arrows indicate the direction of the hydrogen flow.

forms the exit window and is 0.31 mm thick. The entrance window is also made of aluminum and is 0.18 mm thick. Because the end caps are spherical in shape, a change in beam position can mean an effective change in target length. The error is estimated to be 0.05% in length for a 1 mm change in the beam location. Figure 2.11 shows a detail of the target loop.

The Hall C cryotarget is able to dissipate up to 200 W of power deposited by the electron beam in the liquid hydrogen. However, for typical E91-013 conditions, 25 μA and a 4.2 cm target, the beam heating is only ~30 W. By circulating the hydrogen through a heat exchanger, the hydrogen is maintained at 19 K and 29 PSIA.

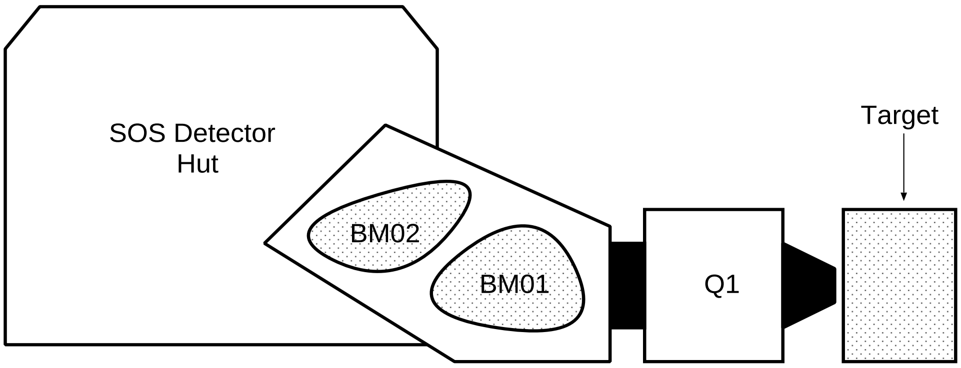

Figure 2.12: Schematic of the Short Orbit Spectrometer (SOS).

At this pressure, the hydrogen has a density of 0.7320 ± 0.00036 g/cm^3 and is 3 K below its boiling point. The density dependence on temperature is $\frac{1}{\rho}\frac{d\rho}{dT} = -1.25\%/\mathrm{K}$; whereas the density dependence on pressure is smaller: $\frac{1}{\rho}\frac{d\rho}{dP} = 0.01\%/\mathrm{PSIA}$. Thus, a precise monitoring of the temperature is critical. Two Lakeshore Cernox resistors are installed in each loop, and their resistance is converted to temperature using an Oxford ITC502 [41]. The error in the temperature read out is 50 mK which corresponds to an uncertainty in the density of less than 0.1%. The temperature is controlled with a feedback loop consisting of the temperature read out module and a low power heater.

Because the beam can deliver so much energy to a small volume, local boiling (and thus decreased effective target thickness) may be a problem. To study this effect, elastic scattering from deuterium was measured at various beam currents. The yields scaled with current to better than 1% for currents up to 70 μA (the largest current used during E91-013) [42].

The largest contaminant in the hydrogen is expected to come from HD, and is estimated to be less than 0.3% by mass.

2.5 Short Orbit Spectrometer

The Short Orbit Spectrometer (SOS) is depicted in Fig. 2.12. It is described

Table 2.5: SOS Characteristics.

Parameter	Value
Max. Central Momentum	~ 1.8 GeV/c
Momentum Bite	$\pm$ 20 %
Resolution ($\delta p/p$)	<0.1%
Solid Angle Acceptance	10.7 msr
Scattering Angle Bite	$\pm$ 40 mr
Scattering Angle Range	$11^\circ - 120^\circ$
Out of Plane Angle Range	$\pm$ 40 mr
Horizontal Angle Precision	0.8 mr
Vertical Angle Precision	0.8 mr

in detail in Refs. [43, 44] and the references therein. The SOS is designed to detect and identify electrons, protons, pions, and kaons of momenta up to 2 GeV/c. It is composed of three magnets: a horizontally-focusing quadrupole (Q1), followed by two, vertically-bending, dipoles (BM01, BM02). The first dipole produces a vertical bend of 33° upwards, the second 15° downwards, for a net vertical bend of 18°. The magnets are tuned in point-to-point mode in the vertical direction, meaning that particles with the same momentum and position at a point target are focused to the same point in the focal plane at the exit of the spectrometer. (The focal plane is discussed in Section 3.1.) Table 2.5 lists the properties of the SOS.

The magnets are conventional (non-superconducting), and powered by three supplies that are controlled remotely from the counting house. The SOS magnet program determines the correct power supply currents for a given spectrometer momentum setting. If the given setting is in the chosen direction of the hysteresis curve, the program will adjust the power supplies to approach the target current value. If, however, the requested setting is in the other direction on the hysteresis curve, the program will notify the user of the need to degauss the magnets. In this case, the current is increased to the maximum value, brought back down to zero, the polarity of the magnet is reversed, the current is then increased to the maximum in the opposite direction, and then finally, the magnets are ramped back up to the requested

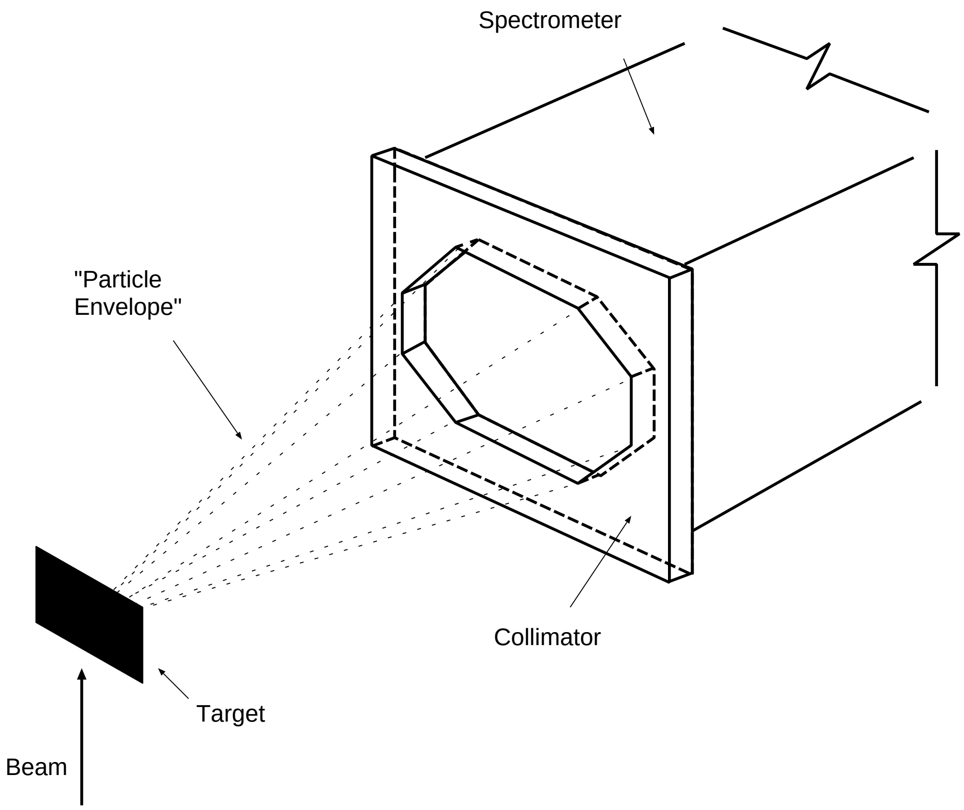

Figure 2.13. Schematic of a collimator. The collimator defines the solid angle at the entrance of the spectrometer. The edges of the octagonal hole are beveled so as to match the envelope of the particles emerging from the target.

value. During E91-013, the hysteresis curve convention for the SOS magnets was an increase in the currents away from zero field. That is, a degauss was not performed if the magnitude of the momentum was increased from setting to setting.

The acceptance in solid angle for the SOS is defined by one of three available Hevimet [45] (an alloy of 90% W, 5% Cu, 5% Ni; $\rho = 17$ g/cm^3) collimators. E91-013 typically used the large aperture collimator which has an acceptance of 7.55 msr. The small collimator, often used in calibration runs, has an acceptance of 4.98 msr (approximately 65 mrad horizontally, 70 mrad vertically). The openings are beveled to match the envelope from the (point) target to the spectrometer entrance (Fig 2.13). The third "collimator" is actually an array of holes, often called a "sieve

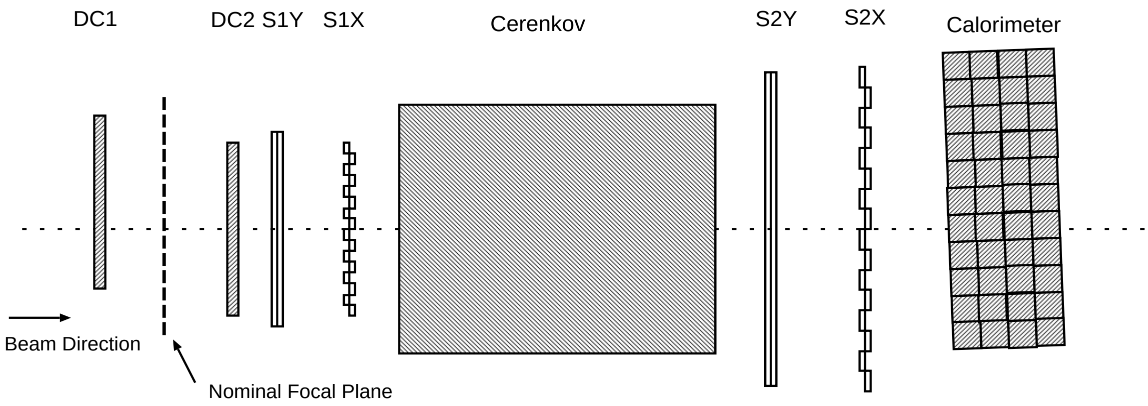

Figure 2.14: Schematic of the SOS detector stack, shown approximately to scale.

slit." It is used in optics tests to map trajectories at the entrance of the spectrometer to those at the focal plane. The reconstruction of focal plane quantities to vertex quantities will be discussed in Section 3.2.

2.5.1 SOS Detectors The SOS has an array of detectors that allow precise determination of a particle's trajectory (and hence momentum) and identity. After a particle enters the detector hut it traverses two sets of drift chambers, two planes of hodoscopes, a gas filled Čerenkov radiation detector, two more planes of hodoscopes, then four layers of Pb-glass blocks. Figure 2.14 shows a schematic of the SOS detector stack.

It is useful at this point to define the spectrometer hut coordinate system. The SOS (and HMS) uses the TRANSPORT [46] coordinate convention in which $\hat{x}$ lies in the bend plane and is directed towards particles with higher momentum; thus vertically downward in both spectrometers. (The SOS has a net vertical bend.) Figure 2.15 shows the coordinate system. The $\hat{z}$ axis is along the central ray of the spectrometer, positive being in the direction of the particles. The $\hat{y}$ axis is then horizontally to the left as seen by a particle, so as to maintain a right-handed coordinate system. Note that with the HMS to the right of the beam and the SOS to the left, the positive $\hat{y}$ axis points towards smaller scattering angle in the HMS,

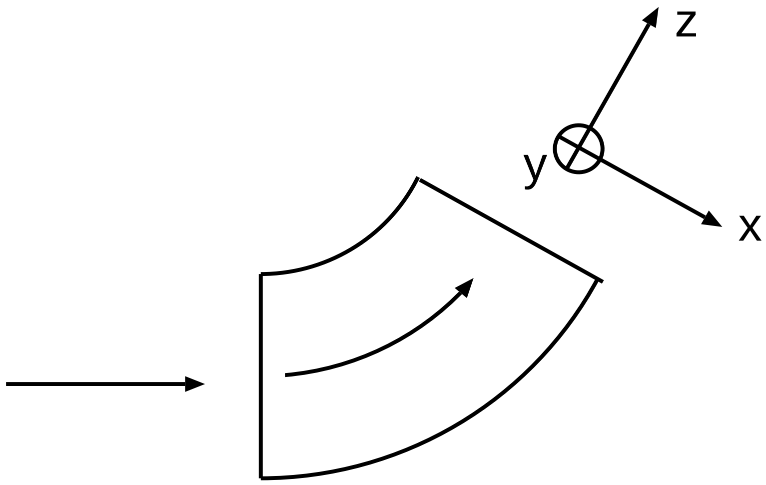

Figure 2.15. Side view of the spectrometer coordinate system. (True for both the SOS and HMS.)

and larger scattering angle in the SOS.

Drift chamber (or wire chamber) information is used by the tracking algorithm (Section 3.1) to calculate a particle's trajectory in the detector hut. A drift chamber is a gas-filled volume containing a grid of fine wires. As a charged particle traverses the chamber, it ionizes the gas, and the liberated electrons are attracted to sense wires. The electrons form a pulse on the sense wire indicating that the particle was somewhere in the vicinity of that wire. The time it takes the electrons to reach each wire is measured and converted to a distance from the wire using an empirically determined position-drift time relationship. However, it is not possible, with the information of one wire alone, to determine on which side of the wire the ionizing particle went ("left/right" ambiguity), nor where along its length the ionization occurred. A second plane with wires parallel to, but offset from, the first plane, is used to help eliminate the left/right ambiguities. In addition, planes with wires of a different orientation are used to locate the particle along the length of a given wire. Figure 2.16 shows a simplified wire chamber: The track is seen end on, and the solid lines represent firing wires. The second U' plane determines which side

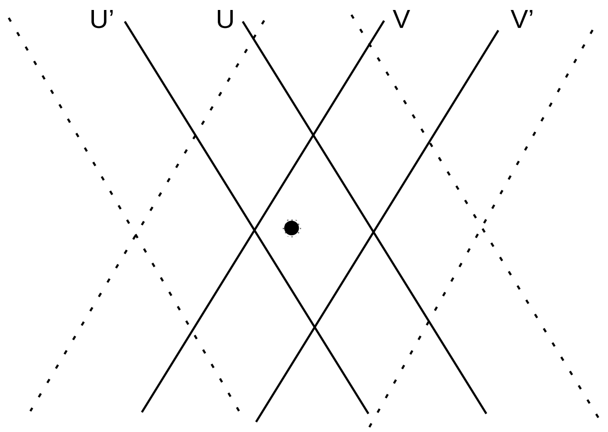

Figure 2.16. A simplified model of a wire chamber displaying the left/right ambiguity determination. The solid lines are meant to represent firing wires. See text for details.

of the U wire the particle went, and the crossing V wires locate the trajectory along the U wires.

The two sets of drift chambers in the SOS are identical, and they are placed at ±24.75 cm in $\hat{z}$ relative to the spectrometer focal plane. The active area for the chambers is $\sim$67 cm in the X (vertical) direction, and $\sim$40 cm in the Y (horizontal) direction. There are six planes in each chamber labeled: U, U', X, X', V, V'. The X planes, so called because they measure vertical, or $\hat{x}$ position, are oriented horizontally, the V planes are at 60° to the horizontal, and the U planes at 120°. The primed planes are just duplicates, offset by half the wire spacing. Figure 2.17 shows the layout as seen by an incoming particle. The basic cell is depicted in Fig. 2.18, and it is 6.35 mm thick in the z direction. The electric field that guides the ions is shaped by the cathode foils (0.012 mm mylar coated with 0.12 μm copper) and the potential wires (60 μm diameter, gold-plated tungsten) which are both typically kept at roughly -2000 V. The sense (anode) wires (30 μm diameter, gold-plated tungsten) are kept at ground potential. The sense wire spacing in the plane is 10.0 mm.

The volume between the wires and foils is filled with a mixture of argon-ethane gas (50/50 by mass) that is mixed remotely and then fed to the chambers.

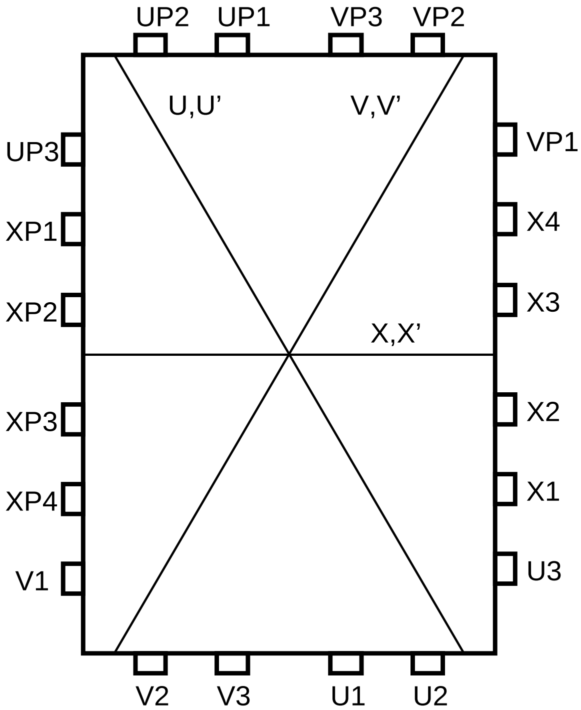

Figure 2.17: Layout of SOS drift chamber planes as seen by an incoming particle.

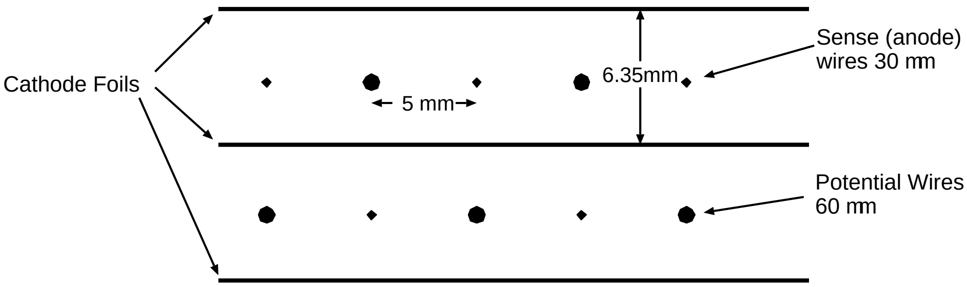

Figure 2.18: Layout of SOS drift chamber cell.

A typical flow rate was 200 cm^3/minute. The mixture and flow rate were monitored approximately once every eight hours, and a bad gas mixture was usually noticed immediately by a marked decrease in chamber efficiency.

Each sense wire is connected to a preamplifier/discriminator card and is read out individually. If the signal is above the discriminator threshold a logic pulse starts a Fastbus multi-hit time-to-digital-converter (TDC). The TDC (LeCroy LRS1877 [47]) information for the last 32 μs is read out only if there is a trigger (common stop mode). (The trigger is discussed in detail in Section 2.7.) The time for each wire is converted into a distance which is then used by the tracking algorithm (Section 3.1) to locate the particle trajectory. The time-to-distance calibration is done by creating a histogram of the drift times for many events (for all hit wires), and mapping the distribution in time to a uniform distribution over the ± 5 mm cell width. The drift time-distance relation is then stored and used by the tracking algorithm.

Hodoscopes are thin strips, or "paddles," of scintillating plastic wrapped in a light-tight coating. As radiation traverses the plastic, its atoms are ionized, and, as the atomic electrons reorganize, visible light is emitted (the plastic "fluoresces" or "scintillates"). This light is collected at the ends of the paddles and detected by photomultiplier tubes (PMTs). The light is produced and collected very quickly (a few nanoseconds), and this fast response allows precise determination of the time that the particle was at the scintillator. The plastic must have the following characteristics: a high efficiency for converting the incoming radiation into visible light, a short decay time, and it must be transparent to the emitted fluorescent radiation.

In both Hall C spectrometers, four planes of hodoscopes are used. A combination of scintillators firing in coincidence (each plane responding to a particle as it passes by) can define a trigger which is then used to read out the rest of the

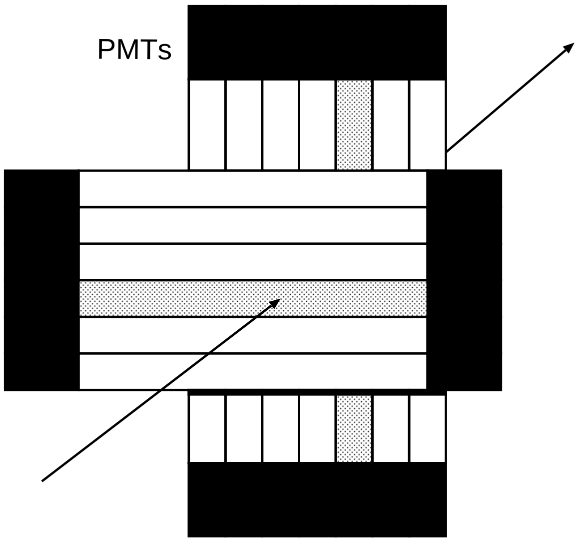

Figure 2.19. Perspective view of two hodoscope planes. The particle's position can be roughly determined using the location of the firing (shaded) scintillators.

detectors. By using multiple planes, separated by sizeable distances, one can determine the velocity of the particle using its "time of flight." In addition, using small, sectioned paddles (Fig. 2.19) with different orientations (much like the different wire orientations in the drift chambers), one can also determine a rough position of the particle's trajectory.

There are four hodoscope planes in the SOS; two before and and two after the gas Čerenkov detector. The separation between the two sets of planes is approximately 1.76 m. The first and third planes, labeled S1Y and S2Y, are oriented vertically (and thus measure position in the horizontal, or $\hat{y}$ direction). Both planes contain nine paddles each. Those of S1Y measure 10 mm $\times$ 45 mm x 635 mm, and those of S2Y, 10 mm $\times$ 45 mm $\times$ 1125 mm. The paddles are slightly overlapped to avoid dead regions, resulting in an active area of approximately 365 mm (horizontally) by 635 mm (vertically) for S1Y, and 1125 mm $\times$ 365 mm for S2Y. The second and fourth scintillator planes, labeled S1X and S2X, are oriented horizontally. S1X and S2X contain nine and sixteen paddles, respectively. In both cases, the paddles measure 10 mm $\times$ 75 mm $\times$ 365 mm. Again, the paddles are overlapped, resulting in an active area of 365 mm (horizontally) by 635 mm (vertically) for S1X and 1125 mm (horizontally) by 365 mm (vertically) for S2X.

The light for each paddle is collected at both ends by Phillips 2282 PMTs. The signals are sent to the counting house where they are sent through a splitter. A third of the signal is sent to a Fastbus analog-to-digital converter (ADC) (LeCroy LRS1881M), and the remainder to a discriminator. The discriminated pulse is sent to a Fastbus TDC (LeCroy LRS1877), a VME scaler, and a coincidence module to become part of the trigger (Section 2.7).

Once in the detector hut, all particles have basically the same momentum. And, at typical CEBAF energies, light particles such as electrons and pions are, for all practical purposes, traveling at the speed of light. Therefore, time of flight methods to separate particle identities are infeasible, and other means must be found. A particle that exceeds the velocity of light in a medium will emit Čerenkov radiation. A particle of mass m in a medium with an index of refraction of $n = 1 + \eta$ will emit this radiation of its energy exceeds the threshold energy given by

$$E_{\text{th}} = \frac{m(1+\eta)}{\sqrt{\eta(2+\eta)}}. \tag{2.5}$$

A threshold Čerenkov detector contains a medium chosen such that the faster of two particles emits the radiation, while the slower does not, and the particles are thus separated.

The SOS Gas Čerenkov detector is designed to separate electrons and pions (or positrons from positively charged pions). It is a box, approximately 1 m^3 in volume, filled with gaseous Freon-12 (CCl_2F_2, n = 1.00108) at room temperature and atmospheric pressure. This corresponds to a Čerenkov threshold of $\sim$ 10 MeV for electrons and $\sim$ 3000 MeV for pions. As electrons (or positrons) traverse the volume, they emit light which is reflected by four overlapping mirrors at the back of the detector onto four Burle 8854 PMTs. The signals from each PMT are sent upstairs to the counting house where they are split. One half goes to a Fastbus ADC (LeCroy LRS1881M), and the rest are summed in a linear fan in/fan out whose output is sent to a discriminator. This pulse (or lack thereof) can then be used in the trigger to identify electron events[1].

The last detector in the SOS detector stack is the calorimeter (or shower counter). Its purpose is to measure the energy of electrons, and it consists of forty-four Pb-glass blocks each connected to a PMT. As an electron decelerates in the vicinity of atomic nuclei in the glass it emits bremsstrahlung radiation. These bremsstrahlung photons can then go on to produce more e^+/e^- pairs, which in turn radiate producing more photons, and so on. The electrons and positrons emit Čerenkov radiation in the glass. This light is detected by the PMTs, and the amount of light collected is proportional to the energy deposited in that block. Because electrons and positrons are stopped in the calorimeter, summing the contribution from each block gives an energy proportional to that of the original electron.

The shower counter is usually used in conjunction with the Čerenkov detector for particle identification. Electrons (and positrons) are identified because they lose a constant fraction of their energy in each calorimeter layer, whereas a pion (or any hadron) will usually lose a constant amount of energy per layer (typically 300 MeV in both the SOS and HMS calorimeters). It is possible however, that a pion undergoes a charge exchange reaction, creating a neutral pion that then decays into two photons. These photons then shower to produce a large signal in the detector, causing a high energy tail in the calorimeter spectrum.

The SOS shower counter consists of four layers of eleven Pb-glass blocks each. The Pb-glass has a radiation length of 2.54 cm. Each block is 10 cm $\times$ 10 cm $\times$ 70 cm, meaning the entire stack is approximately 16 radiation lengths. As shown in Fig. 2.14, the array of blocks is tilted with respect to the central ray, and each row of

[1]Note that neither the SOS or HMS gas Čerenkov detectors were used in the trigger during E91-013.

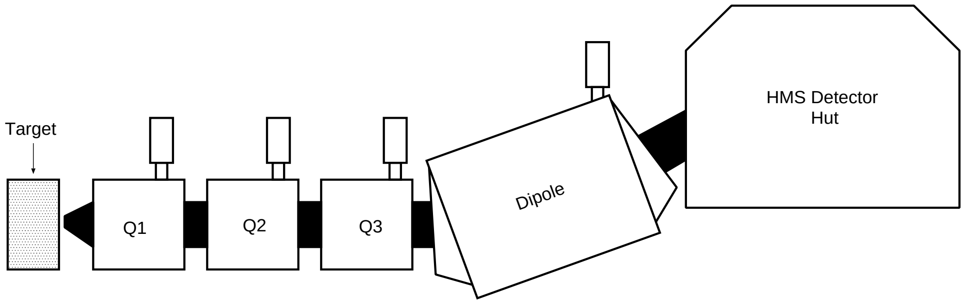

Figure 2.20: Schematic of the High Momentum Spectrometer.

blocks is slightly offset from the others to avoid dead regions. Each block is wrapped in 25 μm of aluminized mylar and 0.076 mm of Tedlar [48] for light tightness.

The signal from each PMT is sent to the counting house where it is split. Half of the signal goes to a Fastbus ADC (LeCroy LRS1881M), and the rest is summed in a series of linear fan ins/fan outs as follows: A sum is formed for each layer, then the first two layers are added to form a preshower sum (PRSUM), and then all are added to form a shower sum (SHSUM). Although the calorimeter was not used in the E91-013 trigger, these last two signals are sent to discriminators and then to the trigger where they can be used to identify electrons and pions.

2.6 High Momentum Spectrometer

A diagram of the High Momentum Spectrometer (HMS) is shown in Fig. 2.20. It is designed to detect particles with momenta up to 6 GeV/c, have a large momentum acceptance, and provide excellent resolution [43]. The HMS is a $QQQD$ spectrometer, meaning it consists of three focusing quadrupoles followed by a dipole which bends the particles vertically through 25°. The characteristics of the HMS are listed in Table 2.6. As in the case of the SOS, the HMS magnets were tuned in point-to-point mode during E91-013.

The HMS magnets are all superconducting although the quadrupoles contain soft iron cores. The transverse focusing in the HMS is provided by the quadrupoles,

Table 2.6: HMS Characteristics.

Parameter	Value
Max. Central Momentum	7.5 GeV/c
Momentum Bite	$\pm$ 9 %
Resolution ($\delta p/p$)	<0.1%
Solid Angle Acceptance	8.1 msr
Scattering Angle Bite	$\pm$ 32 mr
Out of Plane Angle Range	$\pm$ 85 mr
Angle Precision (Horizontal)	0.8 mr
Angle Precision (Vertical)	0.8 mr

labeled Q1 (horizontally focusing), Q2 (vertically focusing), and Q3 (horizontally focusing). The magnets are all cooled by 2 K liquid helium provided by the CEBAF End Station Refrigerator (ESR). A program was written to take a requested momentum setting and calculate the required magnetic fields and supply currents for each magnet. The quadrupoles power supplies are set by current, meaning it was necessary to map the fields as a function of excitation current. The dipole contains a Hall effect probe linked in a feedback loop to the power supply. This enables one to set the magnet directly by specifying the desired field.

As in the case of the SOS, the acceptance in solid angle is defined by one of three Hevimet collimators (5 cm thick). There are two octagonal collimators, and the larger was used during the experiment. It defines an acceptance of roughly 6.8 msr. The third collimator is a "sieve slit" which consists of an array of holes that were used to map locations at the entrance of the spectrometer to the focal plane.

2.6.1 HMS Detectors The HMS detector stack is quite similar to that of the SOS. As shown schematically in Fig. 2.21, it consists of four planes of hodoscopes, two six-plane wire chambers, a gas threshold Čerenkov detector, and a four layer Pb-glass shower counter.

The HMS contains two identical sets of drift chambers that are operationally quite similar to those of the SOS [50]. However, instead of three plane

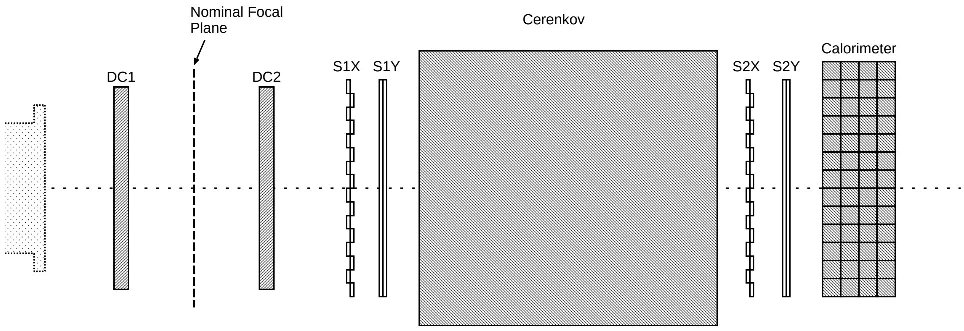

Figure 2.21: Schematic of the HMS detector stack shown approximately to scale.

orientations, the HMS chambers have two horizontally oriented planes (X, X'), two vertically oriented planes (Y, Y'), a 15^o plane (V), and a 165^o plane (U). As shown schematically in Figure 2.22, the order as seen by an incoming particle is $XYUVY'X'$. The chambers are set apart by 81 cm so as to be equally spaced about the nominal focal plane, and have an active area of approximately 113 cm (vertically, or X) by 52 cm (horizontally, or Y). Again, the duplicated planes are offset by one half the cell width to aid in left/right determination. The basic cell is repeated in the z direction every 1.8 cm. The field shaping wires (cathodes) are 150 μm in diameter and are made of gold-plated copper-beryllium, and the sense wires (anodes) are 25 μm in diameter and are made of gold-plated tungsten wire. The chambers use the same gas mixture as the SOS chambers: argon-ethane (50/50 by mass) at a typical flow rate of 200 cm^3/minute.

The signals from the sense wires are amplified and discriminated in either Nanometrics [51] and LeCroy 2735DC drift chamber cards. As in the case of the SOS, only pulses above threshold form a start in the drift chamber TDCs (Section 2.7). The time-to-distance conversion procedure is identical to that in the SOS.

There are four hodoscope planes in the HMS; two immediately after the wire chambers (S1) and two more after the Čerenkov detector (S2). The spacing between the two sets is approximately 2.2 m. The first and third planes, labeled S1X and

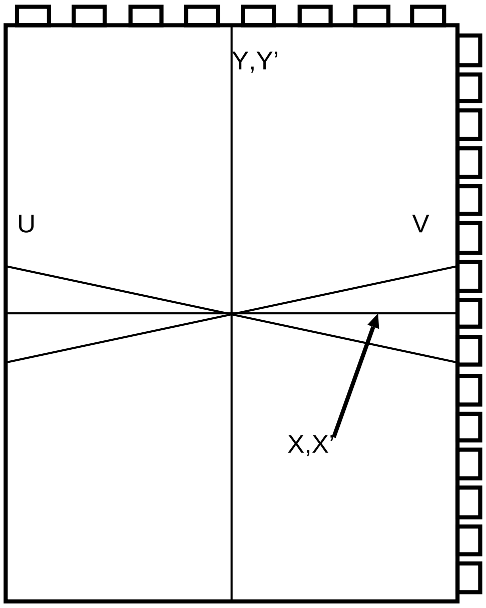

Figure 2.22: Layout of HMS drift chamber planes as seen by an incoming particle.

S2X, are oriented horizontally and contain sixteen paddles each. The paddles in the X planes measure 21 mm $\times$ 80 mm $\times$ 750 mm. The second and fourth planes are labeled S1Y and S2Y, respectively. They are oriented vertically, and each contain ten paddles that measure 21 mm $\times$ 80 mm $\times$ 1205 mm. The active area of the HMS scintillators is 120 cm vertically by 75 cm horizontally.

The signal processing of the HMS scintillators is performed in a manner identical to that of the SOS. The signals are sent to a splitter in the counting house, where a third of the signal is sent to a Fastbus ADC, and the rest to a discriminator. These pulses are then sent to a Fastbus TDC, a VME scaler, and then to the trigger electronics (Section 2.7).

The HMS Čerenkov detector sits between two the sets of hodoscope planes. It has a 1.8 m length, and was filled with N_2 gas at approximately 14.7 PSIA. The energy threshold for Čerenkov radiation is $\sim$ 20 MeV for electrons and $\sim$ 4 GeV for pions. As in the case of the SOS gas Čerenkov, the photons were reflected to the phototubes (also Burle 8854) by spherical mirrors.

The final detector in the HMS stack is the shower counter. Its design is identical to that of the SOS with the exception of having thirteen blocks in each of the four layers.

2.7 Trigger Electronics

The detector ADCs and TDCs for each spectrometer are read out only in the case of a trigger. Quite simply, a trigger is defined by the firing of each hodoscope plane as a particle passes through the detector stack. This is called a "singles" trigger meaning the that there was a trigger in a single spectrometer. During E91-013, both spectrometers were operated in "coincidence" mode in which the relative timing of triggers in both the SOS and HMS is used to tag two particles as originating from the same reaction vertex.

Although it is possible to include particle identification in the trigger (e.g., require a calorimeter signal for electrons, or lack of a Čerenkov signal for pions), E91-013 ran with a simple three-out-of-four (3/4) hodoscope plane requirement. This was implemented as follows: As shown in Fig. 2.23, the signals from the hodoscope PMTs are fed to a splitter in the counting house where approximately 1/3 of each signal is sent through delay to a LeCroy Fastbus ADC (LRS1881M).

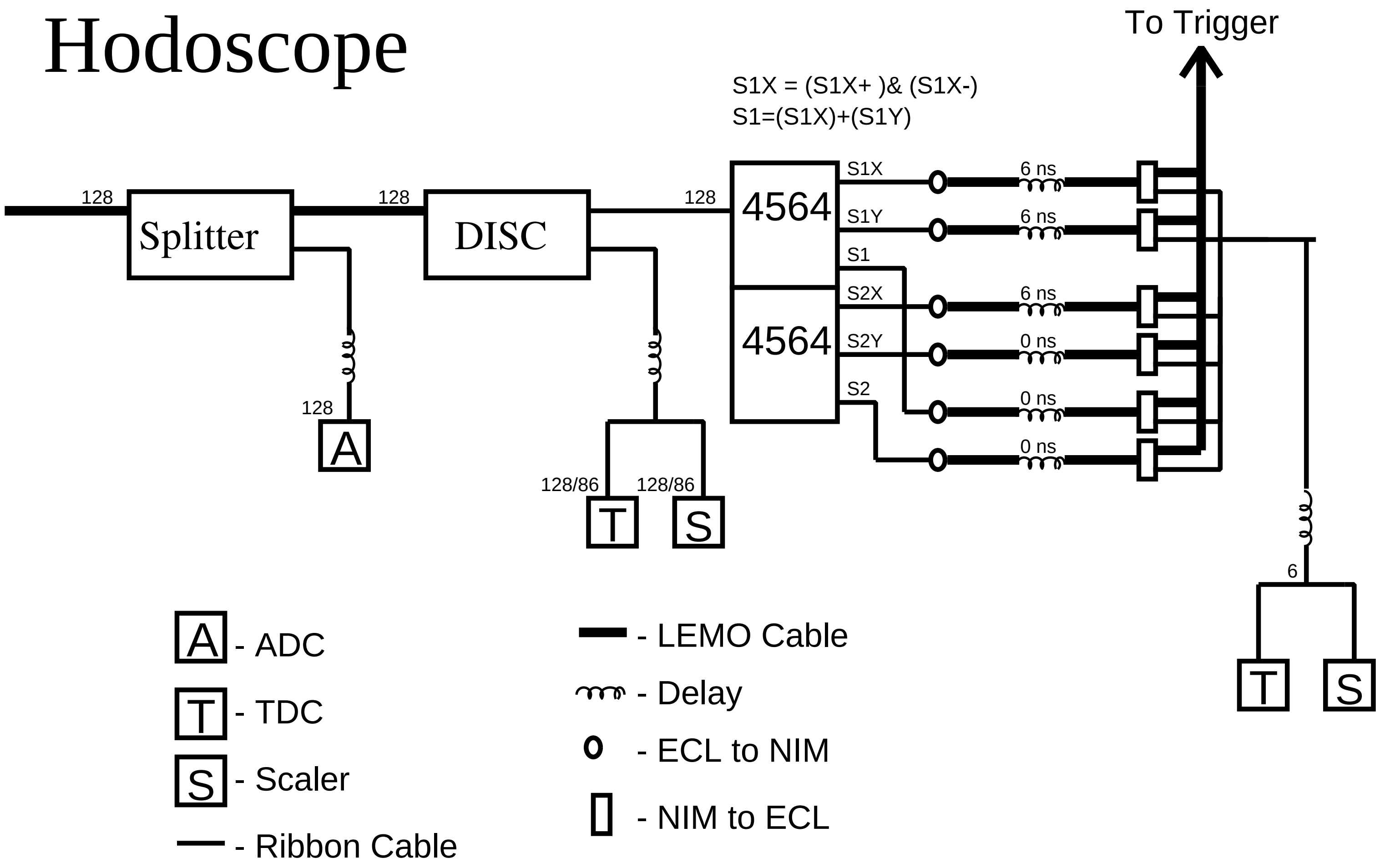

Figure 2.23: Schematic of the Hodoscope Electronics.

The remaining 2/3 of each signal is sent to a Phillips 16 Channel Discriminator Latch (CAMAC Model 71106). A LeCroy 64 channel logic unit (LRS4564) is used to OR the tubes from a given side of each hodoscope plane. Each side is then ANDed together to form four plane pretrigger signals, $S1X, S1Y, S2X, S2Y$. The signals, $S1X$ ($S2X$) and $S1Y$ ($S2Y$) are then ANDed together to form $S1$ ($S2$). These signals are sent to Phillips delay modules (792) where they are delayed by up to 64 ns to adjust the relative timing of the four planes. The delayed signals are then sent to a LeCroy logic unit (LRS365AL) where the pretrigger, SCIN (one among others not used in E91-013), is defined as a 3/4 OR of $S1X, S1Y, S2X, S2Y$. A pretrigger differs from a trigger only in that while it is counted, its detector information may not actually get read out; the data acquisition computer may be busy, or it may be set to only read out every nth event so as to maintain a manageable data rate (this is known as "prescaling"). The output of the logic unit is a gate that is set to 30ns wide in the case of the HMS and 100ns wide in the case of the SOS. This is to allow a comfortable overlap for a coincidence trigger.

The pretrigger signals from each spectrometer are then sent to a LeCroy 8LM programmable logic module. This device is programmed to classify an event either an HMS single, an SOS single, or a coincidence, depending on the timing of the inputs. A third input to the 8LM is a BUSY from the Trigger Supervisor (TS) [52]. The logic signal outputs of the 8LM can be either an HMS single, and/or an SOS single, and/or a coincidence pretrigger. Each of these signals has both a BUSY and non-BUSY version depending on the state of the TS. This information is used for data acquisition dead time calculations (Section 3.6). Note that every pretrigger output of the 8LM is sent to a scaler.

The trigger information is used by Trigger Supervisor to read out the Fastbus ADCs and TDCs as follows. We consider an HMS singles event that is not prescaled as an example (the SOS information is retrieved in precisely the same manner). After the 8LM, the HMS TRIG signal is split; one part is delayed while the other is sent to the TS, as shown in Fig. 2.24. The TS creates two long HMS gates, that last until each Fastbus crate reports finished. These gates are ANDed with the original HMS TRIG that was split off after the 8LM. Once this AND is formed, the gates are sent to read out the HMS ADCs, and the (common) start is sent to the HMS TDCs. The ADC and TDC signals have each been delayed by the precise amount of time so as to be in time with these gates. Note that it is the delayed HMS TRIG signal that determines the timing of the gates, and that this insures that the HMS signals are read out in time with the HMS trigger. This process is often referred to as "retiming," and it is important because in the case of a coincidence trigger it allows each spectrometer to read out its respective signals relative to the timing of its own trigger.

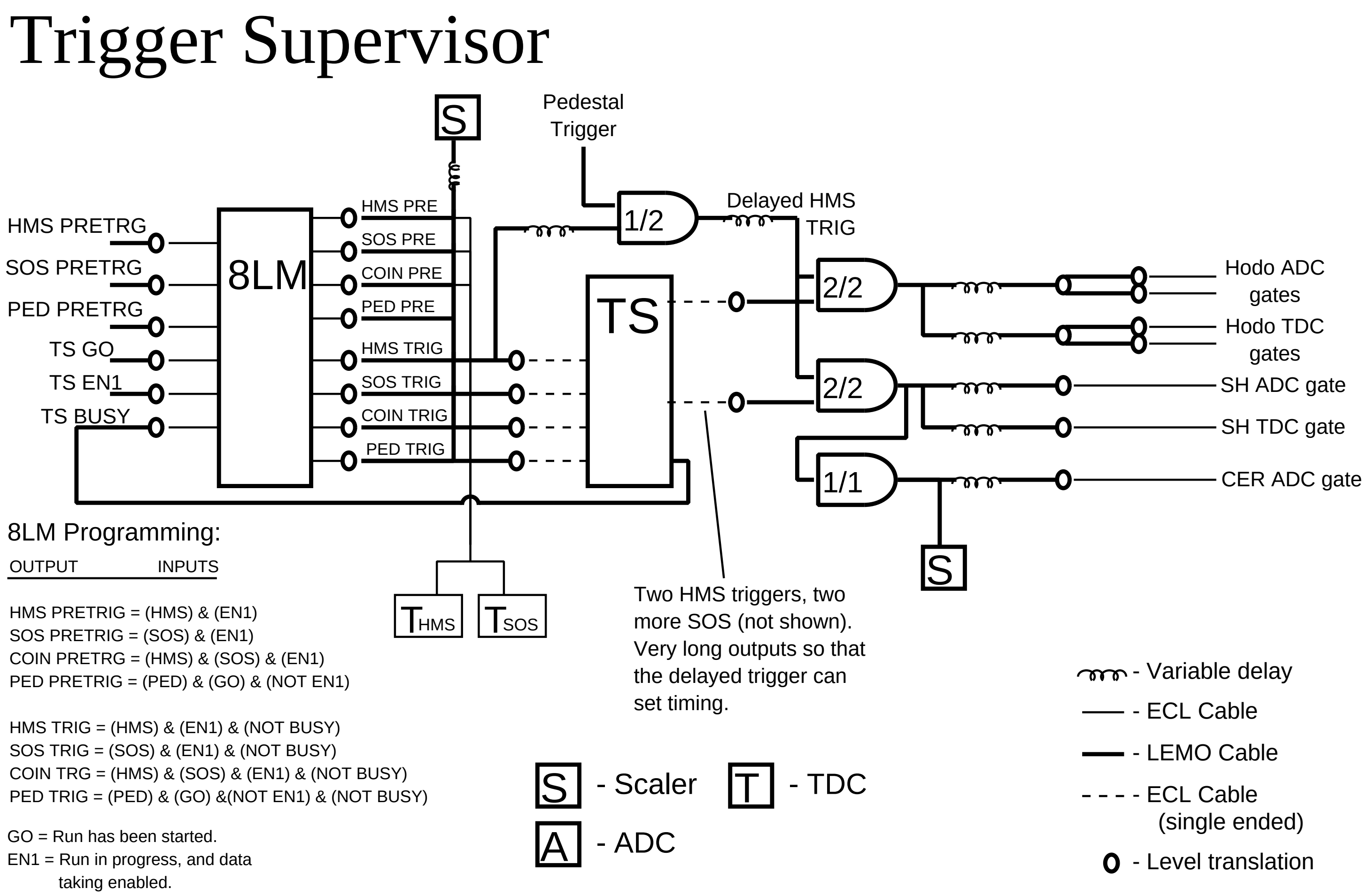

Figure 2.24: Trigger Supervisor.

A coincidence trigger is slightly more complicated in that there exists the additional timing information between the two spectrometers. There are two coincidence times, one reported by the HMS and the other by the SOS, and they are measured as follows. The HMS coincidence time is started by the HMS TDC start; namely the retimed HMS TRIG signal ANDed with the TS output. The stop comes from the SOS TRIG (shown in the bottom of Fig. 2.24). There is also a time started by a retimed SOS TRIG and stopped by the HMS (not shown in Fig. 2.24).

2.8 Data Acquisition

The Fastbus ADC and TDC data were read out through an FDDI (fiber optic) link to a Hewlett-Packard 9000 Unix workstation [53]. The data were written directly to hard disk in CEBAF Online Data Acquisition (CODA) format [54]. During normal running, every coincidence trigger was written to disk, and SOS and HMS singles were each prescaled separately so as to maintain a manageable data rate. Coincidence data were typically read at a rate of approximately 500-1000 Hz. Scaler values were written to disk every two seconds.

In addition to the Fastbus data and scaler values, slow control information was included in the data stream every thirty seconds. "Slow controls" refer to static, or slowly changing, parameters that includes things like high voltage settings, magnet power supply settings, and beam line parameters.

The Fastbus data were acquired in "sparsified" mode in which only non-zero data were read from each ADC and TDC (often known as "zero-suppression"). The TDCs were sparsified by reading out only those channels that had stops. The ADCs have a programmable threshold which was typically set fifteen channels above zero. The zero (or "pedestal") of the ADC was determined at the beginning of each run by creating one thousand artificial triggers. These thousand events show up as a narrow peak in a histogram of the ADC output. This automatic determination of

Table 2.7: Runs taken in buffered mode.

Kinematics	Run Range	Run Mode
A	5307 – 5327	Not Buffered
A	5329 – 5350	Buffered
A	5351 – 5354	Not Buffered
A	5355 – 5374	Buffered
A	5437 – 5448	Buffered
A	8168 – 8194	Buffered
B	5377 – 5422	Buffered
B	8196 – 8215	Buffered
C	5473 – 5573	Not Buffered
C	8216 – 8238	Buffered
D	5613 – 5707	Not Buffered
D	8308 – 8349	Buffered
E	8466 – 8541	Buffered
E	8554 – 8563	Buffered
F	8571 – 8680	Buffered

the channel corresponding to zero signal for each ADC can then be used as input to the data acquisition code such that it only reads out data above zero. Any time there was a reason to believe a pedestal may have changed, a short run was taken to get the new values, and the input to the DAQ was modified.

During part of the December 1995 run and all of the May 1996 run, the data were recorded in "buffered" mode meaning that the Fastbus modules buffered the event information (up to sixteen events) while the DAQ computer was busy. Note that buffering only occurs at high rates; at lower rates, the computer can keep up, precluding the need to buffer the events. Table 2.7 lists the runs taken in buffered mode.

CHAPTER 3

DATA ANALYSIS

Each particle must be tracked, timed, reconstructed to the target, and identified, before physics quantities (i.e., missing energy and momentum) for that event can be calculated. Corrections due to inefficiencies in the detectors and processes that prevent the detection of valid trajectories must also be applied. This chapter starts with a discussion of the tracking algorithm, which fits a trajectory through the spectrometer focal plane. Next is a discussion of the reconstruction of this trajectory back to the target vertex, followed by a description of the corrections that need to be applied to the trajectory. The standard parameters used to define good events (often referred to as "cuts") are then presented before the chapter concludes with a description of the experimental simulation, SIMC.

3.1 Tracking Algorithm

The tracking algorithm fits a trajectory through the detection plane given the wire chamber information. The detection plane is located halfway between, and parallel to, the two wire chambers and marks the approximate location of the focal plane (Fig. 3.1) [55]. The focal plane is defined to be the surface along which, in the dispersive direction, a particle's position depends only on its momentum. (This is true to first order; aberrations can cause dependencies on other quantities. See Section 3.2.) Note that the terms "detection plane" and "focal plane" are often taken to be synonymous, and unless otherwise noted, the subscript "fp" will be used to denote quantities measured in the detection plane.

Except for details arising from slight differences in wire chamber designs,

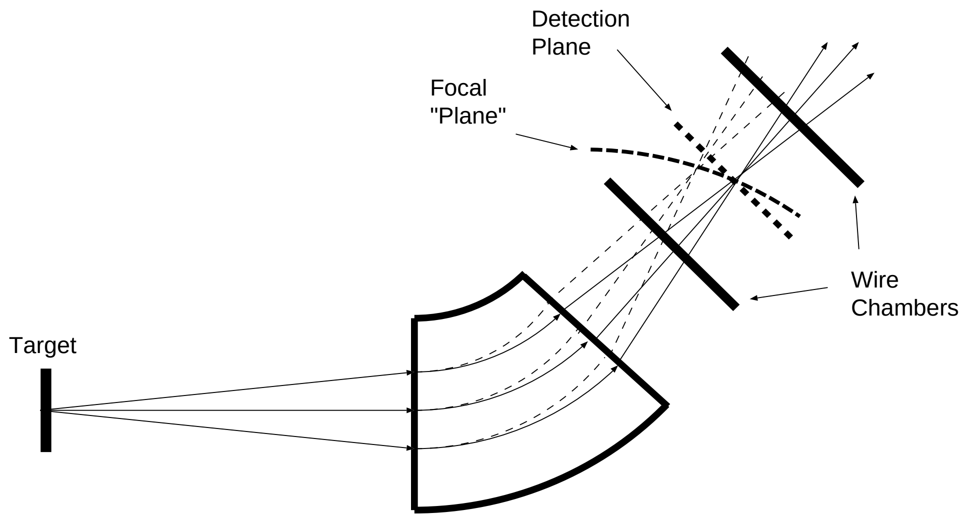

Figure 3.1. The difference between focal and detection planes. Particles with different momenta are focused to different spots along the focal plane which is actually a surface “near” the detection plane.

the tracking algorithms for the two spectrometers are very similar. The algorithms work by grouping pairs of non-like wires into “pairs.” A non-like wire is a wire that is sufficiently perpendicular to its partner. For example, the X and U wires in the SOS (60° apart) are considered non-like. Other than parallel wires, only the $X-U$, $X-V$, and $U-V$ pairs in the HMS are considered too similar to be paired. The algorithm then loops over pairs, grouping pairs of pairs into “combos.” Combos that are sufficiently near each other are grouped into “space points.” Finally, a miniature track through the one chamber, called a“stub,” is fitted through each space point. Stubs from the two chambers that have positions and slopes such that they are approximately collinear are then linked into tracks. A χ^2 is formed for each track, and in the case of multiple tracks, is used to select the best track. The efficiency of the algorithm and issues related to multiple tracks are discussed in Section 3.3.

There are many user defined parameters that govern the tracking algorithm. Those used in E91-013 are listed in Table 3.1. Both a minimum and maximum number of hits per chamber are defined as five and thirty, respectively. Ideally, each

Table 3.1: Tracking algorithm parameters. See text for explanation of terms.

	HMS	SOS
Maximum Hits	30	30
Minimum Hits	5	5
Minimum Combos	6	6
Space Point Criterion (cm)	1.2	1.2
x Stub Criterion (cm)	30	50
y Stub Criterion (cm)	10	10
x' Stub Criterion	0.5	0.75
y' Stub Criterion	0.5	0.5

track fires one wire per plane resulting in six hits per chamber. However inefficiencies (Section 3.3) can result in five or fewer planes with firing wires. In the case of the HMS, the minimum of five was chosen to insure that at least one Y plane fired (recall that four of the six planes in the HMS are X-like). On the other hand, it is often the case that a particle will fire two adjacent wires in a plane resulting in approximately twelve hits per chamber. If multiple tracks occur, the number of hits can grow rapidly, and thus the maximum was set to thirty. As discussed in Section 3.3, however, the chambers are very efficient, and the number of tracks with less than five hits or more than twelve is actually very small ($< 0.1\%$), and thus the results are quite insensitive to the choice of the allowed number of hits. The "space point criterion" is the radius in which all combos must lie in order to be considered part of the same space point. Finally the stub criteria define the vertical (x, x') and horizontal (y, y') distance and slope ranges in which two stubs must lie to be considered part of the same track.

Once a particle has been tracked, its focal plane quantities are determined. The focal plane quantities consist of x and y (the vertical and horizontal coordinates, respectively), and x' and y' (the vertical and horizontal trajectory slopes, respectively).

3.2 Event Reconstruction

The focal plane quantities define a trajectory that then must be reconstructed back through the spectrometer to the reaction vertex in the target. These target quantities depend on the focal plane quantities through the transformation,

$$x^i_{tar} = \sum_{j,k,l,m}' (M^i_{jklm}) x^j_{fp} x'^k_{fp} y^l_{fp} y'^m_{fp}, \tag{3.1}$$

where the prime indicates that the sum over j, k, l, m is constrained such that

$$j + k + l + m \leq N, \tag{3.2}$$

where N is the order of the transformation, and

$$\begin{aligned} x^1_{tar} &= x'_{tar}, \\ x^2_{tar} &= y_{tar}, \\ x^3_{tar} &= y'_{tar}, \\ x^4_{tar} &= \delta. \end{aligned}$$

The quantities M^i_{jklm} are matrix elements, and δ is the momentum of the particle expressed relative to the spectrometer's central momentum, p_c:

$$\delta = \frac{p - p_c}{p_c}.$$

Note that information on the vertical position at the target has been exchanged for knowledge of the momentum, and therefore x_{tar} is assumed to be zero.

The matrix elements for both spectrometers are determined through an iterative process. The program COSY INFINITY is used to calculate the matrix elements (5th order for the HMS; 6th order for the SOS) for a nominal description of the spectrometer [56]. Data are then taken with a point target and with the

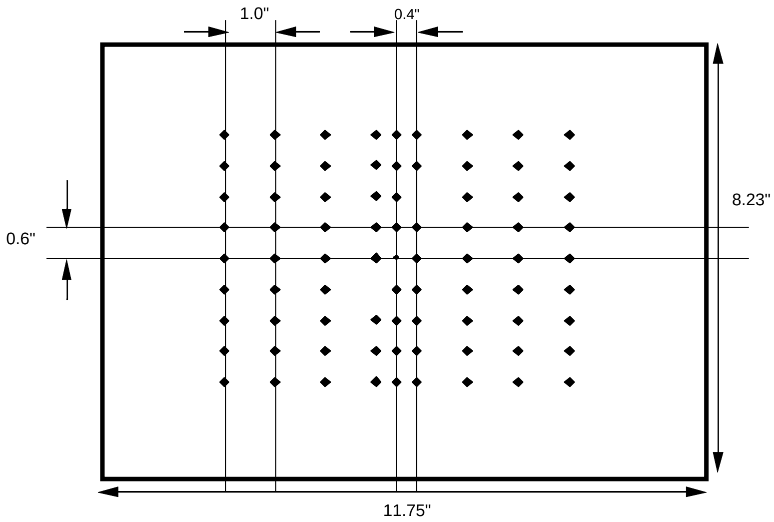

Figure 3.2. The SOS sieve slit. The known position of the holes at the entrance to the spectrometer are used to fit the reconstruction matrix elements. The missing holes are used to verify the orientation of the slit. Note that the holes are angled so as to take into account the expanding particle envelope from the target to the slit. The hole diameters are ~ 0.1 inches. The HMS sieve slit is similar.

sieve slit in place at the entrance of the spectrometer. (Figure 3.2 shows the SOS sieve slit. The HMS slit is similar.) The COSY simulation is sufficient to take the focal plane data, reconstruct back to the sieve slit position, and determine with high probability which of the holes the particles most likely went through. Then, knowing the true position of the holes, the matrix elements are adjusted to fit the particle tracks through the center of holes. The process is then repeated with the new matrix elements until the values converge.

3.3 Tracking Efficiency

Because the tracking algorithm requires both a minimum and a maximum number of hits, inefficient planes or noise hits can cause the algorithm to fail to find a track even if the event was valid. Thus, the measured yields need to be corrected for the tracking efficiency. The efficiency is measured by placing tight cuts on the position of the triggering scintillators which insures that the particle trajectories went through the wire chambers, and should thus be tracked. The fraction of these events that are tracked is taken to be the "tracking efficiency." Note that this measures both the efficiency of the wire chambers and the tracking algorithm together.

Two tests of this as a true measure of the efficiency were performed. After correcting for the efficiency, yields from runs with quite different tracking efficiencies were seen to agree at the 1% level. The second test determined that the measured tracking efficiency agreed with what was expected given the wire chamber plane efficiency. The efficiency for a given plane, P_i, is defined by taking events with the same fiducial scintillator cuts as above and calculating the fraction of the time that the plane fired. The average plane efficiency, P, is then the average efficiency of all twelve planes in both chambers. The fact that the algorithm requires at least five firing planes in both chambers means that the probability, $\mathcal{P}$, of finding a track goes as

$$\mathcal{P} = (6P^5 - 5P^6)^2. \tag{3.3}$$

The probability of finding a track given the average plane efficiency was found to match the measured tracking efficiency at the 1% level. The two tests described were used to assign a 1% error due to the wire chamber efficiency/tracking algorithm.

The tracking efficiencies for both spectrometers were typically $> 97\%$. However, there are some examples—the hydrogen Kinematics F data being the most prominent—of runs that have efficiencies as low as 50%. In this case, the problem was traced to a bad gas mixture. Table 3.2 lists the mean tracking efficiency for both spectrometers at each kinematics.

It is possible that the tracking algorithm finds multiple tracks for a given event. These multiple-track events fall into two classes: those that are actually two real particles in the spectrometer at the same time, and those that are artifacts of the algorithm (often referred to as "ghost" tracks). The latter are usually caused by a few extra, or "noisy" wires that upset the left/right determination such that two or

Table 3.2. Mean tracking efficiencies for each target at each kinematic setting. A "—" indicates that there was just one run at that setting.

Kinematics	Target	HMS Eff.	Error	SOS Eff.	Error
A	Carbon	0.983	0.001	0.992	0.000
A	Iron	0.983	0.001	0.992	0.000
A	Gold	0.983	0.001	0.992	0.000
A	Hydrogen	0.989	—	0.991	—
B	Carbon	0.955	0.018	0.994	0.001
B	Iron	0.979	0.003	0.994	0.001
B	Gold	0.979	0.002	0.993	0.001
B	Hydrogen	0.982	—	0.990	—
C	Carbon	0.984	0.003	0.991	0.003
C	Iron	0.985	0.002	0.975	0.017
C	Gold	0.985	0.002	0.979	0.012
C	Hydrogen	0.950	—	0.954	—
D	Carbon	0.981	0.003	0.991	0.001
D	Iron	0.978	0.004	0.991	0.001
D	Gold	0.966	0.007	0.990	0.001
D	Hydrogen	0.964	0.001	0.986	0.001
E	Carbon	0.938	0.003	0.925	0.055
E	Iron	0.918	0.003	0.982	0.002
E	Hydrogen	0.981	—	0.990	—
F	Carbon	0.970	0.009	0.992	0.001
F	Iron	0.975	0.007	0.990	0.001
F	Gold	0.975	0.006	0.992	0.001
F	Hydrogen	0.520	0.030	0.991	0.000

more tracks can be fit through a space point. In this case the track with the lowest χ^2 is chosen as the "selected" track. Most of the multiple-track events fall into this latter category. Because the fraction of events for both cases is always less than 0.1% of the total, errors induced by the presence of multiple tracks are neglected.

3.4 Proton Absorption

Because protons are strongly interacting particles, there is a significant chance that they will undergo a nuclear interaction as they traverse the detector stack. If such a reaction removes the proton from the acceptance before it causes a trigger, the measured coincidence yield will be artificially low. Given the nuclear interaction lengths (the mean free path between nuclear interactions) of the materials in the proton's path, it is possible to estimate the "proton absorption" [9]. One can also use H(e,e$'$p) to measure the absorption directly, because every electron in the coincidence acceptance region must have caused the emission of a corresponding proton. The fraction of "missing" protons is the absorption (and, consequently, the fraction that survive is the transmission).

Table 3.3 (3.4) lists the properties of the materials that a proton must traverse on its way from the target through the SOS (HMS). The mean free path between nuclear collisions, $\bar{\lambda}$, is derived as follows. Reference 9 lists both the mean free path between nuclear collisions, λ_T, and the mean free path between inelastic interactions, λ_I, as calculated from $\lambda_i = \frac{A}{N_A \times \sigma_i}$, where N_A is Avogadro's number, and σ_i is the corresponding cross section. Because the cross section is very peaked in the forward direction, elastic scattering will only remove a small fraction of the protons from the acceptance. To account for this, the average of the total interaction length and the inelastic contribution, is used in the absorption estimation. Assuming that a proton traversing one quarter of the third scintillator is sufficient to cause a

Table 3.3: Materials in the SOS.

Absorber	Density (g/cm^3)	Thickness (cm)	$\bar{\lambda}$ (g/cm^2)	X (g/cm^2)	$X/\bar{\lambda}$ (10^{-3})
3.37cm LH	0.0708	3.37	47.3	0.239	5.04
5 mil Al target	2.70	0.0127	88	0.0343	0.39
window					
8 mil Al chamber window	2.70	0.0203	88	0.0548	0.62
Air	0.00121	~ 15	75	0.0182	0.24
Kevlar	0.74	0.0127	~ 70	0.0094	0.13
Mylar	1.39	0.0076	72	0.0106	0.15
Kevlar	0.74	0.0381	~ 70	0.0282	0.40
Mylar	1.39	0.0127	72	0.0177	0.25
Air (DC1 - S2)	0.00121	~ 149	75	0.180	2.40
Mylar cathode	1.39	14(0.00125)	72	0.0244	0.34
Wire (effective) W $(12 \times 30 + 12 \times 60)\mu m$	19.3	24(0.0002)	147.7	0.00938	0.06
Ar/Ethane (50/50 weight)	0.00154	12(0.6178)	~ 70	0.01142	0.16
Poltysty. (1.04 overlap)	1.03	2(1.04)(1.0)	70	2.142	30.61
Čerenkov windows (2mil tedlar, 10mil lexan)	~ 1.39	2(0.030)	~ 70	2(0.042)	1.21
Freon 12 (1atm)	0.00493	100	87	0.493	5.67
Mirror (rohacell, mylar, carbon)	-	-	~ 70	0.45	6.43
Poltysty. (1.10 overlap)	1.03	$\frac{1}{4}(1.10)(1.0)$	70	0.283	4.05
Total					58.2

Table 3.4: Materials in the HMS.

Absorber	Density (g/cm^3)	Thickness (cm)	λ (g/cm^2)	X (g/cm^2)	X/λ (10^{-3})
3.37cm LH (after scatt.)	0.0708	3.37	47.3	0.239	5.04
5 mil Al target window	2.70	0.0127	88	0.0343	0.39
16 mil Al chamber window	2.70	0.0406	88	0.1096	1.24
Air	0.00121	~ 15	75	0.0182	0.24
Kevlar	0.74	0.0381	~ 70	0.0282	0.40
Mylar	1.39	0.0127	72	0.0177	0.25
Kevlar	0.74	0.0381	~ 70	0.0282	0.40
Mylar	1.39	0.0127	72	0.0177	0.25
Air (exit pipe through S2	0.00121	~ 256	75	0.310	4.13
4 mil Mylar (entr/exit)	1.39	0.0102	72	0.0142	0.20
Sense Wires (effective) 25μm W, 12 planes	19.3	0.000076	147.7	0.00146	0.010
Field Wires (effective) 150μm Al/Au (99/1) 18 planes	2.70	0.0068	89.1	0.0184	0.21
Ar/Ethane (50/50 weight)	0.00154	16.6	~ 70	0.0256	0.36
Field Wires (effective) 150μm Cu/Be (50/50) 18 planes	5.40	0.0068	87.9	0.0368	0.42
Poltysty. (1.067 overlap)	1.03	2(1.067)(1.0)	70	2.198	31.40
Čerenkov windows 40mil Al (entrance/exit)	2.70	2(0.102)	88.5	2(0.275)	6.22
Čerenkov gas N_2	0.00125	150	64.2	.1875	2.92
Rohacell Mirror support Mirror SiO_2	~ 0.05 2.20	~ 1.8 0.3	~ 70 83.1	0.09 0.66	1.3 3.13
Poltysty. (1.067 overlap)	1.03	$\frac{1}{4}(1.067)(1.0)$	70	0.275	7.94
Total					67.34

3/4 trigger, the predicted transmission in the SOS is

$$PT_{SOS\ calculated} = e^{-\sum_i X_i/\bar{\lambda}_i} = e^{-0.0582} = 0.943, \tag{3.4}$$

and for the HMS:

$$PT_{HMS\ calculated} = e^{-\sum_i X_i/\bar{\lambda}_i} = e^{-0.0673} = 0.935. \tag{3.5}$$

Measurements of the proton absorption in the SOS were performed as follows: hydrogen coincidence runs (electrons in the HMS, protons in the SOS) were analyzed twice; once coincidences only, and then electron arm only. Looking at hsx'_{tar} versus hsy'_{tar} (the vertical and horizontal slopes at the target, respectively) for the coincidence data reveals the region in the HMS that kinematically corresponds to the coincidence region for the SOS. That is, events in this region had to cause a proton to enter the SOS; if the proton did not cause a trigger it must have been absorbed. Note that this only works with hydrogen targets; protons in carbon, for example, may be absorbed do to final state interactions in the nucleus or have sufficient initial Fermi momentum so as to be outside the SOS's acceptance. Fig. 3.3 shows plots of the coincidence events and electron-only events. The coincidence data were used to put tight cuts on the electron arm quantities. By counting the number of coincidences and electrons-only in this region the proton transmission is determined via

$$PT_{measured} = \frac{N_{coins}}{N_{coins} + Prescale_{HMS} N_{e^- only}}. \tag{3.6}$$

Table 3.5 lists the measured values for five Hydrogen runs with protons in the SOS. Note that they are independent of the proton momentum (at least over this limited range). Taking the average, the proton transmission in the SOS is measured to be 0.951 ± 0.005, in agreement with the theoretical estimate. This value is used in the analysis of E91-013.

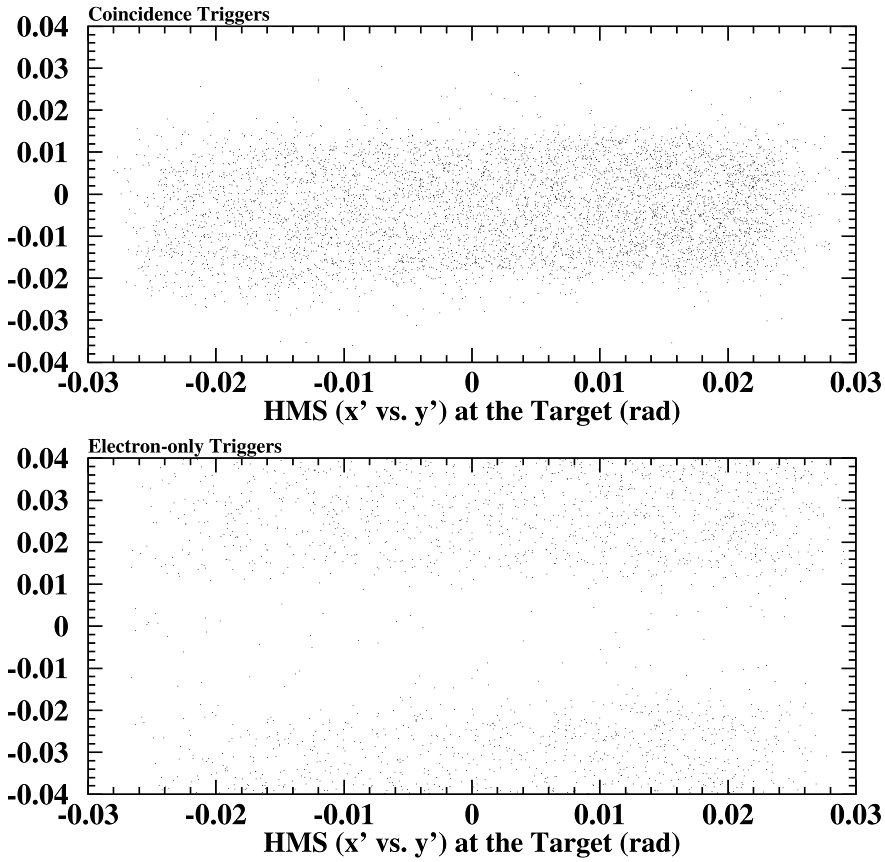

Figure 3.3. x' versus y' at the target for electrons in the HMS. The top plot is coincidences-only and thus defines the kinematic region in the HMS in which coincidences occur. The bottom plot is electrons-only for the same kinematic region. Electrons in the "coincidence" region in the second plot were paired with protons that were apparently absorbed before detection.

Table 3.5. Measured proton transmission in the SOS. Note that "e-only" takes the HMS prescale factor into account.

Run #	8168	8197	8235
δ (%)	$-2.0 \rightarrow 2.0$	$-2.0 \rightarrow 2.0$	$-2.0 \rightarrow 2.0$
x'_{tar} (rad)	$-0.009 \rightarrow 0.003$	$-0.02 \rightarrow 0.02$	$-0.02 \rightarrow 0.02$
y'_{tar} (rad)	$-0.01 \rightarrow 0.02$	$-0.015 \rightarrow 0.015$	$-0.015 \rightarrow 0.015$
y_{tar} (cm)	$-0.5 \rightarrow 0.25$	$-0.7 \rightarrow 0.7$	$-0.4 \rightarrow 0.4$
$Prescale_{HMS}$	25	3	4
# coins	64804	20215	12412
# e-only	3600	1161	660
$P_{proton}(GeV/c)$	0.840	1.275	1.550
Absorption	0.947±0.004	0.946±0.003	0.950±0.004
Run #	8310	8560	
δ (%)	$2.0 \rightarrow 3.5$	$-2.5 \rightarrow 0.0$	
x'_{tar} (rad)	$-0.05 \rightarrow 0.05$	$-0.4 \rightarrow 0.4$	
y'_{tar} (rad)	$-0.1 \rightarrow 0.15$	$-0.01 \rightarrow 0.02$	
y_{tar} (cm)	$-1.5 \rightarrow 0.75$	$-2.0 \rightarrow 0.8$	
$Prescale_{HMS}$	4	1	
# coins	15513	14114	
# e-only	684	691	
$P_{proton}(GeV/c)$	0.840	1.550	
Absorption	0.958±0.003	0.953±0.002	

Table 3.6. Measured proton absorption in the HMS. Note that "e-only" takes the HMS prescale factor into account. Run 8584 had 55% tracking efficiency in the HMS. The coincidence counts were increased by 1/0.55.

Run #	12256	12284	8584
δ (%)	$5.0 \to 15.0$	$10.0 \to 15.0$	$-1.0 \to 8.0$
x'_{tar} (rad)	$-0.03 \to 0.03$	$-0.03 \to 0.03$	$-0.035 \to 0.035$
y'_{tar} (rad)	$0.0 \to 0.025$	$-0.02 \to 0.02$	$-0.02 \to 0.02$
y_{tar} (cm)	$-1.0 \to 1.0$	$-1.0 \to 1.0$	$-1.0 \to 1.0$
$E_{electron}(GeV)$	> 0.8	> 0.8	> 1.0
$Prescale_{SOS}$	5	5	1
# coins	925	1325	6163
# e-only	50	70	427
$P_{proton}(GeV/c)$	1.500	1.500	2.550
Absorption	0.95±0.15	0.95±0.013	0.935±0.003

Experimental determination of the proton absorption in the HMS is more difficult only in that hydrogen coincidence runs with protons in the HMS (and non-coincidence electrons in the SOS that are not prescaled away) are rare. The following three hydrogen coincidence runs were used: 12256, 12284, two experiment E94-014 runs from November 1996, and 8584, an E91-013 run from April 1996. None of the runs are ideal. The E94-014 runs require tight constraints on the kinematic variables to insure that the electron should have caused a coincidence, and this results in a low number of counts. Run 8584 had roughly ten times the number of events but had an HMS tracking efficiency of only 55%. For all of these runs, a calorimeter signal was required in the SOS to insure that the particles were indeed electrons. (Note: this was also tried for the runs with electrons in the HMS, but the effect was negligible.) Table 3.6 lists the results.

The value of 0.945 ± 0.02 is in agreement with the theoretical 0.935, but the large error bar (relative to the SOS measurement) reflects the large tracking correction (run 8584) or the low number of counts (runs 12256 and 12284), and the fact that the values are dependent on the kinematic constraints at the few percent level. As in the case of the SOS a value of 0.95 was actually used in the analysis.

3.5 Dead Time Corrections

When measuring absolute cross sections, one needs to account for valid events that arrive while the data acquisition/trigger hardware is busy. This busy, or "dead," time stems from two sources: the electronic dead time, due to the trigger hardware being busy, and the computer dead time, due to the finite time it takes the data acquisition computer to process events. Note that the dead time is actually most often quoted in terms of the fraction of time the data acquisition system is busy. The live time is then defined as 1 - dead time.

The electronic dead time is due to the fact that the logic pulses in the trigger all have a finite width (30 ns). If another event arrives during this interval it will be missed. Given an average event rate, r, the probability of n events occurring in an interval t is given by the Poisson distribution,

$$P(n) = \frac{(rt)^n e^{-rt}}{n!}. \tag{3.7}$$

The probability then, of zero events occurring in time t is thus,

$$P(0) = e^{-rt}, \tag{3.8}$$

which, because the rates in E91-013 were small enough relative to the gate width, can be approximated by,

$$P(0) \approx 1 - rt. \tag{3.9}$$

That is, the probability of no new events arriving in an interval t after a trigger goes linearly with t for small rates. Thus, to measure the counts lost in the 30 ns gate width, four additional gate widths (30, 60, 90, and 120 ns) were used, and the counts measured with each were recorded. Then, assuming the linear form of Eqn. 3.9, an extrapolation is made back to zero gate width to arrive the true number of counts. The ratio of the number of counts actually measured to the true number of counts is the electronic live time. (The dead time is one minus the live time.) In all runs, the electronic dead time was less than 0.1%, and thus neglected.

The second source of dead time is due to the finite time it takes the Trigger Supervisor to read out the Fastbus modules and the data acquisition computer to write an event to disk. It can take up to 800 μs to process a non-buffered coincidence event.[1] Because this is comparable to the typical average time between events (500 - 1000 μs), the computer dead time can be quite sizeable. To measure this dead time, the ratio of the number of TRGs to the total number of PRETRGs is taken. PRETRG is a hardware trigger, and TRG is the same hardware trigger ANDed with TS-BUSY. Thus the ratio is the fraction of time the data acquisition system was ready to process triggers. Note, that one can use either spectrometer to calculate the computer dead time, because the same fraction of triggers is lost in both arms (the agreement in reported dead time between the two spectrometers is always better than 0.02%).

Because most runs were taken in buffered mode, the computer dead time corrections were usually quite small—on the order of 0.5%. The early carbon runs in kinematics A, however, were not taken in buffered mode, and for these runs the corrections can be as large as 50%.

3.6 Timing Corrections

The coincidence time is used to determine the likelihood that an electron in one arm and a proton in the other arm both originated from the same reaction. It is the difference between the times the electron and the proton were at the target, and as such, is ideally a narrow peak centered at zero. Figure 3.4 shows a typical corrected coincidence time spectrum. The central shaded peak contains the true coincidences, and the shaded regions to the sides are used in the calculation of the background (discussed in Section 3.7). Note that one is even able to resolve the 2 ns micro-structure of the beam. However, to obtain such a spectrum, one has

[1] Note that buffered events can be read every 100 μs although it still takes $\sim$ 800 μs to fully process each event.

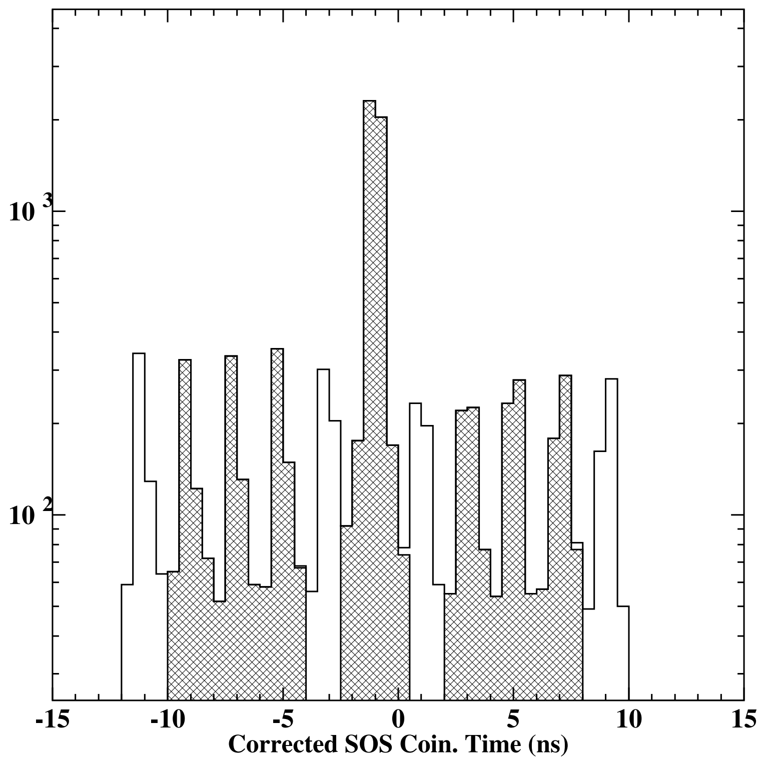

Figure 3.4. Corrected Coincidence Time Spectrum (Log scale). The central shaded region is taken as the good peak, and the shaded regions to the sides are used to calculate the background.

to account for pulse height dependencies in the TDCs, light propagation time in the scintillators, signal propagation in the electronics, and path length differences through different parts of the spectrometer acceptance. These are collectively known as timing corrections. Further corrections, due to random background events and Fastbus synchronization problems, are discussed in Section 3.7.

When measuring (relative to some start) the time at which a scintillator's phototube fires, one has to correct for the fact that a large pulse will cross a discriminator threshold earlier than a smaller pulse. Thus, "pulse height corrections" need to be applied to each phototube, meaning that the measured time (TDC signal) is adjusted based on the pulse shape (ADC signal). The correction used is empirical, and of the form,

$$\Delta t = PHC\sqrt{ADC/PHOFF - 1} + t_{offset}, \tag{3.10}$$

where ADC is the raw ADC value, and $PHC, PHOFF$, and t_{offset} are the timing correction parameters. The parameters are fit as follows. To minimize variations due to propagation of light in the scintillators, a small area of interest is defined by using pairs of crossed scintillators. Then the pulse height correction for one of the four tubes in the crossed pair is determined by adjusting its parameters so as to match the time as given by the other three tubes (which, at the beginning of this boot-strapping process, have been fit with rough corrections). Actually, for a given scintillator, the average time of both tubes at each end is used so as to eliminate dependence on position along the scintillator. The process is then iterated for all scintillators.

Given the pulse height corrections, the light propagation time in the scintillators can then be measured. Because the light usually arrives at the phototubes via a series of internal reflections, the time is not simply the distance from the track divided by the speed of light in the scintillator. An effective speed of light is determined empirically by plotting the position of the hit versus the time difference between the phototubes on either end of the scintillator, and taking the slope. In E91-013, an average was taken over the velocities for all the scintillators in each plane.

Next, corrections for differences in cable lengths need to be included. Again, pairs of crossed scintillators are used, but the pulse height corrections and light propagation time corrections have been applied. An offset for each tube is adjusted so as to make the time produce the correct β for the particles of interest ($\beta = 1$ for electrons, and $\beta = \frac{1}{\sqrt{1+M^2/p^2}}$ for protons).

Finally, to determine the time at which the particle was at the reaction vertex, path length corrections need to be applied. That is, the time taken to traverse the spectrometer depends on the particle's trajectory in addition to its velocity. Using a COSY model of the spectrometer, the path length is given as a function of $x_{fp}, x'_{fp}, x_{fp}x'_{fp}, x^2_{fp}, x'^2_{fp}$, and y'^2_{fp}. The difference between the actual and central path lengths divided by β gives the path length timing correction.

3.7 Blocking and Synchronization Corrections

Even with the timing corrections discussed in the previous section, one still needs to account for various problems and inefficiencies in the trigger and data acquisition (Sections 2.7 and 2.8) before the corrected coincidence time can be used to define good (e,e$'$p) events. These problems fall into three categories: events in which a random singles trigger blocks a true coincidence, events in which a late trigger causes both the start and stop of the coincidence TDC ("self-timing" events), and events in which a loss of synchronization occurred between detectors in a spectrometer or between the two spectrometers themselves. The first two effects were expected and affect a small fraction ($< 1\%$) of the events. The synchronization problems were due to unexpected problems with running the Fastbus modules in buffered mode.

Blocked coincidences occur when a random singles trigger arrives just before

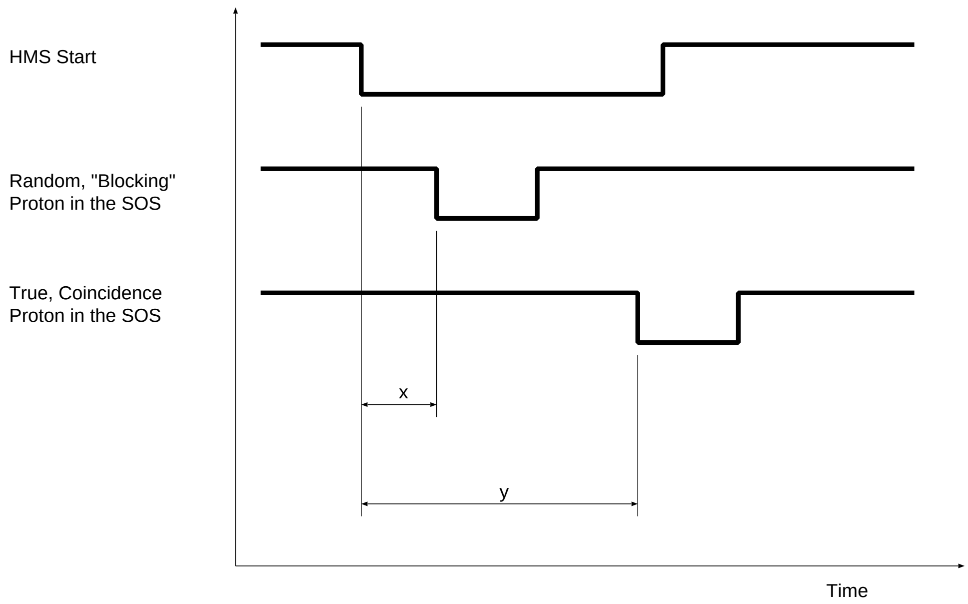

Figure 3.5. Coincidence Blocking. An early, random, proton in the SOS causes an early stop of the HMS coincidence time (time x). The true proton is a time $y > x$ behind the HMS.

a true coincidence event. As an example, if a random proton arrives in the SOS just before the true, coincidence proton, the stop for the HMS coincidence time and the SOS TDCs will be early, and the gates for the SOS ADCs will be too narrow (Fig. 3.5). In addition, tight cuts on the coincidence time will then remove events that were possibly good. In E91-013, the rates in the SOS were, on average, higher than those in the HMS, and thus the majority of these coincidence blocking events were of this type—random SOS events causing early SOS stops. To correct for this, a cut defining coincidence blocked events is placed on the HMS coincidence time. The fraction of the total that are blocked is used to correct the final yields. In all kinematics, this was a very small effect. The worst run (5375) only had 1.8% of its coincidences blocked.

The other problem is the fact that a late SOS trigger, for example, can cause the output of the trigger supervisor (Fig. 2.24) to arrive at the AND gate after the delayed HMS TRIG. This means that the HMS ADCs and TDCs (in this

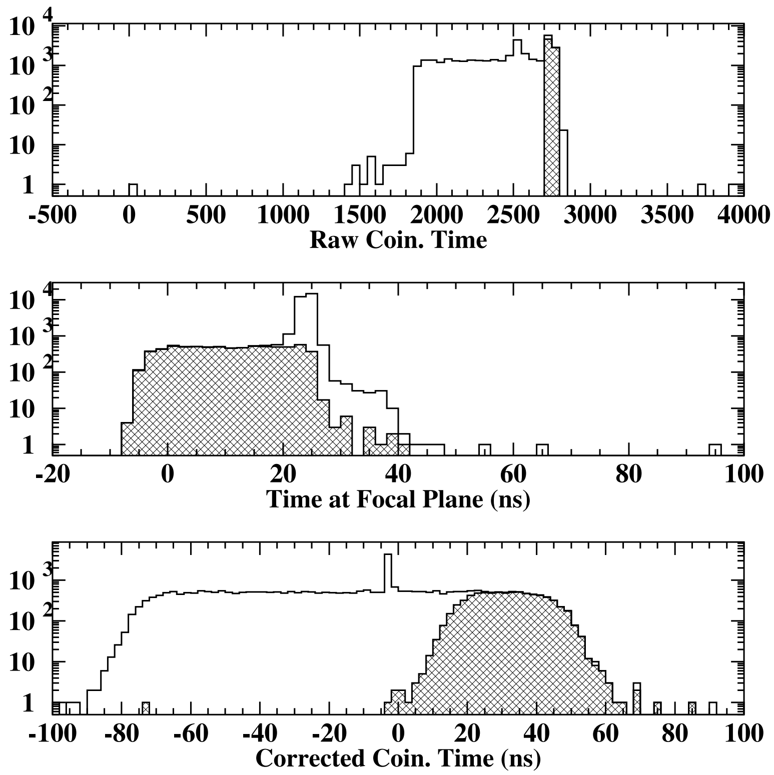

Figure 3.6. Self-Timing Events in Run 5370 (Log scales). The self-timing events are shaded. Panel 1 shows the raw HMS coincidence time, panel 2 shows the HMS time at the focal plane, and panel 3 shows the (path length) corrected coincidence time.

example), which are delayed so as to be in time with the HMS TRIG, are read out at a time dictated by the SOS. Furthermore, the HMS coincidence time—normally started by the HMS and stopped by the SOS—is now both started and stopped by the SOS. This "self-timing" causes a peak in the raw coincidence time (the shaded region at approximately channel 2700 in the top panel of Fig. 3.6). Due to details in the delay wiring, it turns out that this problem only occurred in the HMS. The SOS had more freedom in its ADC and TDC delays so as to insure the SOS TRIG always arrived after the COIN TRIG.

The problem with the self-timing events is actually fixed by the path length corrections (Section 3.6). These events have an HMS coincidence time that is too small (the shaded area in the top panel of Fig. 3.6 should extend to the right). This results in an HMS focal plane time (middle panel of Fig. 3.6) that is too small, because the start, induced by a late SOS TRIG, arrives too late. However, in calculating the corrected coincidence time, the focal plane time is subtracted from the raw coincidence time:

$$CT_{corr} \sim \frac{CT_{raw} - A}{B} - t_{fp}, \tag{3.11}$$

where CT_{raw} is the raw coincidence time TDC value, A is a TDC offset, B is is the TDC channel-to-time conversion factor, and t_{fp} is the corrected time at the focal plane. The errors then cancel when subtracting something that is too small from something that is itself is too small by the same amount. As is seen in the HMS coincidence time spectrum (bottom panel of Fig. 3.6), these self-timing events comprise the part of the random background expected for events with a late SOS trigger. Thus these events are left in throughout the analysis until they are eliminated in a standard random background subtraction.[2]

As was mentioned in Section 2.8, the data for certain runs were taken in buffered mode (Table 2.7). It was not noticed that the buffered information was often written to disk with the wrong synchronization. That is, event information from one set of detectors was being mixed with detector information from that of another event. And, in the case of coincidence triggers, event information from the SOS was sometimes paired with HMS information for a different event. It is important to remember that in both cases the effect is rate dependent, and once the data acquisition computer "catches up," the synchronization is restored. It is also true that the synchronization problems of both types usually comprised less than 1% of the events. Only in the forward proton angles of Kinematics A (high background) did the fraction of approach 15%.

[2]Note however, that in the correction of the synchronization errors discussed below, the blocking events are removed.

Synchronization problems in the coincidence data show up distinctly in the raw coincidence time TDC spectra. Figure 3.7 shows these spectra for the SOS and HMS, respectively (Run 5370; unusually bad). The SOS spectrum (upper panel) has a good coincidence time peak at roughly channel 1500 on a background the width of the gate. Everything below channel 1000 and above channel 2500 has a "wrong" HMS event paired with it, resulting in a bogus coincidence time.

To correct the coincidence data, the following algorithm was devised. First, the coincidence blocking events are removed. Then, to measure the fraction of events that are out of sync, a "checksum" is formed with the raw HMS and SOS coincidence times. As discussed in Section 2.7, for normal coincidence events, a late HMS trigger will correspond to a small HMS coincidence time (the SOS shows up relatively quickly to form the stop). However, from the point of view of the SOS, the HMS stop shows up relatively late, forming a large SOS coincidence time. Thus, for good events, the coincidence times as reported by the two spectrometers will always add to a value in a well defined, small, range; a so called checksum. Figure 3.8 shows a histogram of the sum of the raw HMS and SOS coincidence times (It is an event by event sum of the two histograms in Fig. 3.7.). The shaded area marks events with good synchronization (the small flat region to the left of the main peak at channel 4000 is due to the retiming events discussed above), and the rest are discarded. The fraction, good/total, along with the fraction of coincidence blocking events is then used to correct the final yields. Note that for this run (5370) roughly 10% of the events have lost synchronization. For comparison, Fig. 3.9 displays this checksum for a run with negligible synchronization problems (Run 5307).

Now that the out-of-sync and blocking events have been removed, a standard background subtraction is performed with the remaining data to arrive at the final coincidence yield. That is, the peak ± 1.5 ns in the corrected SOS coincidence time spectrum (the central shaded region of Fig. 3.4), with cuts on HMS δ, SOS δ,

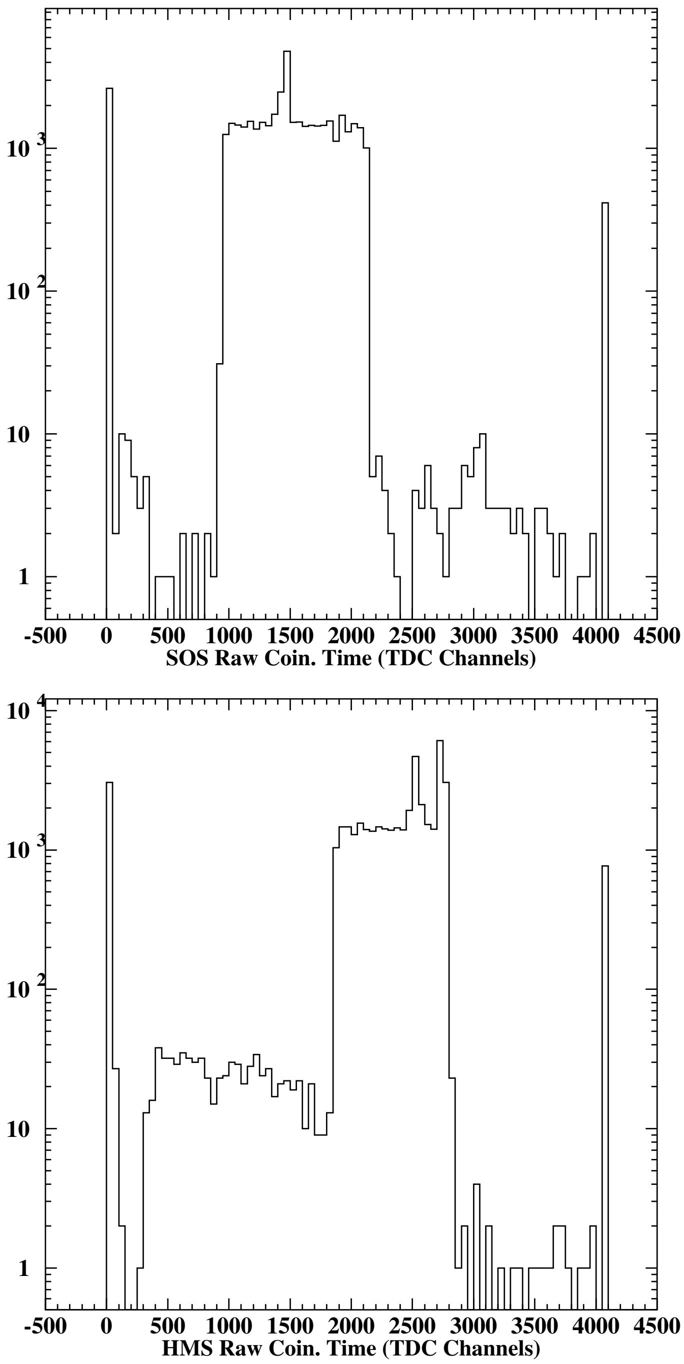

Figure 3.7. Raw SOS and HMS coincidence time TDC spectra, respectively (log scales).

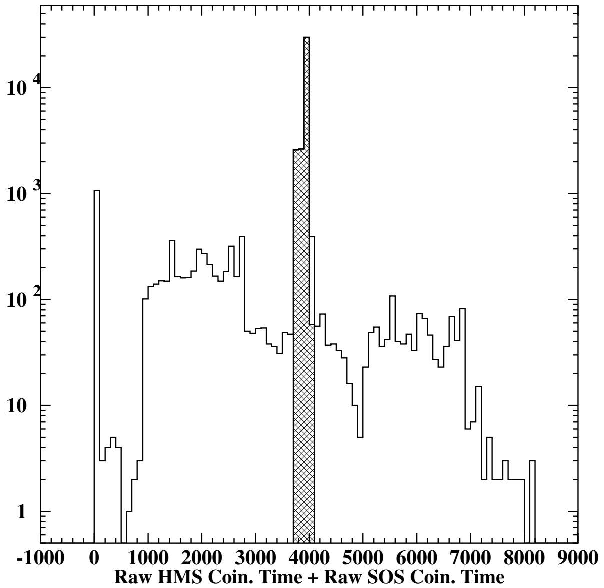

Figure 3.8. Sum of Raw HMS and SOS Coincidence Times in Tun 5370 (Log scale). The shaded area near channel 4000 is taken as "good."

missing energy and momentum, θ and ϕ for both spectrometers, and PID cuts on the electron arm, is taken as good. Two areas away from this peak, each 6 ns in width, are used to calculate the average background/ns (ideally each area consists of an integral number of RF "bumps"). The average background/ns is multiplied by the width of the good peak to give the number of background events in the good coincidence time cut. To arrive at the coincidence yield, the events passing the coincidence time cut minus the background is divided by the fraction of events that were in sync and did not have coincidence blocking protons. Equation 3.12 summarizes the calculation.

$$\text{Coin. Yield} = \frac{RC_s - B}{(F_c \times F_b)\,(Q \times TE_{HMS} \times TE_{SOS} \times PT \times LT)}, \qquad (3.12)$$

where RC_s is the number of raw coincidence events that are in sync (with the blocking events removed), B is the background contribution, F_c is the fraction of events with

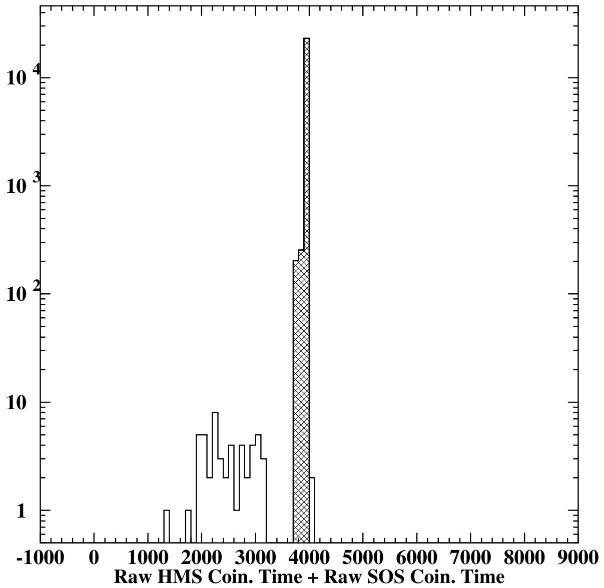

Figure 3.9. Sum of Raw HMS and SOS Coincidence Times in Tun 5307 (Log scale). The shaded area near channel 4000 is taken as "good."

a good checksum, F_b is the fraction of events without coincidence blocking protons, Q is the accumulated charge of the incident electrons, $TE_{HMS(SOS)}$ is the measured tracking efficiency of the HMS (SOS), PT is the proton transmission, and LT is the computer live time. Note the bremsstrahlung radiation emitted by the electrons (and to a lesser extent, the protons) may cause the electron energy to drop out of the experimental acceptance. The experimental yields are not corrected for these losses, rather they are compared with a simulation (Section 3.9) that includes radiative effects.

A different method was used to correct the singles yields for synchronization problems. A test was formed that counted the number of electron-only events that had calorimeter and Čerenkov ADC values of 0 or 4095; so-called "singles zeroes." An overflow (4095) occurs when the stop for a TDC shows up late, but still within a specified time window, and the zeroes occur when the stop fails to show up at all. These events obviously fail to pass the PID cuts, and so need to be re-included in the final yield. Of course not all of these events would have passed all the cuts and contributed to the yield; a certain fraction may have been just outside of the acceptance. To correct for this, we multiply the number of zeroes by the number of events that pass the acceptance/PID cuts over the raw number (minus the zeroes). Then, in calculating the singles yield, this number of corrected singles zeroes is added to the number of electron only events (that have passed the cuts) which is then multiplied by the electron arm prescale factor. The coincidence yield (which has further corrections discussed above) is then added to that to get the final yield. For example, in the HMS:

$$\text{Singles Yield} = \frac{(\text{HMS}_{\text{corr}} \times \text{PS}) + \frac{\text{HMS}_{\text{coin}}}{\text{TE}_{\text{SOS}}}}{\text{Q} \times \text{TE}_{\text{HMS}} \times \text{LT}}, \tag{3.13}$$

where

$$HMS_{corr} = HMS_{e^-only} + Z \times \left(\frac{HMS_{e^-only}}{HMS_{rawe^-only} - Z} \right), \tag{3.14}$$

and where HMS_{e^-only} is the number of electron-only counts with HMS δ, angle, and calorimeter cuts, HMS_{rawe^-only} is the raw number of HMS electron-only counts with no cuts, and HMS_{coin} is the number of coincidence triggered HMS counts (corrected for the fraction that are in sync–see above) with only HMS δ and HMS angle cuts. Z is the number of "singles zeroes, " PS is the electron arm prescale factor, and, as in Equation 3.12, Q is the accumulated charge of the incident electrons, $TE_{HMS(SOS)}$ is the measured tracking efficiency of the HMS (SOS), and LT is the computer live time.

3.8 Particle Identification

Due to the coincidence nature of the experiment, particle identification in E91-013 is a relatively small problem: If produced, a pion ($\beta \approx 1$) in the proton ($\beta < 1$) arm does not have the correct time of flight to be in time with the electron. Pions in the electron arm are easily removed using Čerenkov and calorimeter responses. The efficiency of the Čerenkov detector and the calorimeter are discussed in Reference 57. Both were measured by using the elastic scattering of electrons from hydrogen. The ratio of events with electron signals (Čerenkov signal corresponding to three or more photoelectrons, or a calorimeter response greater than, or equal to the scattered electron energy) to the total number of events, is taken as the efficiency. The requirement is made that the invariant mass, W, for each event must be below the pion production threshold: $W^2 < 1.15$ (GeV/c)^2. The Čerenkov efficiency is found to be $> 99.5\%$ for electron energies from 0.5–2.1 GeV. The calorimeter efficiency is typically $> 99\%$, although it falls to approximately 98% at low (< 1 GeV) electron energies.

3.9 Simulation

In addition to the PWIA calculation needed for the transparency results, a simulation of the experiment is needed to extract the spectral functions and model the radiative corrections. The simulation used is an Independent Particle Shell Model (IPSM) calculation done in the PWIA. The program, SIMULATE Hall C (SIMC), is based on SIMULATE, written by Makins for experiment NE-18. With the exception of modifications used to make it Hall C specific, a complete discussion of the simulation can be found in Reference 58.

3.9.1 Overview The simulation of an event begins with an incoming electron whose position and energy are chosen randomly from distributions matching those of the actual beam. In addition, corrections due to ionization losses and Coulomb distortions in the target are applied. A basic scattering vertex is then formed by choosing the scattered electron and proton trajectories, energies, and momenta at random over a range of kinematics that exceeds the experimental acceptance. The electron kinematics are used to calculate the momentum transfer q, and, given the proton's final momentum p', the missing energy and momentum are determined. Unphysical kinematic situations, or events that result in a particle outside of the experimental acceptance, are assigned a weight of zero (see below). The probability that each particle at the vertex emits a real or virtual bremsstrahlung photon is then calculated, and the trajectories and energies are modified accordingly. Forward matrix elements are used to transport the electron and proton through the target and their respective spectrometers, where multiple scattering and ionization losses are included. The simulated focal plane quantities are then reconstructed back to the target as for the data, and these reconstructed target values (as opposed to the generated values) of the electron and proton trajectories are used to calculate the missing energy and momentum. These results are then written to the output files. Each event that has both the electron and proton arrive successfully at their respective focal planes is assigned a weight of

$$E'p'\sigma_{ep}S(E_m,p_m)W_{rad},$$

where σ_{ep} is the off-shell electron-proton cross section (Section 3.9.2), and $S(E_m,p_m)$ is the model spectral function value for the given E_m and p_m (Section 3.9.3). Note that in the calculation of the weight, the vertex values of E_m and p_m are used, as opposed to the reconstructed values. Note also that the product $E'p'\sigma_{ep}S(E_m,p_m)$ is the coincidence cross section in the PWIA. The factor W_{rad} is a correction for the emission of both real and virtual photons by the incoming electron, scattered electron, and the recoiling proton. (Section 3.9.4). Finally, all events are weighted by

$$\frac{\mathcal{L}\Delta E_p\Delta\Omega_p\Delta E_e\Delta\Omega_e}{N_{gen}},$$

where $\mathcal{L}$ is the experimental luminosity, $\Delta E_p\Delta\Omega_p\Delta E_e\Delta\Omega_e$ is the phase space volume, and N_{gen} is the number of generation attempts. The SIMC output files are thus created such that the Monte Carlo output is ready for direct comparison with the experimental data.

3.9.2 Off-Shell Cross Section The off-shell cross section used in SIMC employs the σ_{cc1} prescription of deForest [6], described in Section 1.3.1. In order to facilitate comparison with experiment NE-18, the same form factor calculations are used in E91-013. The dipole form is used for the proton electric form factor, G_E^p,

$$G_E^p = \left(1 + \frac{Q^2}{0.71}\right)^{-2}, \tag{3.15}$$

and the parameterization of Gari and Krümpelmann is used for the proton magnetic form factor (Eqns. (2) and (3) of Ref. 59).

3.9.3 Model Spectral Functions For the results in Reference 60 (that is, with the exception of some tests—see Appendix A), the model spectral functions used in E91-013 are the same as those in experiment NE-18. They are based on the IPSM, and the approximation is made that they factor as

$$S(E_m, p_m) = (2j+1) \sum_{n,l,j} \rho_{n,l,j}(p_m) \mathcal{L}_{n,l,j}(E_m). \tag{3.16}$$

The momentum distributions, $\rho(p_m)$, were calculated using the program DWEEPY [61] with the following nuclear mean-field model potential:

$$V = -V_0 f(r, R_0, a_0) + V_{so} \left(\frac{\hbar}{m_\pi c}\right)^2 \frac{2}{r}\frac{df}{dr} \vec{l} \cdot \vec{s} + V_C(r), \tag{3.17}$$

where

$$f(r, R, a) = \frac{1}{1 + e^{\frac{r-R}{a}}}, \tag{3.18}$$

is the usual Woods-Saxon form for the radial shape. The parameter a defines the "thickness" over which the nuclear density falls off, and R is taken to be the approximate radius of the residual, $A-1$, system:

$$R = r_0(A-1)^{1/3}. \tag{3.19}$$

The volume term in the potential, V_0, depends only the radial position of the nucleon in the nucleus, and the spin-orbit term, V_{so}, describes the interaction between the nucleon's spin and its orbital angular momentum. The Coulomb term, V_C, is due to the presence of the other $Z-1$ protons, and is approximated by the potential due to a uniform spherical charge distribution of radius R_C ($\equiv r_c A^{1/3}$):

$$V_C(r) = -\frac{(Z-1)e^2}{4\pi\epsilon_0 R_C}\left(\frac{3}{2} - \frac{r^2}{2R_C}\right). \tag{3.20}$$

The wave functions calculated in this nuclear mean-field framework are strictly local. In reality however, the potential (and thus the wavefunction) at a given position is non-local, depending on the nuclear wave function elsewhere. Note that this is equivalent to the statement that the nuclear mean-field potential is energy dependent. To take this into account, the program DWEEPY still utilizes a local potential, but a so-called Perey-factor is used to distort the wave functions: [62]

$$\Psi_{NL}(r) = \frac{\Psi_L(\vec{r})}{\sqrt{1 + 2M\beta^2 V(r)}}, \tag{3.21}$$

where β, the range of the non-locality, is approximately 1 fm. (Note that $\Psi_{NL}(r)$ then has to be renormalized.) According to Elton and Swift [63], non-locality only becomes important for $A \geq 40$, and therefore only the ^{56}Fe and ^{197}Au wave functions were corrected for the effect.

The binding energy distributions, $\mathcal{L}(E_m)$, are taken to be roughly Lorentzian in shape:

$$\mathcal{L}_i(E) = \frac{1}{\pi}\frac{\Gamma_i(E)/2}{(E - E_{B_i})^2 + (\Gamma_i(E)/2)^2}, \tag{3.22}$$

where E_{B_i} and $\Gamma_i(E)$ are the binding energy and widths of the i^{th} shell, respectively. The shell widths are either taken from fits to low-Q^2 data, or calculated from the formula of Brown and Rho [64]:

$$\Gamma_i(E) = \frac{(24\text{MeV})(E_i - E_F)^2}{(500\text{MeV}^2) + (E_i - E_F)^2}, \tag{3.23}$$

where E_i is the binding energy of the i^{th} shell (E_{B_i} in Equation 3.22), and E_F is the Fermi energy of the nucleus. Note that is exceedingly difficult to determine the

Table 3.7: Model parameters for ^{12}C.

Shell	E_B (MeV)	Γ (MeV)	V_0 (MeV)	r_0 (fm)	a_0 (fm)	V_{so} (MeV)	r_{so} (fm)	a_{so} (fm)	r_C (fm)
$1s_{1/2}$	38.1	20	66	1.36	0.55				1.3
$1p_{3/2}$	16.2	5	55	1.36	0.55	9	1.36	0.55	1.3

shell widths of the deeply bound states in iron and gold. The NE-18 model spectral functions were used in E91-013 for the sake of comparison, but it should be pointed out that in some cases the agreement between data and simulation was somewhat poor. Section 4.3.3 discusses the dependence of the results on the model used, and Appendix A discusses the use of an alternative ^{56}Fe spectral function model.

The parameters for the carbon model spectral function were originally obtained as follows. The central binding energies for the $1s$ and $1p$ shells were determined empirically to be 38.1 MeV and 16.2 MeV, respectively, from an examination of the Saclay data [2] and Table X of Ref. 1. The shell widths were also derived from an examination of Saclay ^{12}C(e,e$'$p) data taken at $Q^2 = 0.16$ (GeV/c)^2. The $1s$ shell width is 20.0 MeV, while that of the $1p$ shell is 5.0 MeV. The mean-field potential parameters for the missing momentum distribution were taken from the Saclay data. Table 3.7 lists the carbon parameters.

The shell energies for ^{56}Fe were taken from the Hartree-Fock calculation of Reference 65. The binding energies were all increased by 2.0 MeV to reflect the difference in separation energy of ^{58}Ni and ^{56}Fe. Equation 3.23 was used to calculate the shell widths using a Fermi energy of 8 MeV. The parameters for the mean-field model potential were taken from the ^{58}Ni values in Reference 2, but they were modified slightly so as to obtain a better fit with the data. Table 3.8 summarizes the ^{56}Fe model parameters. As was mentioned, the agreement between the ^{56}Fe model and the data was somewhat poor, and Appendix A discusses a Hartree-Fock calculation used to provide consistent binding energies and momentum distributions.

Table 3.8: Model parameters for ^{56}Fe.

Shell	E_B (MeV)	Γ (MeV)	V_0 (MeV)	r_0 (fm)	a_0 (fm)	V_{so} (MeV)	r_{so} (fm)	a_{so} (fm)	r_C (fm)
$1s_{1/2}$	50	18	80.7	1.30	0.60				1.3
$1p_{3/2,1/2}$	37	14	69.0	1.30	0.60	40	1.30	0.60	1.3
$1d_{5/2,3/2}$	23	6	58.2	1.30	0.60	23.5	1.30	0.60	1.3
$2s_{1/2}$	16.7	3	52.7	1.30	0.60				1.3
$1f_{7/2}$	11.3	1.0	52.7	1.30	0.60	13.8	1.30	0.60	1.3

The binding energies for ^{197}Au were derived from the ^{208}Pb data of Reference 65. To account for the difference in separation energies of the two nuclei, 2.2 MeV was subtracted from each binding energy. The widths of the $1g$, $2d$, and $1h$ shells were taken from Reference 65, while the widths of the more deeply bound shells were calculated using Equation 3.23. As in the case of ^{56}Fe, the mean-field model parameters were a best fit of data and calculations from various sources: the ^{208}Pb data of Reference 65 and the calculations of Reference 66. Table 3.9 lists the model parameters for ^{197}Au.

3.9.4 Radiative Corrections Corrections to the (e,e′p) cross section need to be applied due to the fact that the electron (and to a much lesser extent, the proton) will emit photons as it is accelerated in the vicinity of nuclei. These modifications can be divided into two categories: "Internal" bremsstrahlung describes the emission of photons by both the electron and proton at the reaction vertex. This includes both real photons (Fig. 3.10) and higher order modifications due to the emission of virtual photons (Fig. 3.11). "External" bremsstrahlung is induced by material incidental to the reaction. Both categories are known collectively as radiative corrections. Calculations of these corrections in the inclusive ^{1}H(e,e′) reaction were first performed by Schwinger [67], and were later modified by Mo and Tsai [68]. A more recent treatment was given by de Calan, Navelet, and Picard [69]. In the analysis of the NE-18 data, Makins *et al.* reformulated the (e,e′) calculations of Mo

Table 3.9: Model parameters for ^{197}Au.

Shell	E_B (MeV)	Γ (MeV)	V_0 (MeV)	r_0 (fm)	a_0 (fm)	V_{so} (MeV)	r_{so} (fm)	a_{so} (fm)	r_C (fm)
$1s_{1/2}$	46	19	71.9	1.31	0.65				1.2
$1p_{3/2,1/2}$	41	17	71.3	1.31	0.65	6	1.15	0.65	1.2
$1d_{5/2,3/2}$	32	14	67.8	1.31	0.65	6	1.15	0.65	1.2
$2s_{1/2}$	28	12	66.5	1.31	0.65				1.2
$1f_{7/2,5/2}$	22.9	9.4	65.1	1.31	0.65	6	1.15	0.65	1.2
$2p_{3/2,1/2}$	17.2	7.9	63.2	1.31	0.65	6	1.15	0.65	1.2
$1g_{9/2,7/2}$	12.5	6.0	63.7	1.27	0.65	6	1.15	0.65	1.2
$2d_{5/2}$	8.3	3.7	62.0	1.32	0.65	6	1.15	0.65	1.2
$1h_{11/2}$	7.7	4.0	67.0	1.29	0.65	6	1.15	0.65	1.2
$2d_{3/2}$	6.2	1.5	57.2	1.36	0.65	6	1.15	0.65	1.2

and Tsai for the case of coincidence (e,e′p) reactions. A summary of these calculations is provided below, while a more detailed description can be found in Refs. 58 and 70. As in the case of the model spectral functions, the radiative correction prescription of Makins *et al.* was used in the simulation of E91-013.

Following the discussion of Makins, the internal bremsstrahlung radiation cross section for the emission of multiple photons can be calculated to all orders as

$$\begin{aligned}\frac{d\sigma}{d\Omega_e dE_{\gamma e} dE_{\gamma e'} dE_{\gamma p'}} &= \left.\frac{d\sigma}{d\Omega_e}\right|_{ep} (1-\delta_{hard}) \\ &\times \frac{\lambda_e \lambda_{e'} \lambda_{p'}}{(\sqrt{kk'})^{\lambda_e} (\sqrt{kk'})^{\lambda_{e'}} (\sqrt{Mp^{0'}})^{\lambda_{p'}}} \frac{1}{E_{\gamma e}^{1+\lambda^e} E_{\gamma e'}^{1+\lambda^{e'}} E_{\gamma p'}^{1+\lambda^{p'}}},\end{aligned} \tag{3.24}$$

where $\left.\frac{d\sigma}{d\Omega_e}\right|_{ep}$ is the one-photon exchange, electron-proton cross section, Ω_e is the scattered electron solid angle, and $E_{\gamma e}$, $E_{\gamma e'}$, and $E_{\gamma p'}$ are the total energies emitted by photons along the direction of the incoming electron, scattered electron, and recoiling proton, respectively. The four-momenta of the incoming and scattered electrons (mass m) are given by k and k', respectively, and the momentum of the recoiling proton (mass M) is given by p'. The λs in Eqn. 3.25 are given by

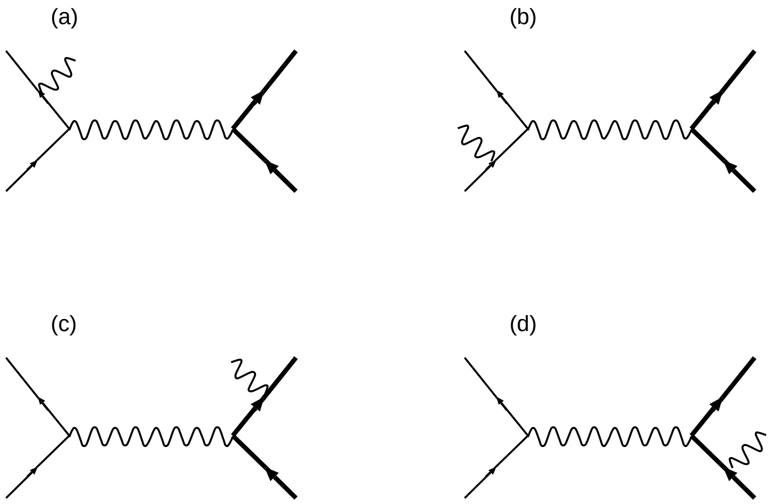

Figure 3.10: The four first order bremsstrahlung radiation Feynman diagrams.

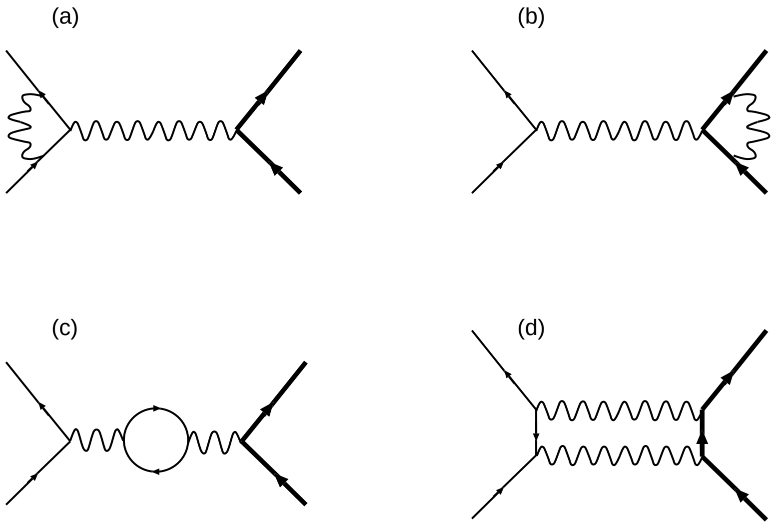

Figure 3.11. The Feynman diagrams of the four included, second order, virtual photon corrections to the one-photon exchange electron-proton cross section. Note that only terms necessary to cancel divergences are kept in diagrams (b) and (c).

$$\lambda_e = \frac{\alpha}{\pi}\left[\ln\left(\frac{4k^2}{m^2}\right) + 2\ln(\frac{k}{k'}) + \ln\left(\frac{1-\cos\theta_e}{2}\right) - 1\right], \tag{3.25}$$

$$\lambda_{e'} = \frac{\alpha}{\pi}\left[\ln\left(\frac{4k'^2}{m^2}\right) + 2\ln(\frac{k}{k'}) + \ln\left(\frac{1-\cos\theta_e}{2}\right) - 1\right],$$

$$\lambda_{p'} = \frac{\alpha}{\pi}\left[\ln\left(\frac{p^{0'} + |\vec{p}'|}{p^{0'} - |\vec{p}'|}\right) - 2\right],$$

where θ_e is the scattered electron angle, and δ_{hard} is the contribution from second order virtual photon emission:

$$\delta_{hard} = 2\alpha\left[-\frac{3}{4\pi}\ln\left(\frac{-q^2}{m^2}\right) + \frac{1}{\pi} - \sum_i \delta_i^{\text{vp}}(q^2)\right]. \tag{3.26}$$

Here q^2 is the momentum transferred from the electron $(k - k')$, and δ_i^{vp} is due to the vacuum polarization corrections (the sum over i running over the three lepton flavors, each with mass m_i):

$$\delta_i^{\text{vp}} = \frac{1}{3\pi}\left[-\frac{5}{3} + \ln\left(\frac{-q^2}{m_i^2}\right)\right]. \tag{3.27}$$

Makins makes the following approximations and assumptions in arriving at Eqn. 3.25. First, on-shell form factors and kinematics are used in the calculation of the proton-photon vertex. Note that both of these approximations are assumed to have little effect on the results as the total proton radiation is negligible. Second, the derivation encounters two sets of "infrared" divergences as both the mass of the photon and the total energy lost to radiation, ΔE, are taken to zero. The first set is removed when the interference between the first-order and second-order diagrams (two-virtual-photons; Fig. 3.11) is included (actually, second-order diagrams that include photon interactions with the poorly understood proton current are generally omitted; only terms necessary to cancel the first-order divergences are kept). The second set of divergences are caused by terms $(\delta_{soft}(\Delta E))$ that go to infinity as ΔE goes to zero. That is, the cross section for emitting photons with vanishingly small energies becomes infinite. The situation is remedied by a cancellation that occurs between terms that have multiple photons, each with energy less than ΔE, and

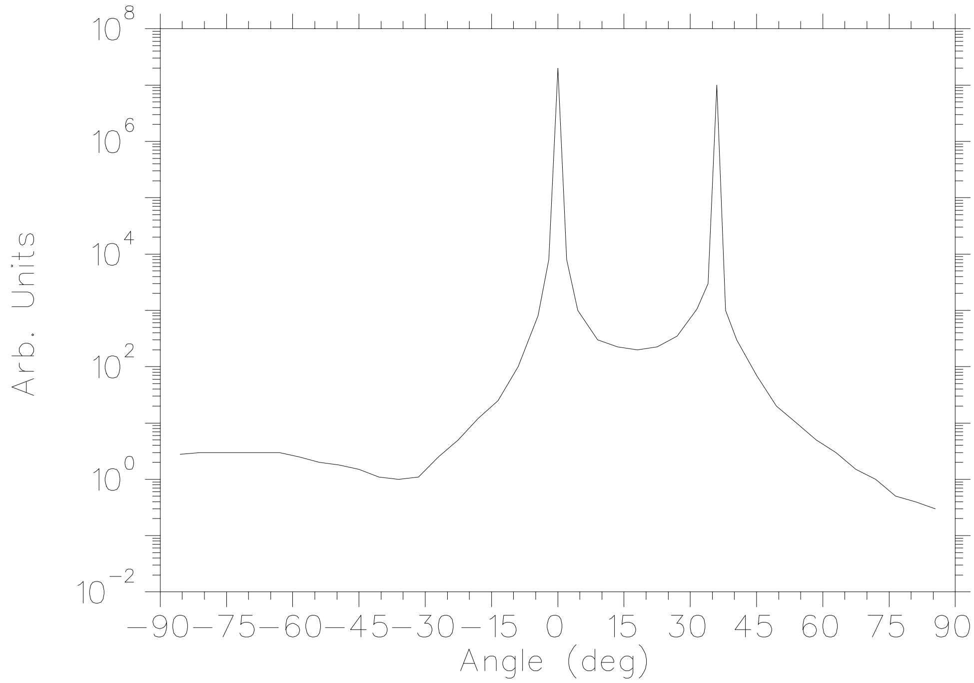

Figure 3.12. Angular Distribution of Bremsstrahlung Photons. The kinematics consist of an electron (beam at 0°) scattered through 35° and a recoil proton at -45°. $Q^2 = 1$ GeV/c^2. (Vertical log scale.)

terms that have the total energy of all emitted photons less than ΔE. To order α^2, $\delta_{soft}(\Delta E)$ can be approximated by $e^{-\delta_{soft}(\Delta E)}$. Note that this "exponentiated" form goes to zero as $\Delta E \rightarrow 0$, as expected physically: there is zero probability of of losing no energy to radiation. Third, the cross section for internal bremsstrahlung factorizes into three functions; one for each arm of the (e,e$'$p) vertex. It is noticed empirically that the emission of radiation by a particle is strongly peaked in the direction of that particle (Fig. 3.12), and thus the angular distribution is approximated as

$$A_{peaking}(\hat{\omega}) = \lambda_e \delta(\hat{\omega} - \hat{k}) + \lambda_{e'} \delta(\hat{\omega} - \hat{k}') + \lambda_{p'} \delta(\hat{\omega} - \hat{p}'), \quad (3.28)$$

where $\hat{\omega}$ is the direction of the emitted photon. This "peaking" approximation is utilized in the derivation of Equation 3.25. Finally, although the peaking approximation is used in the calculation of the emission of a single photon, the angular distribution of multiple photons is approximated by calculating the total energy lost in each arm, and taking the vector sum:

$$\vec{\omega}_{total} = E_{\gamma e}\hat{k} + E_{\gamma e'}\hat{k}\,' + E_{\gamma p'}\hat{p}\,'. \tag{3.29}$$

External bremsstrahlung is defined as radiation induced by nuclei other than the one participating in the (e,e′p) reaction. SIMC takes external bremsstrahlung into account for electrons traversing the target, scattering chamber windows, air between the chamber and the spectrometer, and the spectrometer entrance window. After the electrons have traversed the spectrometer dipole magnet(s), multiple scattering is a much larger effect in terms of energy smearing. Early [71] calculates the probability of an electron with momentum $|\vec{k}|$ radiating total energy E^{ext} when traversing t radiation lengths of material with atomic charge, Z, as

$$P(|\vec{k}|, E^{ext}, t) = \frac{1}{\Gamma(1+bt)}\frac{bt}{E^{ext}}\left[\frac{E^{ext}}{|\vec{k}|}\right]^{bt}, \tag{3.30}$$

where

$$\begin{aligned} b &= \frac{1}{9}\left(12 + \frac{Z+1}{ZL_1 + L_2}\right), \qquad (3.31)\\ L_1 &= 5.216 - \frac{1}{3}\ln(Z),\\ L_2 &= 7.085 - \frac{2}{3}\ln(Z). \end{aligned}$$

Noting that both internal and external radiation emitted by a charged particle are emitted along the direction of the charged particle's momentum, one can rewrite the total energy radiated along $\vec{k}$ and $\vec{k}'$ as E_i and E_f, respectively. Then, the internal (Equation 3.25) and external radiation can be combined, resulting in

$$\begin{aligned} \frac{d\sigma}{d\Omega_e dE_i^{int} dE_i^{ext} dE_f^{int} dE_f^{ext} dE_{p'}^{int}} &= \left.\frac{d\sigma}{d\Omega_e}\right|_{ep}(1-\delta_{hard}) \qquad (3.32)\\ &\times \frac{1}{\Gamma(1+bt_i)}\frac{1}{\Gamma(1+bt_f)}\\ &\times \frac{(bt_i+\lambda_i)}{k^{bt_i}(\sqrt{kk'})^{\lambda_i}}\frac{(bt_f+\lambda_f)}{k'^{bt_f}(\sqrt{kk'})^{\lambda_f}}\frac{\lambda_{p'}}{(\sqrt{Mp_0'})^{\lambda_{p'}}}\\ &\times \frac{dE_i}{E_i^{1-\lambda_i-bt_i}}\frac{dE_f}{E_f^{1-\lambda_f-bt_f}}\frac{dE_{p'}}{E_{p'}^{1-\lambda_{p'}}}. \end{aligned}$$

Note that the external radiation by the proton—suppressed by a factor of $(\frac{m}{M})^2$—is neglected.

The above formulae are applied in SIMC as follows. As can be seen in Eqn 3.33, the peaking approximation results in a cross section that factors into independent distributions for each arm in the (e,e′p) reaction. Each factor is of the form

$$\frac{1}{\Gamma(1+bt)}\frac{bt+\lambda}{k^{bt}(\sqrt{kk'})^{\lambda}}\frac{dE}{E^{1-\lambda-bt}}, \tag{3.33}$$

(except that $bt = 0$, and $\sqrt{kk'} \to \sqrt{Mp^{0'}}$ for the proton). An energy distribution function suitable for randomly weighting events is formed by defining

$$\begin{aligned} g_i &\equiv bt_i + \lambda_i, \\ C_i &\equiv \frac{bt_i+\lambda_i}{k_i^{bt_i}(\sqrt{kk'})^{\lambda_i}}, \end{aligned} \tag{3.34}$$

where i indicates both the incoming and scattered electrons, and

$$\begin{aligned} g &\equiv \lambda_{p'}, \\ C &\equiv \frac{\lambda_{p'}}{(\sqrt{Mp_0'})^{\lambda_{p'}}}, \end{aligned} \tag{3.35}$$

for the recoiling proton. The energy distributions for each arm of the reaction can then be written as

$$C_i \times E_i^{g_i-1} dE_i, \tag{3.36}$$

where i now stands for all three arms of the reaction. Normalizing the distributions via

$$N\int_{E_{min}}^{E_{max}} E^{g-1} dE = 1, \tag{3.37}$$

weighting functions of the form

$$G = \frac{gE^{g-1}}{E_{max}^g - E_{min}^g}, \tag{3.38}$$

are obtained that are then used to randomly weight the energy lost in each arm due to radiation. The limits, E_{min} and E_{max}, are chosen so as to exceed the the beam energy or the spectrometer acceptance for the incoming electrons and scattered electrons and protons, respectively. This is to allow for the possibility that a higher energy electron, for example, may radiate "into" the acceptance.

With the energy lost by each particle now determined ($E_{\gamma e}$, $E_{\gamma e'}$, and $E_{\gamma p'}$ for the incoming electron, scattered electron, and recoiling proton, respectively), the vertex values of the energy and momentum for each arm are adjusted accordingly. In addition, the event is assigned a radiation weight which gives the total probability for the occurrence of this particular set of radiative losses:

$$W_{rad} = W_{rad}^{soft} \Phi_e^{ext} \Phi_{e'}^{ext} (1 - \delta_{hard}), \tag{3.39}$$

where the factors Φ_i^{ext} are corrections for the emission of external photons with large energies,

$$\Phi_i^{ext} = 1 - \frac{bt_i}{bt_i + \lambda_i} \frac{E_i}{k_i}. \tag{3.40}$$

W_{rad}^{soft} is given by the product of the three internal radiation weights for the incoming and scattered electrons and the recoiling proton,

$$W_{rad}^{soft} = W_{rad}^{e} W_{rad}^{e'} W_{rad}^{p'}, \tag{3.41}$$

where

$$W_{rad}^{i} = \frac{C}{g} \left[(E_{max}^{i})^g - (E_{min}^{i})^g \right], \tag{3.42}$$

and where i indicates the three arms of the reaction.

The effect of the radiative corrections is most easily understood in terms of a missing energy and momentum basis. As an example, if a real photon with four-momentum ω is emitted, the missing energy and momentum are both shifted (c.f. Eqns. 1.6 and 1.7):

$$\begin{aligned} \vec{p}_m &= \vec{p}\,' - \vec{q} + \vec{\omega} = \tilde{\vec{p}}_m + \vec{\omega}, \qquad (3.43) \\ E_m &= E - E' - T_p + \omega^0 = \tilde{E}_m + \omega^0, \end{aligned}$$

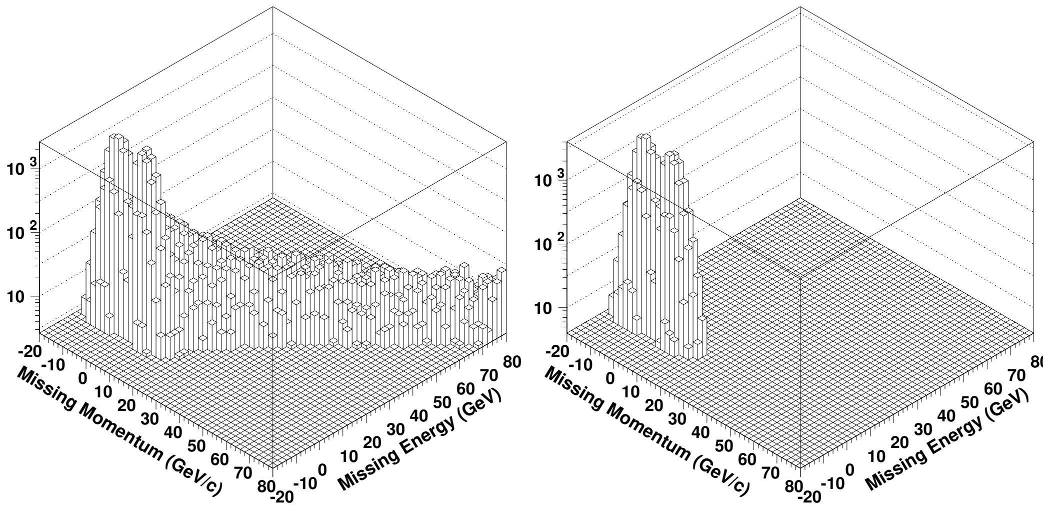

Figure 3.13. Effects of Radiation on Hydrogen E_m and p_m Spectra. Simulated E_m vs. p_m spectra are plotted with and without radiative effects in the left and right panels, respectively. The radiation of real photons appears as a tail of events with $E_m = p_m$. (Vertical log scale)

where $\tilde{\vec{p}}_m$ and $\tilde{E}_m$ are the measured missing energy and momentum, and E_m and $\vec{p}_m$ are the true vertex values. Thus, in a two-dimensional histogram of E_m versus $\vec{p}_m$ (Fig. 3.13), the radiative effects show up as a "tail" of events along $E_m = |\vec{p}_m|$. The effect of the radiation weight then, is to reduce the number of events in a given $(E_m, |\vec{p}_m|)$ bin, accounting for radiation "out of" that bin. And, by adjusting the energy and momentum vertex values of the particles, events can radiate "into" other $(E_m, |\vec{p}_m|)$ bins.

Comparisons of data and Monte Carlo for ^{1}H and nuclear targets can be found in Sections 4.1 and 4.3.1, respectively.

3.9.5 Spectrometer Simulation With the vertex values of the trajectories and momenta now determined, the particles must next be transported through their respective spectrometers to the focal plane. In addition, energy loss and multiple-scattering corrections to the trajectories need to be applied as the particles traverse the various materials in the spectrometer.

The forward transformation—the inverse of the process described in Section 3.2—must be performed in order to calculate the transport of the particles from the target to the focal plane. The forward matrix elements were calculated to fifth order using COSY Figure 3.14 shows a comparison of experimental and simulated quantities at the focal plane.

As the particles traverse materials in the spectrometer (entrance and exit windows, air, wire chambers, etc. See Tables 3.3 and 3.4), they suffer both energy loss and angular deviations due to multiple scattering (bremsstrahlung losses have already been included in teh radiative corrections). The energy loss of the protons due to ionization of the material is calculated using the Bethe-Bloch equation,

$$\frac{dE}{dx} = -0.307 \frac{Z}{A} \frac{1}{\beta^2} \left[\frac{1}{2} \ln \frac{2m_e c^2 \beta^2 \gamma^2 T_{max}}{I^2} - \beta^2 \right], \tag{3.44}$$

where Z and A are the atomic number and atomic mass number, respectively, β and γ are the usual relativistic quantities, $T_{max} \approx 2m_e c^2 \beta^2 \gamma^2$ is the maximum kinetic energy that can be imparted by the proton to an electron, and $I \approx Z \times 10$ eV is the mean excitation energy of the material. [9] The units are such that the energy is measured in MeV, and the thickness, dx, is measured in g/cm^2. The electron energy loss due to ionization is slightly modified to take into account their light mass, and the fact that the scattering now occurs between identical particles:

$$\frac{dE}{dx} = -0.1535 \frac{Z}{A} \left[19.26 + \ln \left(\frac{t}{\rho} \right) \right], \tag{3.45}$$

where t and ρ are the thickness (in g/cm^2) and the density (in g/cm^3) of the material, respectively, and $\beta \to 1$. [72] Multiple scattering is into account separately in both the in-plane and out-of-plane directions using Gaussian angular distributions with widths given by

$$\sigma = \frac{13.6}{p\beta} z \sqrt{\frac{x}{X_0}} \left[1 + 0.038 \ln\left(\frac{x}{X_0}\right) \right], \tag{3.46}$$

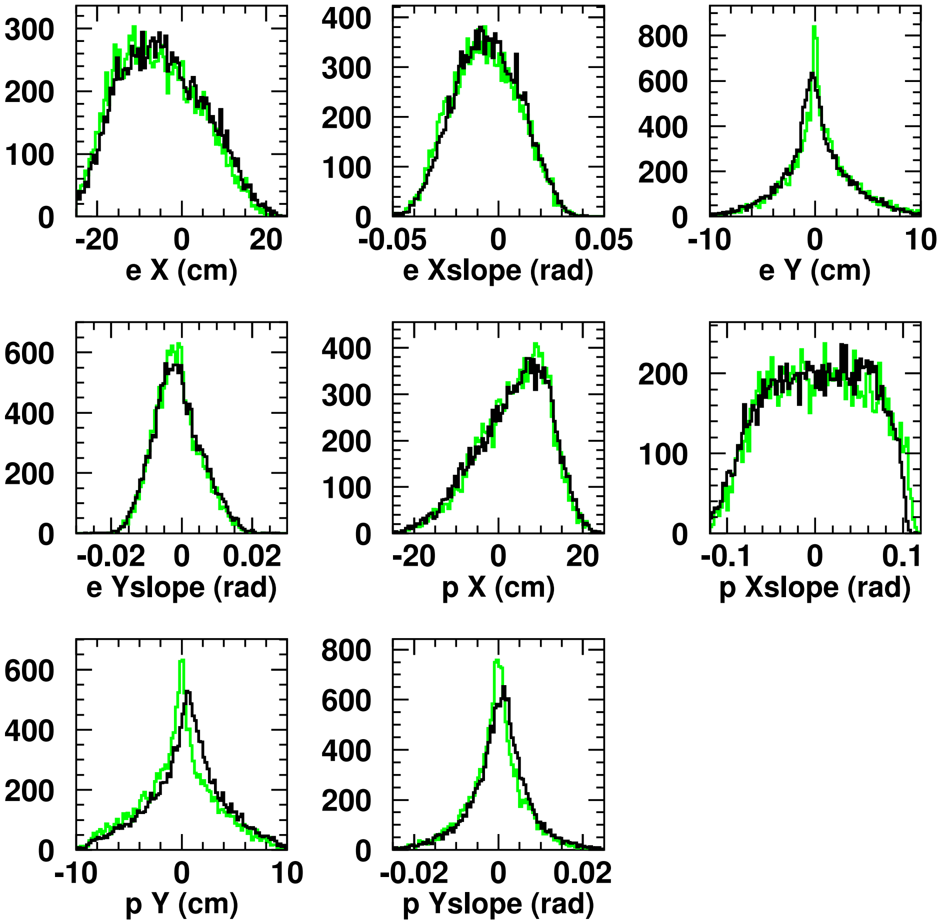

Figure 3.14. Carbon Focal Plane Spectra: Simulation vs. Experiment. Shown are the horizontal position and slope, and vertical position and slope spectra for the electron (e) and proton (p). The experimental spectra are solid and the simulated spectra are grey. ^{12}C data at $Q^2 = 0.64$ (GeV/c)^2.

where p and z are the particle momentum and charge, respectively, and x and X_0 are the material thickness and radiation length, respectively. [9] Energy loss and multiple scattering are taken into account throughout the spectrometer, up to the position of the wire chambers (focal plane). The focal plane values of x, x', y, and y' are then used to reconstruct the trajectory back to the target. The reconstruction is performed using COSY-calculated matrix elements that invert the forward transformation.

3.9.6 Further Refinements A series of refinements to the PWIA calculation are necessary before comparison with the experimental data is possible. First, Coulomb distortions can significantly change the energy of the electron at the reaction vertex. The electron is accelerated to a higher energy than expected at the vertex, and then decelerated on its way out of the nucleus:

$$\vec{k}^{\,\text{eff}}_{i,f} = \vec{k}_{i,f} + \eta \hat{k}_{i,f}, \tag{3.47}$$

where i and f refer to the initial and final electron momentum, respectively, and

$$\eta \equiv f_C \frac{\alpha Z}{R_C}. \tag{3.48}$$

Here R_C is the effective charge radius of the target nucleus, and $f_C \approx 1.5$ for a spherical charge distribution. [73] The first effect is a change in momentum transfer of

$$\vec{q}^{\,\text{eff}} = \vec{q}\left(1 + \frac{\eta}{k_f}\right) + \hat{k}_i\left(\eta - \frac{\eta k_i}{k_f}\right). \tag{3.49}$$

The second effect is a net increase in the electron flux near each nucleus due to the Coulomb attraction. In SIMC, the Coulomb corrections are taken into account by shifting the reported missing momentum via $\vec{p}^{\,\text{eff}}_{m} = \vec{p}\,' - \vec{q}^{\,\text{eff}}$, and changing the de Forest off-shell cross section by [73]

$$\sigma^{corr}_{cc} = \left(\frac{\vec{k}^{\,\text{eff}}_{i}}{\vec{k}_i}\right)^2 \sigma_{cc}, \tag{3.50}$$

Table 3.10: Coulomb Corrections in SIMC for each kinematics.

Kine	Target	$\vec{q}$ (GeV/c)	$\Delta\vec{p}_m$ (MeV/c)	$\left(\frac{\vec{k}_i^{eff}}{\vec{k}_i}\right)^2$
A	^{12}C	0.84	0.75	1.0026
	^{56}Fe		2.16	1.0077
	^{197}Au		4.55	1.0162
B	^{12}C	1.27	1.06	1.0026
	^{56}Fe		3.06	1.0077
	^{197}Au		6.45	1.0162
C	^{12}C	1.55	0.79	1.0020
	^{56}Fe		2.30	1.0058
	^{197}Au		4.80	1.0122
D	^{12}C	0.84	3.20	1.0077
	^{56}Fe		9.30	1.0220
	^{197}Au		19.60	1.0471
E	^{12}C	1.55	2.70	1.0039
	^{56}Fe		7.90	1.0113
	^{197}Au		16.80	1.0241
F	^{12}C	2.55	1.60	1.0020
	^{56}Fe		4.70	1.0058
	^{197}Au		9.90	1.0122

Table 3.10 lists the change in $\vec{p}_m$ and σ_{cc} for each kinematics and each target. The backwards angle kinematics (D and E) have the largest Coulomb distortions due to the small energy of the incoming electron. And, as expected, the largest distortions for a given kinematics are on the gold target.

Finally, the simulation is based on the IPSM, and as such, fails to take into account correlations between the nucleons. As discussed in the introduction, these correlations can shift the nucleon momenta beyond the Fermi momentum and thus out of the experimental acceptance. The Monte Carlo therefore overestimates the experimental yield. The approximation is made that a constant fraction of the spectral function strength is shifted beyond the experimental acceptance. Thus a single "correlation correction factor" can be defined that corrects the simulated yields for this effect (As defined here, the simulated yields are divided by the correction factor). The factors are calculated via

$$F_{correl} = \frac{\int_{E_m,\vec{p}_m} S_{IPSM} d\vec{p}_m dE_m}{\int_{E_m,\vec{p}_m} S_{correl} d\vec{p}_m dE_m}, \tag{3.51}$$

where S_{correl} is a correlated spectral function calculated for each target nucleus. The same correction factors are used here as in experiment NE-18: The carbon correlated spectral function is taken from a Brueckner finite nuclei theory calculation for the ^{16}O nucleus [33], and the iron and gold correlated spectral functions come from nuclear matter calculations by Ji and Engel, corrected for finite nucleus effects [74]. Table 3.11 lists the correlation correction factors for each nucleus. The uncertainties are derived from the model dependencies in the various calculations, and are discussed in more detail in Section 4.3.3.

Table 3.11: Correlation Correction Factors

Nucleus	F_{correl}
^{12}C	1.11 ± 0.03
^{56}Fe	1.26 ± 0.08
^{197}Au	1.32 ± 0.08

3.10 Extraction of the Transparency

As was mentioned in Section 1.4.1, nuclear transparency is defined to be the ratio of the measured (e,e$'$p) yield to that calculated in the PWIA:

$$T_\theta \equiv \frac{\int_V d\vec{p}_m dE_m N_\theta^{exp}(E_m, \vec{p}_m)}{\int_V d\vec{p}_m dE_m N_\theta^{PWIA}(E_m, \vec{p}_m)}, \tag{3.52}$$

where the θ subscript refers to the fact that this ratio is to be constructed at a given proton angle setting. The integrals are taken over the kinematic phase space V, and a range of missing energy and momentum (discussed below).

To calculate the experimental yield, N_θ^{exp}, the coincidence data from a given proton angle setting are binned from 0 to 80 MeV in missing energy and -300 to 300 MeV/c in missing momentum. In addition, constraints are placed on other kinematical quantities to insure that both the electron and proton are in well-understood regions of the spectrometers. Table 3.12 lists the standard constraints used in E91-013. Next, the aforementioned corrections—proton absorption, dead time, timing, synchronization, and background—are applied to the data. Note that the correction of synchronization problems and the removal of coincidence blocking protons are performed for each run individually, and hence, are not listed here. The sensitivity to these constraints is discussed in Section 4.3.2. Finally, the data with above constraints and corrections are weighted by,

$$\frac{1}{Q \times TE_{HMS} \times TE_{SOS} \times PT \times LT},$$

where Q is the accumulated charge of the incident electrons, $TE_{HMS(SOS)}$ is the measured tracking efficiency of the HMS (SOS), PT is the proton transmission, and

Table 3.12. Standard Data Constraints for E91-013. The calorimeter requirement depends on the kinematics. Note that there is no Čerenkov constraint for kinematics F, with electrons in the SOS.

Parameter	Constraint
Missing Energy (MeV)	0 - 80
Missing Momentum (MeV/c)	± 300
HMS δ (%)	± 8
SOS δ (%) (p in SOS)	-10 - 20
SOS δ (%) (e^- in SOS)	± 15
HMS X'_{tar} (rad)	± 0.075
HMS Y'_{tar} (rad)	± 0.040
SOS X'_{tar} (rad)	± 0.045
SOS Y'_{tar} (rad)	± 0.060
Kine. A e^- Calorimeter (GeV)	> 1.0
Kine. B e^- Calorimeter (GeV)	> 1.0
Kine. C e^- Calorimeter (GeV)	> 1.0
Kine. D e^- Calorimeter (GeV)	> 0.2
Kine. E e^- Calorimeter (GeV)	> 0.4
Kine. F e^- Calorimeter (GeV)	> 0.8
e^- Čereknov (npe)	1
Coincidence time cut (ns)	± 1.5
Backgrd. Sample Width (ns)	6×2

LT is the computer live time. In the case of duplicated runs, the weighted average of the yields is taken. The weights are calculated from the $\sqrt{N}$ statistical error, where N is the raw number of events surviving the constraints.

The PWIA calculation yields, N_θ^{PWIA}, are obtained by performing the experimental simulation using the same kinematical constraints as for the data (Table 3.12). This is done for each target at every proton angle setting at each Q^2. In addition to providing simulated yields, the Monte Carlo results are also used to correct slight offsets in the experimental data. As the spectrometer positions are changed for the various kinematic settings, small offsets in the detectors and relative position of the target occur. These offsets manifest themselves as overall shifts angle and missing energy spectra. Therefore, when applying the constraints to both experiment and simulation, the relative position of both sets of spectra must agree. Thus, the experimental spectra are offset by a constant (that differs from run to run) such that means of both the vertical and horizontal angle distributions and the least bound states in the missing energy distribution match those of the simulation. That the means of the distributions are used is reasonable as long as the shapes of both the experiment and simulation agree. While this is true for the angular distributions, the missing energy distributions can sometimes differ depending on the target and kinematics. For this reason, the missing energy yields are only compared from 0–25 MeV so as to align the threshold separation energies. The sensitivity of the transparency to these adjustments are discussed in Section 4.3.2.

Given the experimental and simulated yields, the transparency is calculated via Eqn. 1.14 for each proton angle setting. The weighted average of each angle setting is then taken to arrive at the transparency for a given Q^2:

$$T = \frac{\sum_\theta T_\theta w_\theta}{\sum_\theta w_\theta}, \tag{3.53}$$

where w_θ is the weight calculated from the statistical uncertainty in each ratio, T_θ.

CHAPTER 4

RESULTS

This chapter presents the results of the data analysis. The hydrogen coincidence yields are used to test various aspects of the Monte Carlo, followed by a presentation of inclusive (e,e$'$) yields for all targets. The coincidence data and nuclear transparency results are then presented, followed by a discussion of the systematic and model-dependent uncertainties. The chapter then concludes with comparisons of the experimental results and various theoretical calculations.

4.1 Hydrogen Coincidence Results

The elastic scattering of electrons from hydrogen is used to test several aspects of the experimental simulation, SIMC. Coincidence H(e,e$'$p) data at each E91-013 kinematic setting are used to test both the understanding of the spectrometers' acceptance, the Monte Carlo's radiative correction procedure, and the absolute normalization.

Because the spectral function of hydrogen is simply the product of delta functions centered at $E_m = 0$ and $\vec{p}_m = 0$, there is no spectral function model dependence in the Monte Carlo. This makes H(e,e$'$p) data ideal for measuring the acceptance of both spectrometers; the agreement between data and simulation does not rely on the quality of a nuclear model. Figure 4.1 shows a comparison of experimental and Monte Carlo H(e,e$'$p) spectra at $Q^2 = 0.64$ (GeV/c)^2 (Kinematics A: electrons in HMS, protons in SOS). The two sets of spectra are normalized to the same luminosity, and corrected for background, proton absorption, and detector inefficiency. The angle spectra are reconstructed to the target and are measured with

Table 4.1. Hydrogen Coincidence Yields: Data vs. Simulation. The ratio of data to simulation is taken using events passing the standard constraints (Section 3.10). The yields are normalized to charge and corrected for background, tracking inefficiencies, and proton absorption. The uncertainties are statistical. Note that the very low ($\sim$ 55%) tracking efficiency for the hydrogen run at kinematics F causes an additional uncertainty, and therefore the inclusive yields have to be relied upon for normalization (Section 4.2).

Kinematics	Q^2 (GeV/c)^2	Data/Simulation
A	0.64	1.006 $\pm$ 0.005
B	1.28	1.007 $\pm$ 0.006
C	1.79	0.991 $\pm$ 0.006
D	0.64	0.986 $\pm$ 0.007
E	1.84	0.987 $\pm$ 0.007
F	3.25	0.94 $\pm$ 0.02

respect to the central ray of the respective spectrometers: θ is the angle in the scattering plane, and ϕ is the out of plane angle. The longitudinal position of the reaction vertex (in the extended hydrogen target) as seen by the electron spectrometer is given by Y_{tar}. Note that because the electron arm is at 20.5°, the 4.2 cm length of the target is foreshortened to approximately 1.5 cm. In addition to the standard constraints, each event was required to have an invariant mass equal to that of the proton to insure that the scattering was indeed elastic.

Table 4.1 lists the ratio of experimentally measured to simulated coincidence yields. The error bars reflect only the statistical uncertainty of both yields, and with the exception of Kinematics F, there is very good agreement (1%). As was mentioned, a bad gas mixture in the HMS wire chambers caused extremely low ($\sim$ 55%) tracking efficiencies in the Kinematics F hydrogen runs. Both the accuracy of the efficiency correction and the validity of the events that were detected are considered suspect for these runs, and thus the inclusive yields (Section 4.2) have to be relied upon for comparison.

Coincidence H(e,e$'$p) data can also be used to test the radiative correction

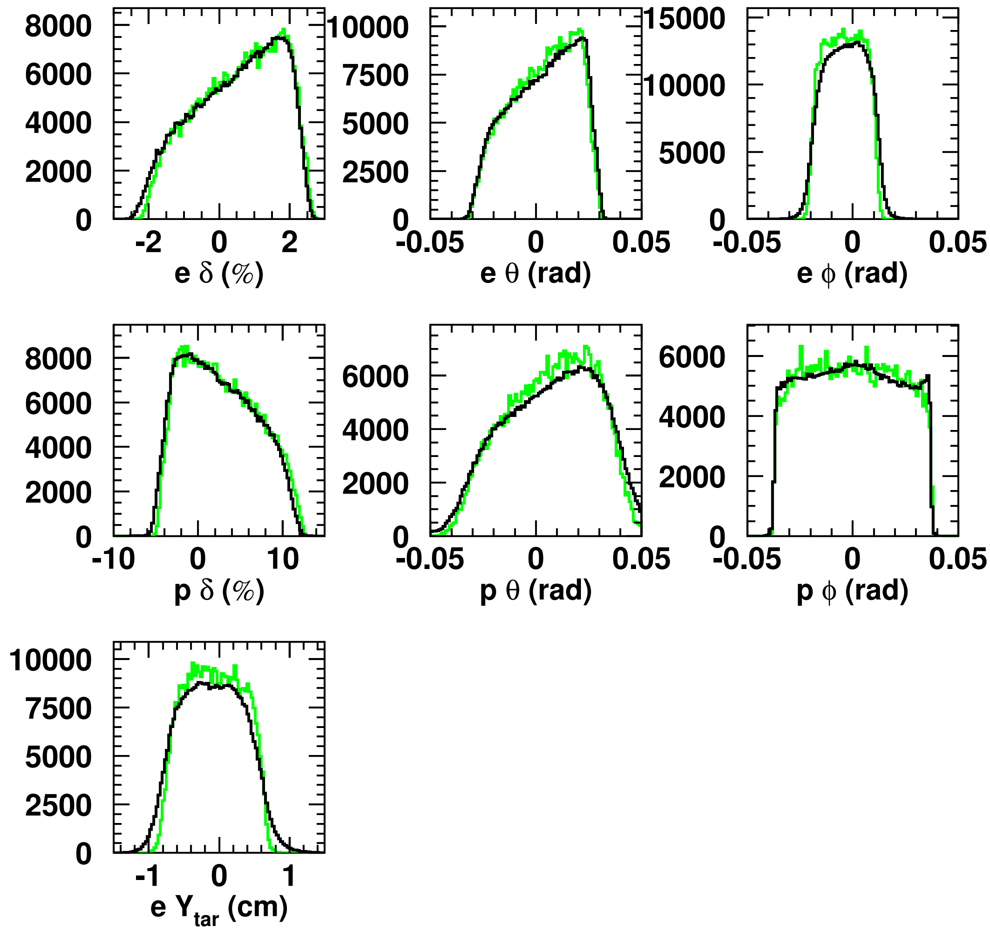

Figure 4.1. Hydrogen Coincidence Data vs. Simulation Reconstructed to Target. Data (solid) and simulation (dashed) for Kinematics A: ($Q^2 = 0.64$ (GeV/c)^2). The yields are normalized to charge, corrected for background, tracking inefficiencies, and proton absorption, and an invariant mass cut is applied to the experimental yields.

procedures employed in the Monte Carlo. Because the true missing energy distribution of hydrogen is a delta function centered at $E_m = 0$, all missing energy strength beyond roughly 10 MeV (the width reflecting the experimental resolution) is due to radiative effects. Figure 4.2 shows hydrogen missing energy spectra for each kinematic setting. The highest electron momenta occur at kinematics C and E, and hence these kinematics have the poorest resolutions. In all kinematics, however, there is excellent agreement in the radiative spectra all the way out to 80 MeV in missing energy. Figure 4.3 shows the corresponding missing momentum distributions.

4.2 Inclusive Cross Sections

As a test of both the data analysis and the normalization of the model spectral functions, the inclusive yields of both the experiment and simulation were calculated. The extraction of the experimental inclusive yield is discussed in Section 3.7, but briefly, the prescaled, electron-only events are added to the coincidence yields, giving the experimental counts, N. The cross section, in units of nb/sr/MeV, is then calculated via:

$$\frac{d^2\sigma}{dEd\Omega} = \frac{NM_A 10^{33}}{tN_A \mathcal{L}\mathcal{E}N_e \Delta\Omega\Delta E}. \tag{4.1}$$

Here, M_A is the target mass in amu, t is the target thickness in g/cm^2, $\mathcal{L}$ is the DAQ live time, $\mathcal{E}$ is the tracking efficiency of the electron arm, N_e is the total number of incident electrons, and $\Delta\Omega$ and ΔE are the accepted ranges of solid angle and energy loss, respectively. The only constraints placed on the inclusive data are electron particle identification (shower counter and Čerenkov signals) and the same δ and angle ranges used in the coincidence analysis for the electron arm.

Although SIMC is designed to simulate coincidence data, it can be used to calculate inclusive yields by opening up the acceptance of the proton arm. This enables every proton scattered by an electron to be detected in an all-inclusive proton "spectrometer." However, the output of the simulation still needs to be corrected for

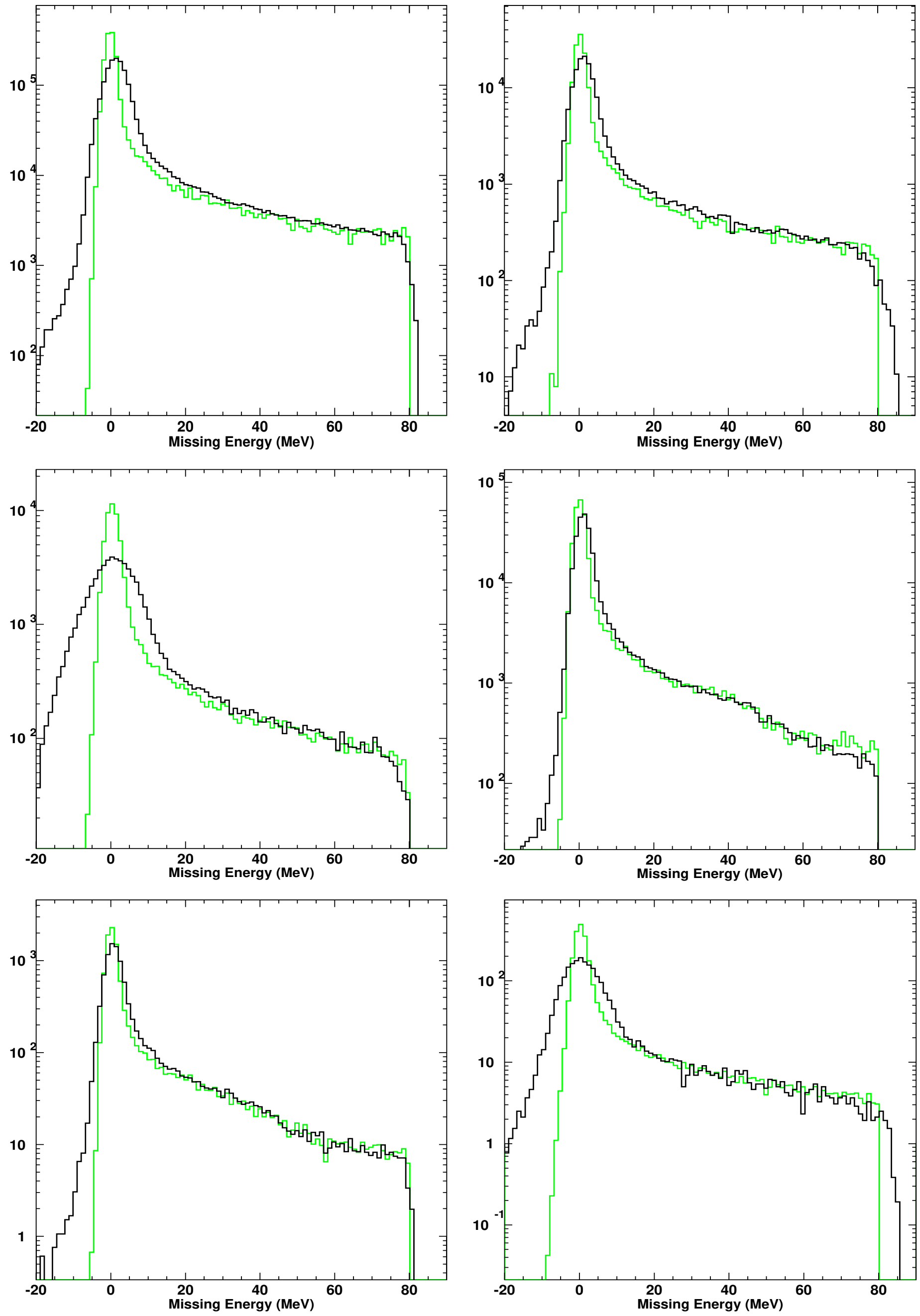

Figure 4.2. Hydrogen Missing Energy Spectra (Log scale). Data (solid) and simulation (dashed), Kinematics A - F, left to right, top to bottom. The yields are normalized to charge and corrected for background, tracking inefficiencies, and proton absorption (a comparison of the integrated yields is given in Table 4.1). See text for details.

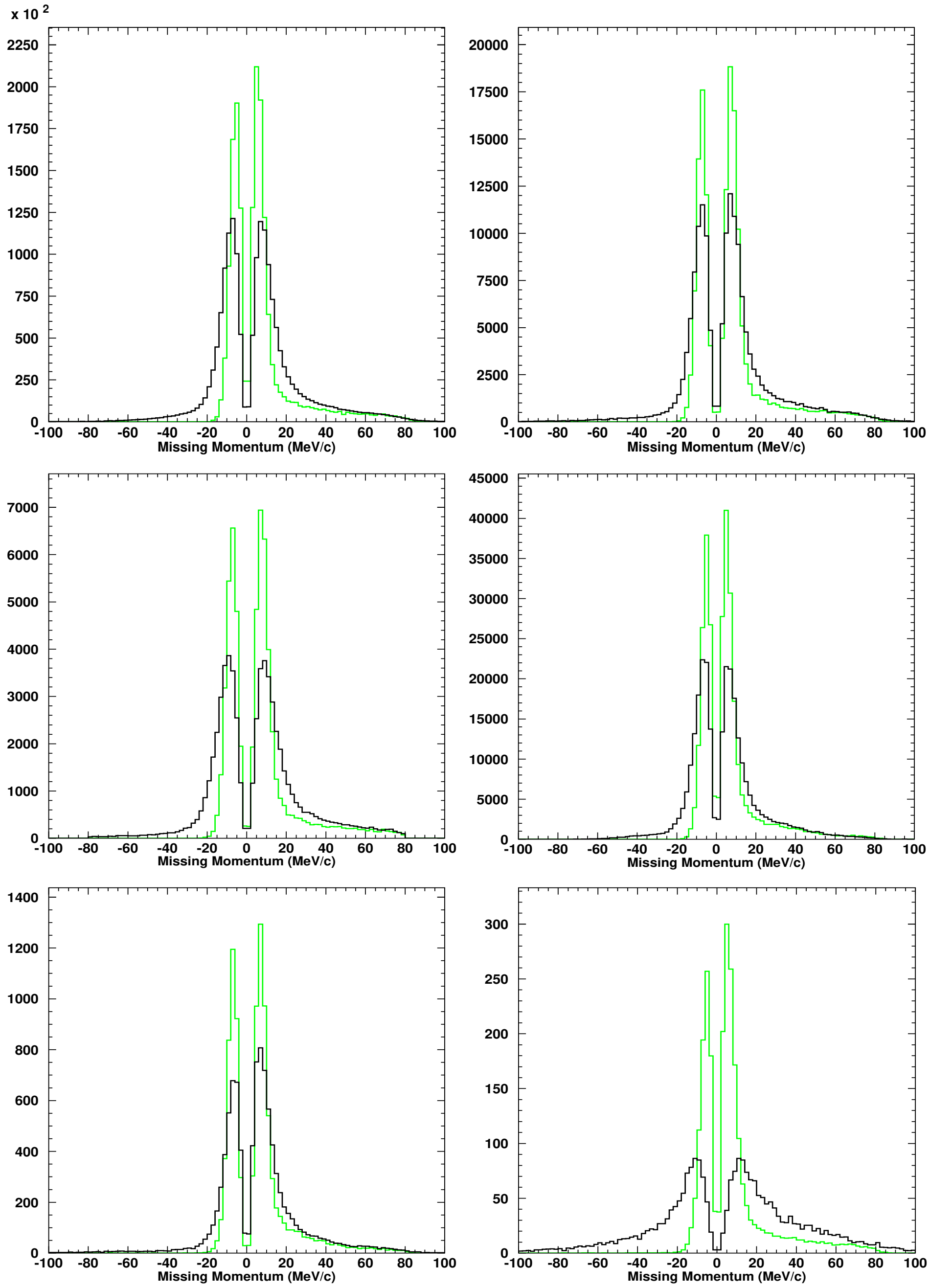

Figure 4.3. Hydrogen Missing Momentum Spectra (Log scale). Data (solid) and simulation (dashed), Kinematics A - F, left to right, top to bottom. The yields are normalized to charge and corrected for background, tracking inefficiencies, and proton absorption (a comparison of the integrated yields is given in Table 4.1). See text for details.

the fact that SIMC does not include effects like neutron scattering, pion production, and Δ excitation. The neutron contribution is taken into account at each kinematics as follows: Using the parameterizations of Gari and Krümplemann [59] for both neutron form factors, the elastic electron-neutron cross section is calculated. The electron-proton cross section is calculated using the Gari and Krümplemann magnetic proton form factor and the dipole electric form factor. The SIMC yield is then multiplied by

$$\frac{Z\sigma_{ep} + N\sigma_{en}}{Z\sigma_{ep}}.$$

To correct for the inelastic contributions, the electron-nucleus scattering code of Lightbody and O'Connell [75] was modified to provide both the total and quasifree radiated cross sections as a function of energy loss, ω. For each ω bin, the difference

$$\left.\frac{d^2\sigma}{dEd\Omega}\right|_{\mathrm{tot}} - \left.\frac{d^2\sigma}{dEd\Omega}\right|_{\mathrm{qfree}}$$

is added to the neutron-corrected SIMC yield. Because the comparison is being made between experimental and simulated yields, no attempt has been made to correct for "bin-centering" effects. (Bin-centering refers to the fact that it is necessary to convert the total integrated counts in a given ω bin to the number expected at the center of that bin. This can be an important effect when the shape of the distribution is changing rapidly over the bin width.) However, because the binning used in the two sets of spectra is the same, both effects are expected to roughly cancel. Note that the inelastic contributions are not corrected for either the bin-centering effects or the experimental acceptance. Both effects are expected to be small except possibly at the edges of the acceptance. Finally, note that because the kinematics are such that the quasifree reaction is expected to dominate, the correlation factors listed in Table 3.11 have been applied to the SIMC yields to correct for the over-estimation of the quasielastic strength.

For completeness, the experimentally measured inclusive hydrogen yields are compared those of the simulation. Because there is no Fermi motion in hydrogen, it is possible to isolate the quasifree peak by placing constraints on the invariant mass of the particle from which the electron scattered. Thus, corrections for the inelastic contribution are not necessary.

Figures 4.4—4.7 show both the experimental and simulated cross sections at each kinematics for carbon, iron, gold, and hydrogen, respectively, and the experimental cross sections are tabulated in Appendix C. The grey points on the solid target plots are the SIMC yields corrected for correlations and neutron contribution only. They are plotted so as to illustrate the size of the inelastic contribution as calculated by Lightbody and O'Connell. As Q^2 increases, these contributions become larger, and indeed dominate at Kinematics F. Note also that radiative effects have not been removed from the data but have instead been included in the simulation and inelastic contribution calculation. Table 4.2 lists the ratios of experimentally measured yield to simulated yield and the corresponding statistical uncertainty for each target at each kinematic setting. With the exception of Kinematics F, the experimental yields for the solid targets are, on average, 5.6%, 11.1%, and 9.5% higher than those of the simulation for carbon, iron, and gold, respectively. However, the discrepancies do vary with the kinematic setting. At Kinematics F the results are highly dependent on the accuracy of the Lightbody and O'Connell code, as the majority of the strength is inelastic. The experimental and simulated inclusive hydrogen yields do, however, agree quite well and are consistent with the coincidence results (Table 4.1). In particular, there is good agreement at Kinematics F, where the exclusive results were suspect due to the poor HMS (proton detector) tracking efficiency.

Note that only statistical uncertainties are plotted in Figs. 4.4—4.7. The uncertainties in the tracking efficiency, current measurement, and run stability each contribute 1% to the total systematic uncertainty (See Section 4.3.2), and SIMC

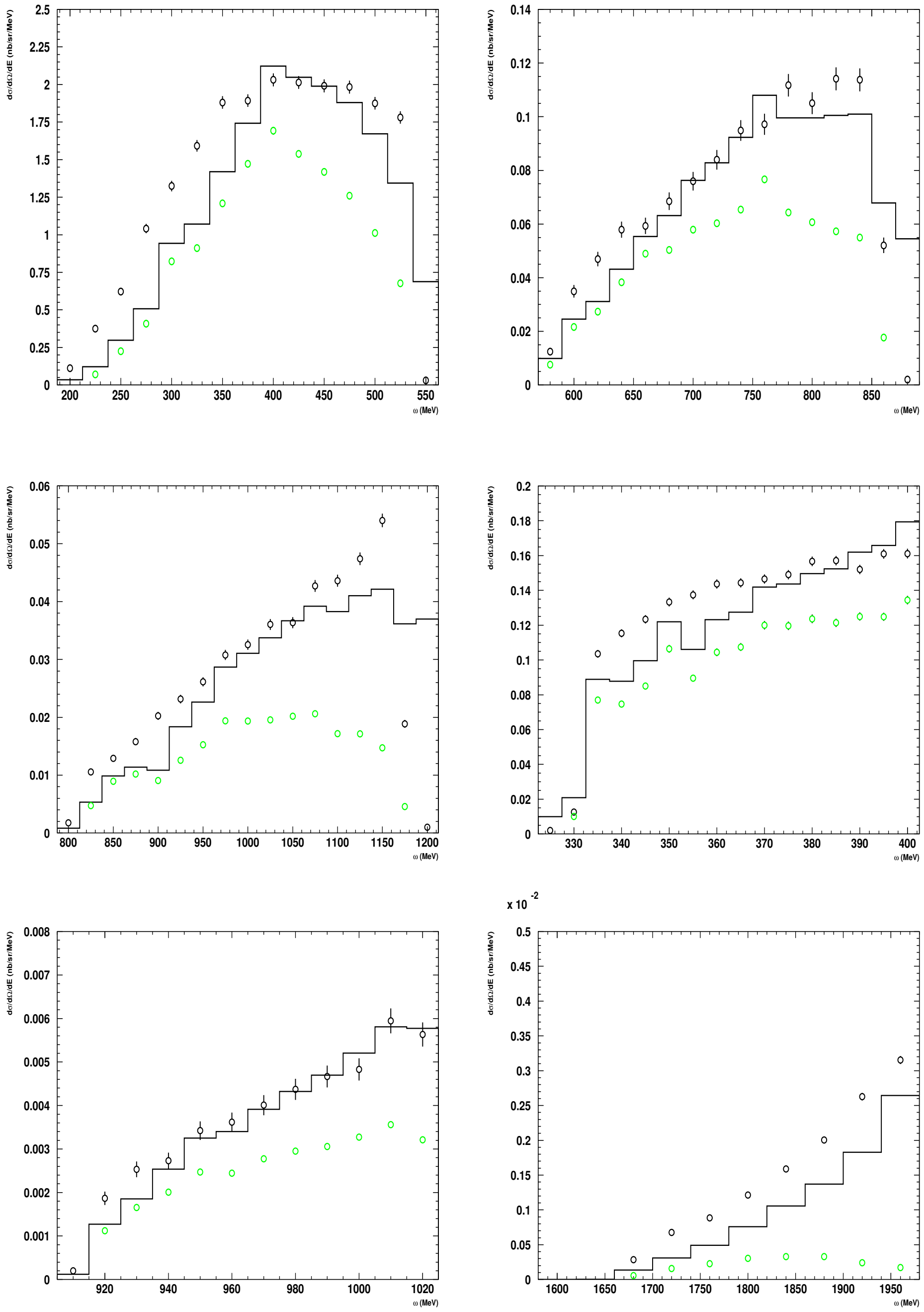

Figure 4.4. Carbon Inclusive Cross Sections. The experimental results are shown with statistical uncertainties only (each point has a 10% systematic uncertainty), and the curve is the corrected model. The model results with only correlation and neutron corrections are shown in grey. The integrated yields are listed in Table 4.2. Kinematics A–F, left to right, then down.

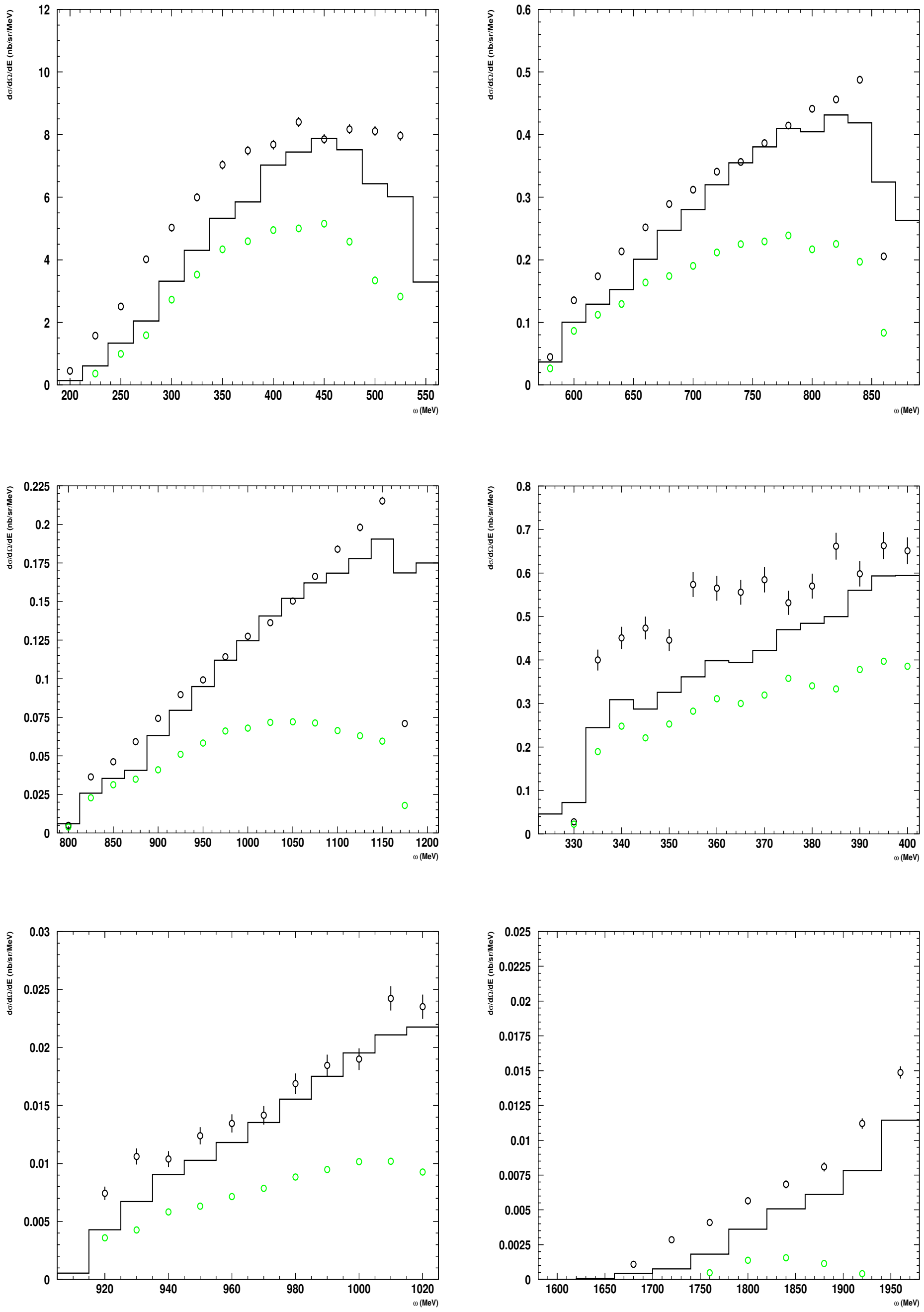

Figure 4.5. Iron Inclusive Cross Sections. The experimental results are shown with statistical uncertainties only (each point has a 10% systematic uncertainty), and the curve is the corrected model. The model results with only correlation and neutron corrections are shown in grey. The integrated yields are listed in Table 4.2. Kinematics A–F, left to right, then down.

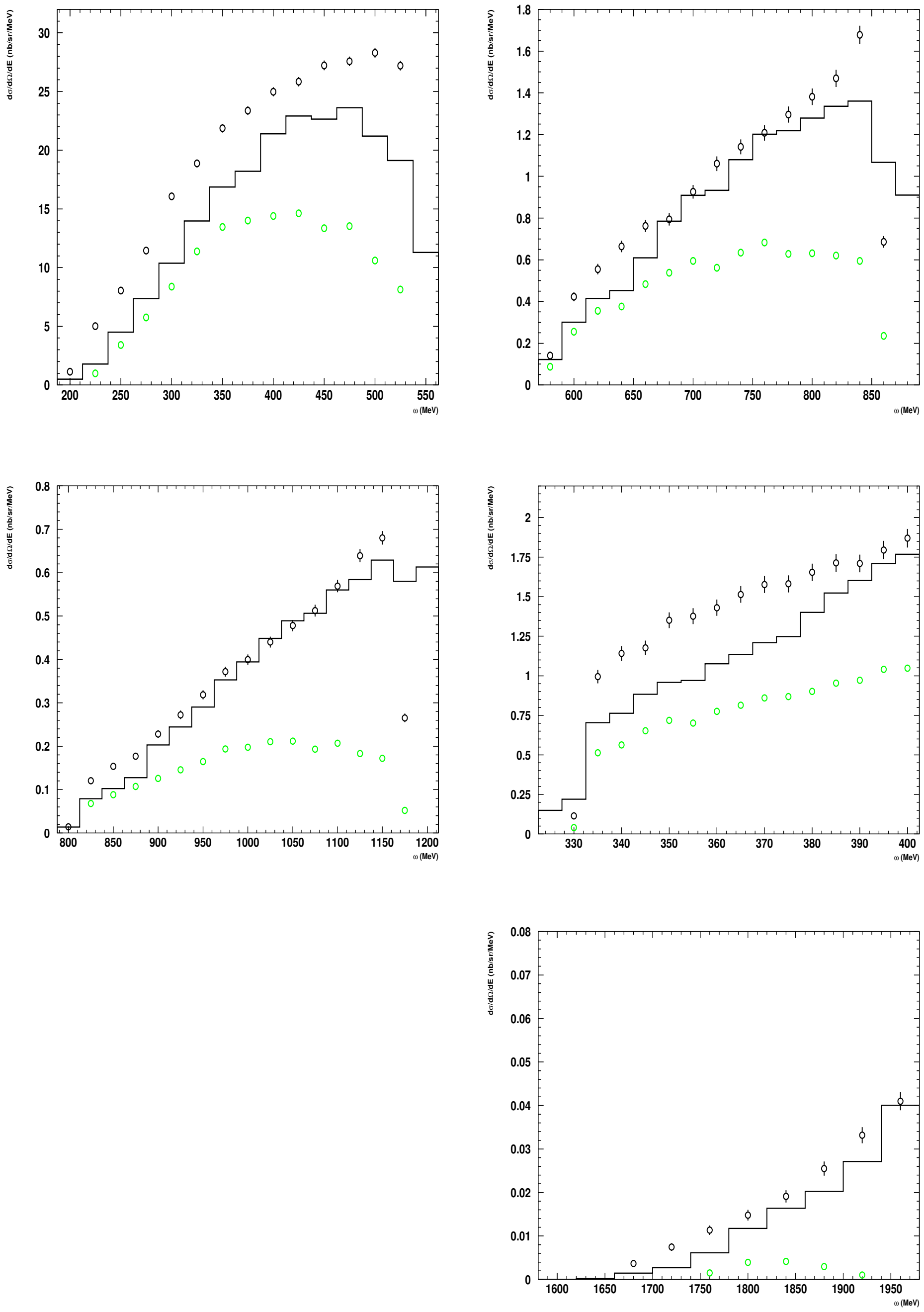

Figure 4.6. Gold Inclusive Cross Sections. The experimental results are shown with statistical uncertainties only (each point has a 10% systematic uncertainty), and the curve is the corrected model. The model results with only correlation and neutron corrections are shown in grey. The integrated yields are listed in Table 4.2. Kinematics A–F, left to right, then down.

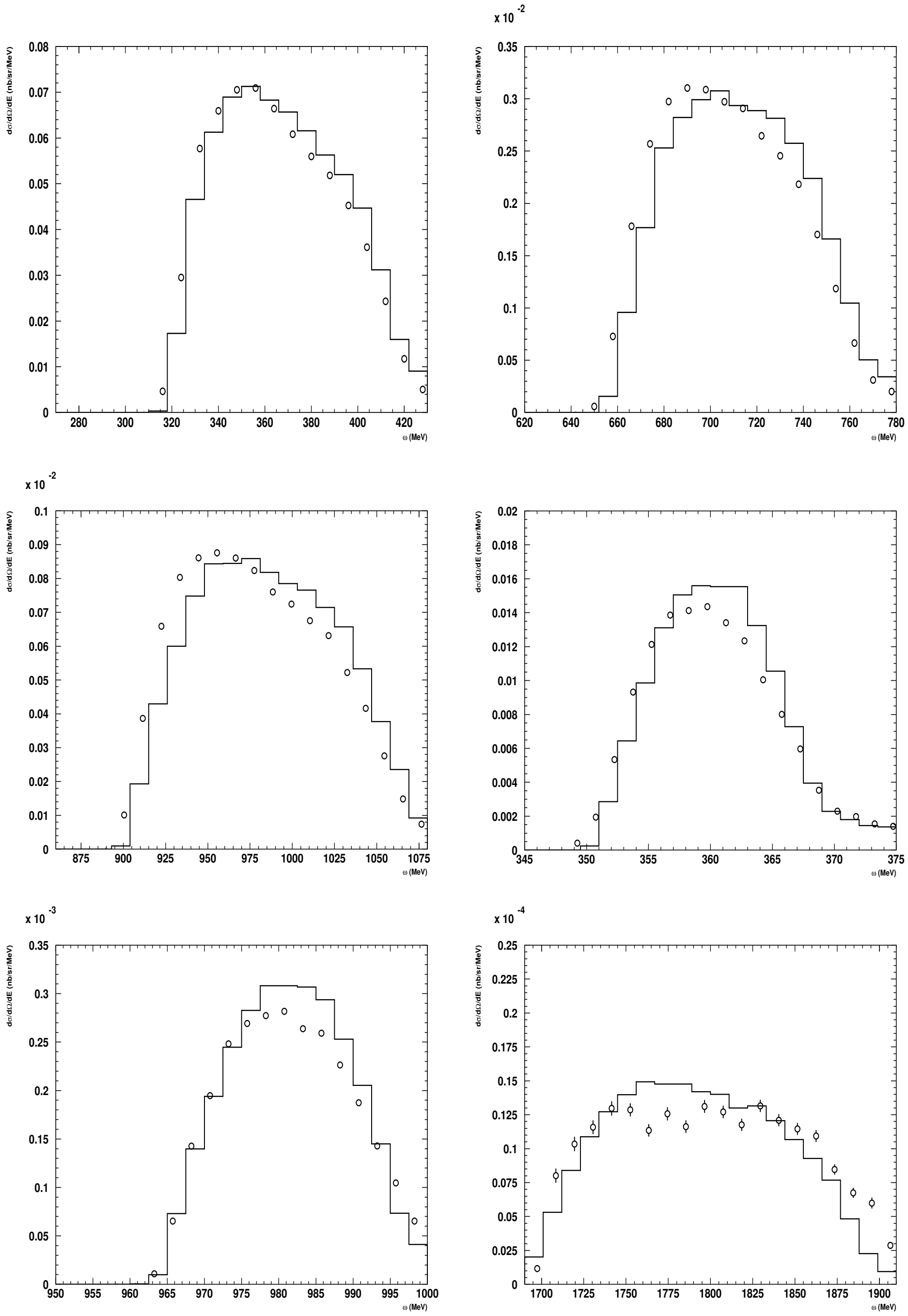

Figure 4.7. Hydrogen Inclusive Cross Sections. The experimental results are shown with statistical uncertainties only (each point has a 10% systematic uncertainty), and the curve is the model. The experimental yields have invariant mass constraints to insure quasielastic scattering. The integrated yields are listed in Table 4.2. Kinematics A–F, left to right, then down.

Table 4.2. Inclusive Yields: Data vs. Simulation. Listed are the ratios of data yield to simulated yield. The uncertainties are statistical only and do not include the 10% systematic uncertainty.

Target	Kinematics	Expmt./Simulation
^{12}C	A	1.15 ± 0.01
	B	1.02 ± 0.01
	C	1.02 ± 0.01
	D	1.06 ± 0.01
	E	1.04 ± 0.02
	F	1.45 ± 0.02
^{56}Fe	A	1.20 ± 0.01
	B	1.01 ± 0.01
	C	0.93 ± 0.01
	D	1.28 ± 0.02
	E	1.13 ± 0.02
	F	1.47 ± 0.03
^{197}Au	A	1.24 ± 0.01
	B	1.02 ± 0.01
	C	0.91 ± 0.01
	D	1.21 ± 0.01
	F	1.24 ± 0.03
^{1}H	A	0.98 ± 0.01
	B	1.01 ± 0.01
	C	1.01 ± 0.01
	D	0.97 ± 0.01
	E	0.97 ± 0.01
	F	1.01 ± 0.03

was used to estimate a 10% systematic uncertainty due to a lack of experimental acceptance corrections. (However, to the extent that the simulation correctly models the acceptance, the systematic uncertainty is not expected to affect the agreemeent between the experimental and simulated cross sections.) The sum, in quadrature, of the above contributions is used to assign an overall systematic uncertainty of 10% to the inclusive yields. A more careful analysis of the experimental acceptance is expected to reduce this figure.

The purpose of comparing the experimental and simulated inclusive yields for the solid targets is to test the normalization of the model spectral functions. While the variation in agreement displayed in Table 4.2 seems to be large, note that the size of the discrepancy depends more on the kinematic setting than on the target. Indeed, even the discrepancy in spectra shape is similar for each kinematic setting for the three targets (Figs. 4.4–4.6). This indicates that the differences probably do not stem from problems with the spectral functions but rather from the way in which the inelastic corrections are applied. One possibility is simply that the accuracy of the Lightbody and O'Connell calculation changes as the kinematic range of E91-013 is covered. Another possibility is that the inelastic corrections are sensitive to the acceptance and bin-centering effects. To conclude, there is no dramatic evidence that the model spectral functions give rise to an inclusive yield that is inconsistent with experiment. The observed average discrepancy of approximately 10% seems to be dependent more on the kinematic setting than on the target model.

4.3 Nuclear Transparency

This section presents the nuclear transparency results of experiment E91-013. Coincidence yields and missing energy spectra for the solid targets are compared with the simulation, and then the transparency is presented as a function of Q^2 and A.

The dependence of the transparency on the models in the Monte Carlo is then discussed, followed by a description of various theoretical calculations of the nuclear transparency.

4.3.1 Transparency Results Experimental and simulated missing energy spectra for each E91-013 kinematic setting are presented for each target in Figures 4.8–4.10, where the spectra are normalized to the same number of counts in order to facilitate comparison of the shapes. The simulated carbon spectra seem to show more strength near $E_m \approx 30$ MeV (between the $1p_{3/2}$ and $1s_{1/2}$ states) than do the experimental spectra. This strength is reduced if the location of the $1s$ peak in the model spectral function is moved just a few MeV towards higher missing energy. Of the three targets however, the largest discrepancy between simulation and experiment clearly occurs for iron (Fig. 4.9). Here the strength of least bound states is underestimated, and the (simulated) shell widths of the deeply bound states (near $E_m \approx 45$ MeV) seem to be too small. However, as discussed below, the yields for all targets are integrated over 0–80 MeV in missing energy, and are largely insensitive to the shapes of the missing energy spectra. The dependence of the transparency on the models is discussed in Section 4.3.3, and an alternative model spectral function for ^{56}Fe is discussed in Appendix A. The corresponding missing momentum distributions for the three targets are presented in Figures 4.11–4.13. Note that in all cases, the agreement is quite acceptable. Radiative effects are responsible for the asymmetry about $\vec{p}_m = 0$, and are well described by the simulation.

The distribution of the experimental coincidence yields as a function of proton angle are presented for each target in the upper panels of Figures 4.14–4.16, respectively. Note the complete coverage of the Fermi cone in proton angle. The lower panels display the transparency as a function of proton angle. The lines represent the Monte Carlo yields (calculated for individual proton angle settings, but connected smoothly) normalized to match the data at the central (conjugate)

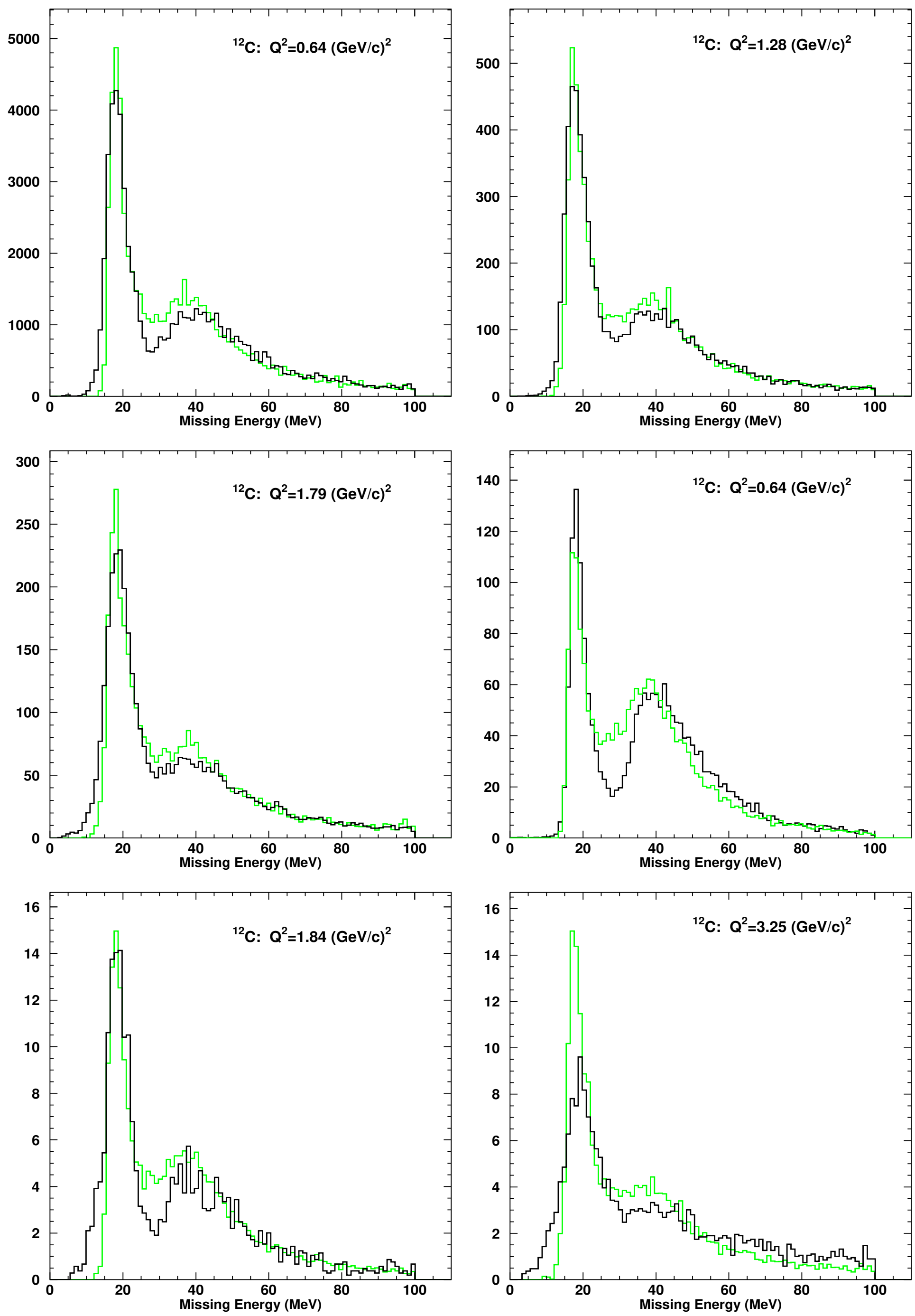

Figure 4.8. Carbon Missing Energy Spectra. Data are black and simulation is grey. Kinematics are A-F, left to right, then down.

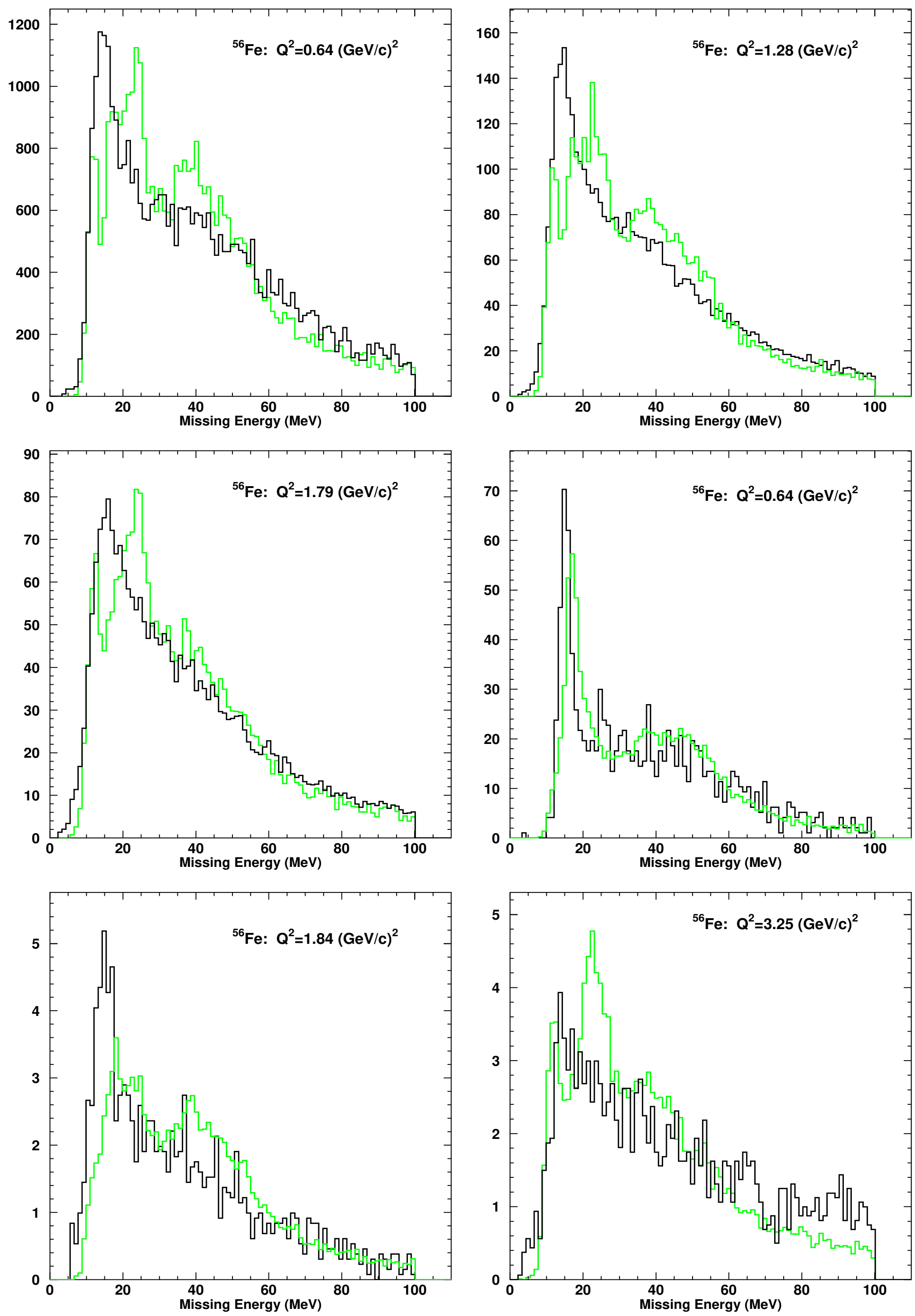

Figure 4.9. Iron Missing Energy Spectra. Data are black and simulation is grey. Kinematics are A-F, left to right, then down.

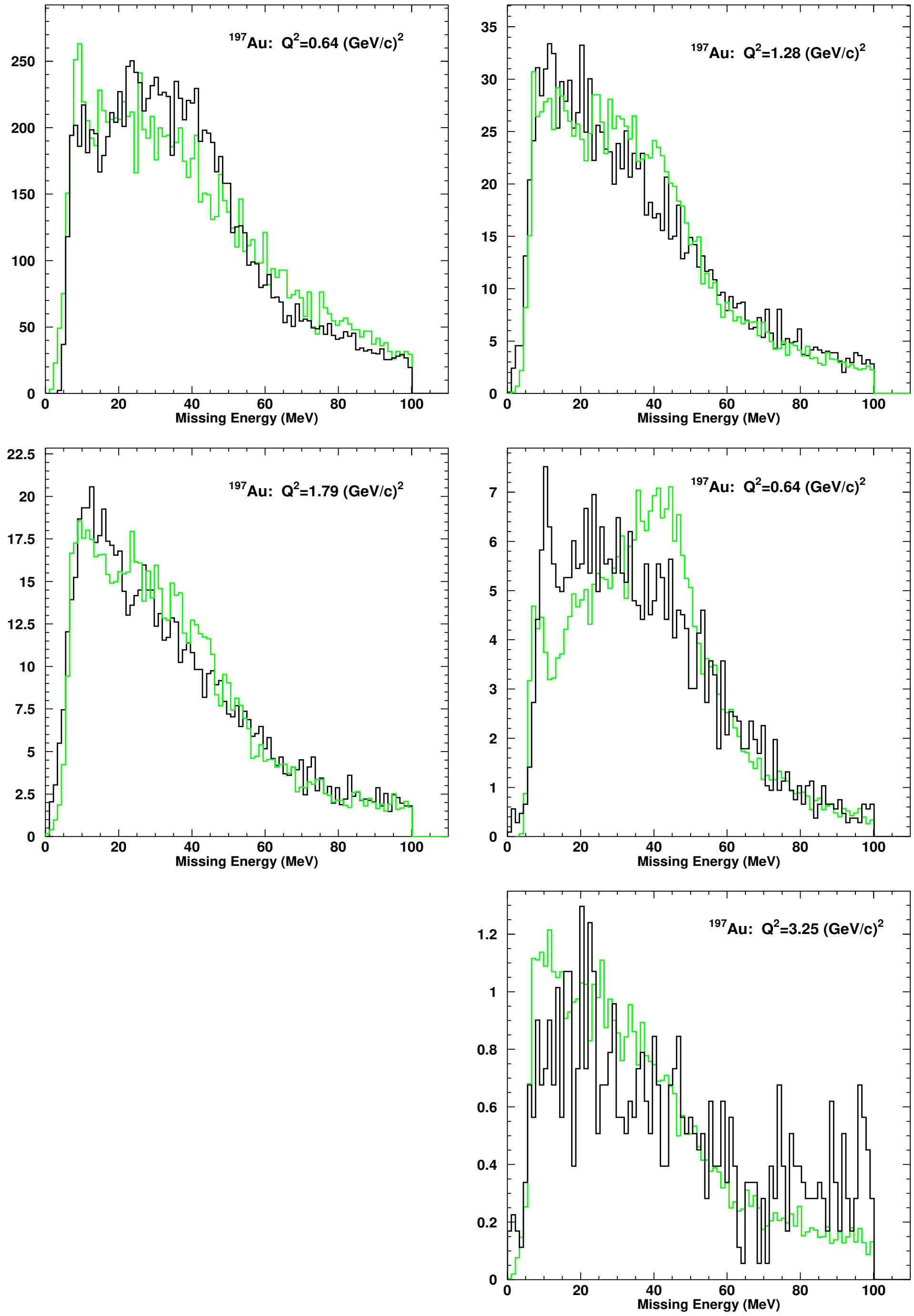

Figure 4.10. Gold Missing Energy Spectra. Data are black and simulation is grey. Kinematics are A-F, left to right, then down. Note gold data were not taken for Kinematics E.

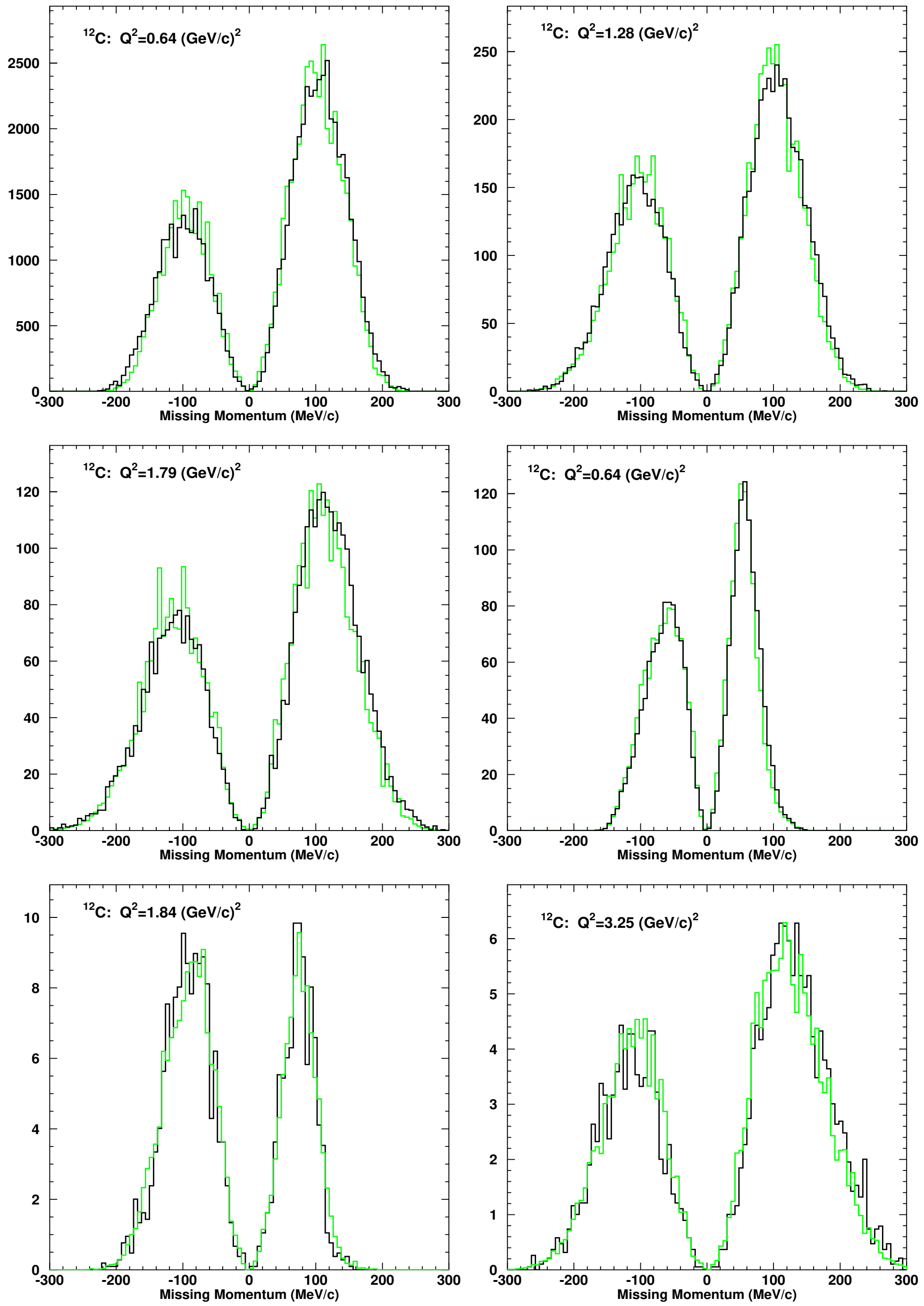

Figure 4.11. Carbon Missing Momentum Spectra. Data are black and simulation is grey. Kinematics are A-F, left to right, then down.

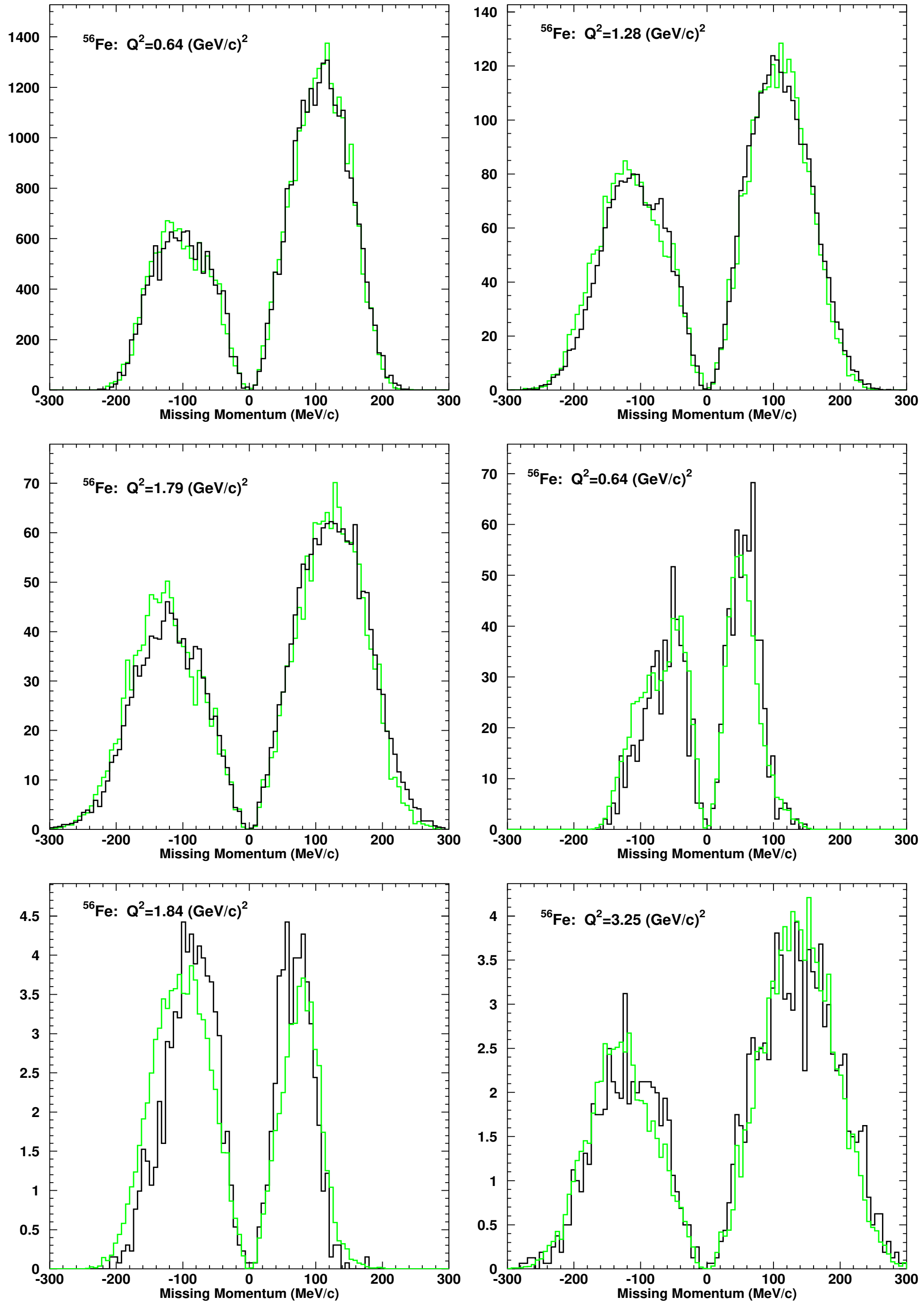

Figure 4.12. Iron Missing Momentum Spectra. Data are black and simulation is grey. Kinematics are A-F, left to right, then down.

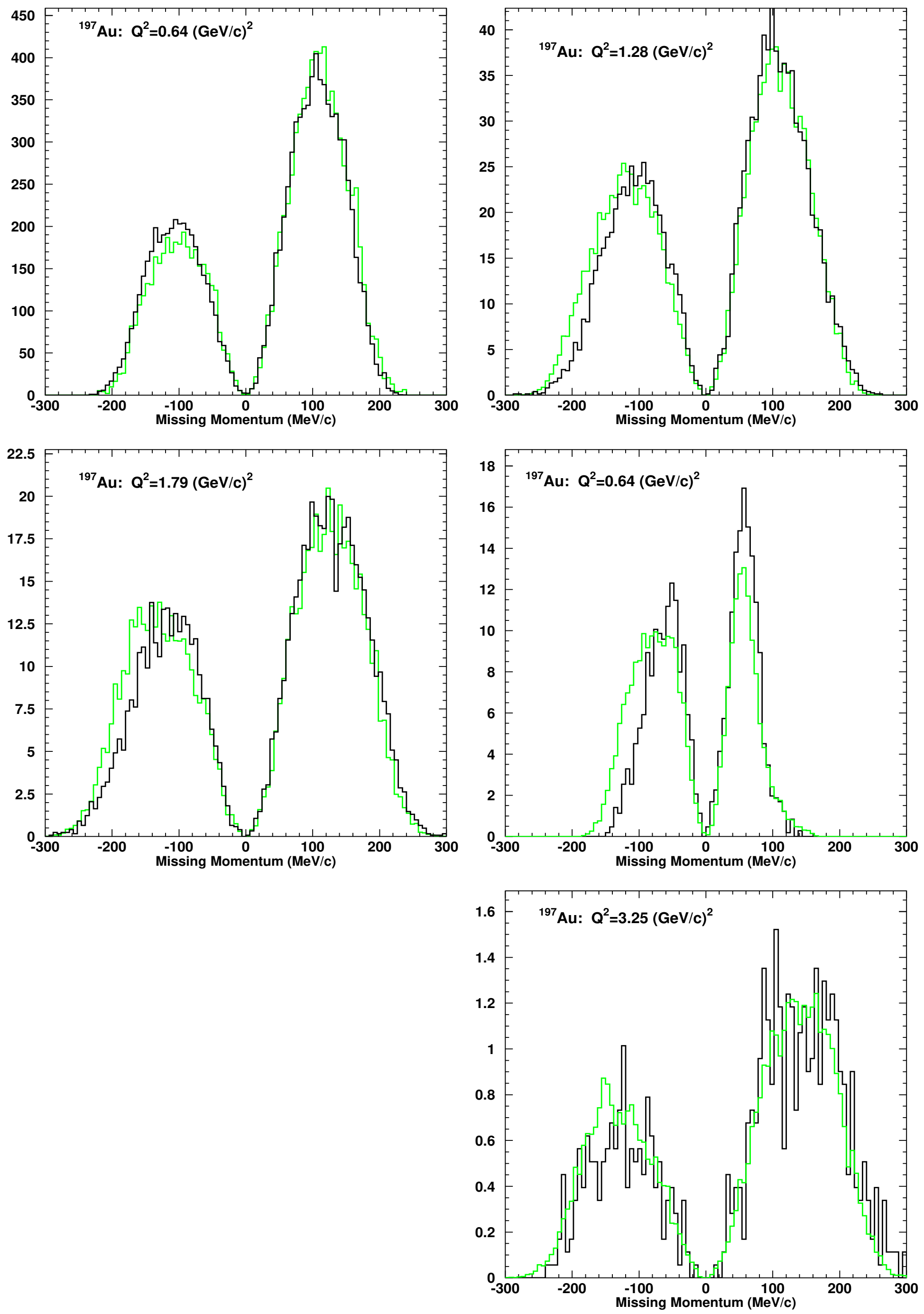

Figure 4.13. Gold Missing Momentum Spectra. Data are black and simulation is grey. Kinematics are A-F, left to right, then down. Note gold data were not taken for Kinematics E.

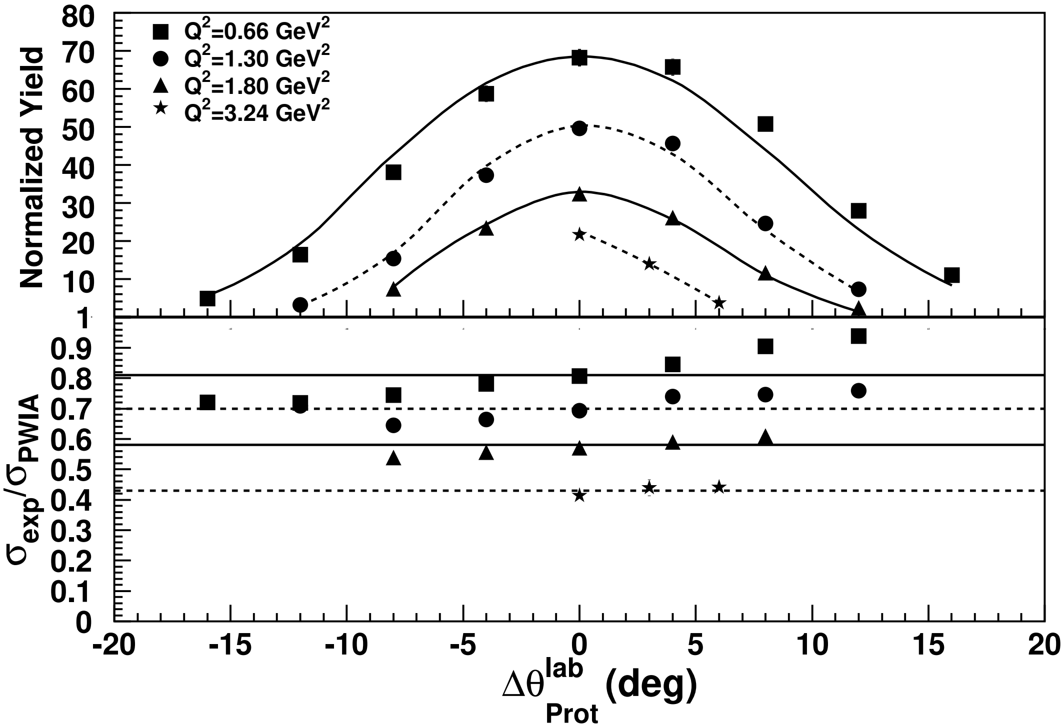

Figure 4.14. Carbon Transparency vs. Proton Angle. The upper panel displays coincidence yields as a function of proton angle for kinematics A-C, and F. For clarity, scale factors of 0.12, 0.8, 1.0, and 14.0 have been applied to each kinematics, respectively. The lower panel displays the transparency as a function of proton angle. Again for the sake of clarity, the data are offset by 0.2, 0.1, 0.0, and -0.15 for kinematics A-C and F, respectively. The lines in both cases are the simulation yields normalized to the measured value of the transparency (Table 4.3). In each case the statistical errors are smaller than the plotting symbols. The systematic and model uncertainties are omitted.

angle transparency value. In each of the lower panels of Figs. 4.14–4.16, for a given Q^2, there is a slight slope in the transparency as a function of proton angle. This left/right (of $\vec{q}$) asymmetry in the cross section is due to the LT interference term in the off-shell cross section. [35] The fact that the experimental cross section divided by the σ_{cc1} prescription of de Forest still shows a slope indicates that the magnitude of the term is underestimated in σ_{cc1}—especially at low Q^2. At these

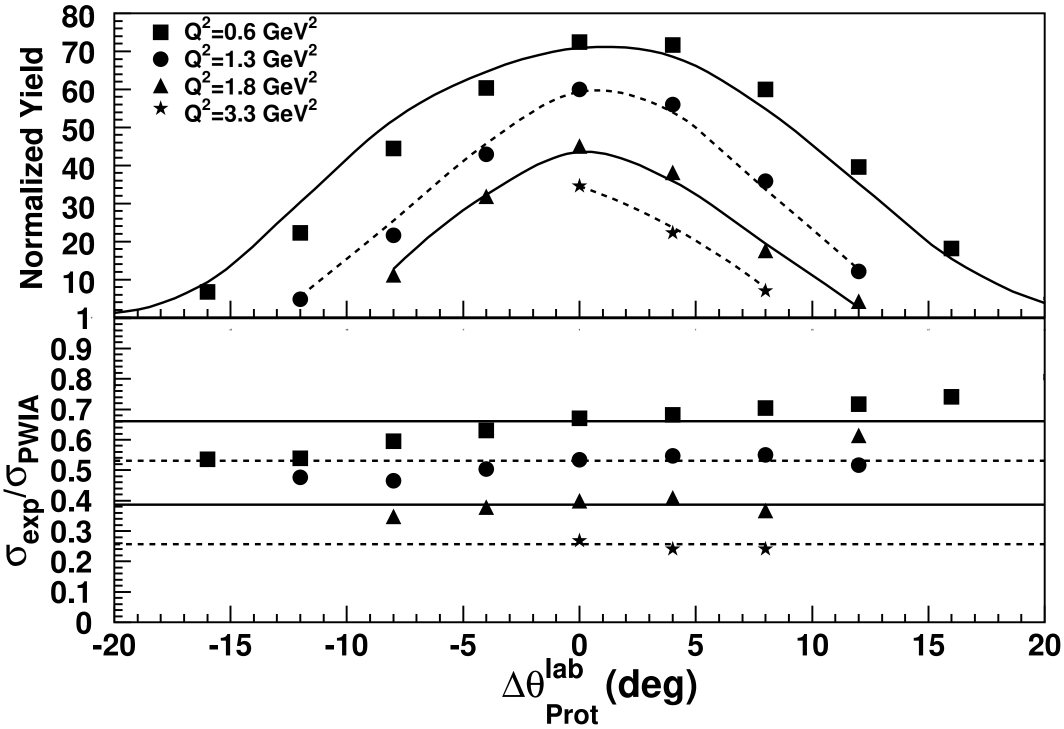

Figure 4.15. Iron Transparency vs. Proton Angle. The upper panel displays coincidence yields as a function of proton angle for kinematics A-C, and F. For clarity, scale factors of 0.21, 1.6, 2.25, and 35.0 have been applied to each kinematics, respectively. The lower panel displays the transparency as a function of proton angle. Again for the sake of clarity, the data are offset by 0.2, 0.1, 0.0, and -0.15 for kinematics A-C and F, respectively. The lines in both cases are the simulation yields normalized to the measured value of the transparency (Table 4.3). In each case the statistical errors are smaller than the plotting symbols. The systematic and model uncertainties are omitted.

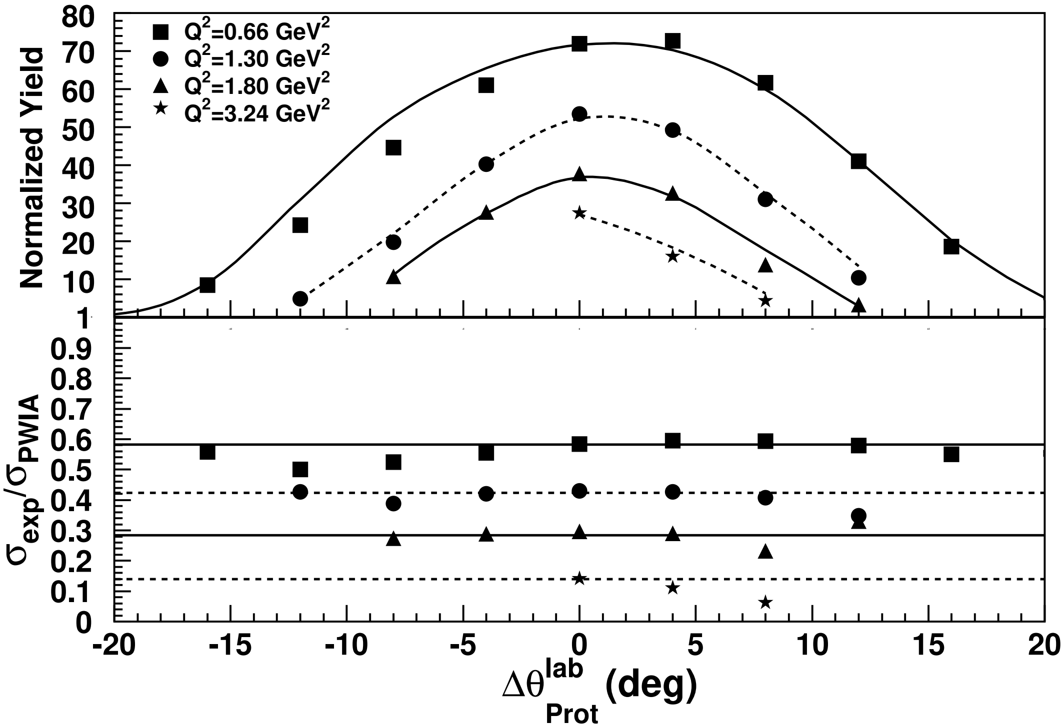

Figure 4.16. Gold Transparency vs. Proton Angle. The upper panel displays coincidence yields as a function of proton angle for kinematics A-C, and F. For clarity, scale factors of 0.55, 0.4, 5.5, and 80.0 have been applied to each kinematics, respectively. The lower panel displays the transparency as a function of proton angle. Again for the sake of clarity, the data are offset by 0.2, 0.1, 0.0, and -0.15 for kinematics A-C and F, respectively. The lines in both cases are the simulation yields normalized to the measured value of the transparency (Table 4.3). The systematic and model uncertainties are omitted.

momentum transfers, where the asymmetry is largest, data were taken on both sides of $\vec{q}$, allowing the average over the proton angle to be used for the transparency. At Kinematics F, where data were only collected on the larger-angle side of $\vec{q}$, the effect of the term is negligible. An analysis of this asymmetry is currently underway and is expected to allow the extraction of the LT term for all three targets at $Q^2 = 0.64$, 1.28, and 1.79 (GeV/c)^2.

As discussed in Section 3.10, the transparency for a given Q^2 is calculated by taking the charge-weighted average of the ratio of the experimental coincidence yield to the Monte Carlo yield over each proton angle setting. Table 4.3 lists the nuclear transparency for each target at each kinematics. The indicated uncertainties reflect the 1% statistical uncertainty, the 2.3% (2.5% for Kinematics F) systematic uncertainty (Section 4.3.2), and the model-dependent uncertainty (Section 4.3.3) added in quadrature. The transparency as a function of Q^2 and A is presented in Figures 4.17 and 4.18, respectively. Note that in most cases the statistical uncertainties are smaller than the plotting symbols. Figure 4.17 also includes the MIT-Bates data (^{12}C, ^{58}Ni, and ^{181}Ta targets at Q^2=0.34 (GeV/c)^2) and the NE-18 data (^{12}C, ^{56}Fe, and ^{197}Au targets at Q^2=1.0, 3.1, 5.0, and 6.8 (GeV/c)^2). The E91-013 data are in agreement with the NE-18 data, but have a much higher statistical precision. It is true however, that the E91-013 carbon transparencies, while within the NE-18 error bars, seem to be systematically slightly lower. It should also be mentioned that the model-dependent uncertainties listed for the E91-013 iron and gold results is slightly larger than that quoted in NE-18. As discussed in Section 4.3.3 and Appendix A, the uncertainty in the the normalization of the spectral functions of these targets is thought to be underestimated by $\sim 2\%$ in NE-18. Therefore, when looking at Fig. 4.17, it is important to remember that the E91-013 data are presented with these slightly larger uncertainties, whereas the NE-18 results are not.

Figure 4.17 also presents the transparencies for the Rosenbluth separation

Table 4.3. Nuclear Transparency. The error bars indicate the total uncertainty: systematic (2.3%), statistical (1%), and model dependencies (target-dependent) added in quadrature. The errors in parentheses include only the statistical and systematic uncertainties.

Kine.	Q^2 $(\mathrm{GeV/c})^2$	^{12}C T	^{56}Fe T	^{197}Au T
A	0.64	0.61 ± 0.03 (0.02)	0.47 ± 0.05 (0.01)	0.38 ± 0.04 (0.01)
B	1.28	0.60 ± 0.03 (0.02)	0.44 ± 0.05 (0.01)	0.32 ± 0.04 (0.01)
C	1.79	0.57 ± 0.03 (0.01)	0.40 ± 0.04 (0.01)	0.29 ± 0.03 (0.01)
D	0.64	0.64 ± 0.03 (0.02)	0.54 ± 0.06 (0.01)	0.43 ± 0.05 (0.01)
E	1.84	0.59 ± 0.03 (0.01)	0.44 ± 0.05 (0.01)	-
F	3.25	0.58 ± 0.03 (0.02)	0.42 ± 0.04 (0.01)	0.28 ± 0.03 (0.01)

kinematics (D and E) at Q^2=0.64 and 1.79 (GeV/c)^2. For all targets, at both momentum transfers, these L-T points (shown as triangles) have a slightly higher transparency. This is because these backward kinematics emphasize transverse scattering, particularly from meson exchange currents. As this effect is not included in the model, the transparency is slightly increased. More discussion of the model's reliability at the backwards kinematics can be found in Ref. 34.

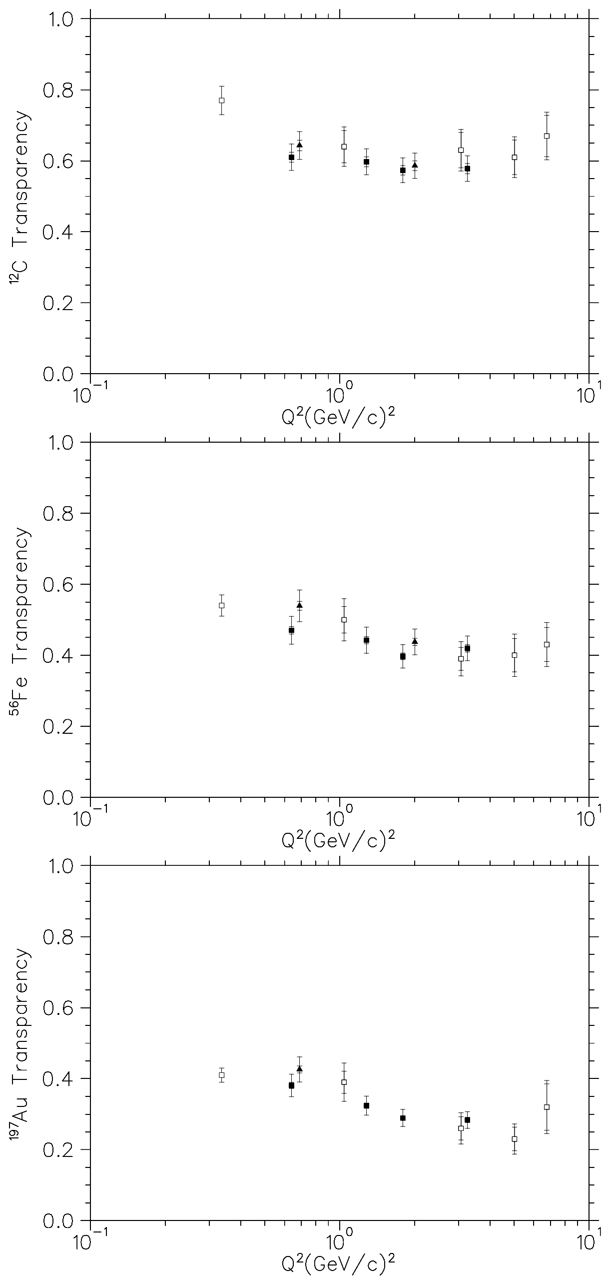

Figure 4.17. Transparency vs. Q^2. From top to bottom: ^{12}C, ^{56}Fe, and ^{197}Au. The filled symbols are E91-013 data, and the open symbols are data of Makins *et al.* (with the exception of the MIT-Bates data for ^{12}C, ^{58}Ni, and ^{181}Ta at Q^2=0.34 (GeV/c)^2). The outer error bars indicate the total uncertainty, and the inner reflect only the systematic (2.3%) and statistical (1%) added in quadrature. The Q^2 of both backwards, L-T-separation kinematics (D and E) are offset slightly for clarity (triangles). (Horizontal log scale.)

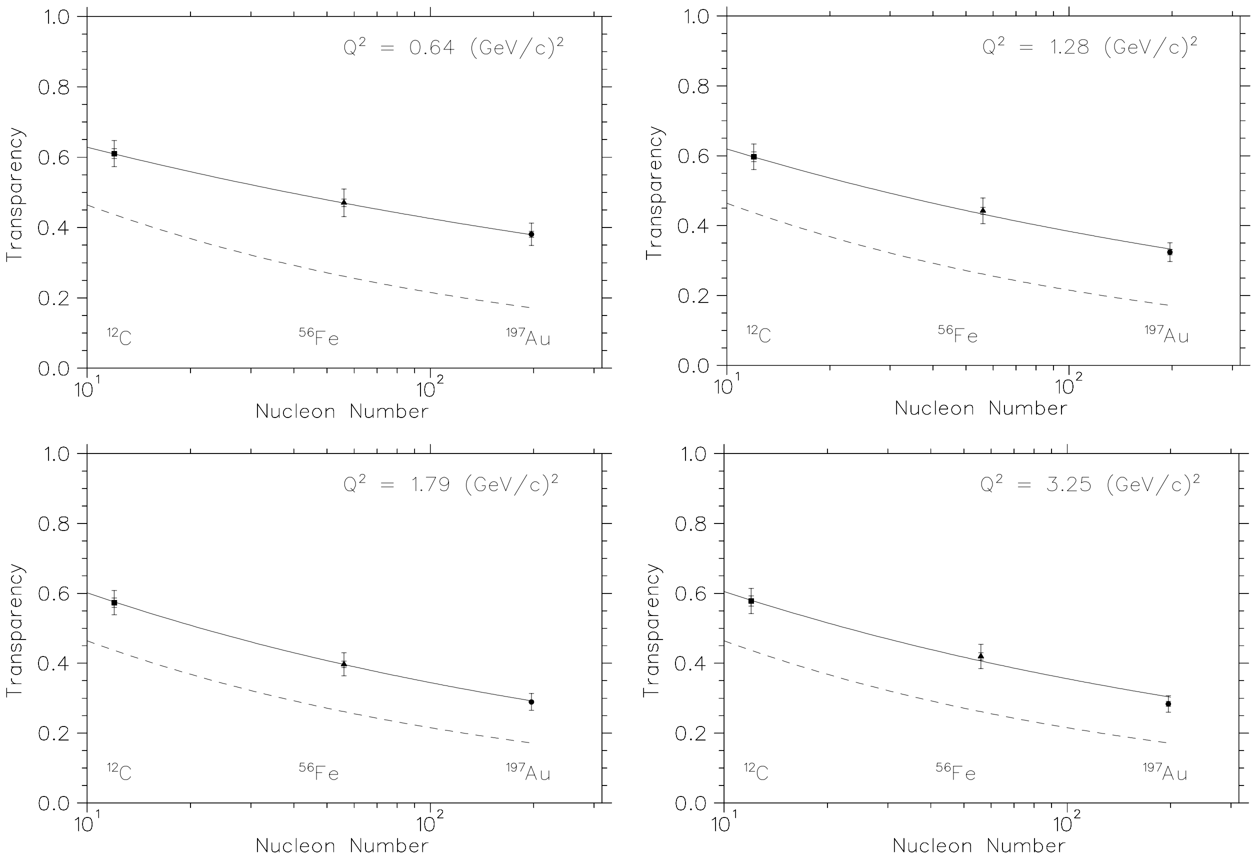

Figure 4.18. Transparency vs Nucleon Number. The kinematics are A–C, F from left to right, then down. Squares are ^{12}C, the triangles are ^{56}Fe, and the circles are ^{197}Au. The outer error bars indicate the total uncertainty, and the inner reflect only the systematic (2.2%) and statistical (1%) added in quadrature. The solid curves are fits to the form $T = T_0 A^{-\alpha}$ (Table 4.4) and the dashed curves follow the function $T = A^{-1/3}$. (Horizontal log scale.)

It is interesting to note that the flatness of T observed in all targets at large Q^2 could be used to place tight boundaries on the possible change of the in-medium proton form factors. (Note that the flatness of the transparency is not dependent on the model spectral functions or the correlation corrections.) Taking the ratio of the transparency at $Q^2 = 3.3$ (GeV/c)^2 to that at $Q^2 = 1.78$ (GeV/c)^2 and averaging over the three targets, one sees a rise of $2.5 \pm 2.4\%$. This is consistent with the measured free p-N cross section which falls by roughly 2% in this range. Therefore there seems to be at most a 2% change in the in-medium p-N cross section.

In order to study the behavior of the transparency for a given missing energy range, the transparency for various E_m bins is plotted in Fig. 4.19 as a function of Q^2 for each target. With the exception of the binning in E_m, the standard transparency extraction was performed. The behavior of the transparency for each E_m range is easily understood in the case of carbon. The region from 0–30 MeV in missing energy is known to be populated by the $1\mathrm{p}_{3/2}$ protons, which, because of their nonzero angular momentum, occupy most of the nuclear surface. Because the nuclear surface of carbon is relatively diffuse, there is decreased density, and hence an increased transparency for protons knocked out of these orbits. On the other hand, the $1\mathrm{s}_{1/2}$ protons feel no such angular momentum barrier and, on average, occupy the nuclear "interior." Thus, the protons with missing energies corresponding to the $1s$ state (30–50 MeV) see a decreased nuclear transparency. At higher missing energies ($>$ 50 MeV), the experimental yields include strength from effects that are not included in the model, such as two-nucleon emission and meson exchange currents. Because the single-particle strength in the simulation is exhausted, there is a net increase in the transparency. This simple picture becomes somewhat clouded for the larger targets, as nuclear shells start to overlap and the relative number of surface nucleons decreases. It is true though that the transparency is largest at high missing energies where the simulated single particle strength is falling.

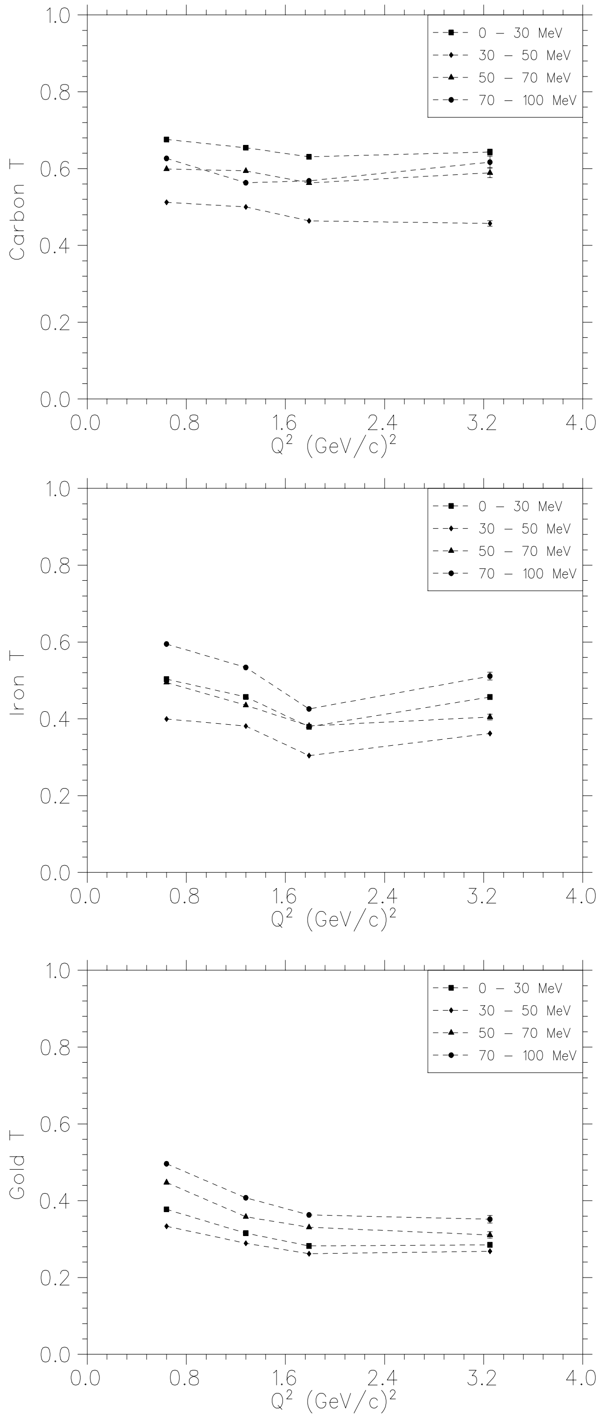

Figure 4.19. Transparency vs Q^2, Binned in E_m. From top to bottom are the transparencies for carbon, iron, and gold, binned in E_m from 0–30 (squares), 30–50 (diamonds), 50–70 (triangles), and 70–100 MeV (circles). The error bars are statistical only, and the lines are only meant to guide the eye.

The transparency as a function of missing energy does seem to have a different behavior for each target as a function of Q^2. It is important to reiterate that the Q^2 dependence is not expected to be sensitive to the model, but that the A dependence might be. The flatness of the carbon transparency with Q^2, exhibited earlier in Fig. 4.17, seems to persist for each missing energy range. The iron results, on the other hand, show a large Q^2 dependence. As is seen in Fig 4.9, the shapes of both the experimental and simulated missing energy spectra change as Q^2 changes (Note that only Kinematics A–C and F are plotted in Fig. 4.19). For example, in Fig. 4.9, the prominent peak in the model at ~ 40 MeV in Kinematics A is somewhat reduced at Kinematics C, and a similar, though somewhat smaller, change occurs for the experimental spectra. Because the simulated iron spectra exhibit such narrow peaks, the transparency as a function of E_m is more sensitive to the bin choices. Note though, that when the integral is taken over the complete missing energy range (Fig. 4.17), this sensitivity is reduced, and the transparency has less dependence on Q^2.

The A-dependence of the transparency is examined by fitting it, for a given Q^2, to the form $T = T_0 A^{-\alpha}$. Because the transparency is a measure of the interaction between the knocked-out proton and residual nucleus, it should scale as the length of the proton's exit path. This path should, in turn, scale as the radius of the nucleus, and therefore it might be expected that $T \propto A^{-1/3}$. The results of the fit are listed in Table 4.4. Note that the decrease in transparency as a function of A is actually better approximated by $A^{-0.2}$ than by $A^{-1/3}$. Indeed, as discussed in Section 4.4, most of the transparency calculations underestimate T for the iron and gold targets.

4.3.2 Systematic Uncertainties The systematic uncertainties in the transparency results of experiment E91-013 can be divided into two classes: those that affect the experimental yields and those that are due to model dependencies in the simulation (discussed in Section 4.3.3). A summary of all the uncertainties

Table 4.4. Nuclear Transparency vs. A. The T vs. A data of Fig. 4.18 are fit to the form $T = T_0 A^{-\alpha}$.

Kinematics	Q^2 (GeV/c)^2	T_0	α
A	0.64	0.927 ± 0.001	0.169 ± 0.0003
B	1.28	1.00 ± 0.04	0.208 ± 0.013
C	1.79	1.05 ± 0.01	0.242 ± 0.003
F	3.25	1.03 ± 0.08	0.231 ± 0.026

in the experimental data, including run stability and constraint sensitivity, will be presented here. Note that the uncertainties due to certain aspects of the analysis (tracking efficiency, charge measurement, and proton absorption, for example) have been discussed previously.

For a given kinematic setting (A–F in Table 2.1), the electron arm was held fixed while the proton arm was swept over the Fermi cone. Thus, after correcting for luminosity and detector inefficiencies, the electron singles yield (the sum of prescaled electron-only events and the coincidence events) should remain constant from run to run. However, drifting current monitor calibrations or changing detector efficiencies, for example, can cause the singles yield to vary. The extent to which the change in yields is larger than the amount expected from statistical fluctuations is a measure of the systematic uncertainty in the absolute normalization of the yields. Table 4.5 lists the percent variation in the singles yields—calculated from the standard deviation—for each kinematics. The run-to-run variations vary from $0.5 - 1\%$, consistent with the statistical uncertainty.

Run stability can also be measured by comparing the coincidence yields for duplicated runs. Table 4.6 lists the variation (calculated as in the case of the singles yields) in coincidence yields for each kinematics. Note that the average extends only over the central (or "conjugate angle") runs, as these settings had the most duplication. Again, the run-to-run stability of the coincidence yields is consistent

Table 4.5. Singles Yield Run Stability. Run stability presented as the percent variation in the average (weighted by charge) of the singles yields. The percent variation is the standard deviation in the yields divided by the average yield. Also listed is the average statistical uncertainty for a given target and kinematics. For Kinematics A-D, both Dec. 1995 and May 1996 data are used in the averages.

Kinematics	Target	% Standard Deviation	Average Stat. Uncertainty	Total # of Runs
A	C	0.88	0.59	16
B	C	1.19	1.49	13
C	C	0.78	0.98	17
D	C	1.48	0.73	16
E	C	2.49	2.33	13
F	C	3.06	1.38	9
A	Fe	0.97	0.62	14
B	Fe	1.03	1.05	11
C	Fe	1.23	1.22	18
D	Fe	2.13	0.91	14
E	Fe	2.36	1.87	14
F	Fe	1.16	1.19	11
A	Au	0.81	0.80	18
B	Au	1.70	1.05	12
C	Au	1.83	1.28	19
D	Au	2.59	0.96	10
F	Au	1.70	1.68	16

Table 4.6. Coincidence Yield Run Stability. Run stability presented as the % variation in the average (weighted by charge) of the coincidence yields for the conjugate angle setting at each kinematics. The percent variation is the standard deviation in the yields divided by the average yield. Also listed is the average statistical uncertainty for a given target and kinematics. For Kinematics A–D, both Dec. 1995 and May 1996 data are used in the averages.

Kinematics	Target	% Variation in Coin. Yield	Average Stat. Uncertainty	Total # of Runs
A	C	1.18	0.76	4
B	C	1.48	1.10	5
C	C	2.28	1.21	5
D	C	3.20	1.19	4
E	C	2.57	3.66	6
F	C	3.01	1.86	2
A	Fe	0.98	1.32	4
B	Fe	0.26	0.93	3
C	Fe	0.21	1.16	2
D	Fe	1.75	2.35	2
E	Fe	1.20	2.66	2
F	Fe	0.96	2.24	4
A	Au	1.30	1.04	4
B	Au	1.12	1.61	5
C	Au	2.06	1.76	4
D	Au	2.28	2.23	5
F	Au	5.29	4.79	8

Table 4.7. Constraint Stability Tests. The standard constraints of Table 3.12 are adjusted as follows to test the dependence of the results.

Label	Item	Values
em100	Missing Energy (MeV)	0 to 100
em120	Missing Energy (MeV)	0 to 120
pm200	Missing Momentum (MeV/c)	-200 to 200
pm200	Missing Momentum (MeV/c)	-250 to 250
pm320	Missing Momentum (MeV/c)	-320 to 320
hsdelta6	HMS δ (%)	-6 to 6
hsdelta10	HMS δ (%)	-10 to 10
ssdelta8to18	SOS δ (% (p in SOS)	-8 to 18
ssdelta12to12	SOS δ (%) (e^- in SOS)	-12 to 12
hsyptar35	HMS Y'_{tar} (rad)	-0.035 to 0.035
ssyptar55	SOS Y'_{tar} (rad)	-0.055 to 0.055
coin8	Backgrd. Sample Width (ns)	8

with the statistical fluctuations at the 1% level. The results are used to assign an uncertainty of 1% to the experimental yields due to run-to-run instabilities.

The standard constraints used in experiment E91-013 are listed in Table 3.12. By varying each constraint slightly, the sensitivity of the results to each constraint can be quantified. Table 4.7 lists the different constraint tests. Tables B.1-B.6 in Appendix B list the discrepancy (nominal/modified) between the nominal transparency value and the value with the modified constraint. The discrepancy for each target is averaged (weighted by the luminosity) over each run at each kinematic setting for all proton angle settings. The results, listed in Table 4.8, are used to assign a constraint-dependence uncertainty of 1% to the experimental yields.

Table 4.8: Constraint Stability Results

Target	Average Discrepancy
C	0.997 ± 0.008
Fe	0.995 ± 0.010
Au	0.994 ± 0.011

Table 4.9: Systematic Uncertainties in the Data.

Item	% Uncertainty in Data Yield
Current Measurement	1
Solid Target Thickness or Cryo. Target Thickness	0.1 0.5
HMS Tracking Eff. SOS Tracking Eff.	1 1
Proton Absorption Kine. A–E Kine. F	 0.5 1
Background Subtraction	0.1
Constraint Stability	1
Run Stability	1
Sum in Quadrature Kine. A–E Kine. F	 2.3 2.5

Because the transparency is the ratio of two missing energy spectra (integrated 0–80 MeV), it is sensitive to slight offsets in one spectrum relative to the other. In E91-013, slight offsets do occur due to things like target position and spectrometer alignment. As discussed in Section 3.10, the experimental angular distributions and missing energy spectra are all offset slightly so as to agree with the simulation before the constraints are applied. Figure 4.20 shows the average shift in each of these five quantities plotted as a function of kinematics. In all cases, the shifts are very small resulting in negligible changes in yield (the largest being less than 1.5%).

Table 4.9 summarizes the systematic uncertainties that affect the experimental yields. (The uncertainties in the Monte Carlo are discussed in Section 4.3.3.) The sum, in quadrature, of the above effects results in a systematic uncertainty on the experimental yields of 2.3% (2.5% for Kinematics F).

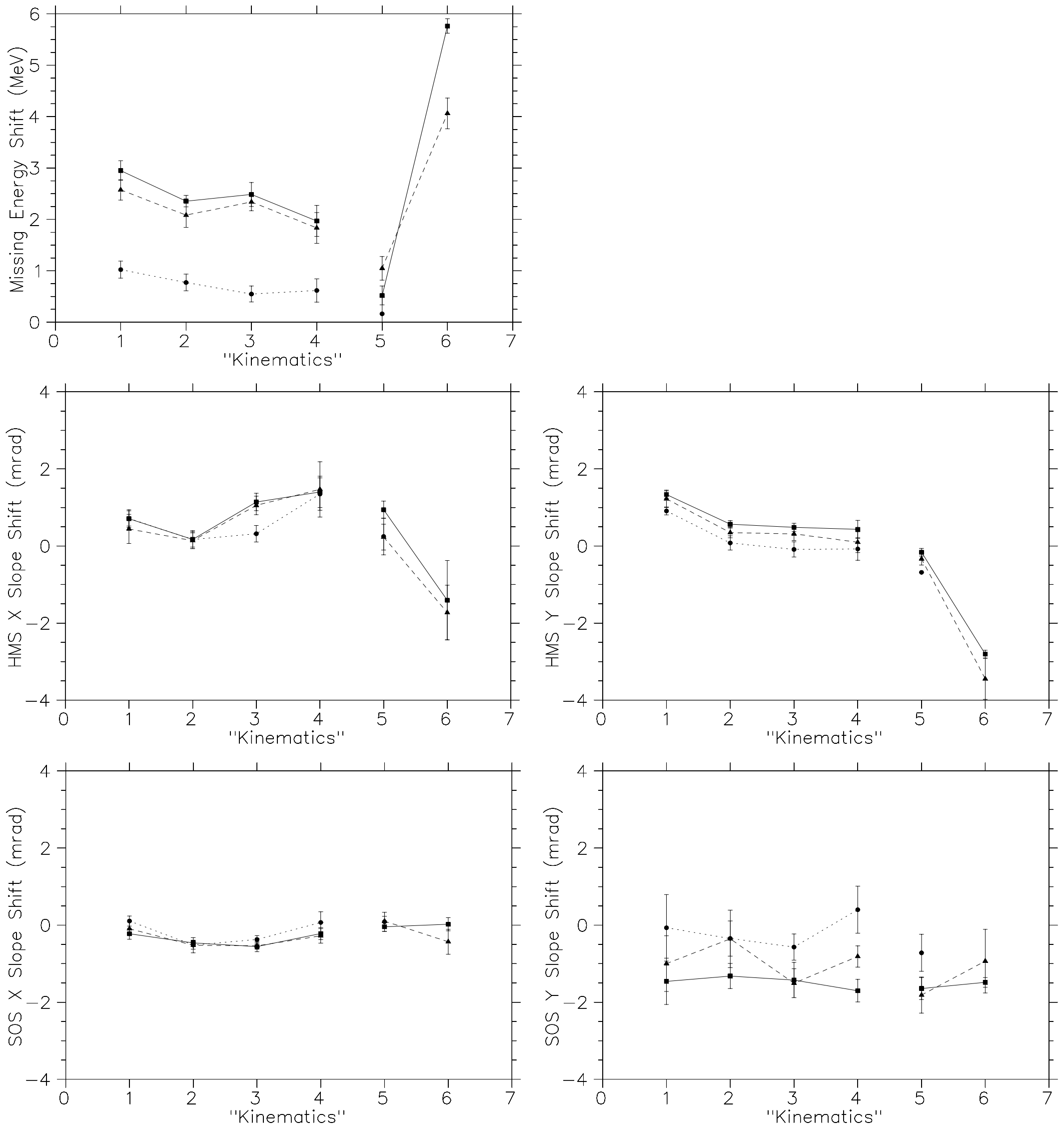

Figure 4.20. Shifts in Selected Spectra. The shifts in the data necessary to obtain agreement with the simulation are shown for the missing energy, HMS x'_{tar}, HMS y'_{tar}, SOS x'_{tar}, and SOS x'_{tar} spectra, respectively (left to right, then down), as a function of kinematics. The "forward" kinematics, A, B, C, and F are labeled 1–4, respectively, and plotted together. The "backwards" (L-T) kinematics, D and E, are labeled 5 and 6 (no gold data were taken at Kinematics E), respectively. Squares are carbon, triangles are iron, and circles are gold.

4.3.3 Model Dependence Because the transparency is defined to be the ratio of the experimental yield to that of a simulation, it is heavily model-dependent. Examples of these dependencies include the off-shell e-p cross section, radiative effects, IPSM spectral functions, and correlation corrections. In order to facilitate a direct comparison between both sets of results, all aspects of the simulation used in experiment E91-013 have been kept as close as possible to those of experiment NE-18.

As discussed in Section 3.9.2, the σ_{cc1} off-shell e-p cross section prescription of de Forest is used for the final results. Substituting σ_{cc2} for σ_{cc1} in the simulation results in 1.5% lower cross sections, independent of target and kinematics. This is used to quote a systematic uncertainty of 1.5%. Pollock *et al.* calculate off-shell cross sections using six different prescriptions (including σ_{cc1} and σ_{cc2}) for kinematics similar to those of E91-013. [7] They find that in general, the discrepancy between results grows as a function of γ, the angle between the detected proton and $\vec{q}$. When averaged over γ—weighted by the experimental yields (i.e. the majority of the experimental data come from small γ. See Figs. 4.14–4.16)—the discrepancy between the off-shell prescriptions is approximately $\pm 3\%$. Because the majority of (e,e$'$p) analyses employ σ_{cc1}, it is used here (with a 1.5% systematic error) in order to facilitate comparison. It is important to remember, however, that when comparing results from different experiments, one must either use the same off-shell prescription, or understand the systematic differences between them.

The estimation of the uncertainties in the radiative correction procedure is described in detail by Makins [58]. Because the region of large missing energy in hydrogen data is completely dominated by radiative effects, it is an ideal environment for testing the agreement between experiment and simulation. The uncertainty in the radiative correction procedure is taken as the variation in the ratio of experimental to simulated yields after changing the upper limit in the missing energy integration range. This provides an estimation of the uncertainty in the internal radiation correction procedure as the (e,e′p) reaction in thin liquid targets is dominated by internal radiation. As in the case of experiment NE-18, this test was performed for hydrogen data with upper limits in missing energy of 50, 80, 100, and 130 MeV. The variation in the agreement of experiment and Monte Carlo for all kinematics was on the order of 1.5%. Makins *et al.* estimated a 2% uncertainty in the external radiation experimentally by noting the variation in yields when changing the radiation thickness of carbon and iron. These results are used to assign an uncertainty of 2.5% on the radiative corrections to the simulated yield.

The dependence of the results on the model spectral functions can be divided into two contributions: the locations and widths of the shell energies, and the widths of the momentum distributions. First, the sensitivity of the transparency to the missing energy constraints is used to assign a model-dependent uncertainty of 2% to the shell energy distributions for all three targets. While it may be argued that the stability of the transparency with respect to the missing energy constraint has already been included in the experimental systematic uncertainties, the value of 2% is taken in order to be conservative. Second, the transparency depends heavily on the widths of the model momentum distributions. These widths are directly related to the normalization of the spectral function as the momentum density is weighted by p_m^2:

$$\int_0^\infty p_m^2 dp_m \rho(p_m) = \frac{1}{4\pi}. \tag{4.2}$$

That is, if one compares two normalized distributions with different widths, the wider distribution will have less strength at a given p_m. Therefore, to test the normalization of the the model spectral functions, the rms charge radius of each nucleus was calculated, and the results, along with experimental results tabulated by de Vries *et al.*, are listed in Table 4.10. Note that the radii of both the carbon

Table 4.10. RMS Charge Radii of the Model Momentum Distributions. The experimental results are from de Vries *et al.* [78].

Target	Model RMS Radius (fm)	Exp. Measured RMS Radius (fm)
^{12}C	2.64	2.47 ± 0.01
^{56}Fe	3.83	3.75 ± 0.03
^{197}Au	5.30	5.32 ± 0.04

and iron models are significantly larger than the experimental values indicating that the model momentum distributions are somewhat narrow. However, as discussed in Appendix A (in the context of the iron model spectral function), if the momentum distributions are too narrow (wide), the transparency as a function of proton angle will exhibit an unphysical, upward (downward) curvature. A slope is certainly allowed, given the LT-term asymmetry discussed in Section 4.3.1, but a curve is unphysical. Using the case of a distribution that is too wide as an example, this curvature is seen to occur as follows: the strength at high missing momentum is emphasized at large proton angles. At these large angles, because the simulated strength (denominator) is too large, the transparency is artificially low, resulting in a downward curve. Therefore, because no such curvature is observed in the transparency of carbon and iron (Figs. 4.14 and 4.15), it is concluded that the wide radii of the models are necessary to both fit the experimental momentum distributions and still provide a physically acceptable LT-term asymmetry. The sensitivity of this method—using the linearity of the transparency versus proton angle to constrain the model momentum distributions—is estimated to correspond to a 4% uncertainty on the transparency (See Appendix A). This, combined in quadrature with the 2% uncertainty on the energy distributions, results in a 4.5% model-dependent uncertainty for each target. Note that this value is in agreement with the $< 5\%$ discrepancies observed by Dutta [34] when comparing the transparency calculated using experimentally extracted spectral function values with the transparencies quote here.

Two additional test were performed to further study the model-dependence of the transparency on the carbon spectral function. First, the locations in missing energy of the $1s_{1/2}$ and $1p_{3/2}$ peaks in the nominal NE-18, model were adjusted by $\sim$5 MeV, and the resulting change in yield was $< 0.7\%$. A second, independent, spectral function, based on a DWIA calculation by Zhalov [76] was also used to generate simulated ^{12}C(e,e$'$p) yields. This spectral function provided the shell binding energies and momentum distributions, but not the shell energy widths. Using the NE-18 values for these widths, the yields for kinematics A, B, and C (the kinematics applicable for Zhalov's spectral function) agreed with the nominal values at the 1–2% level for conjugate proton angles. Note that these results are well within the 4.5% uncertainty quoted above.

Although the integrated strength from 0–80 MeV in missing energy is believed to be insensitive (at the few percent level) to the shape of the model spectral function, an attempt was made to derive an alternative ^{56}Fe model in order to improve the agreement with the experimental spectra (Fig. 4.9). The calculation, discussed in detail in Appendix A, is based on a Hartree calculation by Horowitz [77]. The code, "TIMORA," provides the shell binding energies and momentum distributions but not the shell widths. Therefore, a "best fit" approach was taken in which the widths were adjusted in an *ad hoc* fashion so as to provide the best agreement in the missing energy spectra shapes. The widths are in general much wider than those employed in the NE-18 model and result in approximately 10% of the spectral function strength being shifted beyond the maximum missing energy of 80 MeV. In addition, the TIMORA momentum distributions are slightly wider than those used in NE-18, resulting in a further 10% reduction in simulated strength. While the agreement between the TIMORA-based and experimentally measured E_m spectra seems reasonable, the transparency calculated with the TIMORA-based spectral function exhibits an unphysical curvature when plotted versus proton angle. As was

Table 4.11. Correlation Correction Factors of Benhar. Listed is the fraction of integrated strength for $|p_m| < 300$ MeV/c for various E_m ranges.

Target	$0 < E_m < \infty$	$0 < E_m < 80$ MeV
^{4}He	1.12	1.12
^{16}O	1.11	—
Nuclear Matter	1.12	1.25

mentioned earlier, this curvature indicates that the momentum distributions are actually too wide, and therefore the nominal NE-18 spectral function was employed in the analysis of E91-013.

The uncertainties of the correlation correction factors were estimated by comparing the values used in both E91-013 and NE-18 with independent calculations performed by Benhar. [79] The correlation correction factors for his ^{4}He, ^{16}O, and nuclear matter correlated spectral function calculations are listed in Table 4.11, assuming a maximum missing momentum of 300 MeV/c. (Recall that the simulation is divided by F_{correl} to correct for correlations.) Note that when integrated over all missing energy, the corrections depend only weakly on the target mass. That a constant fraction of nucleons should be shifted to high missing momentum is consistent with the idea that the effect is due to the repulsive core of the nucleon-nucleon interaction; an effect that is largely independent of the target size. It is only when the maximum missing energy cutoff of 80 MeV is imposed that the corrections attain an A dependence. Extrapolating Benhar's ^{4}He result to ^{12}C, one obtains a factor of approximately 1.13. This 2% discrepancy with the NE-18 value is taken as the uncertainty for the ^{12}C correlation correction factor. By calculating the discrepancy between Benhar's nuclear matter value and the NE-18 value for gold (from Ref.74), the uncertainty on both the iron and gold factors is estimated to be 6%. Note that this may actually overestimate the ^{56}Fe uncertainty but that these values are in good agreement with the uncertainties quoted by Makins *et al.*: 3%, 6%, and 6% for ^{12}C,

Table 4.12. Effect of Coulomb Shift on Transparency. The change in missing energy counts (0–80 MeV), $\frac{\Delta N}{N}$, between simulation with coulomb corrected $\vec{p}_m$ and non-Coulomb corrected $\vec{p}_m$ for Kinematics A. ($-300 < \vec{p}_m < 300$ MeV/c).

Proton Angle from $\vec{q}$ (deg)	^{12}C	^{56}Fe	^{197}Au
0	0.000	0.000	0.000
16	0.007	0.005	0.003
-16	0.006	0.002	0.001

^{56}Fe, and ^{197}Au, respectively.

Finally, a slight oversight in the analysis concerns the Coulomb corrections in the simulation. As discussed in Section 3.9.6, the Monte Carlo reports the shifted $\vec{p}_m$ in its output. The analysis of the experimental data however, does not take into account the Coulomb effects on the missing momentum (the nominal beam energy and measured momentum are used for the incoming and scattered momenta, respectively). Thus, when placing the missing momentum constraint on both data sets, and then comparing them in the transparency ratio, one is actually comparing two spectra offset from each other by a few MeV/c (see Table 3.10). By running the Monte Carlo normally, and again with $\vec{p}_m$ shifted by $\Delta\vec{q}$, the error introduced by this oversight can be quantified. The change the yield (missing energy from 0–80 MeV) for Kinematics A is given in Table 4.12. The error introduced is seen to be negligible: $\leq 0.5\%$.

The above uncertainties are assumed to be mutually independent, and are thus added in quadrature to get a total systematic uncertainty for the model-dependence of the results (Table 4.13): 2.5%, 5.7%, 8.0%, 8.0% for ^{1}H, ^{12}C, ^{56}Fe, and ^{197}Au, respectively. Because the model-dependent uncertainties are different for each target, they must be taken into account when studying the A-dependence of the results (Fig. 4.18), or when comparing with experiments and calculations that use different models. However, to the extent that the model-dependent uncertainties

Table 4.13: Model-Dependent Uncertainties.

Item	% Uncertainty in Simulated Yield
σ_{ep}	1.5
Model Spectral Function:	
^{12}C	4.5
^{56}Fe	4.5
^{197}Au	4.5
Correlation Correction:	
^{12}C	2
^{56}Fe	6
^{197}Au	6
Internal Radiation	1.5
External Radiation	2
Total Sum in Quadrature:	
^{1}H	2.5
^{12}C	5.7
^{56}Fe	8.0
^{197}Au	8.0

are independent of Q^2, the shape of the T vs. Q^2curve (Fig. 4.17) for a given target is assumed to be known to within the statistical error bars. For example, predictions based on other models may have higher overall transparency for carbon, but the shape of the dependence on Q^2 should be similar to that measured in E91-013.

4.4 Nuclear Transparency Calculations and Discussion

There are several theoretical frameworks in which to calculate nuclear transparency. The two most common are the distorted wave impulse (DWIA) and Glauber approximations introduced in Sections 1.4.3 and 1.4.4, respectively. Traditionally, the DWIA has been employed at low Q^2 (≤ 2 (GeV/c)^2) and the Glauber approximation at higher Q^2. Issues concerning the range of validity of both sets of calculations is discussed below. Other models used in the calculation of transparency include Intranuclear Cascade models (INC). Examples of each type of calculation are presented below for the targets and kinematics employed in experiments NE-18 and

E91-013.

As described above, the DWIA models the final state interactions of the proton with the residual nucleus via a complex, optical model potential. Figure 4.21 shows the results of one such calculation: the "effective empirical interaction" (EEI) calculation of Kelly. [80] The parameters for the optical model potential are based on the folding of the nuclear density with a density-dependent p-N interaction (here, N means either proton or neutron). This effective interaction is taken from inelastic proton-nucleus scattering data in the energy range $100 \leq T_p \leq 650$ MeV. The real part of the central term in the resulting potential stems from the short-range repulsive force (correlations) between nucleons, and a sizeable damping of the imaginary part is due to Pauli blocking. This is consistent with the conclusion of Ireland *et al.* that the DWIA picture effectively includes medium modifications of the p-N interaction. [16] As is evident in Fig. 4.21, the EEI calculation describes the carbon data quite well, but then progressively underestimates the transparency as a function of target size. Kelly ascribes the small kinks in each curve at $Q^2 \approx 0.5$ (GeV/c)^2 to variations in the independent data sets to which the EEI is fit; no smooth energy dependence was imposed. Therefore, the size of the kinks ($\sim \pm 5\%$) can be taken as a measure of the systematic uncertainty in the calculations. Kelly claims that the increasing discrepancy between the calculations and the data with increasing target size may stem from the fact that the EEI does not take multi-nucleon absorption of the virtual photon into account. These additional channels "artificially" (with respect to the single nucleon knockout picture) enhance the experimental (e,e$'$p) cross section causing a net increase in the transparency. Note that the L–T separation performed in E91-013 [34] can be used to check this.

The second major theoretical framework in which to calculate nuclear transparency is the Glauber approximation. Here, the recoiling proton is assumed to travel in a straight line on its path through the residual nucleus. As discussed in

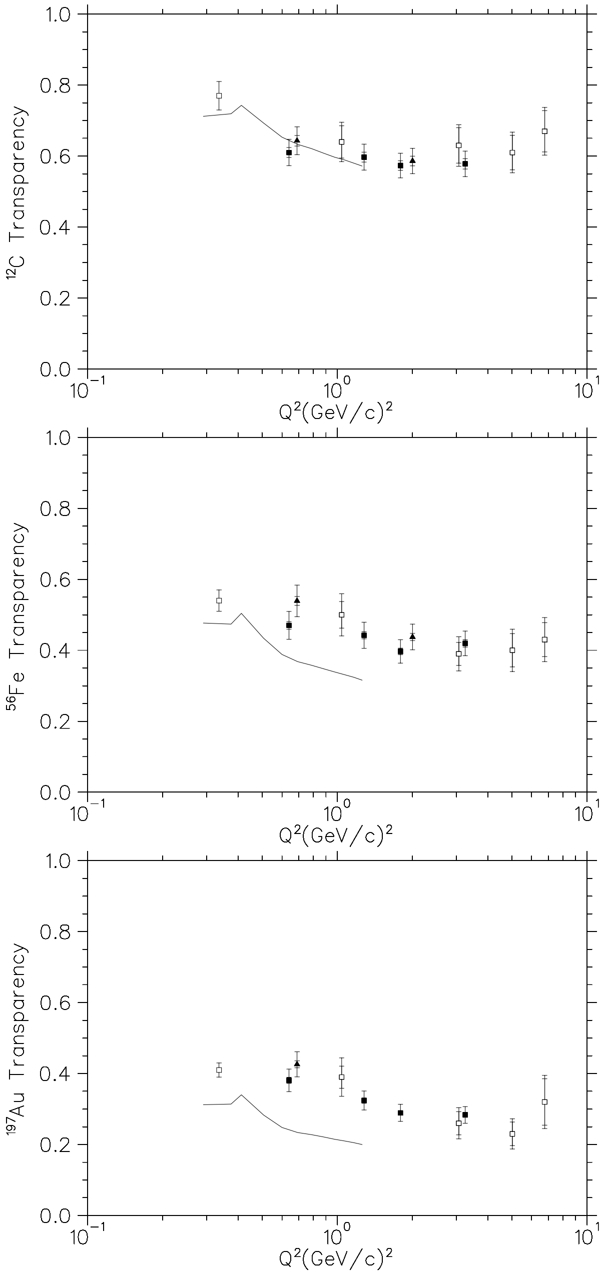

Figure 4.21. Transparency vs. Q^2. From top to bottom: ^{12}C, ^{56}Fe, and ^{197}Au. The curves are the EEI calculations of Kelly. [80] The data are the same as in Fig. 4.17. (Horizontal log scale.)

Section 1.4.4, the nuclear transparency is the probability that no nucleons are in the proton's exit path integrated over all possible paths, and Pauli blocking is included by modifying the p-p and p-n cross sections.

Figure 4.22 shows the results of a Glauber approximation calculation of the transparency performed by Gao *et al.* [14] This calculation explicitly includes p–N correlation effects in the residual nucleus by replacing the probability function $P(\vec{r},\vec{p}')$ in Eqn. 1.23 with a correlated version (Note that correlations between the spectator nucleons are neglected):

$$P_C(\vec{r},\vec{p}\,') = \exp\left[-\int_0^{\infty} ds\, g(s)\rho(\vec{r}+\hat{p}'s)\sigma\right]. \tag{4.3}$$

Here, g is the pair correlation function defined by

$$g_{pa}(\vec{r}\,',\vec{r}\,'') \equiv \frac{\rho_{pa}(\vec{r}\,',\vec{r}\,'')}{\rho_p(\vec{r}\,')\rho_a(\vec{r}\,'')}, \tag{4.4}$$

where $\rho_{pa}(\vec{r}\,',\vec{r}\,'')$ is joint probability of finding a proton at $\vec{r}\,'$ and a nucleon ($a = p$ for protons and n for neutrons) at $\vec{r}\,''$. [81] Note that $[\rho(\vec{r}\,')\rho(\vec{r}\,'') - \rho(\vec{r}\,',\vec{r}\,'')]$ (often referred to as the "correlation hole") is positive, and thus g has the net effect of increasing the transparency. The transparency is then calculated via

$$T = \frac{1}{Z}\int d^3r\, \rho_p(\vec{r})P_C(\vec{r}). \tag{4.5}$$

Note that in the calculation of the cross section, the motion of the spectator nucleons is neglected. Again, the calculation agrees fairly well with experiment for ^{12}C, but underestimates the transparency as the target size grows. As it follows the p-N cross section below $Q^2 \approx 1$ (GeV/c)^2, the calculation also seems to predict a stronger Q^2 dependence than is seen in the data.

The results of a second Glauber approximation calculation, by Nikolaev *et al.*, are shown in Fig. 4.23. Although the Glauber approximation is applied, the calculation is otherwise quite different from that of Gao *et al.* In this case a simple Fermi parameterization is used for the nuclear density, the inelastic p–N cross

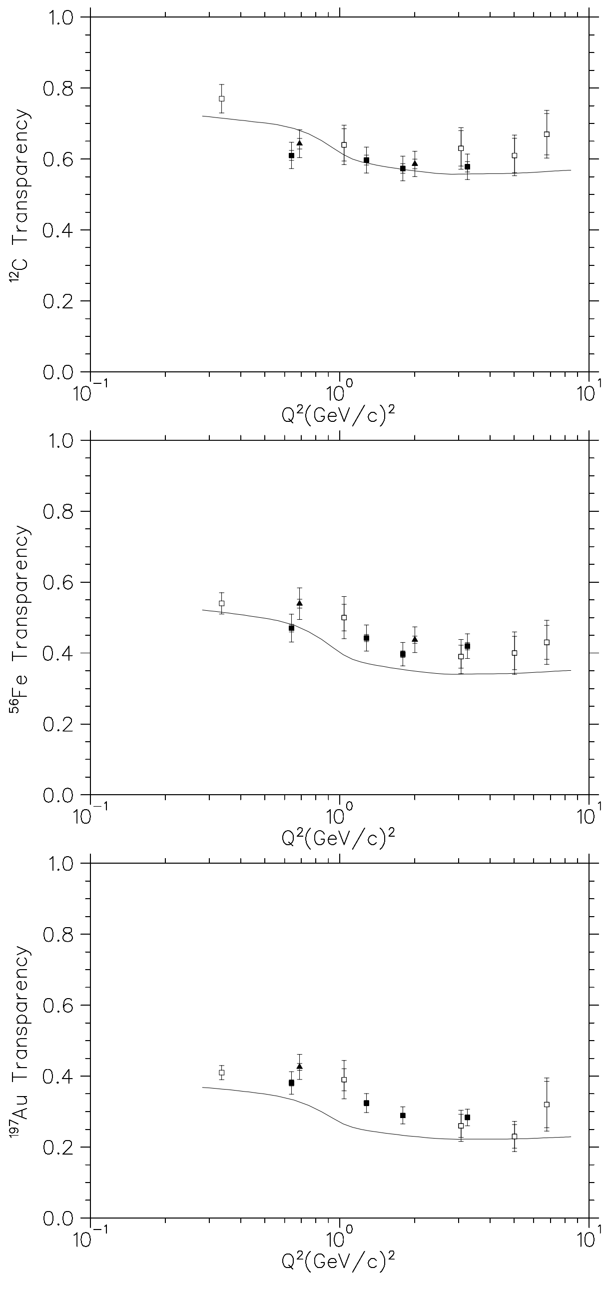

Figure 4.22. Transparency vs. Q^2. From top to bottom: ^{12}C, ^{56}Fe, and ^{197}Au. The curves are the Glauber approximation calculations of Gao *et al.* [14] The data are the same as in Fig. 4.17. (Horizontal log scale.)

section is used, and no correlation effects are included. Even without the inclusion of correlation effects, the calculation actually overestimates the carbon transparency and does reasonably well for the other targets. Note that the calculation includes the NE-18 kinematic constraints ($|\vec{p}_{m\perp}| < 250$ MeV/c) which are similar to, although slightly tighter than, E91-013. Nikolaev *et al.* neglect correlation effects because they claim the "hole effect" (the reduced density around the proton due to repulsive nature of the p-N interaction at short distances) is largely offset by the "spectator effect". In an uncorrelated picture, two (or more) spectator nucleons in the residual nucleus can occupy the same volume. This "shadowing" of nucleons causes a net decrease in the interaction probability with the energetic proton. However, when correlations between the spectators are included, and they can no longer shadow each other, the chance for an interaction with the proton is increased. According to Nikolaev *et al.*, the hole-correlation and spectator-correlation effects roughly cancel. [82]

In general, both the DWIA and Glauber calculations seem to do reasonably well at predicting the carbon transparency, but as the target size increases, both sets of calculations progressively underestimate the nuclear transparency at all momentum transfers. The calculations basically follow a $T \propto A^{-1/3}$ behavior, whereas the data can be approximated by $T \propto A^{-0.2}$ (see Table 4.4). Both Glauber calculations also seem to show more Q^2 dependence than is seen in the data. This is especially true of carbon, where the transparency as a function of Q^2 is remarkably flat.

The Q^2 range covered in experiment E91-013 straddles both the low-Q^2 region, traditionally described by DWIA calculations, and the high-Q^2 region, where the Glauber approximation is usually employed. In fact, both Kelly [80] and Nikolaev *et al.* [84] state that $Q^2 \approx 2$ (GeV/c)^2 is the maximum value for the validity of the DWIA and the minimum for the Glauber approximation. Nikolaev *et al.* make the claim that the optical model cannot describe short-range (high momentum) interactions effectively, and the Glauber approximation—under which the deflections

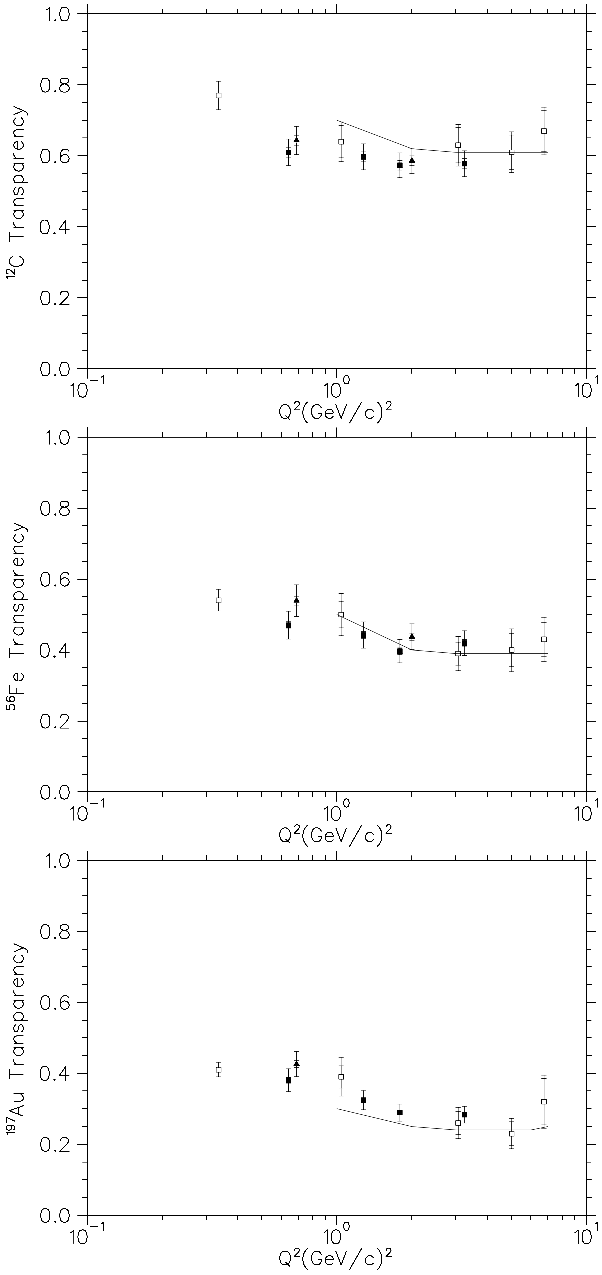

Figure 4.23. Transparency vs. Q^2. From top to bottom: ^{12}C, ^{56}Fe, and ^{197}Au. The curves are the Glauber approximation calculations of Nikolaev *et al.* [83] The data are the same as in Fig. 4.17. (Horizontal log scale.)

Table 4.14: Proton–Nucleon Cross Sections. (Laboratory proton momentum.

Kinematics	Proton Momentum (MeV/c)	$\sigma_{pp,\mathrm{tot}}$ (mb)	$\sigma_{pp,\mathrm{elas}}$ (mb)	$\sigma_{pn,\mathrm{tot}}$ (mb)	$\sigma_{pn,\mathrm{elas}}$ (mb)
A	840	23.8 ± 1	23.2 ± 0.5	32.5 ± 4	—
B	1275	39.8 ± 0.6	25.1 ± 0.8	38.6 ± 0.2	~ 32
C	1550	47.9 ± 0.1	24.1 ± 0.5	39.2 ± 3.0	~ 27
F	2550	45.1 ± 0.8	19.5 ± 0.7	42.9 ± 0.1	~ 19

of the recoiling proton are neglected—breaks down at low momentum. Kelly, on the other hand, attributes the failure of the Glauber approximation at low Q^2 to the following: Derivation of the Glauber transparency, Eqn. 1.22, requires a summation over all final states that contain A–1 nucleons. Thus p-N elastic scattering, which dominates the FSI at low Q^2, is actually not considered absorption. This is true even if the missing energy is much larger than that accepted by experiments. Therefore, as Kelly argues, one expects that, at low Q^2, the transparency calculated in the Glauber approximation will always be larger than that calculated in the DWIA.

Kelly also argues that the total p-N cross section, rather than just the inelastic, should be used in the Glauber calculations because experimentally most elastic rescatterings are removed from the acceptance. For reference, Table 4.14 lists the total and elastic p–p and p–n cross sections. As an estimate of the elastically scattered flux that is removed from the E91-013 acceptance, the SAID program [85], using the SM97 phase shifts, was used to calculate the angular distribution of the elastic p-p and p-n cross sections at each kinematic setting. Using the fact that the spectator nucleon must receive enough momentum so as to be above the Fermi level, it is possible to define a minimum scattering angle for the proton, θ_{min}. The maximum scattering angle is given by the largest proton angle accepted in the experiment. Table 4.15 lists the fraction, η, of the elastically scattered protons accepted in E91-013. As one can see, at low Q^2, where the elastic scattering contribution to the

Table 4.15. Fraction of Accepted Elastically Scattered Protons. Listed are the fraction of elastically scattered protons that are not Pauli-blocked and are within the experimental acceptance. A zero indicates that Pauli-blocking prevented all elastically scattered protons from entering the acceptance. Fermi momenta of 192, 226, and 275 (MeV/c) were used for ^{12}C, ^{56}Fe, and ^{197}Au, respectively.

	Target	Kine. A	Kine. B	Kine. C	Kine. F
p-*p*	^{12}C	0.02	0.10	0.10	0.09
	^{56}Fe	0	0.08	0.05	0
	^{197}Au	0	0.04	0	0
p-*n*	^{12}C	0.03	0.18	0.15	0.12
	^{56}Fe	0	0.13	0.09	0
	^{197}Au	0	0.07	0	0

p-N cross section is highest, a negligible amount of elastically scattered protons are accepted. Only at the intermediate values of Q^2, where the elastic contribution is dropping rapidly, do some scattered protons remain in the acceptance. The correct cross section to use in Glauber calculations is thus given by

$$\sigma_{\text{eff}} = \sigma_{\text{tot}} - \eta\sigma_{\text{el}}, \tag{4.6}$$

where σ_{tot}, σ_{el} are the total and elastic p-N cross sections, respectively. If one does not wish to take the experimental acceptance into account, Kelly is correct in that the values of η given in Table 4.15 indicate that σ_{eff} is better approximated by σ_{tot} than by σ_{inelas}. Note that the transparency calculations of Nikolaev *et al.*, already low for iron and gold, would be further reduced if they were to use the slightly more accurate σ_{eff} for the p-N cross section. On the other hand, if they were to take into account correlations between the nucleons, this effect may be diminished.

Although Kelly claims the EEI transparency calculations should approach the Glauber results as Q^2 increases, the highest Q^2 he provides is only 1.3 (GeV/c)^2. Furthermore, the curves shown in Fig. 4.21 do not show any sign of upward curvature at the highest Q^2, as would be necessary for agreement with the Glauber calculations near $Q^2 \sim 2$ (GeV/c)^2. The calculations of Gao *et al.* do span the entire experimental Q^2 range, although as mentioned, they seem to show more Q^2 dependence than do the data—especially for carbon. Note however, that the prediction of Kelly—that the Glauber approximation will drastically overestimate the transparency at low Q^2—does not seem to be borne out. Indeed the Glauber approximation calculations of Gao *et al.* seem to agree with the DWIA calculations of Kelly, and are only slightly larger for iron and gold.

The final model for the calculation of nuclear transparency considered here is the Intranuclear Cascade (INC) Model. The results of one such calculation, by Golubeva *et al.*, are shown in Fig. 4.24. [86] This model, originally developed to describe hadron-nucleus scattering, describes the nucleus as a mixture of degenerate proton and neutron Fermi gases. Again, a Monte Carlo scheme is employed. For each event, an initial proton is struck by an electron with kinematics (E, Q^2, ω) equal to that of the experiment. Then as the proton propagates through the residual nucleus, it undergoes a series of reactions (elastic or inelastic, including the production of additional particles) whose relative probabilities are governed by their respective cross sections (the free cross sections are used in all cases). Each struck nucleon then starts its own series of interactions, and so on, forming a "cascade" of scattered particles. The Pauli blocking of final states is included by accepting only reactions that create recoiling nucleons with momenta are outside of the Fermi sphere. The fraction of protons that enter a defined acceptance (in this case that of the NE-18 experiment) relative to a PWIA calculation is taken to be the transparency. As is shown in Fig. 4.24, the INC overestimates the transparency for all targets, although the shape of the Q^2 dependence is quite acceptable. This is somewhat surprising given the fact that total p-N cross section is used in the description of the FSI, and that nucleon-nucleon correlations are neglected. It is true that the model is quasiclassical in the sense that each nucleon is treated as independent. Thus coherent scattering of the proton by the residual nucleus, which can, in principle, reduce the transparency by removing protons from the experimental acceptance, is neglected. Golubeva *et al.* claim however, that coherent scattering is a small effect. An interesting result of the calculation, that is not discussed by the authors, is the unexpected increase in T at large Q^2.

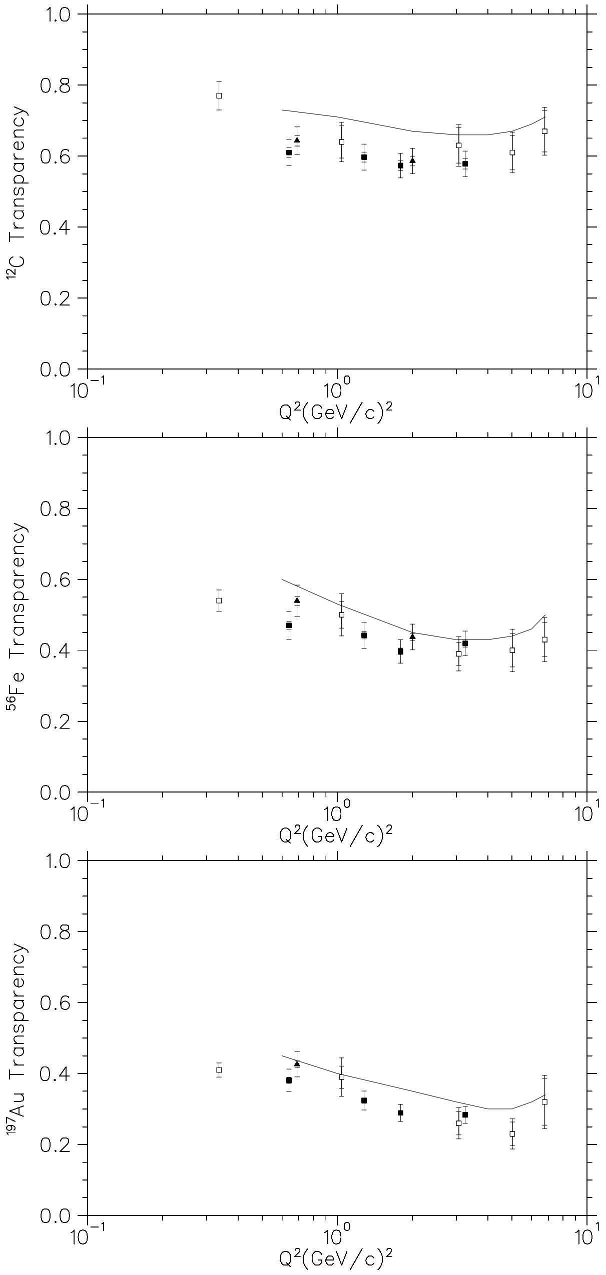

Figure 4.24. Transparency vs. Q^2. From top to bottom: ^{12}C, ^{56}Fe, and ^{197}Au. The curves are the INC calculations of Golubeva *et al.* [86] The data are the same as in Fig. 4.17. (Horizontal log scale.)

CHAPTER 5

DISCUSSION AND CONCLUSIONS

Experiment E91-013 was the first to be performed at CEBAF (now Jefferson Lab), and measured quasielastic exclusive (e,e′p) electron scattering from ^{1}H, ^{12}C, ^{56}Fe, and ^{197}Au targets at squared momentum transfers of 0.64, 1.28, 1.79, and 3.25 (GeV/c)^2. The continuous wave nature of the electron beam allowed for the most statistically precise ($< 1\%$) data in this Q^2 range. The data are well described in a single nucleon knockout picture in which an off-shell proton is struck by the incoming electron, and escapes from the residual nucleus with a probability known as the nuclear transparency. The results agree with previous experiments but have a significantly higher precision.

Because the transparency is the ratio of experimental and simulated yields, the simulation must model accurately every aspect of the A(e,e′p) reaction (with the exception of the final state interactions of the proton). Therefore, knowledge of both the experimental acceptance and the corrections to the cross section due to radiative effects is important. Coincidence H(e,e′p) data were used to test the simulation because interpretation of the results is not complicated by the accuracy of a model spectral function. At each kinematic setting (with the exception of Kinematics F), the integrated experimental and simulated H(e,e′p) cross sections were found to be in agreement at the $\sim 2\%$ level, and the spectra shapes were found to be in reasonable agreement (especially at high missing energy). The agreement in the cross sections is a strict test of the data analysis process, and in particular, knowledge of the acceptance. The validity of the radiative corrections procedure is evident in the good agreement of the yields of both experiment and simulation at large values of missing energy.

The high statistics and reasonable resolution in the missing energy spectra allow for a reassessment of the model spectral functions used in both E91-013 and the previous SLAC experiment NE-18. The $1s$ state in ^{12}C seems to be more deeply bound (by approximately 4 MeV) than the value of 38.1 MeV used in the NE-18 model (a result ultimately derived from Saclay data [2]), but the effect on the transparency results is negligible. Comparisons of experimental and simulated missing energy spectra for ^{56}Fe demonstrate that the model spectral function used in NE-18 underestimates the widths of the low-lying states (1s, 1p, and 1d). This discrepancy prompted the calculation of an alternative spectral function (Appendix A) so as to determine the sensitivity of the transparency results to the choice of model. A relativistic Hartree code (a model quite different from that used to produce the NE-18 spectral functions), TIMORA, was used to provide shell energies and momentum distributions. Due to a lack of theoretical guidance, the energy widths of the nuclear shell states were chosen in an *ad hoc* manner so as to match the shape of the experimental spectra. The large widths determined in this way cause a non-negligible amount of single particle strength to occur above the nominal maximum missing energy of 80 MeV. This appears to be inconsistent with tests that showed the T results are insensitive to the maximum missing energy cutoff. Finally, there also exists an approximate 10% discrepancy in the strengths of the momentum distributions of the NE-18 and TIMORA-based spectral functions. However, it was shown that the TIMORA momentum distributions are too wide and cause an unphysical curvature in a plot of transparency versus proton angle. Therefore, the nominal NE-18 model was employed in the analysis of the E91-013 data. The method of using the linearity of the transparency versus proton angle to limit the width of the momentum distributions did, however, prove to be a valuable tool, as it constrains the simulated yields at the few percent level.

As a function of target size, the transparency falls less quickly than the $T \propto A^{-1/3}$ behavior that one might expect. Both the DWIA and Glauber approximation calculations systematically underestimate the transparency as the target size increases. For example, the iron transparency as calculated by Gao *et al.*, is roughly 15% lower than the experimental result (Fig. 4.22). It is important to realize that this discrepancy is larger than can be explained by known uncertainties in the experimental results. Even though the A-dependence is most sensitive to uncertainties in the simulation, the two largest model-dependencies—correlation corrections and spectral function normalizations—cannot account for the discrepancy with the calculations. Two independent estimations of the correlation corrections were found to be in agreement. In addition, the normalization of the carbon spectral function was found to be in good ($< 2\%$) agreement with an alternative calculation. To conclude, there is no convincing evidence to suggest that the model spectral functions used in the results of E91-013 systematically underestimate the coincidence yield (and hence overestimate the transparency). The failure of the calculations to reproduce the A dependence of the data would still seem to be an open question.

As a function of Q^2, the transparency seems to be remarkably flat, especially for carbon. One would expect the energy dependence of the transparency to be driven largely by the proton-nucleon cross section which changes by over 50% in the E91-013 energy range. Indeed, calculations that take the energy dependence of the p-N cross section into account seem to overestimate its effect. It is true that the fraction of protons that scatter elastically from nucleons and remain in the acceptance is largest for the two central Q^2 points (1.28 and 1.78 (GeV/c)^2), but this should be a few percent effect at most.

If, on the other hand, one then assumes the transparency is independent of Q^2above 1.78 (GeV/c)^2, the results might be used to place constraints on the possible change of the in-medium p-N cross section. Given that the rise in transparency seems to be described well by the decrease in the free p-N cross section, one could conclude that the proton's magnetic form factor (G_E falls more rapidly than G_M with Q^2) changes by at most $< 2\%$. However, as the calculations described here show, the energy dependence of the FSI is not yet understood at a level to perform such an analysis.

Finally, as expected given the NE-18 results, experiment E91-013 saw no rise in T with Q^2—the signature of color transparency. Although one could be tempted to invoke CT to "explain" the large value of T found for iron and gold, the discrepancy between the experimental and theoretical values exists at all momentum transfers.

Nuclear transparency is just one of many aspects of the A(e,e$'$p) reaction currently being investigated with the E91-013 data. Ongoing analyses include Rosenbluth separations at $Q^2 = 0.64$ and 1.78 (GeV/c)^2 and the extraction of de-radiated spectral functions. Discussed in Ref. 34, these measurements will explore the single particle and multi-body contributions to the A(e,e$'$p) reaction. Finally, by measuring the asymmetry in the coincidence cross section left and right of $\vec{q}$, the LT interference term in the off-shell electron-proton cross section can be extracted. Previous data on lighter nuclei indicate that descriptions of the LT term are highly sensitive to relativistic effects. Furthermore, the nuclear transparency results presented here indicate that the popular σ_{cc1} prescription of de Forest underestimates the strength of the LT term, with larger discrepancies at low Q^2. The analyses of previous, low-Q^2 (e,e$'$p) data that employed σ_{cc1}, may need to be corrected if either the size of the LT term was neglected, or if data were only measured on one side of $\vec{q}$. Note that data taken in parallel kinematics are not affected by the LT interference term.

Future transparency experiments are scheduled at Jefferson Lab. Indeed, an extension to E91-013, experiment E91-007, will measure the transparency of carbon, iron, and gold. The experiment is scheduled to run in 1999, and will overlap with the

$Q^2 = 3.3$ (GeV/c)^2 data of E91-013 and extend to $Q^2 = 8.0$ (GeV/c)^2. The thrust of this experiment is to search for CT effects with high statistics data at large Q^2.

Other possible experiments might include a more detailed study of the transparency as a function of Q^2 for ^{12}C and other light targets. As it will soon be possible to sample the entire Q^2 range from $\sim 0.3 - 7$ (GeV/c)^2 in a single set of experiments, it will be interesting to see whether the observed flatness in T observed in E91-013 is verified and exists for other targets. The A dependence of the transparency is now limited by model-dependent uncertainties, but as these come under control, it would be interesting to look at the transparencies for intermediate targets with $A \approx 40$ and $A \approx 100$ to see if the observed $T \propto A^{-0.2}$ behavior persists.

On the theoretical front, the nuclear transparency results of experiment E91-013 suggest three areas of interest. First, the measured nuclear transparency seems to fall off more slowly in A than predicted by current theoretical calculations. Secondly, the transparency results as a function of proton angle indicate that the σ_{cc1} prescription of de Forest underestimates the strength of the LT interference term at low Q^2. Finally, theoretical exploration of the transition from low-Q^2, DWIA calculations to high-Q^2, Glauber calculations is desirable. Specifically, the calculations need to specifically include the energy dependence of the $p-N$ cross section and the missing energy acceptance of experiments.

APPENDIX A

ALTERNATIVE ^{56}FE MODEL SPECTRAL FUNCTION

A.1 Description of the Calculation

As discussed in Sections 3.9.3 and 4.3.3, when using the NE-18 versions of the model ^{56}Fe spectral functions, the agreement between the experimental and simulated missing energy spectra is poor. In particular, the simulation underestimates the strength at low missing energy, and the shell widths for the least bound states are too narrow (Fig. 4.9). In order to improve the agreement between simulation and experiment, and to test the sensitivity of the E91-013 results to the model spectral functions, an alternative ^{56}Fe spectral function was calculated and used as input to SIMC.

The binding energy values and momentum distributions for the shells of ^{56}Fe were extracted from the output of a relativistic Hartree computer code, TIMORA, written by Horowitz. [77]. The code is based on the σ-ω relativistic quantum field theory model of Walecka, in which the nucleus is described by nucleons interacting via the exchange of scalar (σ) and vector (ω) mesons. [87] At high densities, the meson field operators are replaced by their expectation values, resulting in a mean field theory. In this limit, Horowitz also includes the (isovector) exchange of ρ and π mesons. The coupling constants for each field are derived from nuclear matter properties and the rms charge radius of ^{40}Ca. TIMORA also requires initial estimates for the binding energy and occupation number of each nuclear shell, and starts by approximating the mean field potential with a Woods-Saxon shape. The Dirac equation is then solved for each shell to give wave functions and energy eigenvalues. These wave functions are used to construct shell densities which are then integrated over a Green's function to get a new potential. This process is then repeated until the convergence criterion (that no energy eigenvalue changes by 0.05 MeV) is met. The code is quite sensitive to the initial eigenvalue estimates; small changes can mean the difference between reasonable results and a complete lack of convergence. In fact, the code had to be slightly modified such that the energy eigenvalues were held fixed for the first few iterations.

A.2 Model Spectral Function Results

For each shell, TIMORA provides both the upper and lower components of the Dirac wave function, ψ_u and ψ_l. The upper r-space wave functions are shown in Figure A.1 as a function of the nuclear radius, r. TIMORA actually provides $r\psi_u$ and $r\psi_l$, and so the normalization is calculated via

$$\int_0^\infty dr\left(|\psi_u(r)|^2 + |\psi_l(r)|^2\right) = 1. \tag{A.1}$$

The momentum distributions are derived from the TIMORA output by taking the Fourier transform of the r-space wave functions:

$$\begin{aligned}
\tilde{\psi}_i &= \frac{1}{(2\pi)^{3/2}}\int d^3r e^{i\mathbf{k}\cdot\mathbf{r}}\psi_i(\mathbf{r}), \\
&= \frac{1}{(2\pi)^{3/2}}\int d^3r \sum_{l=0}^{\infty}(2l+1)i^l j_l(kr)Y_{l0}(\theta)\sqrt{\frac{4\pi}{2l+1}}\psi_i(\mathbf{r}), \\
&= \frac{1}{(2\pi)^{3/2}}\int d^3r \sum_{l=0}^{\infty}(2l+1)i^l j_l(kr)Y_{l0}(\theta)\sqrt{\frac{4\pi}{2l+1}}Y_{l'm'}(\theta,\phi)R(r), \\
&= \frac{\sqrt{4\pi(2l+1)}}{(2\pi)^{3/2}}\int r^2 dr j_l(kr)\psi_i(r), \\
&= \frac{\sqrt{4\pi(2l+1)}}{(2\pi)^{3/2}}\int r dr j_l(kr)\bar{\psi}_i(r),
\end{aligned} \tag{A.2}$$

where the subscript i refers to either the upper or lower Dirac wave function, and the orthogonality of the Y_{lm}s has been used:

$$\int d\Omega Y_{lm}Y_{l'm'} = \delta_{ll'}\delta_{mm'}. \tag{A.3}$$

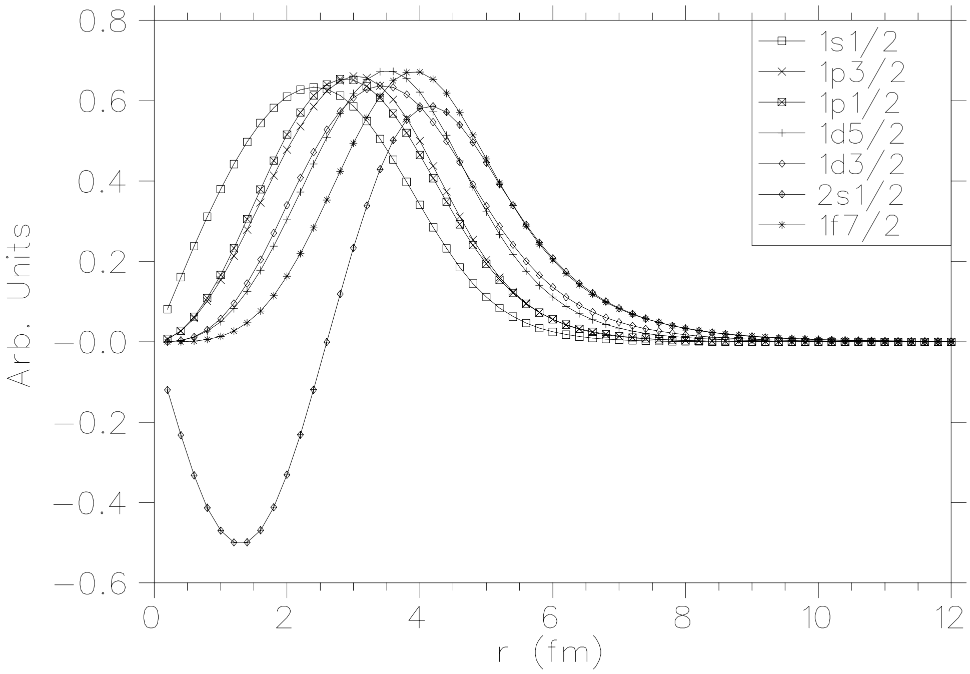

Figure A.1. R-Space wave functions calculated by TIMORA. $r\psi_u$ is plotted versus radius.

The momentum density appears as

$$\rho(k) = |\tilde{\psi}_u|^2 + |\tilde{\psi}_l|^2, \tag{A.4}$$

SIMC requires that the k-space density be normalized such that

$$\int_0^\infty k^2 dk \rho(k) = \frac{1}{4\pi}, \tag{A.5}$$

which means it is necessary to divide the k-space wave functions by $\sqrt{2l+1}$. Figure A.2 shows $\rho(k)$ as a function of momentum.

Both the NE-18 and TIMORA energy values are listed in Table A.1, and the agreement is quite reasonable (note that NE-18 did not split the shells into two j-values). While the shell energies and momentum distributions are provided by TIMORA, the shell widths still have to be specified. Equation 3.23 seems to produce widths that are far too small resulting in narrow "humps" even for the deeply bound shells. The widths were therefore modified by hand in order to form better agreement

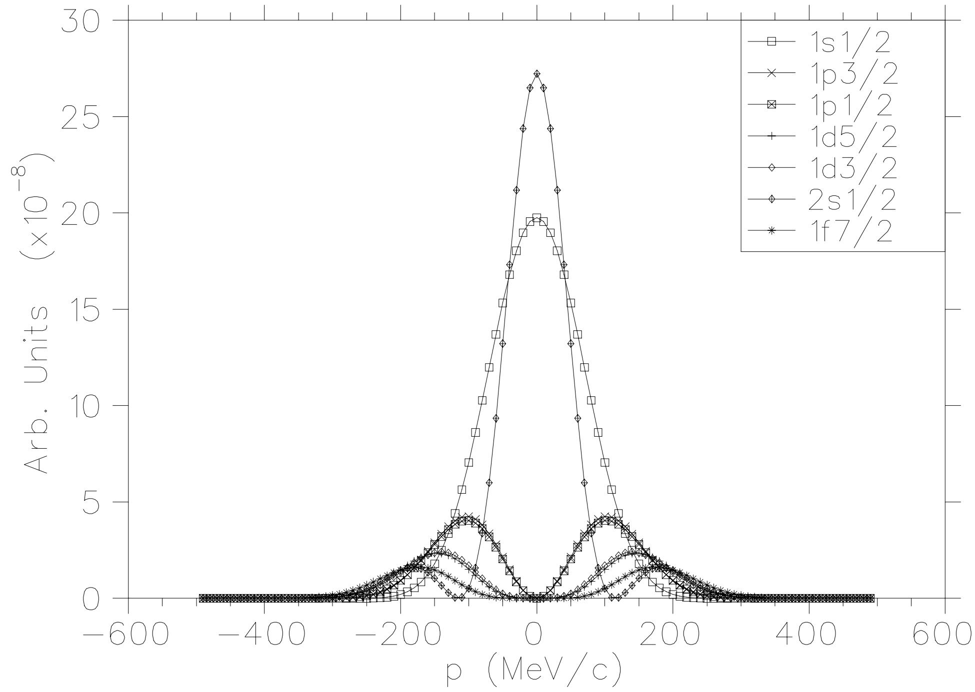

Figure A.2. Momentum-space wave function densities derived from TIMORA output.

Table A.1. NE-18 and TIMORA values for ^{56}Fe shell energies. Note that NE-18 did not split up shells into two j-values.

Shell	NE-18 Energy (MeV)	TIMORA Energy (MeV)
$1s_{1/2}$	50.0	53.0
$1p_{3/2}$	37.0	39.0
$1p_{1/2}$	37.0	35.0
$1d_{5/2}$	23.0	23.0
$1d_{3/2}$	23.0	15.4
$2s_{1/2}$	16.7	13.5
$1f_{7/2}$	11.3	8.3

Table A.2. NE-18 and TIMORA values for the ^{56}Fe shell widths. Note that NE-18 did not split up shells into two j-values.

Shell	NE-18 Width (MeV)	TIMORA-based Width (MeV)
$1s_{1/2}$	18.0	55.0
$1p_{3/2}$	14.0	45.0
$1p_{1/2}$	14.0	40.0
$1d_{5/2}$	6.0	32.0
$1d_{3/2}$	6.0	22.0
$2s_{1/2}$	3.0	6.5
$1f_{7/2}$	1.0	1.5

with the experimental spectra. Table A.2 lists the values used by NE-18 and those used in the new model. Note that in some cases, drastic changes in the widths are necessary to attain agreement (in missing energy spectra shape) with experiment. The real test of this spectral function, however, is in a comparison with experiment. Figure A.3 shows a plot of experiment versus simulation at $Q^2 = 0.64$ (GeV/c)^2 in which the yields have been normalized to the same number of counts. Here SIMC was used with the TIMORA momentum distributions and eigenenergies, and the *ad hoc* widths of Table A.2. The agreement between experiment and Monte Carlo is clearly much better than that shown in Fig. 4.9, but there still seems to be a slight lack of strength for the least bound shells. However, this is only true for this kinematics. Figure A.4 shows the same comparison, still at $Q^2 = 0.64$ (GeV/c)^2, but at a more perpendicular kinematics (the central proton angle is 12° away from $\vec{q}$ upstream of the beam). Note that in the this case, there seems to be an excess of strength for the least bound shells. For completeness, Figure A.5 shows the same comparison, same Q^2, but now 8° towards the beam from $\vec{q}$.

Figure A.6 compares the TIMORA-based and measured missing energy spectra at the conjugate settings at each E91-013 kinematics. With the exception of the underestimated strength of the least-bound states in the backwards kinematics (D and E), the agreement is quite reasonable.

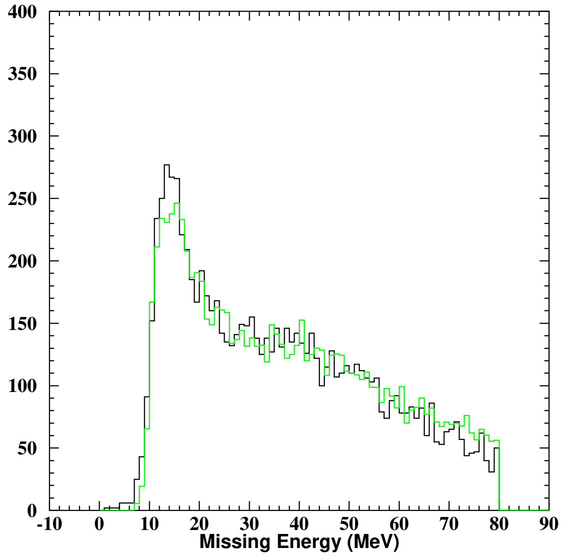

Figure A.3. Experimental ^{56}Fe missing energy spectrum (black) versus SIMC output (grey) with spectral function derived from TIMORA. Conjugate kinematics at $Q^2 0.64$ (GeV/c)^2.

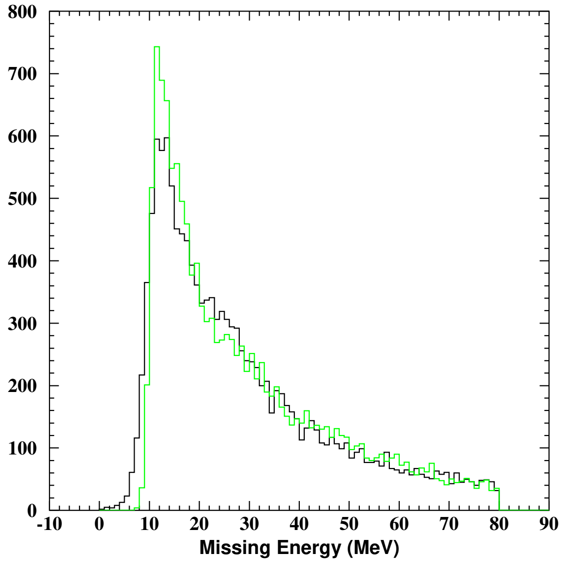

Figure A.4. Experimental ^{56}Fe missing energy spectrum (black) versus SIMC output (grey) with spectral function derived from TIMORA. The central proton angle is 12° away from $\vec{q}$ away from the beam. $Q^2 = 0.64$ $(GeV/c)^2$.

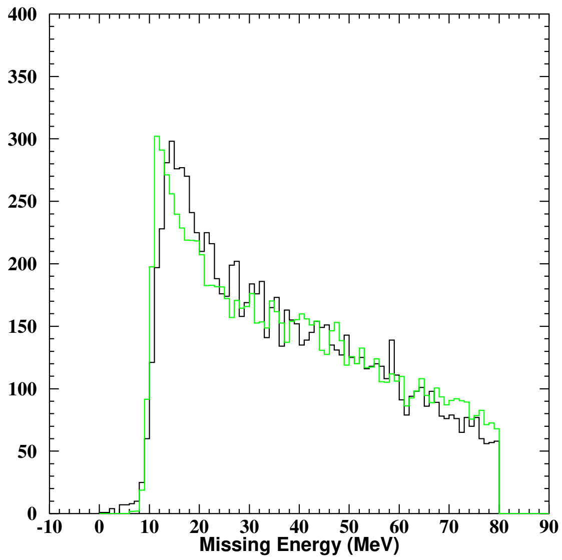

Figure A.5. Experimental ^{56}Fe missing energy spectrum (black) versus SIMC output (grey) with spectral function derived from TIMORA. The central proton angle is 8° away from $\vec{q}$ towards the beam. $Q^2 = 0.64\ (GeV/c)^2$.

A.3 Comparison with the NE-18 Spectral Function

The spectra displayed in the previous section have been normalized to the same number of counts so as to compare their shapes. Thus far, nothing has been said about their normalizations. This section describes a comparison of the TIMORA-based spectral function and the nominal NE-18 spectral function when integrated over the experimental acceptance (0–80 MeV in missing energy, 0–300 MeV/c in missing momentum). Because the transparency is the ratio of the experimental to simulated yield, any discrepancy between different models will translate directly into the same discrepancy in T. Therefore, it suffices to compare the yields of the models directly. Table A.3 lists the integrated yield and "normalization factor" for both spectral functions for the conjugate angle at Kinematics A. The normalization factor is an artifact of the way in which SIMC calculates normalized yields. As discussed in Section 3.9.1, the code generates events, populating a phase space slightly larger than

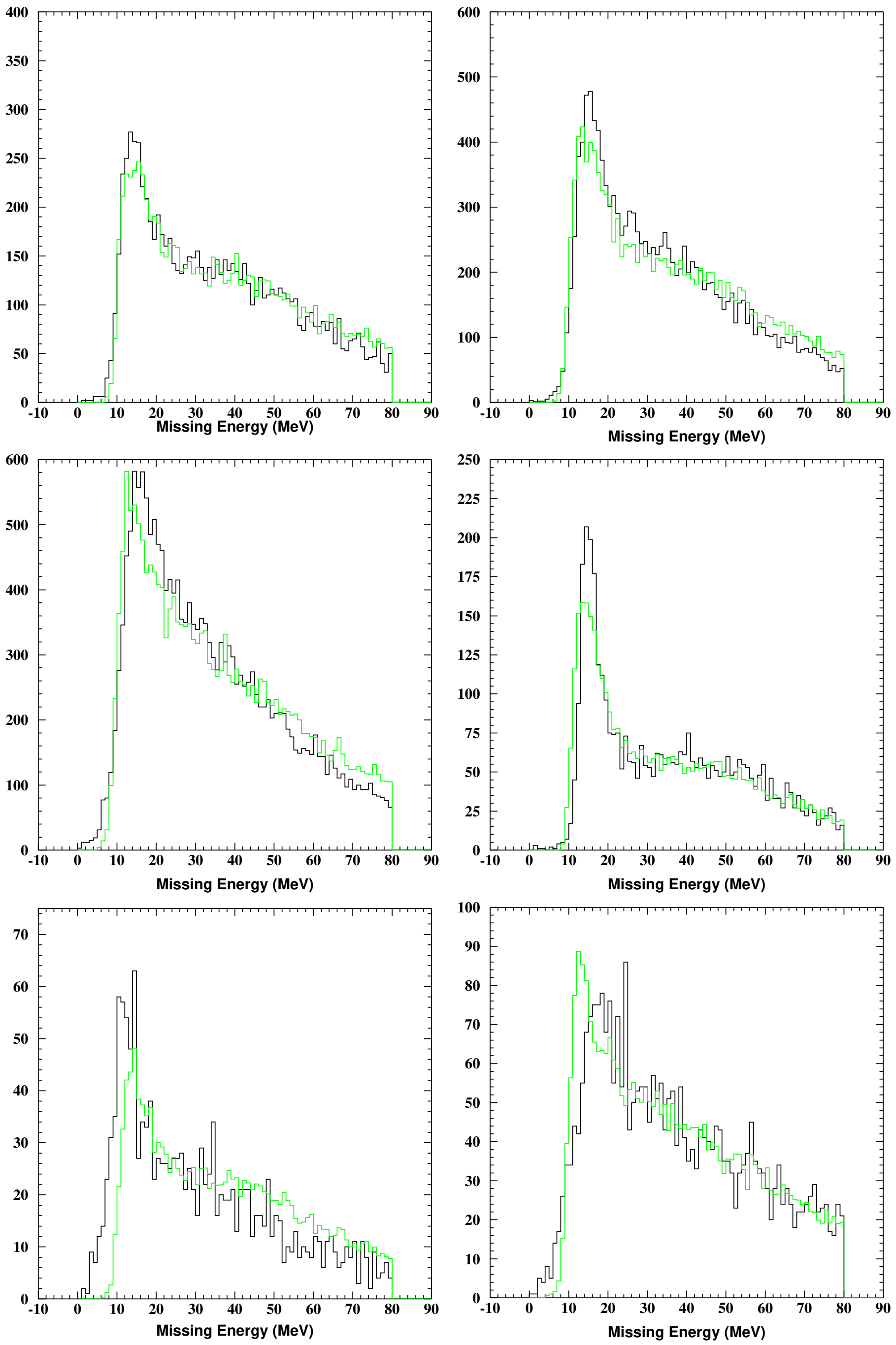

Figure A.6. Comparison of TIMORA-based momentum distributions and experiment at the conjugate angles of each E91-013 kinematic setting, (Kinematics A -F, from left to right, then down.)

Table A.3. Comparison of yields for NE-18 model and TIMORA-based spectral functions for ^{56}Fe at $Q^2 = 0.64$ (GeV/c)^2. See text for explanation.

	NE-18	TIMORA	% Discrepancy
Normalization Factor	1.264×10^8	1.262×10^8	-0.2
Normalized Yield	33838	26247	-22.4

the experimental acceptance. Each event is assigned a weight factor based on the off-shell cross section and spectral function. These weights are written to the output file on an event-by-event basis. Then, when the code has finished, it calculates an overall normalization factor equal to the simulated luminosity (i.e. the experimental charge) divided by the number of attempted events. To calculate the yield then, one integrates over the missing energy, weighting each event by its individual weight factor, and then this sum is multiplied by the overall normalization factor. Comparing the results for the two models, it is evident that while the normalization factors agree very well, the actual yields disagree by a large amount. That the normalization factors agree is not surprising because the phase space being populated is the same in both cases. The weight factor for each event is calculated as:

$$w = \prod_{\alpha} \rho_\alpha(p_m) \times \frac{1}{\pi} \frac{1}{\mathcal{N}_\alpha} \frac{\Gamma_\alpha/2}{(E - E_\alpha)^2 + (\Gamma_\alpha/2)^2}, \tag{A.6}$$

where $\alpha = (n, l, j)$ labels the shell quantum numbers, and $\rho_\alpha(p_m)$, $\mathcal{N}_\alpha$, E_α, and Γ_α are the momentum distribution, occupancy, energy, and energy width of the state α, respectively. Because the energy eigenvalues of both models are quite similar (Table A.1), the discrepancy must be due to either differences in the shape of the momentum distributions and/or the different shell widths employed.

The momentum distributions of both models are compared in Figs. A.7 and A.8. The agreement displayed in Fig. A.7 seems to be quite good, even at large missing momenta, but the TIMORA distributions are actually systematically wider. This extra width is important because the strength is weighted by a factor of k^2 in

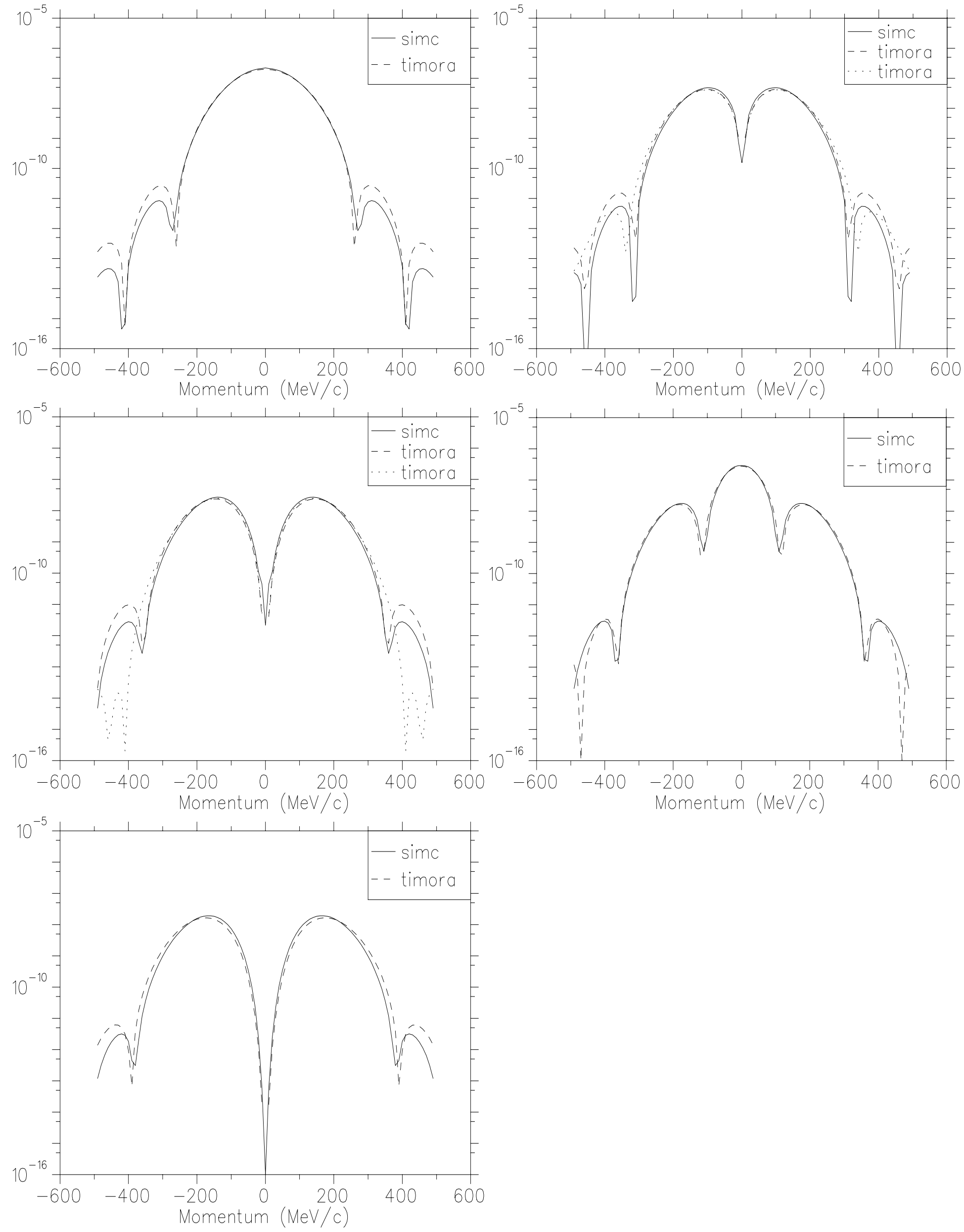

Figure A.7. Comparison of TIMORA-based (dashed) and NE-18(solid) momentum densities. The shells are 1s, 1p, 1d, 2s, 1f from left to right, then down.

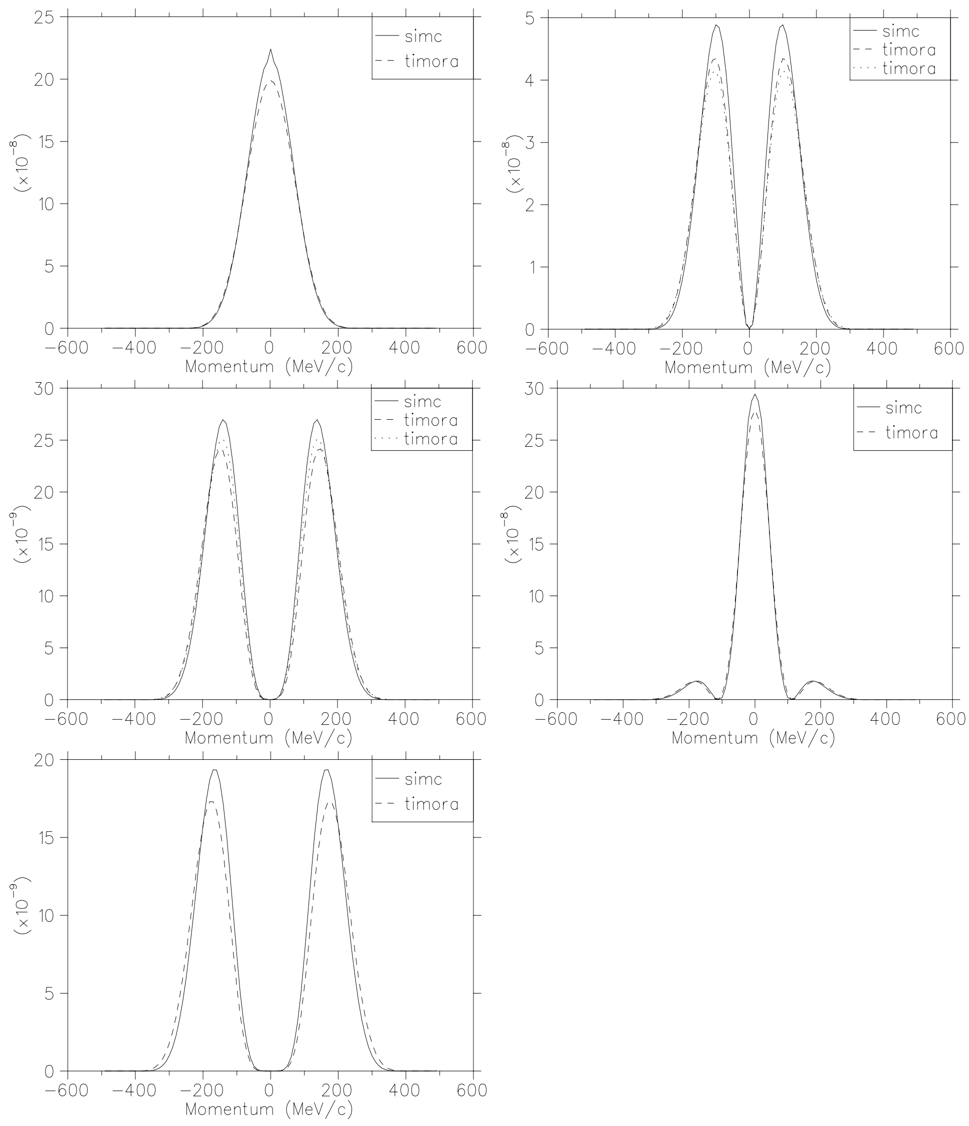

Figure A.8. Comparison of TIMORA-based (dashed) and NE-18(solid) momentum densities. Same as Fig. A.7, but linear scale.

Table A.4. Integrated TIMORA and NE-18 Momentum Densities. Listed are the ratios, TIMORA to NE-18, of the integral from -500–500 MeV/c (not weighted by k^2). For the two different 1p and 1d shells in TIMORA, the occupancy-weighted average was used.

Shell	TIMORA/NE-18
1s	0.922
1p	0.898
1d	0.920
2s	0.900
1f	0.890

the normalization (Eqn. A.5). Therefore, the extra width results in a reduction of the density, relative to the NE-18 model, at momenta lower than $\sim$ 200 MeV/c, as displayed on a linear scale in Fig. A.8. Table A.4 lists the ratio, TIMORA to NE-18, of the integrated strength from 0–300 MeV/c. As one can see there is a constant 10% discrepancy for each shell. This translates into a 10% discrepancy in the final simulated yields, as the events are weighted directly by the momentum density (Eqn. A.6). Although the momentum distribution widths of the TIMORA output can be made narrower by increasing the diffuseness of the Wood-Saxon potentials, there is no compelling reason to do so, and the choice has been made to stay with the parameters used in Ref. 77.

The larger shell widths used in the TIMORA-based spectral function also have an effect on the yields. Given the Lorentzian shape of the energy distributions (Eqn. A.6), one can calculate the fraction of the strength that is spread beyond the nominal E_m cutoff at 80 MeV. These fractions are listed for both models, along with the occupancy-weighted average, in Table A.5 Note that as expected, the large widths of the deeply bound shells cause a non-negligible amount of strength to go beyond the maximum experimentally accepted missing energy. The result is a further 10% discrepancy between the two models. Note that the seemingly large size of these widths is necessary to produce the agreement in spectra shape display in the previous

Table A.5. Integrated TIMORA and NE-18 Energy Distributions. The integral from the single particle removal energy of 10.2 MeV to the maximum of 80 MeV is compared with the same integral to infinity for each shell for both models. For the multiple-j TIMORA distributions, the occupancy-weighted average is used. The last entry lists the occupancy weighted average of all ratios.

Shell	TIMORA	NE-18
1s	0.691	0.900
1p	0.812	0.944
1d	0.899	0.982
2s	0.973	0.992
1f	0.970	0.997
Occ. Avg.	0.885	0.971

section.

To verify that the observed 20% discrepancy is indeed due to the sum of these two effects, three comparisons are made with the nominal NE-18 model: the full TIMORA model, the NE-18 model with its shell energies and widths but with the TIMORA momentum distributions (for multiple j-values, the average width was used), and finally a model with the TIMORA shell energies, *ad hoc* widths, and the NE-18 model momentum distributions. These three cases are compared for a series of maximum missing energies, and the percent discrepancy with the nominal NE-18 results are listed in Table A.6. As the maximum missing energy is increased, the discrepancy between the *ad hoc* shell widths and the nominal NE-18 values decreases

Table A.6. Nominal vs. Alternative ^{56}FeSpectral Function: Yield Tests. The tests compare the nominal NE-18 spectral function with A) TIMORA, B) NE-18 energies and shell widths, but TIMORA momentum distributions, and C) TIMORA energies and the *ad hoc* shell widths and NE-18 momentum distributions.

Kinematic Range	Test A TIMORA E_m TIMORA p_m	Test B Nominal E_m TIMORA p_m	Test C TIMORA E_m Nominal p_m
$E_{m,\max} = 50$ MeV	28.0	12.4	18.3
$E_{m,\max} = 80$ MeV	20.6	11.5	10.5
$E_{m,\max} = 120$ MeV	16.0	11.5	5.6

Table A.7. RMS Charge Radii of Iron Model Momentum Distributions. The experimental result is from de Vries *et al.* [78].

	TIMORA	NE-18	Experiment
RMS Charge Radius (fm)	3.67	3.83	3.75$\pm$0.03

as more of the strength above 80 MeV is recovered (Tests A and C). However, as the maximum missing energy is increased, Tests A and B show that the missing momentum widths of TIMORA cause a consistent 10% discrepancy.

A.4 Conclusions

The discrepancy between the TIMORA and NE-18 momentum distributions prompted the search for an observable that might be used to exclude either model as being unphysical. First, the rms charge radius for both models was calculated, and the results are listed in Table A.7. Note that the TIMORA radius is somewhat small, consistent with its momentum distributions being too wide. However, the radii of the two models straddle the experimental value, and so the charge radius alone can not be used to exclude either the TIMORA or NE-18 model.

It is only when the transparency is plotted as a function of proton angle that a problem with the TIMORA spectral function becomes evident (Fig. A.9; note that, to facilitate comparison of the shapes, the TIMORA-based transparency is offset vertically by -0.12 such that it agrees with the NE-18 model-based transparency at the conjugate angle). One expects the off-shell cross section to be asymmetric about the conjugate angle due to the LT interference term (Eqn. 1.11). If the de Forest description of the LT term were exact, this asymmetry would cancel when dividing the experimental cross section by the simulation. However, as discussed in Section 4.3.1, de Forest underestimates the size of the LT term, and so a slight asymmetry remains when plotting the transparency versus proton angle. This is the cause of the slope in the transparency calculated using the nominal NE-18 spectral

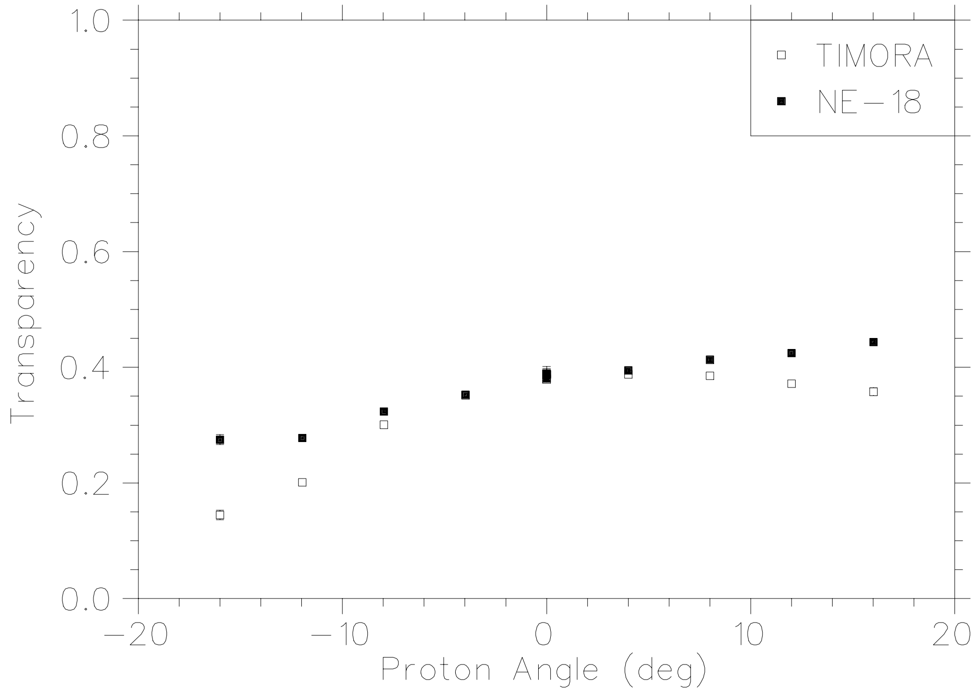

Figure A.9. TIMORA vs. NE-18 Transparency. The transparency calculated using the TIMORA (NE-18) spectral function is shown in open (filled) symbols as a function of proton angle (zero is the conjugate angle) at Kinematics A. To facilitate comparison of the shapes, the TIMORA-based transparency is offset vertically by -0.12 such that it agrees with the NE-18 model-based transparency at the conjugate angle. The error bars are statistical only.

function (solid points in Figure A.9). However, there is no known physical mechanism that can cause the shape seen in the TIMORA-based transparency (open points). The unexpected fall-off at large proton angles is due to excess strength at large missing momentum in the TIMORA-based spectral function.

Because of this result, and a desire to facilitate comparison with the results of NE-18, the nominal NE-18 model spectral function was employed in the analysis of the ^{56}Fe data in E91-013. Because the TIMORA momentum distributions are so wide as to be unphysical, the 10% discrepancy between it and the NE-18 model is too large to use as an estimate of the systematic uncertainty. Figure A.9 was used to conclude that the uncertainty is less than half of this discrepancy, or about 4%. The constraint stability tests (Appendix B) show that the transparency is insensitive to the missing energy cut-off at the 2% level, therefore this value is used for the uncertainty on the transparency due to the model shell energy widths. The two uncertainties added in quadrature total 4.5%, in qualitative agreement with the 6% spectral function uncertainty quoted by Makins *et al.*

APPENDIX B

CONSTRAINT DEPENDENCY OF THE RESULTS

As discussed in Section 4.3.2, Tables B.1-B.6 list the average discrepancy (nominal/modified) between the nominal data yield and the yield with the modified constraint. The discrepancy for each kinematics and each target is averaged (weighted by charge) over each run for all proton angle settings.

Table B.1. Cut stability results for kinematics A. The weighted average of the discrepancy (weighted by the number of counts in the adjusted transparency result).

Kine.	Target	Label	Average Discrepancy	Error	Label	Average Discrepancy	Error
A	C	em100	0.9905	0.0026	hsdelta6	0.9991	0.0029
A	Fe	em100	0.9800	0.0032	hsdelta6	1.0009	0.0036
A	Au	em100	0.9836	0.0032	hsdelta6	1.0048	0.0035
A	C	em120	0.9859	0.0025	hsdelta10	1.0000	0.0028
A	Fe	em120	0.9694	0.0030	hsdelta10	1.0007	0.0035
A	Au	em120	0.9717	0.0030	hsdelta10	1.0000	0.0034
A	C	pm200	1.0092	0.0033	ssdelta8to18	1.0054	0.0030
A	Fe	pm200	1.0086	0.0040	ssdelta8to18	1.0019	0.0037
A	Au	pm200	1.0043	0.0039	ssdelta8to18	1.0038	0.0037
A	C	pm250	1.0052	0.0030	hsyptar35	1.0000	0.0028
A	Fe	pm250	1.0056	0.0036	hsyptar35	1.0000	0.0035
A	Au	pm250	1.0082	0.0036	hsyptar35	1.0000	0.0034
A	C	pm320	0.9970	0.0028	ssyptar55	0.9750	0.0028
A	Fe	pm320	0.9961	0.0034	ssyptar55	0.9760	0.0034
A	Au	pm320	0.9942	0.0034	ssyptar55	0.9771	0.0034
A	C	coin8	0.9999	0.0028			
A	Fe	coin8	1.0000	0.0035			
A	Au	coin8	1.0000	0.0034			

Table B.2. Cut stability results for kinematics B. The weighted average of the discrepancy (weighted by the number of counts in the adjusted transparency result).

Kine.	Target	Label	Average Discrepancy	Error	Label	Average Discrepancy	Error
B	C	em100	0.9974	0.0032	hsdelta6	0.9867	0.0037
B	Fe	em100	0.9869	0.0038	hsdelta6	0.9946	0.0045
B	Au	em100	0.9877	0.0042	hsdelta6	0.9750	0.0049
B	C	em120	0.9957	0.0031	hsdelta10	0.9992	0.0032
B	Fe	em120	0.9798	0.0036	hsdelta10	1.0008	0.0038
B	Au	em120	0.9806	0.0041	hsdelta10	1.0058	0.0043
B	C	pm200	1.0079	0.0038	ssdelta8to18	0.9935	0.0034
B	Fe	pm200	1.0063	0.0046	ssdelta8to18	0.9905	0.0041
B	Au	pm200	0.9884	0.0049	ssdelta8to18	0.9956	0.0045
B	C	pm250	1.0042	0.0035	hsyptar35	1.0000	0.0034
B	Fe	pm250	1.0073	0.0042	hsyptar35	1.0000	0.0041
B	Au	pm250	1.0071	0.0046	hsyptar35	1.0000	0.0045
B	C	pm320	0.9980	0.0034	ssyptar55	0.9770	0.0034
B	Fe	pm320	0.9968	0.0040	ssyptar55	0.9777	0.0040
B	Au	pm320	0.9968	0.0044	ssyptar55	0.9790	0.0044
B	C	coin8	1.0000	0.0034			
B	Fe	coin8	0.9999	0.0041			
B	Au	coin8	0.9999	0.0045			

Table B.3. Cut stability results for kinematics C. The weighted average of the discrepancy (weighted by the number of counts in the adjusted transparency result).

Kine.	Target	Label	Average Discrepancy	Error	Label	Average Discrepancy	Error
C	C	em100	0.9969	0.0033	hsdelta6	1.0024	0.0039
C	Fe	em100	0.9870	0.0038	hsdelta6	0.9840	0.0044
C	Au	em100	0.9854	0.0045	hsdelta6	0.9804	0.0052
C	C	em120	0.9906	0.0032	hsdelta10	0.9919	0.0033
C	Fe	em120	0.9770	0.0036	hsdelta10	1.0006	0.0039
C	Au	em120	0.9726	0.0043	hsdelta10	0.9944	0.0046
C	C	pm200	0.9948	0.0041	ssdelta8to18	1.0020	0.0036
C	Fe	pm200	0.9942	0.0048	ssdelta8to18	0.9996	0.0041
C	Au	pm200	0.9811	0.0053	ssdelta8to18	0.9942	0.0048
C	C	pm250	0.9984	0.0037	hsyptar35	1.0000	0.0035
C	Fe	pm250	1.0034	0.0043	hsyptar35	1.0000	0.0041
C	Au	pm250	1.0068	0.0049	hsyptar35	1.0000	0.0048
C	C	pm320	0.9986	0.0035	ssyptar55	0.9771	0.0034
C	Fe	pm320	0.9966	0.0040	ssyptar55	0.9776	0.0040
C	Au	pm320	0.9952	0.0047	ssyptar55	0.9819	0.0047
C	C	coin8	1.0000	0.0035			
C	Fe	coin8	1.0000	0.0041			
C	Au	coin8	1.0000	0.0048			

Table B.4. Cut stability results for kinematics D. The weighted average of the discrepancy (weighted by the number of counts in the adjusted transparency result).

Kine.	Target	Label	Average Discrepancy	Error	Label	Average Discrepancy	Error
D	C	em100	0.9960	0.0034	hsdelta6	0.9919	0.0039
D	Fe	em100	0.9906	0.0047	hsdelta6	0.9980	0.0056
D	Au	em100	0.9901	0.0072	hsdelta6	0.9821	0.0084
D	C	em120	0.9951	0.0033	hsdelta10	1.0003	0.0032
D	Fe	em120	0.9864	0.0047	hsdelta10	1.0020	0.0045
D	Au	em120	0.9871	0.0071	hsdelta10	1.0131	0.0069
D	C	pm200	1.0040	0.0036	ssdelta8to18	1.0029	0.0035
D	Fe	pm200	1.0106	0.0054	ssdelta8to18	1.0034	0.0050
D	Au	pm200	1.0021	0.0079	ssdelta8to18	1.0026	0.0076
D	C	pm250	1.0015	0.0035	hsyptar35	0.9995	0.0035
D	Fe	pm250	1.0059	0.0050	hsyptar35	0.9996	0.0049
D	Au	pm250	1.0060	0.0076	hsyptar35	0.9997	0.0075
D	C	pm320	0.9998	0.0035	ssyptar55	0.9735	0.0034
D	Fe	pm320	0.9995	0.0049	ssyptar55	0.9743	0.0048
D	Au	pm320	0.9987	0.0074	ssyptar55	0.9745	0.0073
D	C	coin8	1.0000	0.0035			
D	Fe	coin8	1.0000	0.0049			
D	Au	coin8	0.9998	0.0075			

Table B.5. Cut stability results for kinematics E. The weighted average of the discrepancy (weighted by the number of counts in the adjusted transparency result).

Kine.	Target	Label	Average Discrepancy	Error	Label	Average Discrepancy	Error
E	C	em100	1.0011	0.0073	hsdelta6	0.9991	0.0085
E	Fe	em100	0.9938	0.0090	hsdelta6	0.9958	0.0105
E	C	em120	0.9986	0.0071	hsdelta10	0.9914	0.0068
E	Fe	em120	0.9827	0.0087	hsdelta10	1.0069	0.0086
E	C	pm200	0.9949	0.0078	ssdelta8to18	1.0000	0.0075
E	Fe	pm200	0.9917	0.0098	ssdelta8to18	1.0001	0.0093
E	C	pm250	1.0012	0.0076	hsyptar35	1.0000	0.0075
E	Fe	pm250	1.0021	0.0094	hsyptar35	1.0002	0.0093
E	C	pm320	0.9996	0.0075	ssyptar55	0.9785	0.0073
E	Fe	pm320	0.9988	0.0093	ssyptar55	0.9771	0.0091
E	C	coin8	0.9999	0.0075			
E	Fe	coin8	0.9998	0.0094			

Table B.6. Cut stability results for kinematics F. The weighted average of the discrepancy (weighted by the number of counts in the adjusted transparency result).

Kine.	Target	Label	Average Discrepancy	Error	Label	Average Discrepancy	Error
F	C	em100	0.9928	0.0078	hsdelta6	1.0069	0.0088
F	Fe	em100	0.9821	0.0079	hsdelta6	1.0071	0.0091
F	Au	em100	0.9853	0.0117	hsdelta6	1.0055	0.0132
F	C	em120	0.9834	0.0076	hsdelta10	0.9939	0.0080
F	Fe	em120	0.9657	0.0076	hsdelta10	0.9922	0.0083
F	Au	em120	0.9706	0.0112	hsdelta10	0.9927	0.0121
F	C	pm200	1.0238	0.0093	ssdelta8to18	0.9851	0.0084
F	Fe	pm200	1.0258	0.0096	ssdelta8to18	0.9768	0.0085
F	Au	pm200	1.0269	0.0141	ssdelta8to18	0.9607	0.0122
F	C	pm250	1.0090	0.0084	hsyptar35	1.0001	0.0082
F	Fe	pm250	1.0151	0.0088	hsyptar35	1.0000	0.0084
F	Au	pm250	1.0196	0.0128	hsyptar35	0.9998	0.0123
F	C	pm320	0.9965	0.0081	ssyptar55	0.9762	0.0080
F	Fe	pm320	0.9952	0.0083	ssyptar55	0.9762	0.0082
F	Au	pm320	0.9946	0.0122	ssyptar55	0.9779	0.0121
F	C	coin8	0.9997	0.0082			
F	Fe	coin8	0.9997	0.0084			
F	Au	coin8	0.9997	0.0123			

APPENDIX C

INCLUSIVE CROSS SECTIONS

Tabulated below are the experimentally measured inclusive cross sections plotted in Section 4.2 (Figs. 4.4–4.7). Tables C.1–C.3 list the hydrogen results for Kinematics A and B, C and D, and E and F, respectively. Tables C.4–C.9 list the cross sections for the solid targets at Kinematics A–F, respectively. The uncertainties are statistical only and do not include the 10% systematic uncertainty discussed in Section 4.2. Note that the results are not corrected for radiative effects or acceptance (the latter comprising the bulk of the systematic uncertainty). For reference, the kinematic settings are listed in Table 2.1.

Table C.1. Inclusive Hydrogen Cross Sections, Kinematics A and B. Listed are the inclusive cross sections for hydrogen as a function of energy loss, ω. The uncertainties are statistical .

Kine.	ω (MeV)	σ (nb/sr/MeV)	Kine.	ω (MeV)	σ (nb/sr/MeV)
A	276.	0.600E-05 ± 0.10E-05	B	626.	0.000E-00 ± 0.00E-00
A	284.	0.190E-04 ± 0.80E-05	B	634.	0.000E-00 ± 0.00E-00
A	292.	0.820E-04 ± 0.23E-04	B	642.	0.800E-05 ± 0.20E-05
A	300.	0.156E-03 ± 0.32E-04	B	650.	0.580E-04 ± 0.40E-05
A	308.	0.312E-03 ± 0.46E-04	B	658.	0.728E-03 ± 0.14E-04
A	316.	0.464E-02 ± 0.17E-03	B	666.	0.178E-02 ± 0.23E-04
A	324.	0.295E-01 ± 0.40E-03	B	674.	0.257E-02 ± 0.28E-04
A	332.	0.577E-01 ± 0.56E-03	B	682.	0.297E-02 ± 0.31E-04
A	340.	0.660E-01 ± 0.61E-03	B	690.	0.310E-02 ± 0.32E-04
A	348.	0.705E-01 ± 0.64E-03	B	698.	0.309E-02 ± 0.32E-04
A	356.	0.709E-01 ± 0.65E-03	B	706.	0.297E-02 ± 0.31E-04
A	364.	0.664E-01 ± 0.63E-03	B	714.	0.291E-02 ± 0.31E-04
A	372.	0.608E-01 ± 0.60E-03	B	722.	0.265E-02 ± 0.29E-04
A	380.	0.560E-01 ± 0.57E-03	B	730.	0.246E-02 ± 0.28E-04
A	388.	0.518E-01 ± 0.55E-03	B	738.	0.218E-02 ± 0.26E-04
A	396.	0.453E-01 ± 0.51E-03	B	746.	0.170E-02 ± 0.22E-04
A	404.	0.361E-01 ± 0.45E-03	B	754.	0.119E-02 ± 0.18E-04
A	412.	0.243E-01 ± 0.36E-03	B	762.	0.663E-03 ± 0.13E-04
A	420.	0.117E-01 ± 0.25E-03	B	770.	0.311E-03 ± 0.90E-05
A	428.	0.506E-02 ± 0.15E-03	B	778.	0.200E-03 ± 0.60E-05

Table C.2. Inclusive Hydrogen Cross Sections, Kinematics C and D. Listed are the inclusive cross sections for hydrogen as a function of energy loss, ω. The uncertainties are statistical and do not include the 10% systematic uncertainty.

Kine.	ω (MeV)	σ (nb/sr/MeV)	Kine.	ω (MeV)	σ (nb/sr/MeV)
C	867.	0.000E-00 ± 0.00E-00	D	348.	0.210E-04 ± 0.90E-05
C	878.	0.000E-00 ± 0.00E-00	D	349.	0.405E-03 ± 0.30E-04
C	889.	0.400E-05 ± 0.10E-05	D	351.	0.190E-02 ± 0.57E-04
C	900.	0.101E-03 ± 0.30E-05	D	352.	0.521E-02 ± 0.91E-04
C	911.	0.387E-03 ± 0.70E-05	D	354.	0.909E-02 ± 0.12E-03
C	922.	0.659E-03 ± 0.90E-05	D	355.	0.118E-01 ± 0.14E-03
C	933.	0.803E-03 ± 0.10E-04	D	357.	0.135E-01 ± 0.15E-03
C	944.	0.861E-03 ± 0.11E-04	D	358.	0.138E-01 ± 0.15E-03
C	955.	0.876E-03 ± 0.11E-04	D	360.	0.140E-01 ± 0.15E-03
C	966.	0.860E-03 ± 0.11E-04	D	361.	0.131E-01 ± 0.15E-03
C	977.	0.823E-03 ± 0.11E-04	D	363.	0.120E-01 ± 0.14E-03
C	988.	0.760E-03 ± 0.10E-04	D	364.	0.980E-02 ± 0.12E-03
C	999.	0.724E-03 ± 0.10E-04	D	366.	0.781E-02 ± 0.11E-03
C	1010.	0.675E-03 ± 0.90E-05	D	367.	0.582E-02 ± 0.95E-04
C	1021.	0.631E-03 ± 0.90E-05	D	369.	0.344E-02 ± 0.75E-04
C	1032.	0.522E-03 ± 0.80E-05	D	370.	0.224E-02 ± 0.64E-04
C	1043.	0.416E-03 ± 0.70E-05	D	372.	0.193E-02 ± 0.61E-04
C	1054.	0.276E-03 ± 0.50E-05	D	373.	0.151E-02 ± 0.53E-04
C	1065.	0.148E-03 ± 0.40E-05	D	375.	0.137E-02 ± 0.51E-04
C	1076.	0.740E-04 ± 0.20E-05	D	376.	0.127E-02 ± 0.51E-04

Table C.3. Inclusive Hydrogen Cross Sections, Kinematics E and F. Listed are the inclusive cross sections for hydrogen as a function of energy loss, ω. The uncertainties are statistical and do not include the 10% systematic uncertainty.

Kine.	ω (MeV)	σ (nb/sr/MeV)	Kine.	ω (MeV)	σ (nb/sr/MeV)
E	953.	0.000E-00 ± 0.00E-00	F	1697.	0.100E-05 ± 0.00E-00
E	956.	0.000E-00 ± 0.00E-00	F	1708.	0.800E-05 ± 0.10E-05
E	958.	0.100E-05 ± 0.00E-00	F	1719.	0.100E-04 ± 0.10E-05
E	961.	0.100E-05 ± 0.00E-00	F	1730.	0.120E-04 ± 0.10E-05
E	963.	0.110E-04 ± 0.10E-05	F	1741.	0.130E-04 ± 0.10E-05
E	966.	0.640E-04 ± 0.20E-05	F	1752.	0.130E-04 ± 0.00E-00
E	968.	0.141E-03 ± 0.20E-05	F	1763.	0.110E-04 ± 0.00E-00
E	971.	0.192E-03 ± 0.30E-05	F	1774.	0.130E-04 ± 0.00E-00
E	973.	0.244E-03 ± 0.30E-05	F	1785.	0.120E-04 ± 0.00E-00
E	976.	0.265E-03 ± 0.30E-05	F	1796.	0.130E-04 ± 0.00E-00
E	978.	0.273E-03 ± 0.30E-05	F	1807.	0.130E-04 ± 0.00E-00
E	981.	0.277E-03 ± 0.30E-05	F	1818.	0.120E-04 ± 0.00E-00
E	983.	0.260E-03 ± 0.30E-05	F	1829.	0.130E-04 ± 0.00E-00
E	986.	0.255E-03 ± 0.30E-05	F	1840.	0.120E-04 ± 0.00E-00
E	988.	0.223E-03 ± 0.30E-05	F	1851.	0.110E-04 ± 0.00E-00
E	991.	0.185E-03 ± 0.30E-05	F	1862.	0.110E-04 ± 0.00E-00
E	993.	0.141E-03 ± 0.20E-05	F	1873.	0.800E-05 ± 0.00E-00
E	996.	0.103E-03 ± 0.20E-05	F	1884.	0.700E-05 ± 0.00E-00
E	998.	0.640E-04 ± 0.20E-05	F	1895.	0.600E-05 ± 0.00E-00
E	1001.	0.440E-04 ± 0.10E-05	F	1906.	0.300E-05 ± 0.00E-00

Table C.4. Solid Target Inclusive Cross Sections for Kinematics A ($E = 2.445$ GeV, $\theta_e = 20.5°$). Listed are the inclusive cross sections for carbon, iron, gold, as a function of energy loss, ω. The uncertainties are statistical and do not include the 10% systematic uncertainty.

ω (MeV)	^{12}C σ (nb/sr/MeV)	^{56}Fe σ (nb/sr/MeV)	^{197}Au σ (nb/sr/MeV)
200.	0.111 ± 0.009	0.450 ± 0.036	1.13 ± 0.08
225.	0.376 ± 0.018	1.578 ± 0.070	5.02 ± 0.17
250.	0.622 ± 0.024	2.511 ± 0.088	8.05 ± 0.22
275.	1.041 ± 0.031	4.013 ± 0.111	11.45 ± 0.26
300.	1.324 ± 0.035	5.027 ± 0.125	16.07 ± 0.31
325.	1.592 ± 0.038	5.997 ± 0.136	18.88 ± 0.34
350.	1.880 ± 0.042	7.032 ± 0.147	21.88 ± 0.36
375.	1.893 ± 0.042	7.486 ± 0.152	23.38 ± 0.38
400.	2.031 ± 0.043	7.679 ± 0.154	24.98 ± 0.39
425.	2.014 ± 0.043	8.403 ± 0.161	25.84 ± 0.40
450.	1.991 ± 0.043	7.855 ± 0.155	27.23 ± 0.41
475.	1.983 ± 0.043	8.168 ± 0.159	27.58 ± 0.41
500.	1.875 ± 0.042	8.113 ± 0.158	28.30 ± 0.42
525.	1.781 ± 0.041	7.964 ± 0.157	27.21 ± 0.41
550.	0.030 ± 0.000	0.030 ± 0.000	0.03 ± 0.00

Table C.5. Solid Target Inclusive Cross Sections for Kinematics B ($E = 2.445$ GeV, $\theta_e = 32.0°$). Listed are the inclusive cross sections for carbon, iron, gold, as a function of energy loss, ω. The uncertainties are statistical and do not include the 10% systematic uncertainty.

ω (MeV)	^{12}C σ (nb/sr/MeV)	^{56}Fe σ (nb/sr/MeV)	^{197}Au σ (nb/sr/MeV)
580.	0.012 ± 0.001	0.045 ± 0.002	0.141 ± 0.013
600.	0.035 ± 0.002	0.135 ± 0.003	0.423 ± 0.022
620.	0.047 ± 0.003	0.174 ± 0.004	0.555 ± 0.025
640.	0.058 ± 0.003	0.213 ± 0.004	0.664 ± 0.028
660.	0.059 ± 0.003	0.252 ± 0.004	0.762 ± 0.030
680.	0.068 ± 0.003	0.289 ± 0.005	0.794 ± 0.030
700.	0.076 ± 0.003	0.312 ± 0.005	0.926 ± 0.033
720.	0.084 ± 0.004	0.341 ± 0.005	1.060 ± 0.035
740.	0.095 ± 0.004	0.356 ± 0.005	1.141 ± 0.036
760.	0.097 ± 0.004	0.386 ± 0.005	1.209 ± 0.037
780.	0.112 ± 0.004	0.414 ± 0.006	1.296 ± 0.039
800.	0.105 ± 0.004	0.441 ± 0.006	1.382 ± 0.040
820.	0.114 ± 0.004	0.456 ± 0.006	1.469 ± 0.041
840.	0.114 ± 0.004	0.487 ± 0.006	1.678 ± 0.044
860.	0.052 ± 0.003	0.206 ± 0.004	0.686 ± 0.028
880.	0.002 ± 0.000	0.002 ± 0.000	0.002 ± 0.000

Table C.6. Solid Target Inclusive Cross Sections for Kinematics C ($E = 3.245$ GeV, $\theta_e = 28.6°$). Listed are the inclusive cross sections for carbon, iron, gold, as a function of energy loss, ω. The uncertainties are statistical and do not include the 10% systematic uncertainty.

ω (MeV)	^{12}C σ (nb/sr/MeV)	^{56}Fe σ (nb/sr/MeV)	^{197}Au σ (nb/sr/MeV)
800.	0.0018 ± 0.0001	0.0050 ± 0.0004	0.014 ± 0.002
825.	0.0105 ± 0.0005	0.0363 ± 0.0011	0.121 ± 0.007
850.	0.0129 ± 0.0006	0.0462 ± 0.0012	0.153 ± 0.007
875.	0.0158 ± 0.0006	0.0592 ± 0.0014	0.177 ± 0.008
900.	0.0202 ± 0.0007	0.0743 ± 0.0016	0.228 ± 0.009
925.	0.0231 ± 0.0008	0.0897 ± 0.0017	0.272 ± 0.010
950.	0.0261 ± 0.0008	0.0992 ± 0.0018	0.319 ± 0.011
975.	0.0308 ± 0.0009	0.1142 ± 0.0019	0.372 ± 0.012
1000.	0.0326 ± 0.0009	0.1276 ± 0.0020	0.400 ± 0.012
1025.	0.0360 ± 0.0009	0.1363 ± 0.0021	0.440 ± 0.013
1050.	0.0364 ± 0.0009	0.1504 ± 0.0022	0.478 ± 0.013
1075.	0.0427 ± 0.0010	0.1663 ± 0.0023	0.513 ± 0.014
1100.	0.0436 ± 0.0010	0.1839 ± 0.0025	0.569 ± 0.014
1125.	0.0474 ± 0.0011	0.1981 ± 0.0026	0.639 ± 0.015
1150.	0.0540 ± 0.0012	0.2153 ± 0.0027	0.680 ± 0.016
1175.	0.0189 ± 0.0007	0.0710 ± 0.0015	0.265 ± 0.010
1200.	0.0010 ± 0.0000	0.0010 ± 0.0000	0.001 ± 0.000

Table C.7. Solid Target Inclusive Cross Sections for Kinematics D ($E = 0.845$ GeV, $\theta_e = 78.5°$). Listed are the inclusive cross sections for carbon, iron, gold, as a function of energy loss, ω. The uncertainties are statistical and do not include the 10% systematic uncertainty.

ω (MeV)	^{12}C σ (nb/sr/MeV)	^{56}Fe σ (nb/sr/MeV)	^{197}Au σ (nb/sr/MeV)
325.	0.0020 ± 0.0000	0.002 ± 0.000	0.002 ± 0.000
330.	0.0126 ± 0.0007	0.028 ± 0.006	0.115 ± 0.014
335.	0.1035 ± 0.0022	0.400 ± 0.024	0.995 ± 0.043
340.	0.1153 ± 0.0023	0.451 ± 0.026	1.142 ± 0.046
345.	0.1234 ± 0.0024	0.473 ± 0.026	1.177 ± 0.046
350.	0.1333 ± 0.0025	0.446 ± 0.025	1.351 ± 0.050
355.	0.1374 ± 0.0026	0.573 ± 0.029	1.377 ± 0.050
360.	0.1437 ± 0.0026	0.565 ± 0.029	1.431 ± 0.051
365.	0.1444 ± 0.0026	0.556 ± 0.028	1.514 ± 0.053
370.	0.1465 ± 0.0027	0.585 ± 0.029	1.577 ± 0.054
375.	0.1490 ± 0.0027	0.531 ± 0.028	1.581 ± 0.054
380.	0.1566 ± 0.0027	0.570 ± 0.029	1.654 ± 0.055
385.	0.1571 ± 0.0027	0.661 ± 0.031	1.713 ± 0.056
390.	0.1520 ± 0.0027	0.598 ± 0.029	1.710 ± 0.056
395.	0.1610 ± 0.0028	0.663 ± 0.031	1.795 ± 0.057
400.	0.1611 ± 0.0028	0.651 ± 0.031	1.870 ± 0.059

Table C.8. Solid Target Inclusive Cross Sections for Kinematics E ($E = 1.645$ GeV, $\theta_e = 80.0°$). Listed are the inclusive cross sections for carbon, iron, gold, as a function of energy loss, ω. The uncertainties are statistical and do not include the 10% systematic uncertainty.

ω (MeV)	^{12}C σ (/nb/sr/MeV)	^{56}Fe σ (nb/sr/MeV)
910.	0.00020 ± 0.00000	0.0002 ± 0.0000
920.	0.00187 ± 0.00015	0.0074 ± 0.0006
930.	0.00253 ± 0.00018	0.0106 ± 0.0007
940.	0.00273 ± 0.00019	0.0104 ± 0.0007
950.	0.00342 ± 0.00021	0.0124 ± 0.0007
960.	0.00362 ± 0.00022	0.0135 ± 0.0008
970.	0.00401 ± 0.00023	0.0142 ± 0.0008
980.	0.00437 ± 0.00024	0.0169 ± 0.0009
990.	0.00467 ± 0.00025	0.0185 ± 0.0009
1000.	0.00483 ± 0.00026	0.0190 ± 0.0009
1010.	0.00595 ± 0.00029	0.0242 ± 0.0011
1020.	0.00563 ± 0.00028	0.0235 ± 0.0010

Table C.9. Solid Target Inclusive Cross Sections for Kinematics F ($E = 3.245$ GeV, $\theta_e = 50.0°$). Listed are the inclusive cross sections for carbon, iron, gold, as a function of energy loss, ω. The uncertainties are statistical and do not include the 10% systematic uncertainty.

ω (MeV)	^{12}C σ (nb/sr/MeV)	^{56}Fe σ (nb/sr/MeV)	^{197}Au σ (nb/sr/MeV)
1600.	0.00002 ± 0.00000	0.0000 ± 0.0000	0.0000 ± 0.0000
1640.	0.00002 ± 0.00000	0.0000 ± 0.0000	0.0000 ± 0.0000
1680.	0.00028 ± 0.00002	0.0011 ± 0.0001	0.0037 ± 0.0006
1720.	0.00068 ± 0.00003	0.0029 ± 0.0002	0.0074 ± 0.0009
1760.	0.00089 ± 0.00003	0.0041 ± 0.0002	0.0113 ± 0.0011
1800.	0.00121 ± 0.00004	0.0057 ± 0.0003	0.0148 ± 0.0012
1840.	0.00159 ± 0.00004	0.0068 ± 0.0003	0.0191 ± 0.0014
1880.	0.00200 ± 0.00005	0.0081 ± 0.0003	0.0255 ± 0.0016
1920.	0.00263 ± 0.00005	0.0112 ± 0.0004	0.0332 ± 0.0019
1960.	0.00315 ± 0.00006	0.0149 ± 0.0004	0.0410 ± 0.0021

BIBLIOGRAPHY

[1] S. Frullani and J. Mougey, Advances in Nucl. Phys. **14**, Plenum Press, New York 1984.

[2] J. Mougey *et al.*, Nuc. Phys. **A262**, 461 (1976).

[3] D. H. Wilkinson, *Comments on Nucl. Part. Phys.* **2**, 48 (1968).

[4] S. Boffi, C. Giusti, F. D. Pacati, and M. Radici, *Electromagnetic Response of Nuclei*, Oxford Science Publications, Oxford (1996).

[5] James J. Kelly, Advances in Nuclear Physics, 75 (1996).

[6] T. de Forest, Nucl. Phys. **A392**, 232 (1983).

[7] S. Pollock *et al.*, Phys. Rev. C **53**, 2305 (1996).

[8] H. W. L. Naus, Ph. D. thesis, U. Amsterdam (1989) unpublished; H. W. L. Naus and J. H. Koch, Phys. Rev. C **36**, 2459 (1987).

[9] R.M. Barnett et al., Physical Review **D5**4, 72 (1996)

[10] L. Ray *et al.*, Phys. Rep. **212**, 223 (1991).

[11] S. Boffi *et al.*, Nucl. Phys. **A319**, 461 (1979).

[12] S. Boffi *et al.*, Nucl. Phys. **A319**, 461 (1979).

[13] R. J. Glauber, "Lectures in Theoretical Physics," vol. 1, ed. W. E. Brittin and D. G. Dunhan, Interscience (1959).

[14] H. Gao, R. J. Holt, and V. R. Pandharipande, Phys. Rev. C **54** 2779, (1996).

[15] V. R. Pandharipande and Steven C. Pieper, Phys. Rev. C **45** 791 (1992).

[16] D. G. Ireland *et al.*, Phys. Rev. C **50**, 1626 (1994).

[17] A. H. Mueller, *Proceedings of the XVII Rencontre de Moriond, 1982*, ed. J. Tran Thanh Van (Editions Frontieres, Gif-sur-Yvette, France) 13 (1982); S. J. Brodsky, *Proceedings of the Thriteenth International Symposium on Multiparticle Dynamics*, ed. W. Kittel, W. Metzger, and A. Stergiou (World Scientific, Singapore) 963 (1982).

[18] L. L. Frankfurt *et al.*, Commen. Nucl. Part. Phys. **21** 1 (1992).

[19] G. van der Steenhoven *et al.*, Phys. Lett. **B156**, 151 (1985).

[20] G. van der Steenhoven *et al.*, Phys. Rev. C **32**, 1787 (1985).

[21] G. van der Steenhoven *et al.*, Nucl. Phys. **A480**, 547 (1988).

[22] G. van der Steenhoven *et al.*, Nucl. Phys. **A484**, 445 (1988).

[23] G. van der Steenhoven *et al.*, Nucl. Phys. **A517**, 17c (1991).

[24] L. Lapikas, Nucl Phys. **A553**, 297c (1993).

[25] P. Barreau *et al.*, Nucl. Phys. **A402**, 515 (1983).

[26] G. van der Steenhoven *et al.*, Phys. Rev. Lett. **57**, 182 (1986).

[27] P. E. Ulmer *et al.*, Phys. Rev. Lett. **59**, 2259 (1987).

[28] R. W. Lourie *et al.*, Phys. Rev. Lett. **56**, 2364 (1986).

[29] G. van der Steenhoven *et al.*, Phys. Rev. Lett. **58**, 1727 (1987).

[30] D. F. Geesaman *et al.*, Phys. Rev. Lett. **63**, 734 (1989).

[31] G. Garino *et al.*, Phys. Rev. C **45**, 780 (1992).

[32] N. Makins *et al.*, Phys. Rev. Lett. **72**, 1986 (1994).

[33] T. G. O'Neill *et al.*, Phys. Lett. B **351**, 87 (1995).

[34] D. Dutta, Ph. D. thesis, Northwestern University (1998).

[35] H. J. Bulten *et al.*, Phys. Rev. Lett. **74**, 4775 (1995).

[36] M. van der Schaar *et al.*, Phys. Rev. Lett. **68**, 776 (1992).

[37] C. Yan *et al.*, Nucl. Instr. and Meth. **A365**, 261 (1995).

[38] C. Yan *et al.*, Nucl. Instr. and Meth. **A365**, 46 (1995).

[39] P. Gueye, M. Tiefenback, and C. Yan, Hall C Beam Energy Measurement, CEBAF Internal Report (unpublished).

[40] E. A. J. M. Offerman *et al.*, Phys. Rev. C **44**, 1096 (1991).

[41] Oxford Cryosystems, 3 Blenheim Office Park, Lower Road, Long Hanborough, Oxford OX8 8LN, United Kingdom.

[42] K. Gustafsson, TJNAF Hall C Cryotarget Density Dependence on Beam Current, CEBAF Internal Report, 14 Nov, 1996, unpublished.

[43] *Conceptual Design Report Basic Experimental Equipment*, J. Domingo, B. Hartline, H. Grunder, eds., 13 April 1990.

[44] W. J. Cummings, SOS Handbook, CEBAF Internal Report, 17 June 1996, unpublished.

[45] MI-TECH Metals Inc., Indianapolis, IN, USA.

[46] K. L. Brown *et al.*, SLAC Report No. 91, Rev. 2, 1977.

[47] LeCroy Corporation, 700 Chestnut Ridge Road, Chestnut Ridge, NY 10977, USA.

[48] E .I. du Pont and de Nemours and Company.

[49] *Beam Curent Measurement in Hall C*, C. Armstrong, Internal Report, 29 July, 1996, unpublished.

[50] O. K. Baker *et al.*, Nucl. Instr. and Meth. **A367** 92 (1995).

[51] Nanometrics System Inc., Oak Park, IL, USA.

[52] E. Jastremzembski, D. R. Quarrie, W. A. Watson III, "The CEBAF Trigger Supervisor," *Conference Record of the 1991 IEEE Nuclear Science Symposium*, vol. 1, pp. 569-573.

[53] Hewlett-Packard Company, 3000 Hanover Street, Palo Alto, CA 94304 U.S.A.

[54] D. Abbott *et al.*, in *Proc. of the IEEE Conference on Real-Time Computer Applications in Nuclear, Particle, and Plasma Physics*, edited by R. Fox (Michigan State Univeristy-NSCL, East Lansing, 1995), p. 147.

[55] H. Blok *et al.*, Nucl. Instr. and Meth. **A262** (1987) 291.

[56] M. Berz, COSY INFINITY Version 7 Reference Manual, NSCL Technical Report MSUCL-977, Michigan State University, 1995.

[57] *Shower Counter and Čerenkov Efficiencies*, I Niculescu, Internal Report, Apr 22, 1997, unpublished.

[58] N. C. R. Makins, Ph. D. thesis, Massachusetts Institute of Technology, (1994) unpublished.

[59] M. Gari and W. Krümpelmann, Z. Phys. A **322**, 689 (1985).

[60] D. Abbott *et al.*, Phys. Rev. Lett **80**, 5072 (1998).

[61] C. Giusti and F. D. Pacati, Nucl. Phys. **A473**, 717 (1987); C. Giusti and F. D. Pacati, Nucl. Phys. **A485**, 461 (1988).

[62] F. Perey and B. Buck, Nucl. Phys. **32**, 353 (1962).

[63] L. R. B. Elton and A. Sift, Nucl. Phys. **A94**, 52 (1967).

[64] G. E. Brown and M. Rho, Nucl. Phys. **A372**, 397 (1981).

[65] E. N. M. Quint, Ph. D. thesis, U. Amsterdam (1988) unpublished.

[66] J. W. Negele, Phys. Rev. C **1**, 1260 (1970); J. W. Negele and D. Vautherin, Phys. Rev. C**5**, 1472 (1972).

[67] J. Schwinger, Phys. Rev. **76**, 790 (1949).

[68] L. W. Mo and Y. S. Tsai, Rev. Mod. Phys. **201**, 205 (1969).

[69] C. de Calan, H. Navelet, and J. Picard, Nucl. Phys. **B348**, 47 (1991).

[70] *Radiative Corrections for (e,e′p) Reactions*, N. C. R. Makins *et al.*, unpublished.

[71] R. A. Early, Nucl. Inst. and Meth. **109**, 93 (1973).

[72] J. T. O'Brien *et al.*, Phys. Rev. C **9**, 1418 (1974).

[73] Y. Jin, H. P. Blok, and L. Lapikás, Phys. Rev. C **48**, R964 (1993).

[74] X. Ji and J. Engel, Phys. Rev. C **40**, R497 (1989).

[75] J. W. Lightbody and J. S. O'Connell, Computers in Physics, vol. 2, 57 (1988).

[76] M. Zhalov, private communication.

[77] C. J. Horowitz, Nuc. Phys. **A368**, 503 (1981).

[78] H. de Vries *et al.*, *Atomic Data and Nuclear Data Tables* **36**, 505 (1987).

[79] O. Benhar, private communication.

[80] James J. Kelly, Phys. Rev. C **54**, 2547 (1996).

[81] O. Benhar *et al.*, Rev. Mod. Phys. **65**, 817 (1993).

[82] N. N. Nikolaev *et al.*, Phys. Lett. B **317**, 281 (1993).

[83] N. N. Nikolaev *et al.*, Phys. Rev. C **50**, R1296 (1994).

[84] N. N. Nikolaev *et al.*, Journal of Experimental and Theoretical Physics **82**, 1046 (1996).

[85] Available from R. A. arndt and L. D. Roper, Physics Department, Virginia Polytechnic Institute, Blacksburg, VA 24061-0435.

[86] Ye. S. Golubeva *et al.*, Phys. Rev. C **57**, 2618 (1998).

[87] J. D. Walecka, Ann. Of Phys., 491 (1974); *Theoretical Nuclear and Subnuclear Physics*, Oxford Science Publications, Oxford (1995).